REPORT DOCUMENTATION PAGE	READ INSTRUCTIONS BEFORE COMPLETING FORM

1. REPORT NUMBER AFOSR-TR- 82-0610	2. GOVT ACCESSION NO. AD-A117922	3. RECIPIENT'S CATALOG NUMBER

4. TITLE (and Subtitle) A Program of Research on Microfabrication Techniques for VLSI Magnetic Devices	5. TYPE OF REPORT & PERIOD COVERED Interim 9-30-80 - 9-29-81
	6. PERFORMING ORG. REPORT NUMBER

7. AUTHOR(s) M. H. Kryder, C. L. Bauer, J. A. Rayne, A. Guzman	8. CONTRACT OR GRANT NUMBER(s) AFOSR 80-0284

9. PERFORMING ORGANIZATION NAME AND ADDRESS Carnegie-Mellon University Pittsburgh, PA 15213	10. PROGRAM ELEMENT, PROJECT, TASK AREA & WORK UNIT NUMBERS 2305C1 61102F

11. CONTROLLING OFFICE NAME AND ADDRESS Air Force Office of Scientific Research /NE Bolling Air Force Base Washington, DC 20332	12. REPORT DATE October 1, 1981
	13. NUMBER OF PAGES 277

14. MONITORING AGENCY NAME & ADDRESS(If different from Controlling Office)	15. SECURITY CLASS. (of this report) Unclassified
	15a. DECLASSIFICATION/DOWNGRADING SCHEDULE

16. DISTRIBUTION STATEMENT (of this Report)

Approved for public release; distribution unlimited.

DTIC SELECTED AUG 3 1982 H

17. DISTRIBUTION STATEMENT (of the abstract entered in Block 20, If different from Report)

18. SUPPLEMENTARY NOTES

19. KEY WORDS (Continue on reverse side if necessary and identify by block number)

Magnetic Bubble, Memory, Logic, Amorphous Magnetic Materials, Garnet, VLSI, Magneto-Optic, Magneto-Optic Recording, Thermo-Magnetic Recording, Charged Walls, Ion Implantation, Transmission Electron Microscopy

20. ABSTRACT (Continue on reverse side if necessary and identify by block number)

Means of fabricating, selectively modifying, and characterizing single crystal epitaxial garnet and amorphous magnetic thin films are being investigated with the intention of developing new materials and processes for magnetic devices including bubble, recording, magneto-optic, and microwave devices. Techniques for the routine deposition of these materials have been established and several novel characterization techniques developed. Transmission electron microscopy has been used to investigate structural effects of ion implantation

DD FORM 1473 EDITION OF 1 NOV 65 IS OBSOLETE

AD A117922

DTIC FILE COPY

20.

on garnet materials and selected area transmission electron diffraction has been used to study strain profiles at boundaries between implanted and unimplanted garnet material. A magneto-optic photometer system which permits characterization of thin ($\sim$ 1000A) layers of magnetic material with resolution on the order of a micrometer has been developed and used to magnetically characterize ion implanted layers of garnet. Optical spectra of ion implanted garnets are being studied to gain information on the stoichiometric and crystal field deviations produced by ion implantation in garnets. Amorphous magnetic materials are being researched in an attempt to replace the more expensive single crystal magnetic garnets. Furthermore, both contiguous-disk and current-access magnetic bubble devices have been fabricated and a novel current-access ion-implanted device demonstrated to require low power dissipation.

Accession For

NTIS GRA&I

DTIC TAB

Unannounced

Justification

By

Distribution/

Availability Codes

Avail and/or

Dist   Special

A

DTIC
COPY
INSPECTED
2

AFOSR-TR- 82-0610

A PROGRAM OF RESEARCH ON

MICRO-FABRICATION TECHNIQUES

FOR VLSI MAGNETIC DEVICES

ANNUAL INTERIM PROGRESS REPORT No. 1

To: Air Force Office of Scientific Research
      Bolling Air Force Base
      Washington, D.C. 20332

October 1, 1981

M. H. Kryder, C. L. Bauer, J. A. Rayne, A. Guzman

Security Classifcation: UNCLASSFIED

DISTRIBUTION: UNLIMITED

A PROGRAM OF RESEARCH ON MICRO-FABRICATION TECHNIQUES

FOR VLSI MAGNETIC DEVICES

PROGRESS REPORT

TABLE OF CONTENTS '

A PROGRAM OF RESEARCH ON MICRO-FABRICATION TECHNIQUES FOR VLSI MAGNETIC DEVICES

PROGRESS REPORT

Oct. 1, 1981

INTRODUCTION

The Air Force Office of Scientific Research has been funding a research project entitled "A Program of Research on Microfabrication Techniques for VLSI Magnetic Devices since September 29, 1980. This report describes the progress made on this research project during its first year of funding. As is indicated below, during the first year we have established a liquid phase epitaxial growth facility for single crystal garnets to the point that we are now growing materials for both one micrometer and 0.5 micrometer bubble devices. We have furthermore begun investigations of amorphous magnetic bubble materials, amorphous and polycrystalline magnetic materials for drive layers, contiguous disk devices, and polycrystalline cobalt chrome materials for self biasing of bubble devices. We have established facilities for routine cnaracterizaiton of magnetic materials and have developed a unique magneto-optic photometer system which permits characterization of thin layers of magnetic material in devices having micron sized dimensions. We have furthermore developed techniques for using transmission electron microscopy to investigate the structural effects of ion implantation on garnet materials and have used transmission electron diffraction to study strain profiles at boundaries between implanted and non implanted garnet material. Both contiguous disk and current accessed device structures have been fabricated at Carnegie-Mellon University under this grant and a novel current-access ion-implanted device structure invented at CMU has been fabricated and demonstrated to require lower power dissipation than conventional perforated sheet current-accessed devices. Furthermore, investigations of the optical spectra of garnet materials being carried out under this grant hold promise of providing detailed information on the stoichiometric and crystal field deviations present in garnet materials before and after ion implantation. These optical investigations were unanticipated at the time of the original proposal but appear to be quite promising as a tool for understanding the microscopic effects of ion implantation on the crystal structure.

In the first year of this contract, three papers were accepted for publication and one masters degree thesis was produced. Additional publications and theses are expected in the near future.

The work being carried out under this grant is in an area of critical need to our nation. During the past year, three US companies stopped manufacturing magnetic bubble devices, leaving only Intel and Motorola as US vendors of bubble memory devices. Both IBM and Bell Telephone Laboratories continue to be active in the

bubble memory area, however, they typicaly do not sell components to outside users. By comparison, the Japanese are moving ahead continuously and at a great pace in their development of bubble memory devices. Hitachi has clearly marketed more bubble memory devices than any other manufacturer and is presently producing them at a rate exceeding 25,000 memories per month.

The research effort at Carnegie-Mellon University, being funded by this grant, has attracted significant attention from industrial manufacturers and users of bubble memories. Most industrial firms involved in the manufacture of bubble memories have provided some support to this program in the form of equipment donations and/or support of an individual graduate student through a fellowship. Researchers involved in this program are sought out by industrial workers actively involved in bubble memory design and fabrication for consultation on future technology directions. Without the grant support provided by the AFOSR grant number 80-0284, this program would not be possible. Below are contained a progress summary by area and detailed reports from selected areas, as well as appended publications.

SUMMARY OF PROGRESS

THE LIQUID PHASE EPITAXIAL GROWTH OF GARNETS is now a routine procedure at CMU and we are beginning to push the limits of garnets as small bubble materials. During this past year we have developed a liquid phase epitaxial growth facility, grown 108 magnetic garnet films suitable for ion implanted bubble devices and developed characterization techniques to study the epitaxial films, both implanted and unimplanted. Compositions for both 1 micrometer diameter bubbles and 0.5 micrometer diameter bubbles have been developed. The compositions we are pursuing have high magnetostriction and are expected to be suitable for ion implanted devices. We have fabricated ion implanted device structures on the one micrometer bubble materials and have observed bubble propagation, although further evaluation of the materials is still necessary. We are presently trying to fabricate device structures on the 0.5 micrometer bubble diameter materials so that we can evaluate them as device materials. A detailed report on the LPE growth of garnet films at CMU is included later in this report.

In conjuction with the above we have begun to design complete major-minor-loop memory chips using ion implanted contiguous disk technology. This technology is well known to offer an order of magnitude density increase over present generation bubble memory devices. We do not intend to compete directly the device design teams at Bell Laboratories, IBM, Hitachi, Fujitsu and NEC who are also working on this technology, but rather to complement and extend their efforts to higher densities. The industrial efforts are mainly directed at 2 micrometer and 1 micrometer diameter bubbles. We intend to seek out the problems in the submicrometer range.

RF SPUTTERED AMORPHOUS MAGNETIC BUBBLE MATERIALS are being investigated at CMU. Amorphous films were introduced as a possible bubble material in 1973 by Chaudhari, Gambino and Cuomo (P. Chaudhari, J. J. Cuomo, R. J. Gambino, IBM J. Res. Develop. 17, 66 (1973)) and enjoyed a period of substantial interest because of their potential for replacing the comparatively expensive garnet signal crystal films. However, studies showed (A. H. Eschenfelder, "Amorphous Films for Bubbles" Ferromagnetic Materials, vol. 2, 345 (1980)) that GdCoMo amorphous films supporting one micrometer and two micrometer bubbles were significantly more temperature sensitive than garnets. Only in the submicron range did GdCoMo films appear to offer advantage over garnets.

Having the ability to fabricate devices using submicron bubbles and with the emphasis of this contract being to develop new microfabrication techniques for magnetic devices, we have begun to seriously address the potential of rare-earth, transition-metal films for submicron devices. During the past year we have deposited a large number of GdCoMo films and have observed bubble domains ranging in size from submicron dimensions to several microns. We have characterized magnetic parameters of these films using magneto-optic measurements and ferromagnetic

resonance and are now at the point that we feel we understand the influence of RF sputtering conditions on the magnetic parameters of the films. A report detailing this work forms a later chapter of this document.

AMORPHOUS AND POLYCRYSTALLINE NiCoB FILMS are being investigated as a possible replacement for the drive layer of ion implanted contiguous disk bubble devices. These films can be grown with a wide range of magnetization values, very low anisotropy and a low coercive force. Initial studies by M. H. Kryder using Ferrofluid indicated that by etching patterns into the surface of nickel cobalt boron films, it was possible to form weakly charged domain walls which could be used to move bubble domains around pattern boundaries. Bubble propagation margins were, however, quite small and we hoped that a thorough investigation of NiCoB films would yield drive layers which would provide strongly charged walls and good propagation margins. During the first year of this contract we have deposited a large number of NiCoB films and have studied the influence of RF sputtering conditions on the magnetic parameters of the films. Thus far we have, however, been unsuccesful in obtaining strongly charged walls. Recent investigations using transmission electron diffraction to investigate the ion implanted layers of garnets have shown the importance of magnetostriction and stress relaxation at the boundary between the unimplanted and implanted material in forming the charged wall. Furthermore, studies on (100) garnets, which are also described later, confirm the importance of the inverse magnetostrictive effect on the formation of charged walls. We therefore presently feel that to produce an amorphous drive layer, it will be necessary to have high magnetostriction magnetic materials with low coercivity, low anisotropy and magnetization values of a few hundred to a few thousand gauss. It does not appear that the NiCoB films will be able to provide the high magnetostriction. Therefore we are presently reviewing the literature on amorphous magnetic materials to identify compositions offering the desired range of properties and expect to investigate these new materials in the future. A lengthy report on the NiCoB films is in preparation by graudate student R. J. DeCesaris, who will use the report as a Masters degree thesis. This thesis will not be available for a couple more months, however, and is therefore not included with this report. It will be forwarded as soon as it is available.

FILMS OF POLYCRYSTALLINE CoCr AND SmCoCr are being investigated as possible self-bias layers for bubble domain materials. Liu et. al. (J. Appl. Phys. 42, 1360 (1971)) showed that bubble domains could be stablized by the energy of a domain wall separating a high coercive force layer magnetized anti-parallel to the bubble domain and the bubble itself. Devices using such bias layers would require no external bias magnets and therefore would be significantly lighter and more compact than presently manufactured devices. CoCr films have previously been shown to exhibit a preferred direction of magnetization perpendicular to the film plane and a relatively large coercive force. However, these materials are not true permanent magnet materials and do break up into domain structures when the applied field is

removed, although the remanence is quite high. This is due to the fact that the coercive force of these films is less than H_k - $4\pi Ms$. Accordingly we have chosen to investigate samarium additions to cobalt chrome. Samarium cobalt is well known as a permanent magnet material offering coercive forces up to about 30,000 gauss. We therefore believe that high coercive force samarium cobalt chromium films may be suitable for self bias layers on bubble materials. A report describing the influence of sputtering conditions on the properties of cobalt chrome is included later in this report.

MAGNETO-OPTIC MEASUREMENTS OF THE MAGNETIC CHARACTERISTICS OF THE ION IMPLANTED LAYERS OF GARNETS were carried out using a magneto-optic photometer system developed at CMU. These measurements were the first reported in which magneto-optic techniques were successfully used on the thin ion implanted layers of garnets having in-plane magnetization. Values of K_1 = -3150 ergs/cm^3, K_u = 14,500 erg/cm^3, and K_i = -30,000 erg/cm^3 were measured for the crystalline, uniaxial, and ion implantation induced anisotropy constants respectively. In a $(GdTmY)_3$ Ga_x $Fe5-x$ O_{12} garnet driving layer which had been ion implanted and had $4\pi M_s$ = 585 gauss, statistical analysis indicated approximately 8% accuracy in the measured values. Furthermore analysis of the data gives a direct measure of the three-fold anisotropy which the magnetization in the ion implanted layer feels as it is rotated in the plane. These measurements therefore give the first direct measurements of the three-fold critical curve which was first proposed by Lin et. al (IEEE Trans. Magnet. MAG-14, 494 (1978)) to describe the anisotropy in the ion implanted layers.

As described in earlier reports, this instrument had a resolution capability of about 5 microns and used reflected light from the sample for measurements. Furthermore all sample rotations in the photometer were done by hand, making the technique of gathering data on anisotropic affects very time consuming. Since these earlier reports, we have redesigned the magnetometer to improve these characteristics. The photometer is now equipped with a small motor to rotate samples in the plane. Thus the magneto-optic response of the samples may be plotted on a chart recorder directly as a function of the angular orientation of the sample. Furthermore we are in the process of modifying the instrument so that it may use not only reflected light, but also transmitted light for measurement. This modification is expected to provide added sensitivity and simpler data analysis, hopefully obviating the need for complex computer analysis of data. In addition we are adding a Leitz MPV Photometer Unit to our system to make possible submicrometer spot size measurements. With submicrometer spot size resolution, we will be able to probe the magneto-optic response of devices using micrometer and submicrometer dimensions. This is the only magnetometer technique which allows one to make magnetic measurements on such a fine scale.

In addition to using this system for measurements on ion implanted layers of garnet films, we are now beginning to use it also for investigations of amorphous

and polycrystalline magnetic materials. Recently we have begun some investigations on thin film and magneto-resistive recording heads for example.

A report describing this magneto-optic photometer system is included as part of this document and a paper describing the system at an earlier stage of development is attached as an appendix.

STRAIN PROFILES IN ION IMPLANTED GARNETS have been investigated by transmission electron diffraction under this contract. The use of transmission electron microscopy for the investigation of magnetic devices on garnet materials is new, although transmission electron microscopy has been used before on a number of other materials. Its application to garnets was restricted because of the difficulty of thinning the 500 micrometer thick substrate from under a 2000 angstrom thick ion implanted layer. We have developed polishing and ion milling techniques to do this. Although other microstructural investigations of ion implanted layers on garnets have been carried out such as X-ray diffraction measurements, and Mossbauer spectroscopy transmission electron microscopy is the only technique which affords high resolution. Since the thrust of research being carried out under this contract is microfabrication in magnetic devices, transmission electron microscopy with its high resolution capability is especially applicable. Selected area electron diffraction was used to obtain strain profiles around unimplanted disks in thin (less than 2000 angstroms) films of (111) oriented garnets. Measurements of in-plane lattice constant were made as a function of position in $(SmYGdTm)_3Ga_{0.4}Fe_{4.6}O_{12}$ films implanted with oxygen (120 KeV, $1x10^{14}/cm^2$ and helium (80 KeV, $4x10^{15}/cm^2$). In most cases the data show a relaxation of stress normal to and near to the implanted boundary. These results provide experimental confirmation of recently proposed models suggesting that stress relaxation normal to an implanted boundary is critical to the formation of charged walls. These findings have lead us to the conclusion that we must use large magnetostriction materials for the amorphous drive layers discussed earlier. These findings also lead us to consider the affects of the non-uniform stress field on the local anisotropy in the underlying bubble layer of a ion implanted contiguous disk device. Analysis of this stress field showed that under the edge of an implanted region there is a tensile stress perpendicular to the film plane which reduces the perpendicular anisotropy causing reduced bubble nucleation thresholds in bubble materials with large negative values of λ_{111}. A more lengthy report describing the use of electron diffraction for characterizing the ion implanted layers of garnets is included as a later section of this document and a paper presented at the Magnetism and Magnetic Materials Conference in Atlanta, November 10 through 13 is attached as an appendix.

THE INFLUENCE OF STRESS RELAXATION AT THE BOUNDARIES OF ION IMPLANTED AREAS IN (100) GARNET FILMS ON CHARGED WALLS were investigated under an NSF grant but are related to the work using transmission electron microscopy and therefore described here. These investigations, carried out with the use of Bitter

Technique to observe the charged walls, shows that in the (100) film we studied, charged walls are stable only at particular orientations of the applied field. Now that we understand that stress relaxation at the boundary is critical in the formation of charged walls, we have realized that in the (100) film we studied it should be expected that charged walls form only for particular orientations of the applied field. This is due to the fact that λ_{111} and λ_{100} (the magnetostriction constants) are of different sign, causing the preferred axis of magnetization to alternate between perpendicular and parallel to the boundary, depending on the orientation of the boundary relative to the crystalline axese. Thus our work with transmisison electron microscopy as well as our work with the Bitter Technique on (100) oriented films, have led us to the conclusion that we should seek garnet materials with λ_{100} and λ_{111} of the same sign. Such films would presumably support charged walls suitable for bubble propagation and exhibit fourfold rather than threefold symmetry in their anisotropic behavior. In principle it is possible to grow materials with λ_{100} equal to λ_{111} in which case the magnetostriction would be isotropic leading to more isotropic behavior of the charged walls. A draft of a paper describing these new findings is attached as an appendix to this document.

MICROFABRICATION OF ION-IMPLANTED CONTIGUOUS DISK DEVICES having $2\mu m$ minimum features and employing $1\mu m$ bubble materials has been succesfully carried out at CMU. Propagation margins of about 15% were measured in these devices. We have designed and fabricated masks for the propagation of bubbles in a $2\mu m$ cell size having $1\mu m$ miminum features and employing $0.5\mu m$ bubbles using electron beam lithography at the National Research and Resource Facility for submicron structures at Cornell University. We are now in the process of using these masks to fabricate $0.5\mu m$ bubble propagation patterns on garnets grown here at CMU. In parallel with this effort we are also designing complete major-minor loop devices having full data-in data-out memory capability and expecting to demonstrate memory operation with a bit density of 2.5×10^7 bits/cm^2. These masks will most likely find application, not only on ion implanted garnet materials but also on the amorphous materials described earlier. In these efforts we are not trying to compete directly with the efforts in industry but are trying to push the technology to higher density limits than industry is presently actively pursuing. We have performed basic theoretical analyses of the scaling laws of these devices (M. H. Kryder, IEEE Trans. Magnet., MAG-17 2385 (1981)) and wish to explore the validity of these analyses experimentally. Our work is thus directed at understanding the physics of device scaling and device operation in the submicrometer range rather than the development of very high density memories which is properly being carried out by industry. We have had and continue to have a strong influence on industry in its pursuit of high density technology. Evidence of our influence in this area is the fact that several of the industrial companies working in the magnetics area consult with us about the prospects of contiguous disk technology.

MICROFABRICATION OF APERTURED SHEET DUAL CONDUCTOR CURRENT ACCESS DEVICES is also being carried out at CMU. These devices, unlike the presently manufactured bubble devices do not require a rotating magnetic field, hence the rotating field coils which add expense and weight to the presently manufactured devices are not needed. These current access devices are furthermore much higher performance than field access devices, offering more than one order of magnitude higher bit rates. A theoretical analysis of scaling laws of these devices was also carried out (M. H. Kryder, IEEE Trans. Magnet. MAG-17, 2392 (1981)) and indicates that the technology has problems with high on-chip power dissipation and that these problems grow as the device is scaled to higher densities. Because of these power dissipation problems, industry in the United States is not actively pursuing current access devices. In spite of the problems which we in fact identified, we feel that the technlogy has very attractive attributes and is worthwhile pursuing from the long term point of view. In addition to offering the advantages of reduced weight and higher performance we have found the current access technology to be especially suitable for performing logic with magnetic bubbles. We are presently designing chips having both memory and logic capabilities. We have already simulated the logic operations using a computer aided design program which we developed under an NSF contract. We hope to surmount power dissipation problems by using field accessed contiguous disk technology for memory and the current accessed apertured sheet technology on the same chip for logical functions. Since a large portion of the chip is memory, power dissipation problems would be reduced. Thus far we have fabricated current accessed propagation structures, thus demonstrating our capability of fabricating these devices, and are anxious to complete the first chip designs containing logic functions so that we may fabricate and test them. A Masters degree thesis by Michael Alex describing some early results on the microfabrication of current accessed devices is included as an appendix to this document.

A NOVEL CURRENT ACCESSED ION-IMPLANTED DEVICE which combines the ultra high density of ion implanted contiguous disk devices with the high performance and simpler packaging (no rotating field coils) of current accessed devices was invented at CMU and has been pursured under AFOSR contract number AFOSR-80-0284. This new device uses currents in apertured conductor sheets to access charged walls in ion-implanted layers of garnet. By clever design, magnetic poles produced by the charged walls are made to add to the poles produced by the currents flowing around the apertures on the conductor sheets. Measurements made on simple disk shaped structures show that the new current accessed ion implanted device requires only 50% of the drive current of a current accessed device using no charged walls. This factor of two reduction in current represents a factor of four reduction in power dissipation. An article describing this new device structure was presented at the Conference on Magnetism and Magnetic Materials in Atlanta, November 10-13, 1981 and is attached as an appendix to this document. We are now in the process of doing detailed calculations of the in-plane fields around apertures in the conductor

sheets and based upon these calculations are designing structures suitable for bubble propagation using this technology.

A STUDY OF THE OPTICAL SPECTRA OF MAGNETIC GARNET EPILAYERS has been intiated in order to obtain a better understanding of stochiometric and crystal field deviations present with and without ion implantation in garnet materials. Such investigations to our knowledge have not been carried out before on garnet materials and furthermore were not included in the original proposal. However, data obtained thus far make us hopeful that this will evolve into a very fruitful area of research for understanding the damage produced by ion implantation in garnets. Preliminary investigations of gadolinium galium garnet substrates and representative epilayers have determined tentative sample parameters (i.e. substrate and epilayer thickness) best suited to the optical measurements. Design of a low temperature magneto-optical measurement system has been finished with construction of the system expected to be completed by January 1982. From measurements made at room temperature we have been able to clearly identify the energy levels corresponding to the fine structure of Gd^{3+}. We expect that low temperature measurements and the use of Er^{3+} as a probe will enable us to probe the local crystal fields in both unimplanted and implanted garnets. Hence, we hope to be able to identify the actual damage done by ion implantation. For example we hope to be able to identify whether the damage is due to a displaced oxygen atom or due to the presence of unexpected implanted ions in the crystal lattice. This work should shed some light on the issues of why hydrogen implants, for example, are known to produce much larger anisotropy changes without creating dead layers than other implanted ions such as neon. An improved understanding of the actual damage mechamisms could lead to improved implanted devices. Recent work by the Japanese (H. Matsutera, et al., Paper BA-4, Magnetism and Magnetic Materials Conference, Atlanta, Nov. 10-13, 1981) using Monte Carlo simulations suggest that implants of heavier ions such as neon produce multiple collisions of oxygen atoms within the lattice whereas hydrogen implants typically do not cause oxygen atoms to be dislocated with enough energy to cause multiple collisions. Our optical measurements hopefully will provide some experimental basis for judging the validity of these models. A short report describing this work in more detail is included later in this document. It is noted that this work is presently being supported with funds from this grant because we believe it has high potential for some fundamental understanding of the effects of ion implantation on garnets. These investigations were not anticipated at the beginning of this contract, however, and were not accounted for in the budget. We hope that during the next six months we will be able to resolve the issue of how powerful a tool the optical spectra will be so that we may better judge how to allocate our resources and whether additional funding in this area might be necessary to give it the support required.

The Growth of Liquid Phase Epitaxial Garnets

Introduction

Single crystal epitaxial garnets are the basis for bubble devices, magneto-static surface wave devices, and magneto-optic devices being manufactured and investigated in industry throughout the world today. Although we are attempting to develop alternative materials, we are at the same time interested in pushing garnets to their limits. We are interested in increasing our understanding of these very perfect single crystal materials and the effects which ion implantation has on them. Accordingly we have established a facility for the liquid phase epitaxial (LPE) growth of garnets and have developed characterization techniques to study both implanted and unimplanted garnet films. Furthermore, we have developed and refined materials suitable for 1 μm and 0.5 μm bubbles.

Our first goal was to design and build control circuits for the garnet substrate vertical movement and rotation motors. We acquired the equipment necessary to prepare the melt and to grow epitaxial films. The thermal response of the furnace was determined and steps were taken to improve the temperature stability of the melt. Film characterization techniques were developed or improved in order to determine the effects of changes in growth conditions on film parameters. Establishing reproducible growth conditions enabled us to concentrate our effort on optimizing the bubble material without excessive worry about system instabilities.

Characterization equipment developed as part of this project includes:

- double-crystal x-ray diffractometer for lattice mismatch measurements

- ferromagnetic resonance: improvement to existing equipment

- hot stage for measurement of collapse field temperature coefficient

- pulser to nucleate bubbles in the polarizing microscope

We also made use of existing characterization equipment

- polarizing microscope with field coils for stripwidth, collapse field, and defect density measurement

- reflectance spectrophotometer for film thickness measurement

Our effort has been directed towards producing two different melt compositions, one for one micron diameter bubbles and the other for half micron diameter bubbles. Using two crucibles we have been able to speed up this development process. To date, 11/3/81, we have grown 108 films.

The basic composition for the one micron material is a yttrium iron garnet with aluminum and

gallium substituted to reduce the magnetic moment to a suitable value. Three rare earths are substituted for yttrium; samarium, thulium, and gadolinium. The amounts of each substituting rare earth are calculated considering each of the following parameters •

- lattice mismatch between film and substrate

- uniaxial anisotropy

- damping

- magnetic .moment

- magnetostriction

- temperature coefficient

As some of these effects are mutually exclusive, a balance between opposing effects must be sought.

Controllers, Furnace, and Related Equipment

The liquid phase epitaxial (LPE) growth of magnetic garnets is achieved by dipping a garnet substrate (GGG) into a supercooled melt. The process starts with the substrate being lowered into the furnace, slowly through the top and then quickly to the preheat position just above the melt. The preheating time is long enough to ensure that the melt and the substrate are at the same temperature. The substrate is then lowered into the melt and growth occurs, assuming the melt temperature is below saturation. During growth the substrate is rotated at a constant speed, although the direction of rotation is reversed at fixed time intervals to improve film uniformity and to help stir the melt. At the end of the growth period, the rotation is stopped and the substrate is withdrawn from the melt. The substrate is stopped at the preheat position and the rotation speed is gradually increased to a high value (400 rpm) to remove flux drops. At the end of the spin period, the rotation speed is reduced to that used during growth and the substrate is withdrawn from the furnace.

The growth process can be run automatically. The operator sets the desired growth time, preheat time, spin-off time, and rotation reversal period. The rotation speed for growth and spin-off are set separately. The melt must be soaked at a temperature above the saturation temperature for several hours for homogenization. The temperature is reduced stepwise to the growth temperature, with smaller steps taken near the desired growth temperature to minimize overshoot. Once the desired temperature is reached, the growth process may begin. However, one should not keep the melt at supersaturation too long.

In addition to the controllers, we also had to construct a holder for the substrate. This is made out of platinum wire, as most other materials will corrode in the melt and contaminate it.

The trick to designing a good holder is to minimize the thermal capacity and the substrate contact area, but provide enough rigidity in order that the substrate does not create excessive turbulence in the melt or come loose during spin-off. The standard design is a three legged holder with two rings at the top which fit the alumina tube snugly. There are notches at the bottoms of the legs which the substrate fits into. The elasticity of the wire provides adequate force to hold the substrate. The alumina rod is attached to the rotation motor with an adjustable coupler. The coupler enables us to compensate for nonconcentric rotation due to the alumina not being straight.

Characterization

Routine measurements to characterize the magnetic film properties include:

- film thickness

- zero-field stripwidth

- collapse field

- uniaxial anisotropy

- lattice mismatch

Additional measurements to determine the temperature coefficient of collapse field were made on selected films. Composition measurements have not been made yet. Estimates of film composition are made from the melt composition.

Ferromagnetic resonance is used to measure the uniaxial anisotropy $H_K - 4\pi M$. $4\pi M$ is determined from collapse field, stripwidth, and thickness. [1] $H_K/4\pi M$ ($=Q$) is a measure of stability of bubble domains. Improvements have been made to the FMR equipment to increase the signal to noise ratio. This is necessary in order to measure the thin films and also to detect the resonance attributed to an ion-implanted layer. At present, the FMR equipment is optimally designed for scanning frequency at constant field. As we prefer to scan the field at fixed frequency for several different frequencies, some modifications are necessary. In addition, we have found that using the stripline rather than the microstrip configuration results in a significant increase in the signal level. With a stripline, the sample lies between the conductor and the groundplane, whereas with a microstrip the sample is on top of the conductor.

The other significant advance we have made in developing characterization techniques is in measuring lattice mismatch. We initially used single crystal x-ray diffraction to measure 444 and 888 reflections. While this was adequate for films with a relatively large mismatch (>0.003A) resolution limitations prevented more accurate measurement. Also, both the K_{a_1} and K_{a_2} diffraction peaks were present. While this does not pose a problem for measuring the bulk films, it adds confusion to implanted film measurements.

To improve the measurement we first used a quartz monochromator. We were able to remove the K_{a_2} peak but the half value width was not significantly better than that with the single crystal. The next step was to use a GGG crystal instead of the quartz. Due to geometrical constraints in the monochromator we were only able to use the 444 reflection. The G̃GG proved to be more effective than the quartz crystal in removing K_{a_2} and narrowing the half value width, but we felt we could do better by making use of the 888 reflection. In addition aligning the monochromator to eliminate the K_{a_2} peak was difficult.

We designed a monochromator which makes use of the 888 reflection from a GGG crystal. The x-ray diffractometer is shown schematically in Fig. 1.
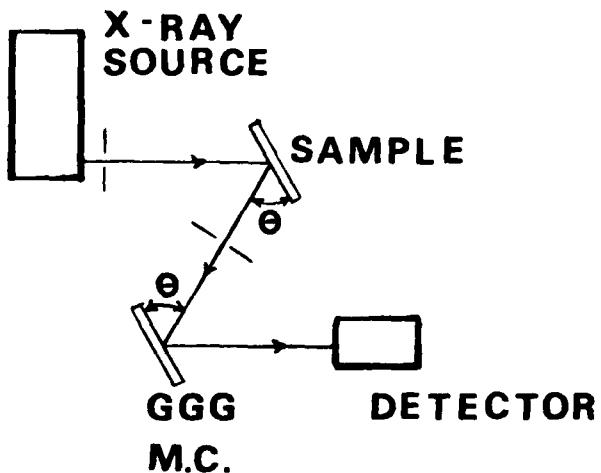
Figure 1: Double Crystal X-Ray Diffractometer

The monochromating crystal angle is adjustable but the detector angle is fixed. This monochromator removes the K_{a_2} peak. The resolution is much higher because of the larger separation of K_{a_1} peaks. The half value width is nearly the same as that obtained using the 444 monochromator. This monochromator was designed to be quickly and easily tuneable. Minor improvements still need to be made, but the basic design appears to work well.

For the mismatch measurement, the relative difference between film and substrate peaks is used. With the 888 monochromator using the 888 sample reflection we can easily resolve mismatches as small as 0.001A with 0.0005A accuracy. Smaller mismatches are detectable, by peak broadening, but the separate peaks are not resolvable.

Discussion of Results

To optimize the material parameters, we first needed to determine the effect of different growth conditions. This included measuring the melt saturation temperature. To determine the optimal growth conditions plots of growth temperature with each of the following parameters were made:

- growth rate

- magnetic moment, $4\pi M$

- mismatch, Δa_o

- anisotropy constant, K_U

- anisotropy field, H_K

We also measured the effect of rotation rate, rotation reversal period, and melt depletion on growth rate.

The saturation temperature is the temperature at which the garnet dissolved in the flux will begin to crystallize if a nucleation site is available. This temperature is determined experimentally by extrapolating on the growth rate versus temperature plot to zero growth. A typical plot is shown in Fig.2. The accuracy in determining T_{sat} is 1°C. We have verified this by trying to grow films at 1°C above and 1°C below the predicted T_{sat}.

Magnetostriction Calculation

The magnetostriction constant (λ_{111}) is a useful measure of the implantability of the garnet. The anisotropy change is determined in part by λ_{111}. To measure λ_{111} several techniques are available but they all require sophisticated equipment. An approximate value may be obtained by using the magnetostriction constants of the rare-earth iron garnets in a method developed by White. [2] White's method involves calculating the effect of gallium dilution on each rare-earth iron garnet, and then summing the diluted rare-earths weighting each in proportion to the stoichiometric amount in the film.

This calculation was done for our 1/2 μm material. The result was $\lambda_{111} = -4.11 \times 10^6$. For comparison, the 1 μm material which IBM is currently using for their single layer film contiguous disk devices has a λ_{111} which we calculated to be -3.50×10^6. Our 1 μm material has a $\lambda_{111} = -3.82 \times 10^6$ based on the expected composition.

White's method deals specifically with gallium dilution. In our 1/2 μm material we are using aluminum instead of gallium. We believe that there should not be a significant discrepancy in estimating λ_{111}.
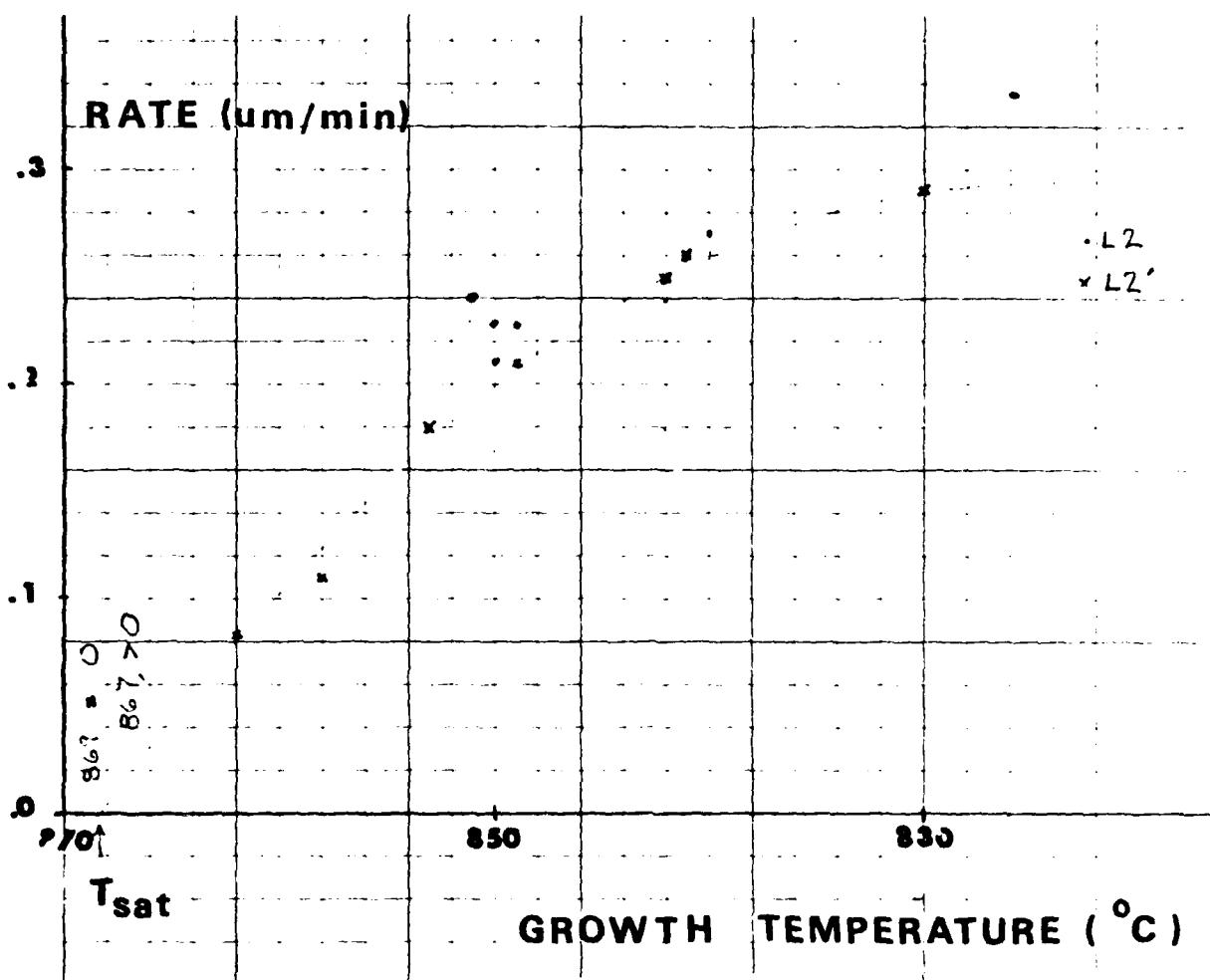
Figure 2: Growth Rate versus Growth Temperature

Growth Rate

The growth rate of the LPE film is determined by the concentration of garnet in the melt, the degree of supercooling, and substrate rotation rate. The rare earth concentration was chosen so that garnet would be the predominant phase. Loss of lead due to flux removal and evaporation appears to be more significant in determining melt saturation temperature than does depletion of other oxides in flux removal and film growth. A typical melt composition is shown below: The expected composition for this melt is

$$Y_{0.8} \ Sm_{0.3} \ Tm_{1.3} \ Gd_{0.6} \ Fe_{4.6} \ Al_{0.2} \ Ga_{0.2} \ O_{12}$$
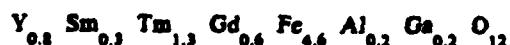
From the melt composition we see that the garnet contributes about 1 mole percent to the total

Oxide	Weight	Moles
Sm_2O_3	.1541 gms	4.42×10^{-4}
Tm_2O_3	.9740	2.52×10^{-4}
Y_2O_3	.3938	1.74×10^{-3}
Gd_2O_3	.4269	1.18×10^{-3}
Ga_2O_3	1.3219	7.05×10^{-3}
Al_2O_3	.5880	5.77×10^{-3}
Fe_2O_3	30.6285	0.192
B_2O_3	7.6079	0.109
PbO	358.75	1.607

flux. The lead accounts for 83 mole percent, iron is 10 mole percent, and boron makes up the difference, 6 mole percent.

Lattice Mismatch

The lattice mismatch of the epitaxial films is measured using a double crystal x-ray diffractometer. The mismatch between film and substrate is measured from the angular separation between their K_{a_1} peaks. A correction is made for the stress attributed to the film being constrained in two directions. The result is the perpendicular lattice expansion of a nonconstrained film. The mismatch is calculated using the following equation.

$$\delta d/d = -\delta\theta/\tan\theta$$
$$\Delta a_o = (1-\nu/ 1+\nu)\ \delta d$$

where $d = 12.383$ Å (lattice constant for GGG), θ is the angle incident x-ray makes with plane of film, $\delta\theta$ is half the angular separation between the film and substrate K_{a_1} peaks, and δd is the uncorrected lattice mismatch. Δa_o is the corrected mismatch, and ν is Poisson's ratio which is 0.29 for garnet.

The sign of the mismatch is determined by the relative position of the peaks. If the film is in compression, the film peak will be at a lower 2θ angle than the substrate. The magnitude of the substrate peak is greater than the film peak for films less than $3\mu m$ in thickness.

A typical curve is shown in Fig.3 The film is in tension, $\Delta a_o = 0.0075$ Å $(a_s > a_f)$. In this trace 2θ was scanned from $119.7°$ to $118.9°$. The K_{a_2} peak for the substrate should appear at $119.6°$ but it was removed by the monochromator. In this trace, 2θ for the GGG 888 reflection is at $119.115°$. The half value width for the substrate peak is $0.03° = \delta 2\theta$.

Uniaxial Anisotropy

The uniaxial anisotropy (K_U) is measured by ferromagnetic resonance. Experimentally, the sample is placed in a microbox with the conductor parallel to the film plane. The microbox is placed in the magnet such that the field is parallel to the film normal. A microwave current is
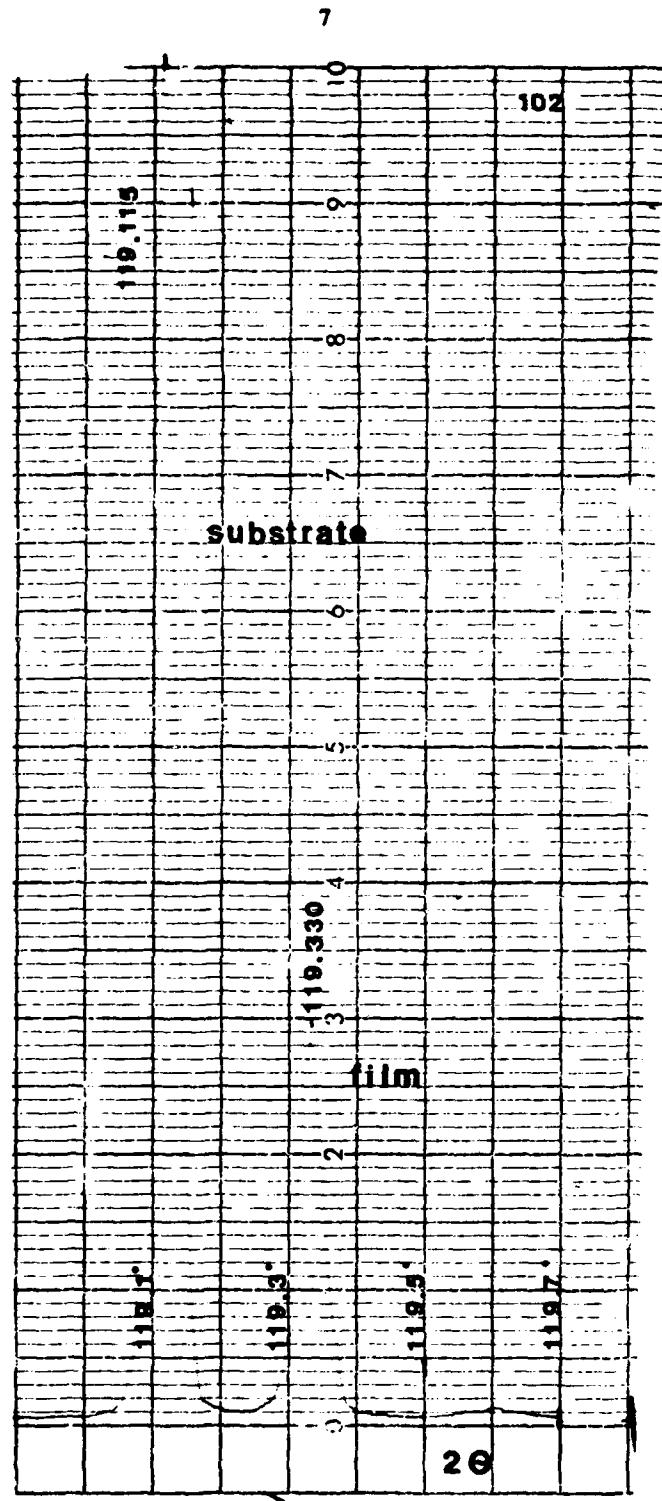
Figure 3: X-ray Diffraction Curve for Magnetic Garnet using GGG Monochromator at 888 Reflection

transmitted through the conductor, setting up a microwave field which is normal to the film's

normal. A modulating field, about 2 Oe in magnitude is superimposed on the applied magnetic field. The microwave signal detected by a diode is demodulated by the phase lock amplifier which is tuned to the modulating frequency. The resultant PLA output is a derivative curve proportional to the absorption of the microwave signal in the sample. A typical FMR trace is shown in Fig. 4.
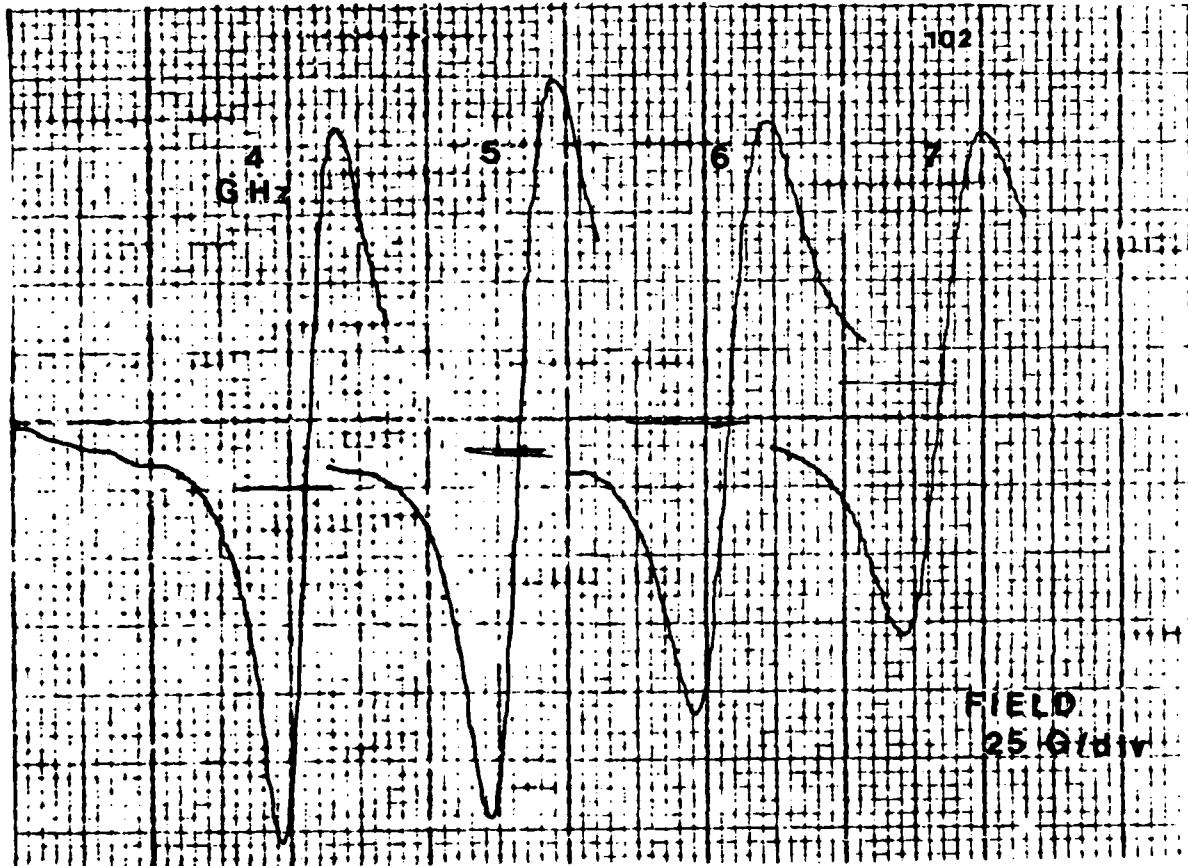
Figure 4: FMR Traces of Resonance Field for Constant Frequency

The four curves correspond to resonances at 4,5,6, and 7 GHz. The linewidth, which is the distance between the peaks (along the ordinate axis), is a measure of the damping in the film. A plot of resonance frequency versus resonance field is shown in Fig.5. The slope and zero field intercept are determined by a least squares fit. The zero-field frequency divided by the slope, γ, is equal to $H_K - 4\pi M - 4/3 \, K_1/M$. Assuming K_1/M is small compared to H_K we can determine H_K if $4\pi M$ is known. We obtain $4\pi M$ from bubble collapse field, zero field stripwidth, and film thickness measurements using the method of Fowlis and Copeland. [1]
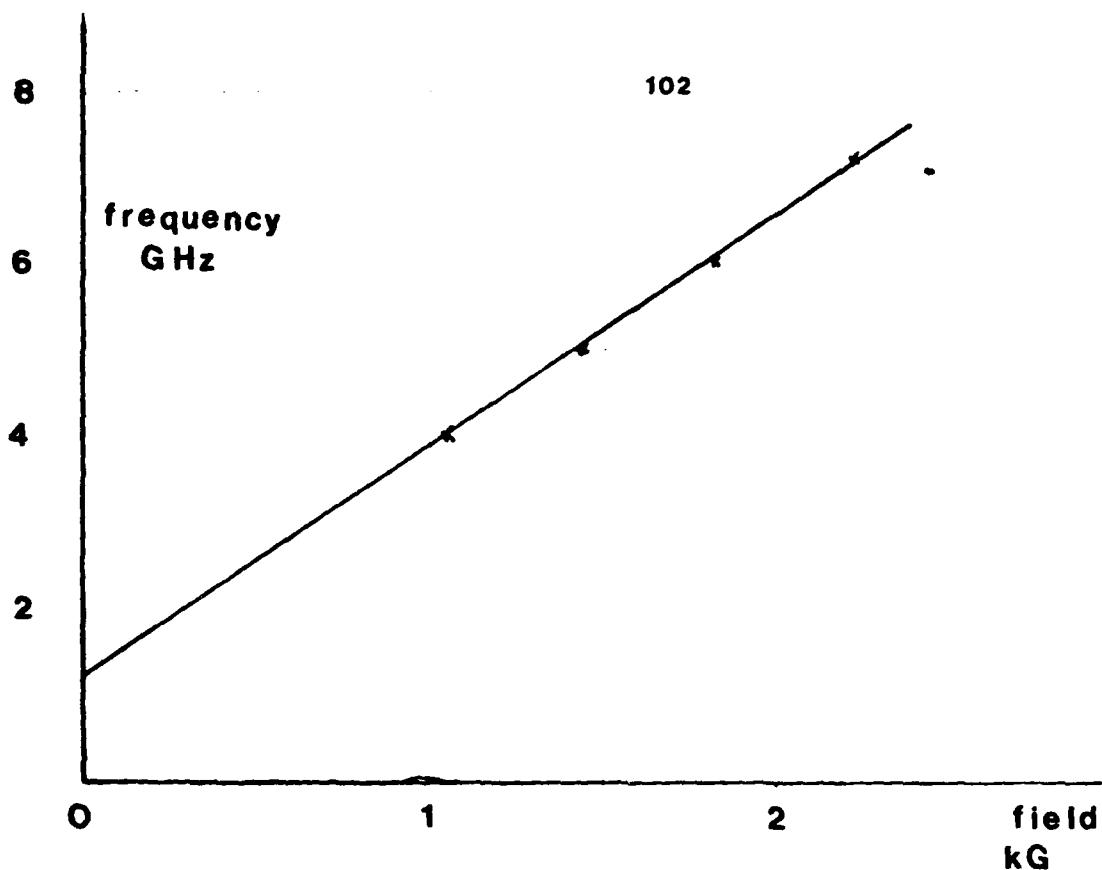
Figure 5: Resonance Frequency versus Resonance Field

Summary of Material Development

The advances we have made in developing material suitable for 1 and 1/2 micron bubbles have resulted from modifications of melt composition. The following is a narrative description of the highlights in this development process.

The initial composition, provided by IBM, is

$$Sm_{0.2} Gd_{0.6} Tm_{1.3} Y_{0.9} Ga_{0.2} Fe_{4.6} O_{12}$$

which has a magnetization $(4\pi M) = 545$ G, a characteristic length $l = 0.137$, and a $Q = 2.5$. For 1 micron bubbles the films are 1.24 microns thick. This composition is designed as a single layer ion implantable material.

Using this composition, we began growing films in a 50 ml crucible. The film uniformity was adversely affected by the small melt size (30 ml). A typical film had the following parameters

film #9, $t = 1.24$, $l = .13$, $4\pi M = 565$

Problems included poor furnace thermal stability and apparently large supercooling temperature

necessary to get a low 1 value. The characteristic length decreased with increased amount of supercooling.

Next, we obtained a larger crucible (125 ml) and mixed a new melt having the same composition as the original but twice the volume. A typical film

film #20, t = 0.99, l = .141, $4\pi M$ = 610

As we were interested in decreasing the bubble size, we increased the magnetization by adding 10% more iron to the melt. A typical film

film #22, t = 1.00 μm, l = .118 μm, $4\pi M$ = 650 G

At this time we obtained a second 125 ml crucible and designed an identical melt. A typical film:

film #37, t = 0.90 μm, l = .103 μm, $4\pi M$ = 656 G, Q=1.8

Not satisfied with the 1 value, we in:reased the iron again by the same amount. A typical film

film #50, t = 0.84 μm, l = .102 μm, $4\pi M$ = 710 G, Q=1.8

We did grow thicker films with the same composition and found the the 1 value was insensitive to film thickness. The problem with the material in film #50 is that the Q is too low. We were aiming for a 2.5 minimum Q. The next step was too add more samarium. Samarium contributes to the uniaxial anisotropy. Increasing the amount of Sm will increase Q at the expense of increased damping. A typical film with 20% iron and 50% Sm over the original composition is:

film #55, t = 0.96 μm, l = .099 μm, $4\pi M$ = 704 G

Using the new crucible with an identical melt composition A typical film:

film #49, t=0.96 μm, l=.115 μm, $4\pi M$ = 642 G, Q=2.2

Two separate accidents under different circumstances occured after these films were grown causing us to dump both melts. At this point we had verified that adding more samarium would help increase Q without significantly increasing 1 or FMR linewidth. We also discovered that the lattice parameter of the film was larger than that of the substrate so the films were in compression. To increase the uniaxial anisotropy energy it is advantageous to put the film in tension. As we were confident that we had a reasonably good rare-earth balance we opted to use aluminum to replace some of the gallium to decrease the film lattice parameter. We calculated our new composition as

$$Y_{0.8} Sm_{0.3} Tm_{1.3} Gd_{0.6} Fe_{4.6} Al_{0.2} Ga_{0.2} O_{12}$$

A typical film from the new melt:

film #59, t = 1.29, l = .119, $4\pi M$ = 653, Q=2.47

We were successful in increasing Q. We attribute our success to the favorable lattice mismatch. Another film from the same melt:

film #69, t = 1.26 μm, l = .136 μm, $4\pi M$ = 636 G,

Q=2.65, Δa_o =.002A tension

For clarity and brevity in this discussion, we have not listed all the growth parameters. Differences in 1 and $4\pi M$ for the same composition are attributed to differences in growth temperature. This material (#59, #69) may be suitable for 1 micron bubble devices. With 10% more iron to decrease the 1 value a typical film:

film #87, t = 1.38 μm, 1 = .125 μm, $4\pi M$ = 680 G,
Q=2.5, Δa_o =0.002 tension

Films 69 and 87 were both grown at 858°C. The temperature coefficient of the collapse field for #87 is plotted in Fig.6.
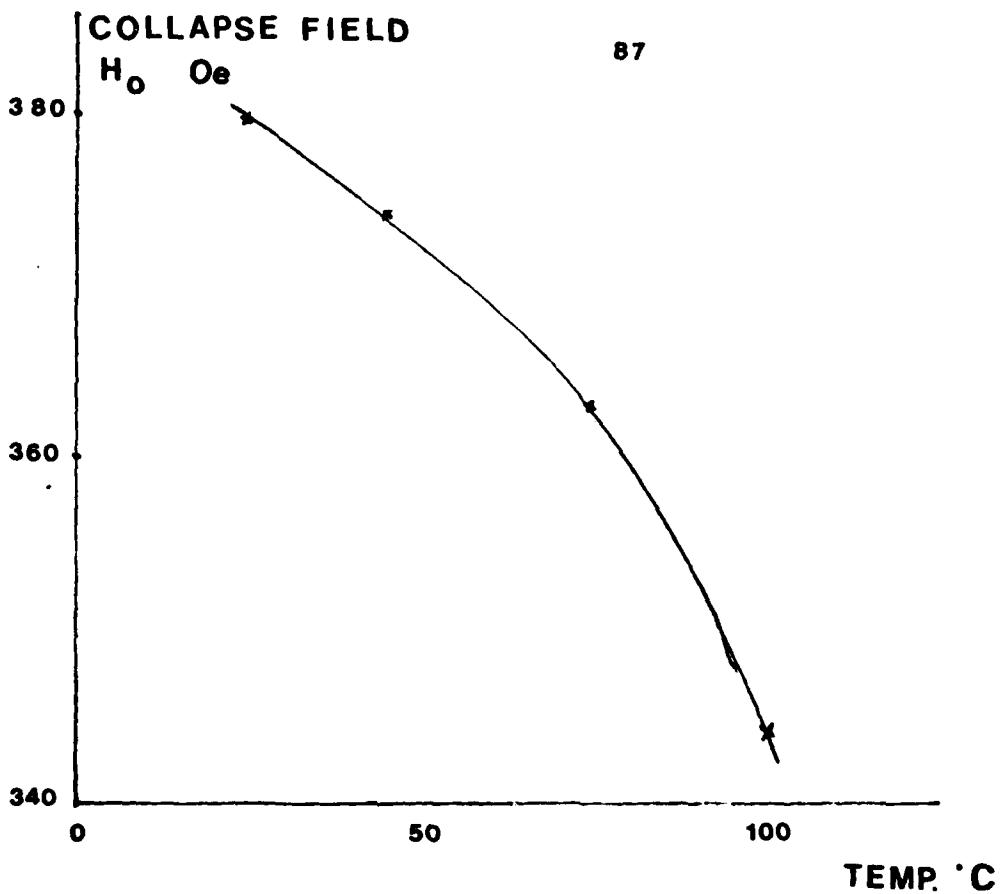
Figure 6: Temperature versus Collapse Field

From 25 to 65°C % $\Delta H_o / \Delta T°C$ =-0.08%/°C. This increased to -0.14%/°C as the temperature approached 100°C. This temperature response is considered acceptable for device purposes. For the next melt modification we decided to decrease the amount of gadolinium and increase the samarium content. The idea was that we could increase Q without causing a serious degradation of the temperature response. We also opted to increase yttrium at the expense of thulium to boost the magnetization. While decreasing thulium will lower the magnetostriction constant λ_{111},

the increase in the magnetization will allow us to substitute more aluminum. We are confident that this will help by putting the film in tension. Initially, we did not add any aluminum or gallium to the melt when we modified the composition. A typical film with the modified rare earth but no extra aluminum:

#94, t=0.85 μm, l=0.111 μm, $4\pi M$=774 G,
Q=2.24, Δa_o=0.003 compression

This brings us up-to-date with this melt. The next step will be to add more aluminum to decrease the magnetization and the film lattice parameter. We expect that the Q for this new composition will be the highest yet for our one micron material.

Half Micron Material Development

The initial composition we designed for 1/2 micron bubbles was

$$Sm_{0.35} Gd_{0.45} Tm_{1.3} Y_{0.9} Fe_{4.7} Al_{0.3} O_{12}$$

A typical film:

#80, t=0.96μm, l=0.083μm, $4\pi M$=960 G,
Q=2.0, Δa_o=0.009A tension

The temperature coefficient of bubble collapse was measured:

25°C - 50°C -0.07%/°C;
50°C-85°C, -0.18%/°C

This material is suitable for 0.75 micron bubbles. We modified the melt to achieve a lower l value. The modified composition is:

$$Sm_{0.35} Gd_{0.3} Tm_{1.3} Y_{1.05} Fe_{4.8} Al_{0.2} O_{12}$$

The temperature stability of this material should be acceptable as the large amount of iron will keep the Curie temperature up. Small changes in the gadolinium content, which is used to improve temperature stability, should not seriously affect the temperature response. In addition, we sought to further increase the magnetization by adding yttrium to replace the gadolinium. The decrease in aluminum will also increase the magnetization. A typical film:

film #83, t=0.69 μm, l=0.061 μm, $4\pi M$=1217 G,
Q=1.44, Δa_o=0.009A tension

The temperature coefficent of collapse field increased to -0.019%/°C. This is still an acceptable value. a similar film from the same melt:

film #83, t=0.79 μm, l=0.057 μm, $4\pi M$=1258 G,
Q=1.4, Δa_o=0.005A tension

This brings us up-to-date on the material development. We have characterized each melt to find the optimal growth conditions. At this time we are not certain if the Q for the 1/2 micron material is high enough. We hope to study the implanted films and make composition changes afterwards to improve the material.

—

Film Parameters

The amount of supersaturation is important in determining several film parameters including:

- Lattice Mismatch, Δa_o
- Characteristic Length
- Uniaxial Anisotropy, K_U
- Magnetization, $4\pi M$

In order to characterize each melt, we typically grew films over a range of temperatures.

Lattice Mismatch

The lattice parameter for our films increases linearly with an increase in supercooling. Typical results are shown in Fig. 7.
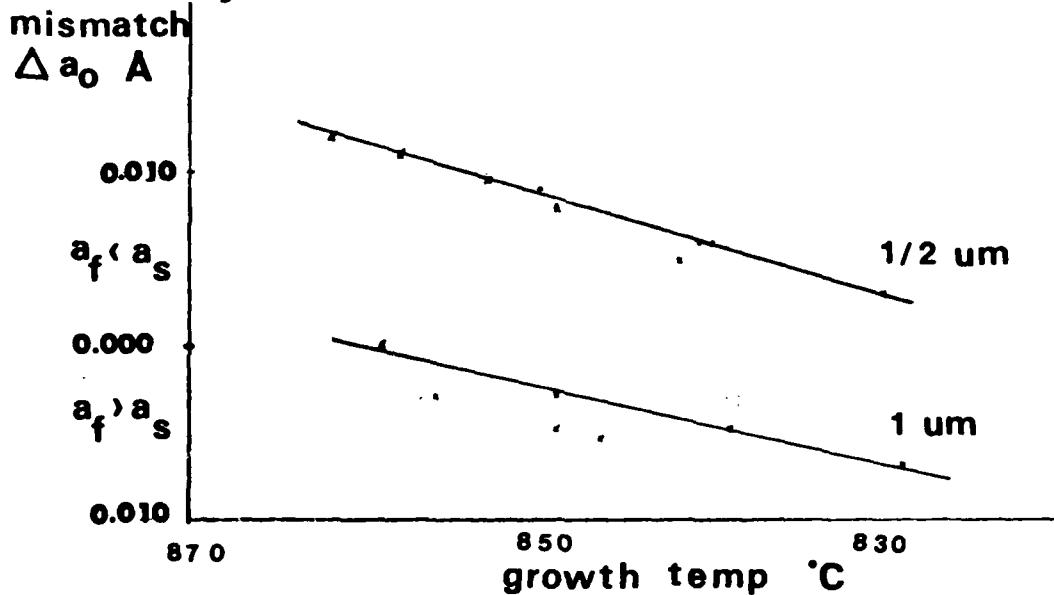

Figure 7: Lattice Mismatch versus Growth Temperature

The upper curve is for the 1/2 micron material and the lower curve is for 1 micron material. The 1 micron material has aluminum substituted for iron. The 1 micron material has both aluminum and gallium in it. The rare earth distribution is not significantly different. The slope for the aluminum substituted garnet is -0.0003 A/°C. The slope for the aluminum and gallium substituted garnet is -0.0002 A/°C. The increase is attributed to smaller size of the aluminum ion compared to gallium.

As the growth temperature decreases, the growth rate increases as does the lead content in the film. Lead will increase the lattice parameter of the film. No measurements of lead concentration have been made.

Characteristic Length

The characteristic length, l, is given by

$$l = 4(4\pi)(AK_U)^{1/2} / (4\pi M_s)^2$$

where A is the exchange constant, K_U is the uniaxial anisotropy energy density, $4\pi M_s$ is the magnetization. The characteristic length is related to the domain wall energy. It determines stable bubble size by accounting for uniaxial anisotropy and demagnetizing energy. The characteristic length decreases with increased undercooling, as shown in Fig.8
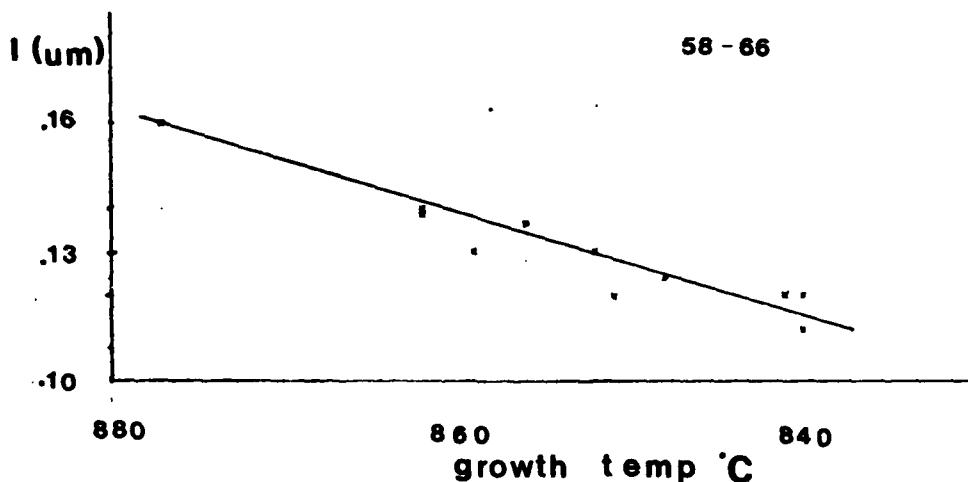

Figure 8: Characteristic Length versus Growth Temperature

The characteristic length is inversely proportional to the square of the magnetization. A and K_U will both increase with undercooling temperature but l is only proportional to the squareroot of these terms. From the l versus T plot, one can select the appropriate growth temperature to get the desired bubble size. The characteristic length is a material parameter and does not vary for films of the same composition with different thickness.

Magnetization

The magnetization decreases with increasing growth temperature. This is attributed to the increase in aluminum or gallium incorporated into the film at lower growth rates. A typical result is shown in Fig.9 One can select the magnetic moment for a given composition by choosing the correct growth temperature.

Film Quality

For device applications, film quality and reproducibility are important. Defects in the films, either induced by the substrate or induced in the growth process will limit their usefulness. The most important defects to control are those created by flux drops remaining on the film. The
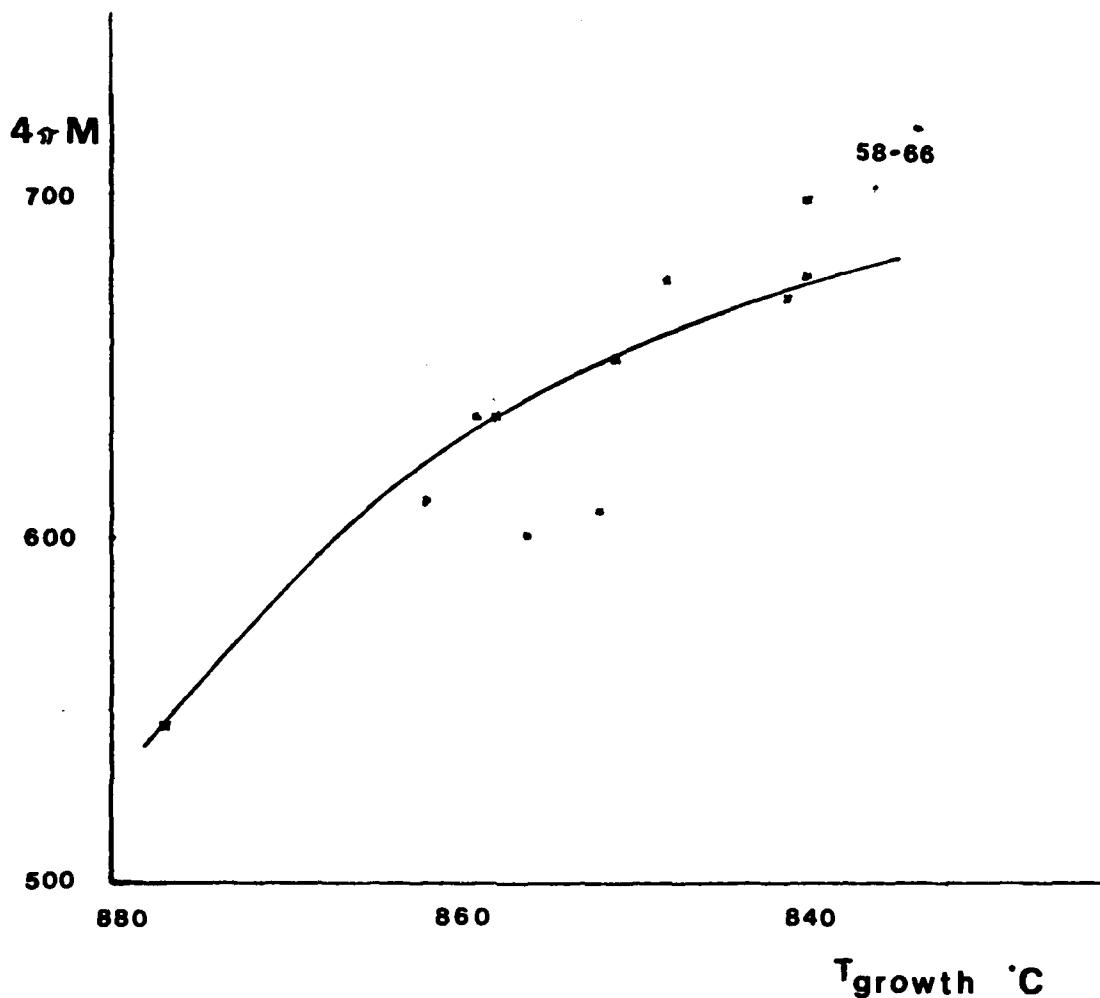
Figure 9:   Magnetization versus Growth Temperature

film will continue to grow beneath the flux drops as the film is removed from the melt, forming hillocks or mesas.   We have tried several different methods to remove the flux drops with limited success.   Tilting the substrate helps but the tilt angle must be kept low to avoid non-uniformity in the film thickness.   Gradually increasing the spin-off speed helps to move the drops to the edge.   With high speed rotation, the drops at the edge can be spun into the melt.   The temperature just above the crucible is slightly above the melt temperature so the flux will not solidify immediately.   The remaining problem is from flux drops which are exactly in the middle of the film or those which break into a large number of small drops.   The drop in the middle experiences no centrifugal force and is impossible to remove by spinning.   The fragmented drops are also difficult to remove.   The best way to avoid them is to increase the spin-off speed slowly.   The film uniformity and defect density still warrant improvement, but this will come

with time. Indeed, we have passed the initial learning period and have become reasonably proficient in producing high quality magnetic garnet films.

Reproducibility

We grew several films to determine the reproducibility of film growth under similar conditions. The following is a listing of films grown under identical circumstances.

Table 1: Reproducibility of 1/2 Micron Material

Film	t μm	4πM G	l μm	T_s °C	growth rate
84	1.00	787	0.063	841	0.26 μm/min
103	0.79	760	0.057	842	0.25

Film	Q	K_U 10^3ergs/cm^3	rotation	Δa_o
84	1.44	87.7	100 rpm	0.006 A tension
103	1.37	86.4	100	0.005

Table 2: Reproducibility of 3/4 Micron Material

Film	t μm	4πM G	l μm	T_s °C	growth rate
78	1.09	973	0.081	849	0.23 μm/min
79	0.90	998	0.085	850	0.21
80	0.96	960	0.083	850	0.23

Film	Q	K_U	rotation	Δa_o
78	2.02	76.1	100	-.008A
79	2.00	79.2	100	
80	2.02	74.2	100	

Table 3: Reproducibility for 1 Micron Material

Film	t μm	4πM	l	T_s	rate
62	1.39	676 G	0.116	840	0.31
64	1.30	668	0.116	841	0.31

Film	Q	K_U	rotation
62	2.28	41.7	100 rpm
64	2.35	41.9	100

We have shown here that the film properties for films grown from the same melt at the same temperature are reproducible. We are not only interested in how close the measured parameters

are but also how small a difference is detectable. The three films described in Table 4 were grown from the same melt at three different temperatures.

Table 4: Comparison of Parameters for 1 Micron Material Grown at Different Temperatures

Film	t μm	4πM G	l μm	T_f °C	rate μm/min
94	0.85	774	0.111	849	0.13
95	0.92	779	0.102	839	0.18
96	0.70	801	0.091	829	0.21

Film	Q	K_U	rotation	Δa_o
94	2.24	53.4	100	0.007 A
95	2.09	50.4	100	0.005
96	1.93	53.4	100	0.003

The trend in lattice parameter and characteristic length are clearly consistent with previous data. The decrease in 4πM with increasing temperature is expected but the uncertainty is greater than the measured difference. Typically, we allow a 20 G margin. Relative errors in thickness will have a stronger effect on the magnetization than on the characteristic length because the latter is normalized to the thickness. The linearity of the lattice mismatch is consistent with measurements on other films.

References

[1]   Fowlis,D.C., and J.A. Copeland.
        Rapid Method for determining the Magnetization and Intrinsic Length of Magnetic Bubble
            Domain Materials.
        AIP Conf. Proc. 5:240-243, 1972.

[2]   White, R.L.
        The Magnetostriction of Rare-Earth Garnets Containing Gallium and Europium: Old Theory
            for New Problems.
        IEEE Trans. on Magn. MAG-9(4):606-609, Dec., 1973.

PROGRESS REPORT

FABRICATION OF SUBMICRON GdCoMoAr BUBBLE MATERIAL

INTRODUCTION

The gadolinium cobalt molybdenum argon system (GdCoMoAr) has, in the past, been investigated as a possible magnetic bubble material. It was discovered by researchers at I.B.M. that a GdCoAr system possessed sufficient perpendicular, uniaxial anisotropy so as to permit the formation of magnetic bubbles (Chaudhari, et. al. 1973). This group also noted that changes in fabrication conditions would easily allow them to alter Curie and compensation temperatures with film composition. The addition of Mo was later found to lower and flatten the magnetization behavior of Co. This partially completed study follows in the footsteps of the previous investigators of this material toward the goal of an optimal submicron compostion.

Garnet, the magnetic bubble material currently in use, is a single-crystal oxide grown on single-crystal, nonmagnetic garnet substrates by the process of liquid phase epitaxy. From an economic standpoint, the necessity of using such substrates and the combined need for expensive rare earth metals in both substrate and grown film push up the cost of garnets. GdCoMoAr, on the other hand, is an amorphous material sputtered onto either glass or silicon substrates. The cost of such commonplace substrates does not even approach that of GGG, a common garnet substrate. The sputtering process is one which is well known in the semiconductor industry; hence it is a thoroughly studied, commonly available fabrication method. Liquid phase epitaxy, although used to grow such semiconductor crystals as GaAs, would probably be included as a capital investment in the developing magnetic bubble laboratory. From a physical point of view, GdCoMoAr systems offer other advantages: a higher mobility than currently available in garnets, a temperature insensitivity in the submicron bubble range and freedom from the equilibrium solubility requirements to which single-crystals are bound. When compared with garnets, the inherent advantages of GdCoMoAr systems make their continued study a worthwhile endeavor.

THEORETICAL SUMMARY OF THE GdCoMoAr SYSTEM

The magnetic nature of GdCoMoAr arises from the ferrimagnetic coupling between Gd and Co atoms. Figure I Illustrates a typical sublattice and total magnetization behavior for a GdCoMoAr system. The sublattice magnetizations are oriented anti-parallel to one another thus yielding the combined effect shown in the figure. Bubble devices are operated in the region where the Co sublattice moment dominates because it is here that the film's overall magnetiztion is most insensitive to temperature. Eschenfelder (1980) notes that it is desirable from the standpoint of

temperature insensitivity for bubble devices to tailor film compositions so as to yield optimal Curie and compensation point placement: the Curie point should be at least 150° above room temperature, the difference between Curie and compensation points should be greater than 300° to insure maximum flatness of the magnetization versus temperature curve and the temperature midway between Curie and compensation points should be less than room temperature to maintain decreasing magnetization with temperature. The latter point may require some clarification : if the magnetization increased with temperature then the corresponding decrease in exchange and anisotropy constants would produce a decrease in the quality factor, Q, and the bubble diameter (Eschenfelder 1980). Figure II illustrates the range of compositions where these conditions are met.

Since the composition is the all important parameter in determining both Curie and compensation temperatures, it is worthwhile to explain the effects of each constituent of the GdCoMoAr system on the overall behavior of the substance. It has been shown that this system complies with the Neel two-sublattice ferrimagnet model (Hasegawa 1975). This study shows that the addition of Gd lowered the Co moment (as is expected of ferrimagnetic ordering), raised the compensation temperature and lowered the Curie point. Molybdenum, a non-magnetic constituent of the system acts as a damping agent of the film's overall magnetization in the temperature region where the Co moment dominates. Bozorth gives data showing that the Co moment is reduced at the rather rapid rate of $6.5\mu_B$ per fraction of Mo atom (Bozorth 1951). Such a rapid quench rate defines Mo as a spin dilutent of Co (Chaudhari, et. al. unpublished) : spin dilution involves the transfer of electrons from Mo to the 3d band of Co thereby lowering its moment (Hasegawa, et. al. 1975). The exhange constant, A, which depends on the individual atomic moment also decreases thereby lowering the Curie point (Chaudhari, etl. al. 1976). The presence of the diluted Co also effectively increases the Gd content of the film thus causing the compensation temperature to rise. The other non-magnetic constituent of the film - Ar - is incorporated as an inevitable by- product of the fabrication process. During sputtering a negative bias is applied to the substrate to induce perpendicular anisotropy (to be discussed further). The Ar trapped within the film during fabrication acts as an alloy dilutent: alloy dilution is merely the displacement of magnetic atoms by non-magnetic atoms thereby lowering magnetization (Chaudhari, et. al., unpublished). The increase in Ar content initiated by increasing the substrate bias does not appreciably affect the Curie or compensation temperatures (Cuomo, et. al., 1975).

The I.B.M. group responsible for recongizing the GdCoAr system as a possible bubble material also noted that during the sputtering process a negative bias had to be applied to the substrate if the samples were to exhibit a positive uniaxial anisotropy constant. It has been postulated that pair or short range atomic ordering is the mechanism of anisotropy in the GdCoAr system and that biasing produces changes in that ordering (Gambino, et. al., 1974). For a given film composition it has

also been found that the uniaxial anisotropy constant - K_u - peaks at a substrate bias of nearly -200V as shown in Fig. III (Burilla, et. al. 1978). The same principles apply to the GdCoMoAr system with the consideration that Mo generally decreases the anisotropy for a given Co/Gd ratio. Of course, anisotropy will also increase as the Co/Gd ratio is increased.

Coercivity in GdCoMoAr films has been found to be consistently higher than corresponding coercivities in garnets. The coercivity of amorphous films depends on the ratio of stripwidth to thickness as illustrated in Fig. IV (Bajorek et. al., 1976). These unusually high coercivities may be due to inadequate substrate cleanliness, admixing of substrate and film constituents caused by substrate biasing or oxidation of the Gd in a thin surface layer of the film (Bajorek et. al., 1976). Thus it is advisable to fabricate thick films such that the stripwidth approximately equals the film thickness.

EXPERIMENTAL SET-UP

Fabrication of GdCoMoAr films is accomplished through the sputtering process, as previously mentioned. The films discussed in this treatise were made using a Perkin-Elmer 2400 sputtering system with a sputter down target-substrate configuration. The target consists of strips of Co ribbon overlaid with triangular sections of Mo and Gd fastened to a copper plate with a low vapor pressure, thermally conductive epoxy. This target plate is then bolted to the system's water-cooled target assembly. It was found that to maintain the integrity of the epoxy under the high temperatures incurred during sputtering, intimate thermal contact must be established with the assembly's water well. Dow Corning high vacuum silicone grease has thus far proved to be an adequate thermal connection. The choice of Corning 0211 cover glasses as substrates is based on their availability, optical purity (an implication of surface cleanliness), dielectric nature (for optimum field absorption during FMR) and track record as GdCoMoAr substrates (eg. Chaudhari et. al., 1976). A high purity sputtering gas, 99.999% argon, is utilized to maintain a low level of oxygen - the principal contaminant of argon. Substrate temperatures must be kept as low as possible during sputtering to insure that the amorphous nature of these films is preserved. Gallium, a common thermal backing for sputtering, has been applied to these glass substrates with good results. Due to the fact that sub-target substrate rotation is unavailable on the Perkin Elmer 2400 sputterer, the compositional uniformity of deposited films has been of great concern. A target-to-substrate distance of 6.35 cm. was chosen with this in mind: the increased distance provides a large area in which the sputtered atoms may mix before falling onto the substrate. Thus with the above equipment and set-up, films can be fabricated with their magnetic properties varied by adjusting substrate bias, argon pressure and target composition.

Observation of strip domains via the polar Kerr effect on an Orthoplan polarizing microscope permits the measurement of $4\pi M_s$ and the characteristic length, l (Fowlis

et. al., 1971). The straight domain configuration, for which the technique is derived, is generated through the application of an a.c. bias field. Care must be taken that the domain configuration after applying the a.c. field is in its lowest energy state. Sample thicknesses are measured with a Dektak stylus device which determines the height of an etched step. Film compositions are analyzed by electron microprobe.

The effective anisotropy field, H_K, is determined by ferromagnetic resonance. Five-by-five millimeter FMR samples are cut from the film's center. The original I.B.M. research group noted that due to oxidation of the Gd in the uppermost layer of the film anomalous FMR readings were generated; this surface condition is remedied by sputtering a thin layer of SiO_2 atop the newly deposited film prior to exposure to atmosphere (Chaudhari et. al. 1976).

RESULTS AND DISCUSSION

Table I presents a compilation of potentially useful fabrication and composition data collected thus far and will be cited quite often in the forthcoming discussion.

Changes in fabrication conditions consist of altering sputtering gas pressure and substrate bias voltage; the target bias is maintained at 1.20 kV for all sputtering runs. As previously mentioned, changes in the fabrication environment manifest themselves in the films' compositions and magnetic properties. The compositions of those films sputtered through 4/14/81 may contain impurities but this is not certain. Microprobe measurements were not performed by the writer and an initial lack of communication between myself and the person who made the measurements is the major cause for this uncertainty. Those sample i.d. numbers exhibiting an asterisk denote FMR samples with an SiO_2 overcoat; the fabrication conditions under which these films were made is mirrored in other specimens without an SiO_2 overcoat on which microprobe data was taken. Future films should have a mitigated possibility of copper incorporation brought about by alterations in the target geometry.

Plots of the Co to Mo ratio and Co to Gd ratio versus substrate bias appear in Figs. V and VI, respectively; the data points correspond to samples 51681A1 through 61181A1. The correspondence of Fig. V and the appropriate plot of Figs. VII is an extremely encouraging result. Figure VI, on the other hand, preserves the linearity of the Co/Gd plot of Fig. VII but a definite disparity can be noted for compositions fabricated with a substrate bias of less than 50V (the dashed portion of Fig. VI). At the present time no exploration of this phenomenon is available and it remains to be seen if this disparity is evident in future composition plots. The linear portion of Fig. VI permits calculation of the sputtering constant, k, in the formula below (Eschenfelder 1980):

$$(Gd/Co)_{film} = (Gd/Co)_{target}[1-k(V_b/V_t)]$$

$(Gd/Co)_{film}$: Gd to Co ratio of a deposited film

$(Gd/Co)_{target}$: Gd to Co ratio of the target

V_b : substrate bias (V)

V_t : target bias (V)

Inserting a suitable set of values yeilds a $k = 4.73$ which after comparison with other sets of data may be used to predict deposited film compositions. The argon content of the films listed in Table 1 was not quantitatively measured for lack of a reliable argon microprobe standard. Figure VII illustrates qualitatively how argon content of these sputtered films increases with substrate bias. The photographs presented in Fig. VIII were taken from an electron microprobe composition analyzer. In the future, an argon standard will be calibrated and used to make quantitative measurements of argon incorporation.

Though stripes were observed in several of the films listed in Table I limitations of the polarizing microscope used did not always permit the measurement of stripwidth and thus $4\pi M_s$. A photograph of the 1.5 μm strip domains exhibited by sample 61181B1* can be found in Fig. IX. The $4\pi M_s$ and I parameter values were found to be on the order of 660 G and 0.19, respectively.

A value of the effective anisotropy field can be approximated from the static bubble parameter chart shown in Fig. X. Having a measured value of $4\pi M_s$ and I, a value of 4.0×10^{-7} erg/cm is chosen for the exchange constant, A, on the basis of the expected quality factor, Q. These values yield a $K_u = 6.0 \times 10^4$ erg/cm^3 and thus an anisotropy field $H_K = 2.27$ k Oe.

CONCLUSION AND FUTURE PLANS

The work comprising this report is far from complete. From the theoretical considerations stated at the outset, it is easy to see that the magnetic properties of amorphous GdCoMoAr are well suited for submicron bubble materials. Additional alloy and spin dilutents can be added in addition to Mo and Ar which would further tailor the properties of GdCoMo to specific industrial applications outside the realm of bubble memories. The experimental set-up outlined and the results achieved thus far provide an optimistic view that a multitude of specific applications for GdCoMoAr can can be addressed properly.

With regard to the development of a submicron GdCoMoAr material, my future plans include modifications in the fabrication process as they are needed. Possible heating effects during sputtering wil be investigated and the degree to which the films are amorphous will be determined using transmission electron microscopy. The limits of optical microscopy for observing submicron domains can be overcome through the use of Lorentz microscopy which has been used to examine GdCoMoAr bubbles with diameters on the order of one hundred angstroms.

BIBLIOGRAPHY

1. Bajorek, C. H. and R. J. Kobliska, I.B.M. Journal of Research and Development, 20 no. 3, 271 (1976).

2. Bozorth, R. M., Ferromagnetism, 292, (1951).

3. Burilla, C. T., W. R. Bekebrede, M. Kestegian and A. B. Smith, Journal of Applied Physics, 49, 1750 (1978).

4. Chaudhari, P., C. H. Bajorek and M. H. Kryder, unpublished.

5. Chaudhari, P. and D. C. Cronemeyer, AIP Conference Proceedings, 29 113 (1976).

6. Chaudhari, P., J. J. Cuono and R. J. Gambino, IBM Journal of Research and Development 17, 66 (1973).

7. Chaudhari, P., J. J. Cuomo, R. J. Gambino, S. Kirkpatrick and L. J. Tao, AIP Conference Proceedings, 24 562 (1975).

8. Cuomo, J. J. and R. J. Gambino, Journal of Vacuum Science and Technology, 14, 152 (1975).

9. Eschenfelder, A. H. Amorphous Films for Bubbles, Ferromagnetic Materials, 2, 345 (1980).

10. Fowlis, D. and J. Copeland, AIP Conference Proceedings, 5, 240 (1971).

11. Gambino, R. J., P. Chaudhari, J. J. Cuomo, AIP Conference Proceedings, 18, 578 (1974).

12. Hasegawa, R., Journal of Applied Physics, 46, 5263 (1975).

13. Hasegawa, R., B. E. Argyle and L. J. Tao, AIP Conference Proceedings, 24, 110 (1975).

Table I

sample	Ar pressure (mt)	substrate bias (v)	deposition time (min)	average % Co	average % Gd	average % Mo	% other impurities	thickness (µm)	stripes observed ?
32281A	25	15	60	64.29	22.03	13.69			
32281B	25	20	60	63.79	21.94	14.26		1.50	
32281C	25	25	60	63.70	20.62	15.68			
32381A	25	30	60	64.77	19.60	15.64			
32381B	25	100	60	64.80	12.87	22.33			
33181A1	30	20	60	66.75	16.04	17.22	-	1.17	✓
33181B1	30	80	60	69.21	14.96	15.82			
41481A1	30	100	60	64.74	20.10	15.16		1.27	
51681A1	30	0	60	57.39	17.83	11.21	13.57(Cu)		
51681B1	30	20	60	58.80	17.90	11.41	11.89 (Cu)		
51781A1	30	80	60	67.01	12.84	13.19	6.95 (Cu)		
51781B1	30	50	60	65.27	13.47	12.40	8.85 (Cu)		
6981B1	30	100	60	70.36	12.80	13.45	3.39(Cu)		
61081A1	30	130	60	70.22	12.05	16.64	1.11 (Cu)		
61081B1	30	10	60	61.05	18.50	10.71	9.74(Cu)	1.40	✓
61181A1	30	15	60	60.36	19.19	10.83	9.62(Cu)	1.34	✓
33181A1	30	20	60	69.88	15.22	14.91	-		✓
6781A1*	30	50	60					.	
6781B1*	30	80	60						
6881A1*	30	20	60						✓
6881B1*	30	100	60						
6981A1*	30	130	60						
61081C1*	30	10	60						✓
61181B1*	30	15	60						✓

TABLE I
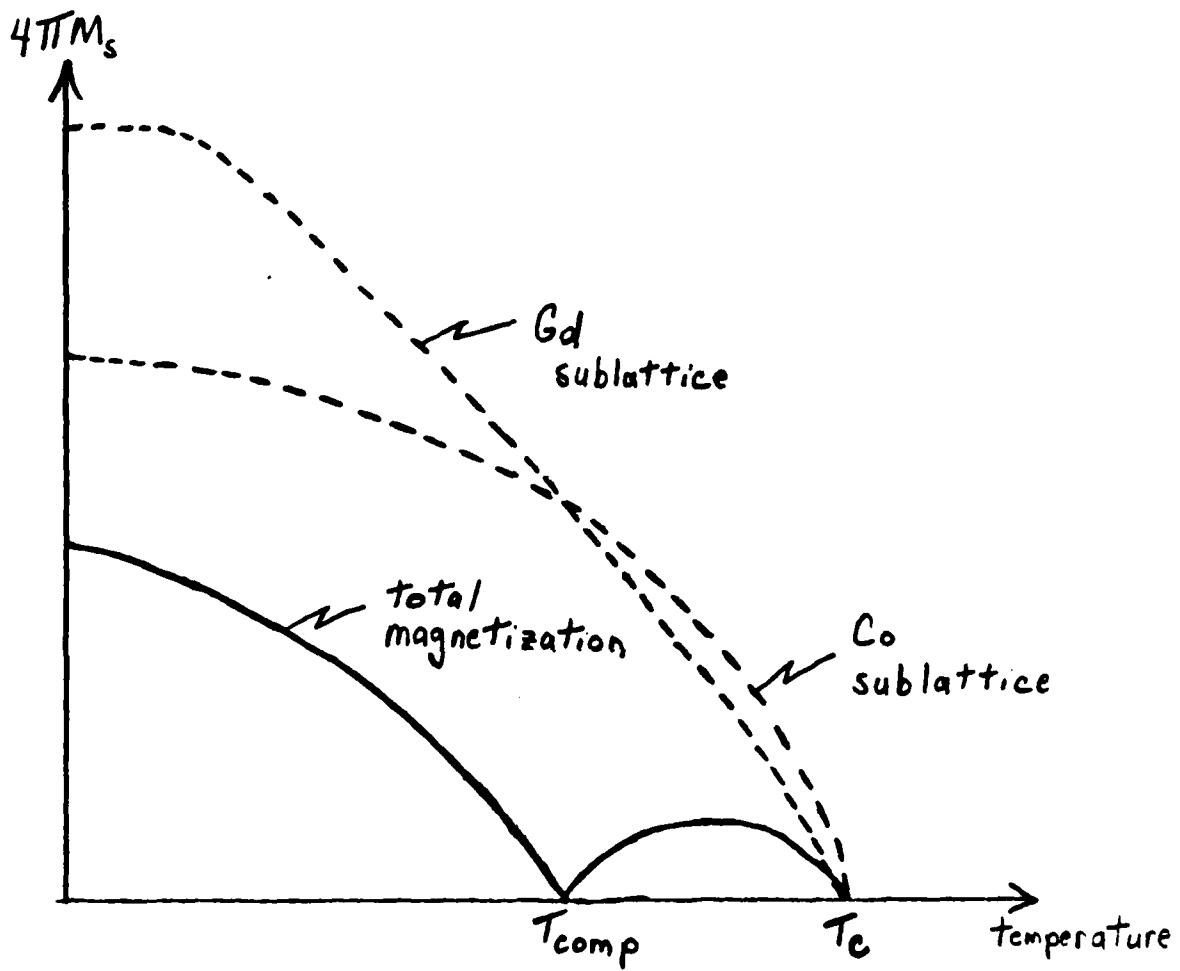
FIGURE I
TYPICAL SUBLATTICE AND TOTAL MAGNETIZATION BEHAVIOR
OF GdCoMoAr SYSTEMS
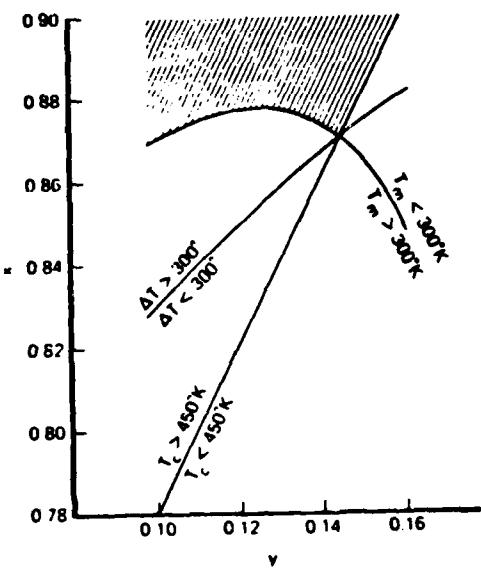
FIGURE II
CRITICAL TEMPERATURE LIMITS AS A FUNCTION OF x AND y
FOR $(Gd_{1-x}Co_x)_{1-y}Mo_y$ (Eschenfelder 1980)
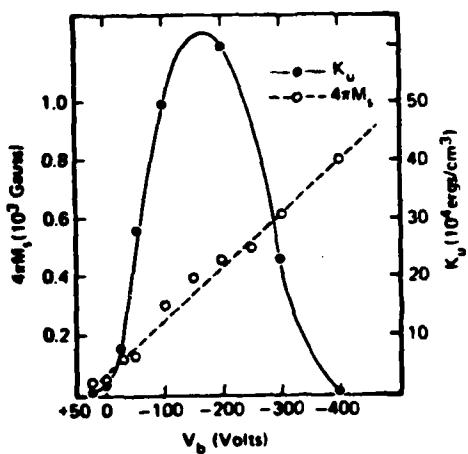
FIGURE III
$4\pi M_s$ and K_u AS A FUNCTION OF SUBSTRATE BIAS,
V_b FOR FILMS FABRICATED FROM A
$Gd_{0.22}Co_{0.78}$ TARGET
(Burilla et. al. 1978)
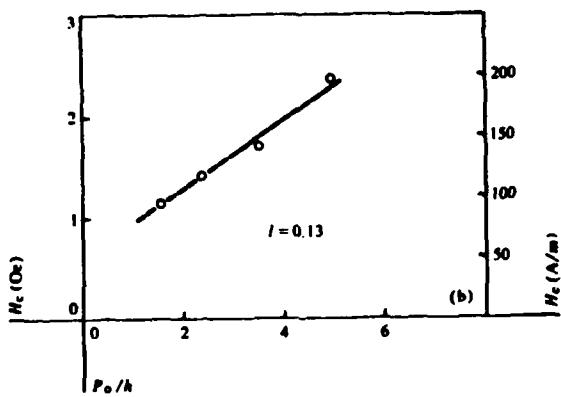
FIGURE IV
PLOT OF COERCIVITY VERSUS THE RATIO OF
STRIPE PERIOD TO FILM THICKNESS
(Bajorek et. al. 1976)
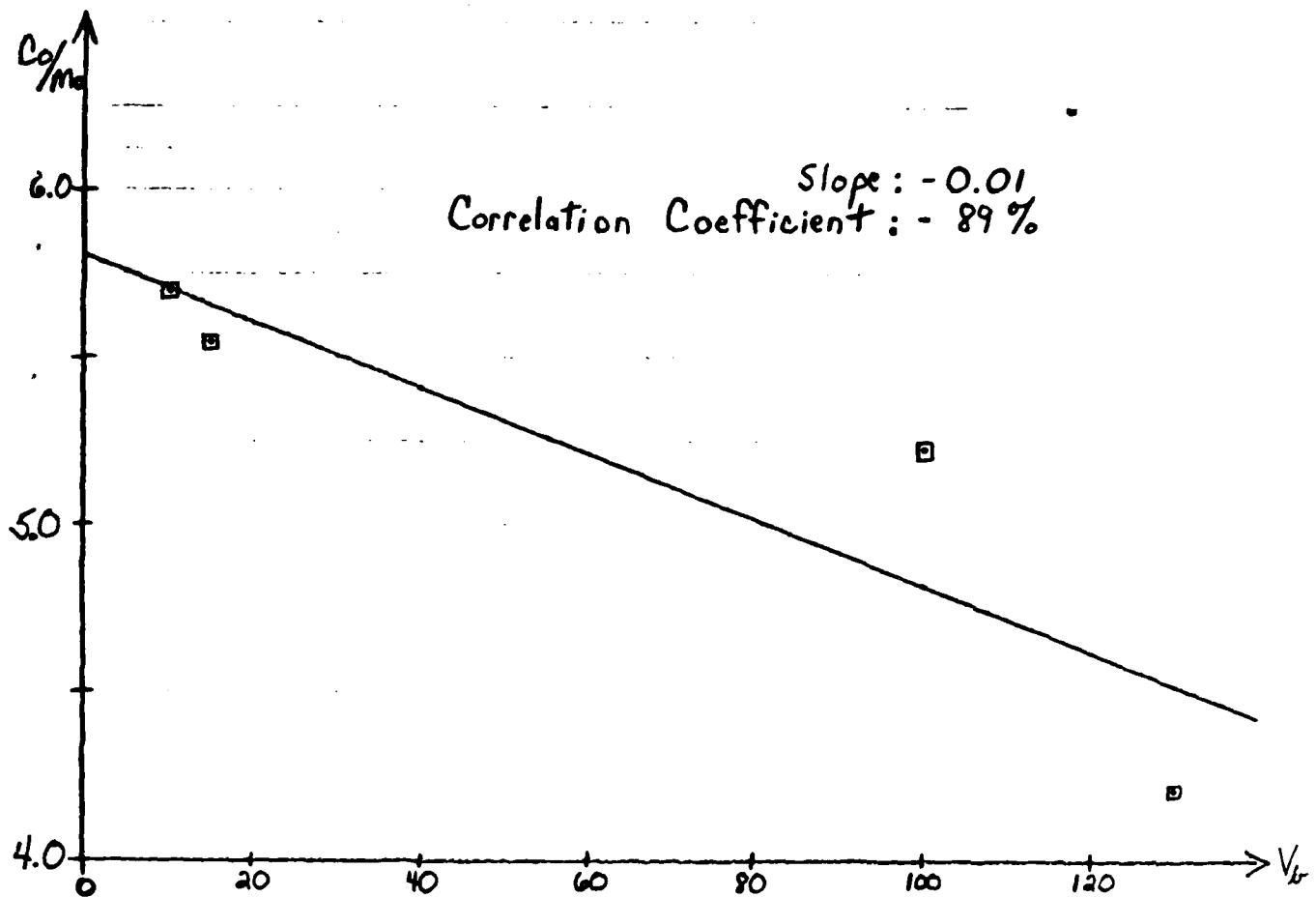
FIGURE V
PLOT OF THE Co/Mo RATIO OF
DEPOSITED FILMS VERSUS SUBSTRATE BIAS
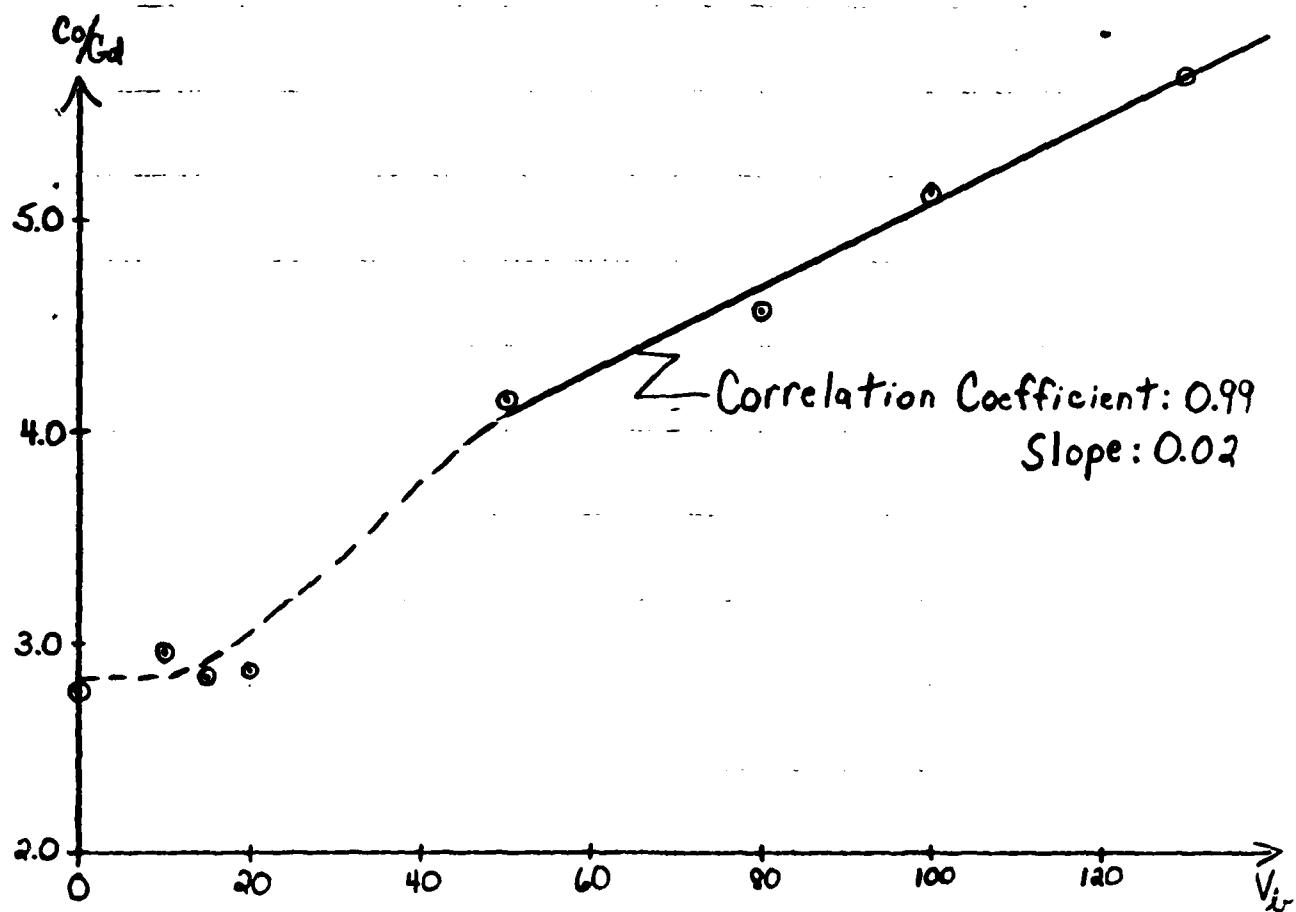
FIGURE VI
PLOT OF THE Co/Gd RATIO OF DEPOSITED
FILMS VERSUS SUBSTRATE BIAS
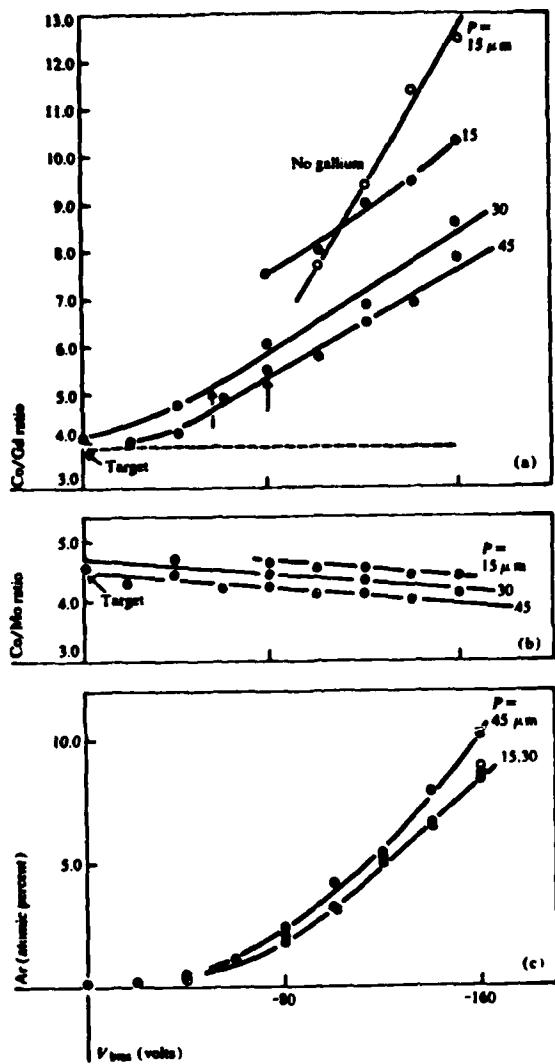
FIGURE VII
PLOTS OF Co/Gd RATIO, Co/Mo RATIO AND Ar
CONTENT OF DEPOSITED FILMS VERSUS
SUBSTRATE BIAS (Bajorek et. al. 1976)

$V_b = 0\,V$
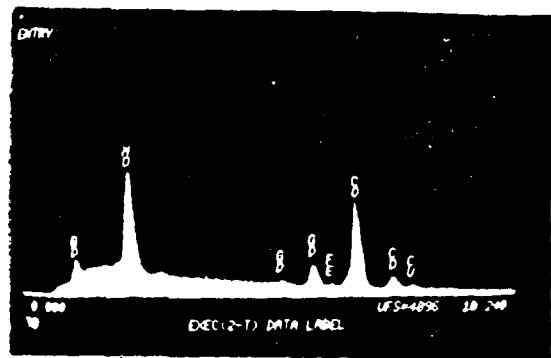
$V_b = 40\,V$
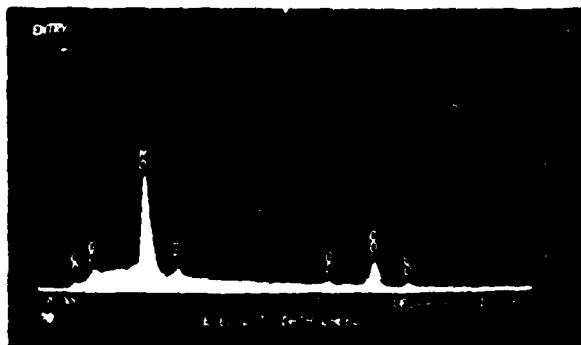
$V_b = 80\,V$
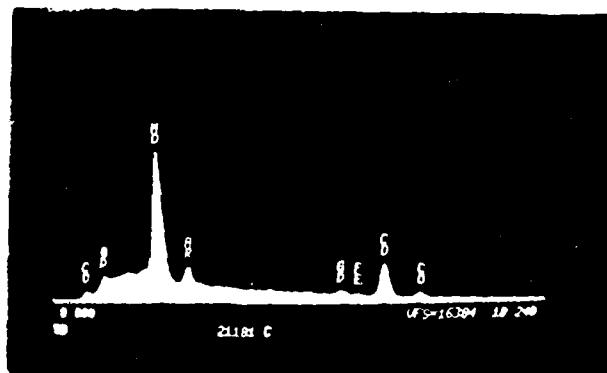
FIGURE VIII
QUALITATIVE RENDITION OF INCREASING Ar CONTENT
WITH INCREASED SUBSTRATE BIAS
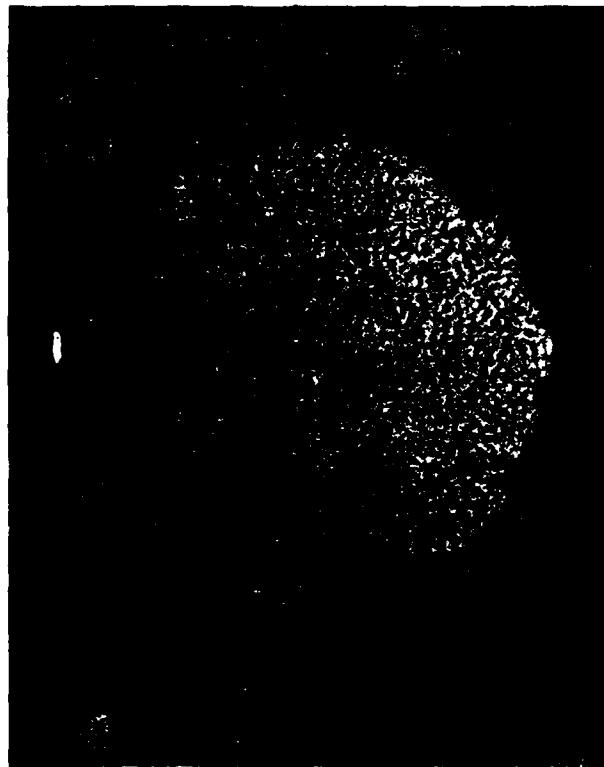
611816

FIGURE IX
PHOTOGRAPH OF SAMPLE 61181B1*
IN THE DEMAGNETIZED STATE
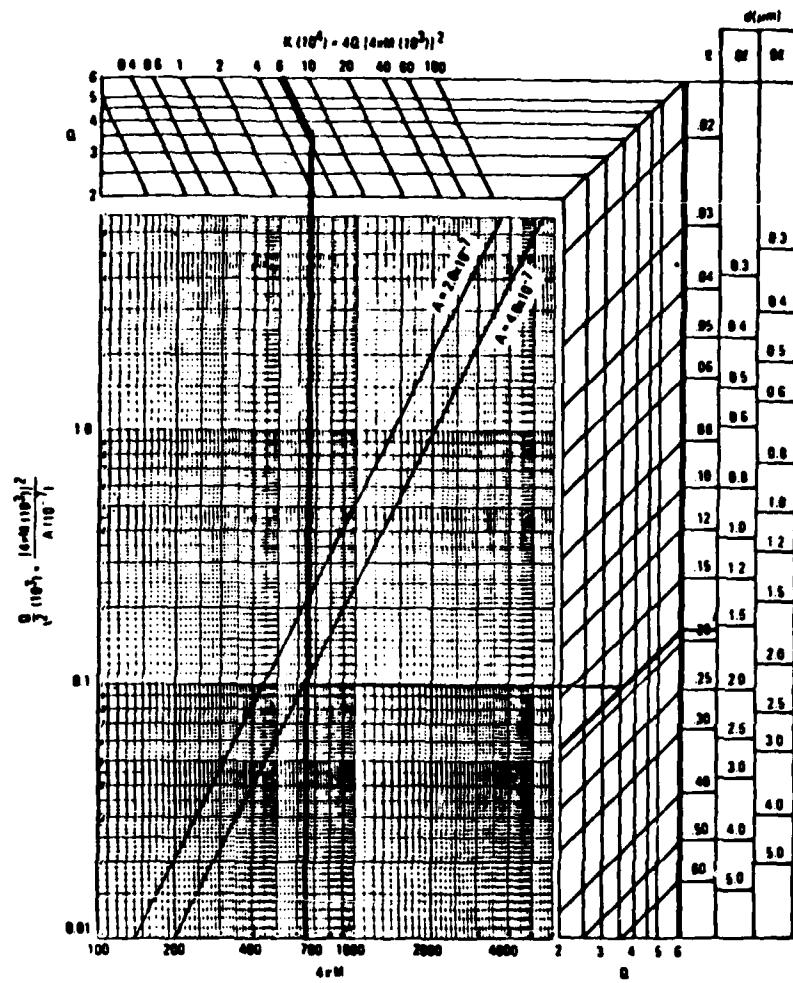
FIGURE X
SUMMARY CHART FOR STATIC BUBBLE PARAMETERS
HAVING THE PROPERTIES OF SAMPLE 61181B1*
(Eschenfelder 1980)

THE EVALUATION OF CoCr MAGNETIC THIN FILMS

AS POSSIBLE SELF-BIASING LAYERS FOR MAGNETIC BUBBLE DEVICES

INTRODUCTION

Self-biasing layers are magnetic thin films structures which provide the
energy necessary to keep magnetic bubbles stable. Such structures could replace
the permanent magnet assemblies of coils presently used to bias magnetic bubble
devices. Self-biasing appears to have a number of advantages. Finished devices
would be easier to prepare (requiring just 1 or 2 extra thin-film processing
steps, rather than manufacture of permanent-magnet assemblies). It would also
be easier to get uniform bias, and devices would be smaller and lighter. In
addition self-biasing layers would open up the possibility of applications which
were sensitive to permanent magnetic fields since the self-bias layer makes es-
sentially no external field.

This report covers background and analysis of self-biasing, experimental
data done to date and discussions, conclusions and plans drawn from that work.

BACKGROUND AND ANALYSIS OF SELF-BIASING

How does self-biasing work? A quick analysis shows that it cannot provide
an external permanent magnet bias field such as present magnets do. If one
thinks in terms of positive and negative magnetic charge, a magnetic thin film
with magnetization perpendicular to the plane of the film is the magnetic analog of
a parallel-plate capacitor. There is negligible external field. The field $-4\pi Ms$
set up by the magnetization is exactly offset by the demagnetizing field, $-4\pi Ms$ of
equal magnitude and in the opposite direction (see Fig. 1).

To correctly explain the self-biasing effect one must consider not only the bias layer but the bias layer, magnetic bubble storage layer, and the interface between them (see Fig. 2). If one assumes a bias layer of higher intrinsic domain wall energy than the magnetic bubble storage layer, and one assumes a bias layer that can be saturated perpendicular to the plane and that will hold that magnetization (more exact property requirements will be discussed later) then a circular domain wall "cap" should form on the end of a magnetic bubble existing in the storage layer. Given that the wall energy in the bias layer is higher, this domain wall "cap" should lie on the storage-medium side of the interface. The equation for the total energy of a magnetic bubble in the storage layer will now have an extra additive term due to the energy of the "cap," and will now read:

$$E_T = \underbrace{2M_sH_a\pi r^2 h}_{\substack{\text{energy due} \\ \text{to any ap-} \\ \text{plied external} \\ \text{bias field}}} + \underbrace{2\pi rh\sigma_w}_{\substack{\text{side domain} \\ \text{wall energy}}} - \underbrace{E_D}_{\substack{\text{de-} \\ \text{magneti-} \\ \text{zation} \\ \text{energy}}} + \underbrace{\pi r^2 \sigma_w}_{\text{"cap" energy}}$$

where M_s = saturation magnetization of the storage medium

   H_a = external applied bias field

   r = radius of the bubble

   h = height of the bubble (i.e. thickness of the storage layer)

   σ_w = intrinsic domain wall energy per unit area of domain wall
      for the storage layer

(Liu et. al., 1971)

To find the equilibrium condition, one takes the partial derivative of the total energy and sets it equal to zero. Thus:

$$\frac{\partial E_T}{\partial r} = 4\pi M_s H_a rh + 2\pi h\sigma_w - \frac{\partial E_D}{\partial r} + 2\pi r\sigma_w = 0$$

Figure 1 - Magnetic Thin Film - Saturated Perpendicular To Plun

negligible external field
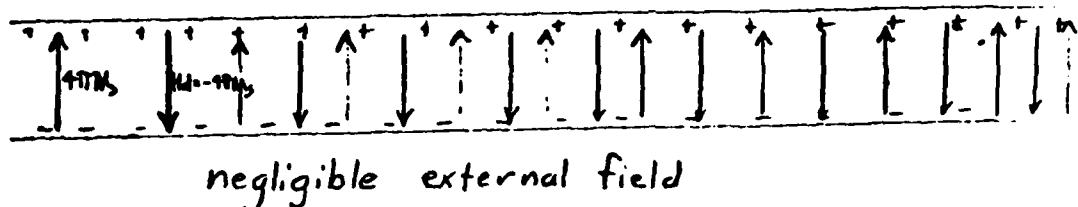
Figure 2 - Bias Layer and Storage Layer

Domain Wall "Cap"

Bias Layer

Storage Layer

Side Domain Wall

Magnetic Bubble
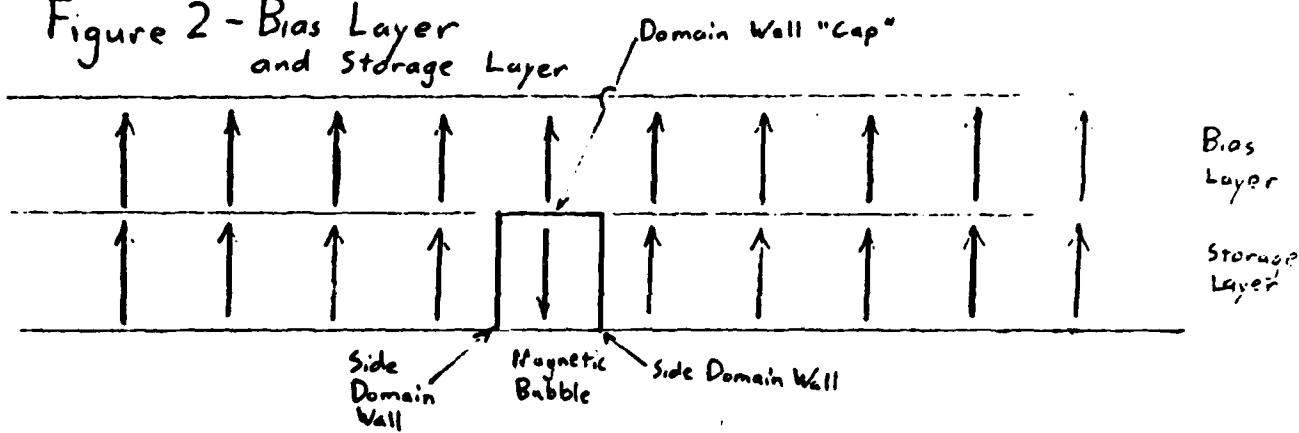
Side Domain Wall

dividing by $4\pi M_s$ rh gives:

$$H_a + \frac{\sigma_w}{2rM_s} - \frac{\partial E_D/\partial r}{4\pi M_s rh} + \frac{\sigma_w}{2M_s h} = 0$$

This can be thought of in terms of "equivalent magnetic fields"

$$H_a + H_w - H_D + H_s = 0$$

where

$$H_w = \frac{\sigma_w}{2rM_s} = \text{"equivalent field" due to side domain wall}$$

$$H_D = \frac{\partial E_D/\partial r}{4\pi M_s rh} = \text{"equivalent field" due to demagnetization}$$

$$H_s = \frac{\sigma_w}{2M_s h} = \text{"equivalent field" due to domain wall "cap"}$$

Note that H_s is independent of bubble radius and can be thought of as an "equivalent bias field." Thus, for equilibrium:

$$\underbrace{(H_a + H_s)}_{} + H_w - H_D = 0$$

        combined effect of external applied bias field
        and self bias "effective field"

<div align="right">(Liu et. al., 1971)</div>

The important question here is whether H_s can be made large enough so that H_a can be zero (i.e. complete self-biasing), re-writing the expression for H_s in terms of the characteristic length "l" gives:

$$H_s = \frac{\sigma_w}{2M_s h} = \frac{4\pi M_s}{2}\left(\frac{l}{h}\right)$$

for $\frac{h}{l} = 4$: (the suggested optimal value (Thiele, 1971)) it follows that:

$$H_s = \frac{4\pi M_s}{2}\left(\frac{l}{4}\right) = 0.125\,(4\pi M_s)$$

Referring to Fig. 3 (from Eschenfelder, 1980), we see that this value for

$\frac{H_s}{4\pi M_s}$ would require an unrealistically low value for $\frac{h}{l}$. The range of $\frac{h}{l}$

used for practical devices is between 3 and 9 (Eschenfelder, 1980). If
one put self-biasing layers on both sides of the storage film, however,
then there would be domain wall "caps" on both ends of the magnetic bubble.
This would have the effect of doubling H_s, so now

$$H_s = \frac{\sigma w}{M_s h} = 4\pi M_s \left(\frac{l}{h}\right)$$

and for $\frac{h}{l} = 4$

$$H_s = 4\pi M_s (0.25).$$

Referring back to Fig. 3, one can see that this value lies within the region
of bubble stability, so complete self-biasing is a definite possibility if two
self-biasing layers are used. Note, however, that this point lies not in
the center of the stable region, but considerably nearer the strip-out limit.

Carrying this analysis further, one can construct the hyperbola formed
by the equation $\frac{H_B}{4\pi M_s} = \frac{1}{\left(\frac{h}{l}\right)}$ and solve for its intersection with the curve

$\frac{H^{so} + H^{co}}{2}$ (i.e. the center of the stability region). This gives the point
at which self-biasing layers will give a device which is in the center of
the stability region. Referring to Fig. 4, one can see that this implies
an $\frac{h}{l}$ value of 3.75, which is fairly close to the optimal value of 4.00
and within the practical limits given by Eschenfelder (in Eschenfelder, 1980).

So complete self-biasing appears possible. What are the required prop-
erties for self-biasing layers? First, one must be able to saturate such a
film perpendicular to the plane and have it stay that way. One possible way

Figure 3
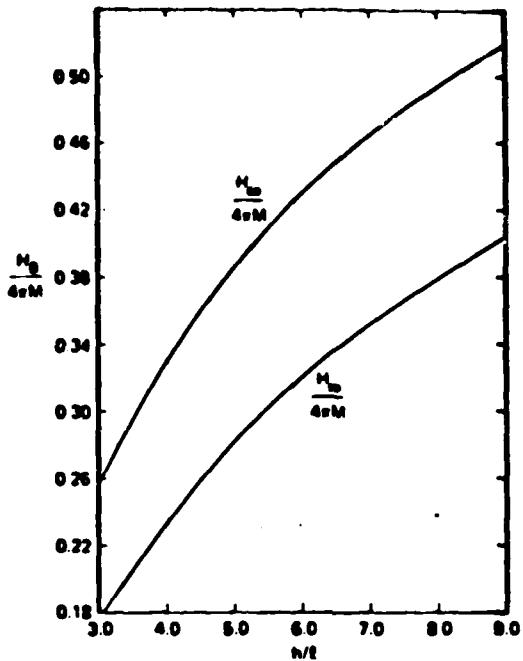
(Eschenfelder, 1980)

Figure 4
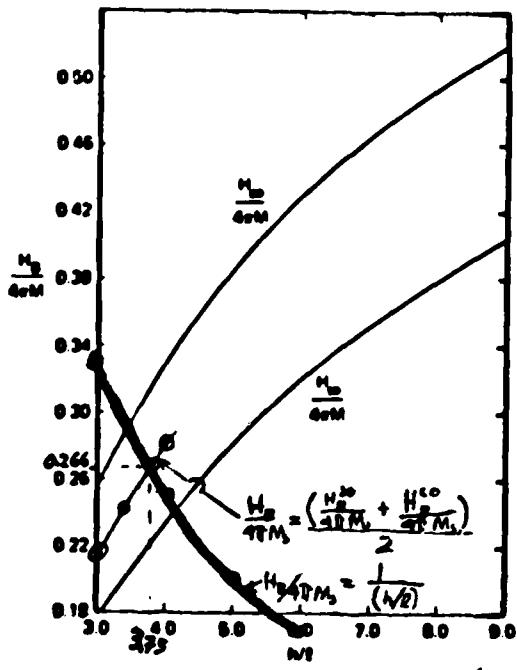
(Eschenfelder, 1980)

to achieve this is with a film of high perpendicular uniaxial magnetic anisotropy (i.e. greater than the sum of $4\pi M_s$ for both the bias and storage layers (Uchischiba, 1974), and high enough coercive force to prevent relaxation into stripe-domains. A second possible way (although not as desirable) would be with a film so highly coercive that it will maintain saturation magnetization in any direction. The second major requirement is that the intrinsic domain wall energy in the bias layer must be greater than that in the storage layer. In addition, it should preferrably be useable with a wide range of storage layer media (including various kinds of garnets, orthoferrites and amorphous materials).

The initial search for materials was directed toward perpendicular magnetic recording media. This was because many of the required properties are similar. A perpendicular recording medium requires high perpendicular anisotropy, fairly high coercive force and high saturation magnetization. In general, the higher the saturation magnetization of a material is, the higher will be its exchange energy so such materials should also have high domain wall energies.

CoCr r.f. sputtered films were the materials chosen. Pure cobalt has high uniaxial anisotropy energy (K_u) but the demagnetizing energy ($2\pi M_s^2$) is considerably higher. Addition of chromium decreases the saturation magnetization (see Fig. 5) and uniaxial anisotropy of the material. Initially, the saturation magnetization (and hence the demagnetization energy) decreases comparatively more quickly than the anisotropy. Therefore, the combined effective uniaxial anisotropy ($K_u - 2\pi M_s$) becomes positive, increases to a peak and later decreases with addition of Cr (see Fig. 6). Peak value of $K_u - 2\pi M_s^2$ (approx. 5×10^5 ergs/cm^3) seems to be at about 18 a.t.% Cr (Iwasaki and Ouchi, 1978).

Figure 5
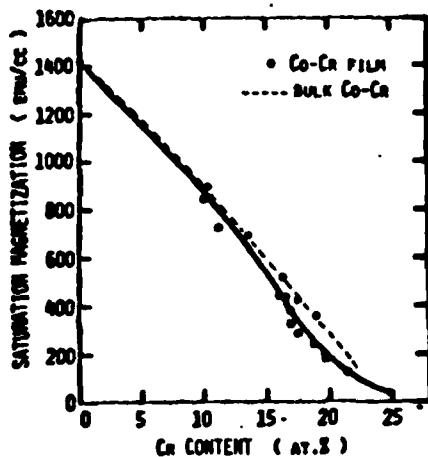
Fig.1 Ms vs. Cr content for Co-Cr film.

(Iwasaki and Ouchi, 1978)

Figure 6
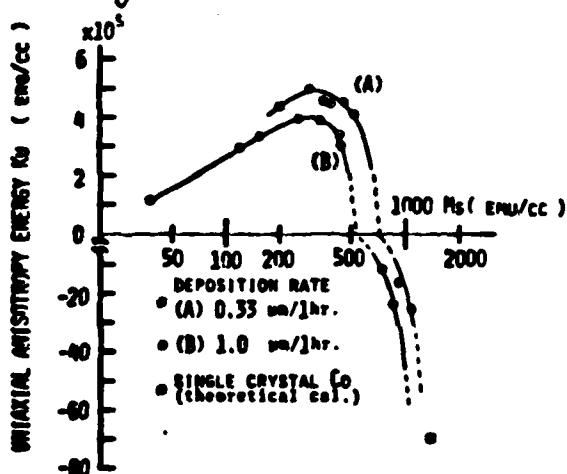
Fig.4 Ku vs. Ms in Co-Cr film for deposition rate (A) and (B).

(Iwasaki and Ouchi, 1978)

The coercive force for the materials was reported to be approximately 1 KØe (Uesaka & Judy, 1981).

EXPERIMENTAL DATA TAKEN TO DATE

CoCr films were fabricated by r.f. diode sputtering with a Perkin-Elmer 2400 sputtering system (with water-cooled substrate table). A variety of different growth conditions were used (refer to Fig. 7 for summary table). In order to determine film thickness, parts of samples were masked with black wax, etched with nitric acid, then stripped and measured with a Dektak profilometer. Atomic compositions were calculated from electron microprobe analyses. The values for combined effective anisotropy ($K_u - 2\pi M_s^2$) were calculated from torque magnetometer data and film thickness data. Values for saturation magnetization were estimated using atomic composition data, together with data of Iwasaki and Ouchi (Iwasaki and Ouchi, 1978). It was not expected that Cr content would be so low (approx. 10 a.t. %). The sputtering target was designed to be 20 a.t.% Cr, but this was apparently decreased due to chipping during fabrication.

Separate graphs were drawn of K_u vs. target bias for the runs using 5 mTorr Ar (Fig. 8) and 10 mTorr Ar (Fig. 9). A graph of K_u vs. sputtering rate was also plotted (Fig. 10).

A second sputtering target was procured and additional films were fabricated. Torque curves for these are as yet unavailable. Film thickness measurements are also not available, since it is preferrable to do them after torque magnetometer runs have been completed (because thickness measurements require breaking off and destroying a part of the film). What data are available for these more recent runs are summarized in Fig. 11.

Figure 7 — Parameters of CoCr Films

Run Identifier	Argon Pressure (mTorr)	Target Bias (volts)	R.F. Power (watts)	Table Height (inch)	Film Thickness (μm)	Sputtering Rate (Å/m)	Atomic Composition (Co:Cr)	$K_u - 2\pi M_s^2$ (ergs/cm³) *	estimated $4\pi M_s$ (Gauss) *	K_u (ergs/cm³)
12/8/80-1	10	1500	180	1.25	0.78	260.	91:9	-9.65×10^6	12.1 K	-3.86×10^6
12/8/80-2	5	1500	150	1.25	0.47	157.	91:9	-5.99×10^6	12.1 K	-1.99×10^5
12/8/80-3	10	1250	120	1.25	0.45	150.	91.9	-7.63×10^6	12.1 K	-1.84×10^6
2/8/80-4	5	1250	100	1.25	0.37	123.	91:9	-5.95×10^6	12.1 K	-1.59×10^5
2/16/80-1	5	1250	120	1.25	0.092⚟	32.	85:15†	-3.63×10^6	7.04 K	-1.66×10^6
2/16/80-2	10	1000	80	1.25	0.355	118.	90:10	-5.62×10^6	11.1 K	-7.54×10^5
2/16/80-3	5	1000	75	1.25	0.34	113.	90:10	-5.70×10^6	11.1 K	-8.30×10^5
1/17/81-1	5	1500	170	3.00	0.47	78.	90:10	-5.37×10^6	11.1 K	-5.03×10^5
1/17/81-2	5	1250	110	3.00	0.25	42.	90:10	-6.81×10^6	11.1 K	-1.94×10^6
1/17/81-3	5	1000	75	3.00	0.22	24.	90:10	-6.93×10^6	11.1 K	-2.07×10^6
1/18/81-1	5	1750	230	3.00	0.60	100.	91:9	-4.74×10^6	12.1 K	$+1.05\times10^6$
1/18/81-2	5	2000	300	3.00	0.83	138.	91:9	-4.60×10^6	12.1 K	$+1.20\times10^6$
1/18/81-3	5	2250	390	3.00	0.48	160.	91:9	-5.32×10^6	12.1 K	$+4.73\times10^5$
1/18/81-4	5	2500	490	3.00	0.57	190.	91:9	-5.51×10^6	12.1 K	$+2.83\times10^5$
1/28/81-1	10	1500	180	3.00	0.57	95.	91:9	-6.18×10^6	12.1 K	-3.86×10^5
1/28/81-2	10	1250	130	3.00	0.45	75.	91.9	-6.26×10^6	12.1 K	-4.69×10^5
1/29/81-1	10	1000	90	3.00	0.51	57.	91:9	-5.35×10^6	12.1 K	$+4.40\times10^5$
1/29/81-2	10	1750	260	3.00	0.87	145.	91.9	-7.28×10^6	12.1 K	-1.49×10^6
1/29/81-3	10	2000	340	3.00	1.07	178.	91.9	-8.64×10^6	12.1 K	-2.85×10^6
1/31/81-1	10	2250	450	3.00	1.35†	225.	91.9	-7.50×10^6	12.1 K	-1.71×10^6

⚟ Film had cloudy appearance and † Film too thin for * determined with torque * using data of

Figure 8 - K_u vs. Target bias - 10 mTorr Ar

Target Bias (kV)

K_u (in 10^5 ergs/cm³)
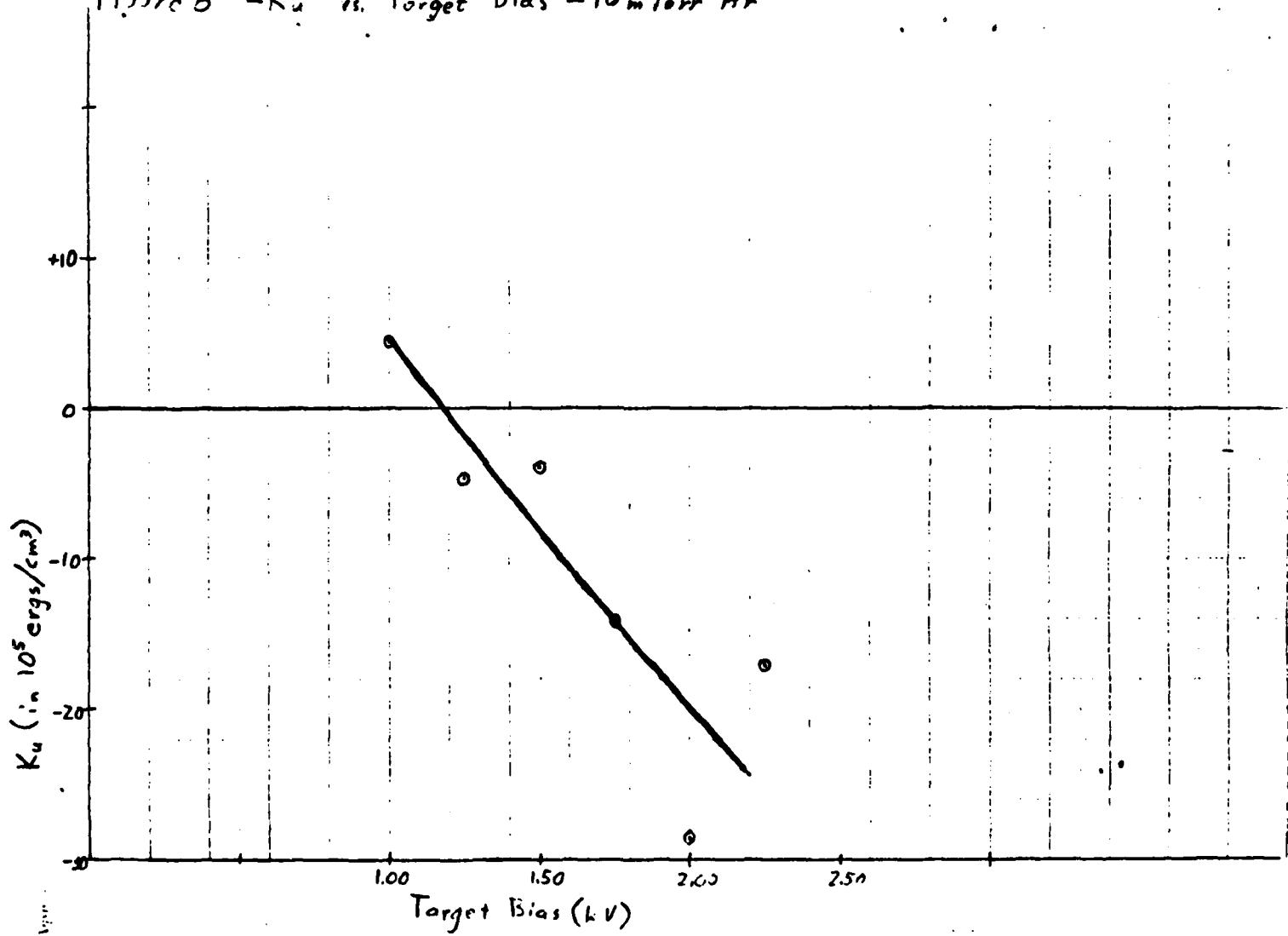
Figure 9 — Ku vs. Target Bias -5mTorr
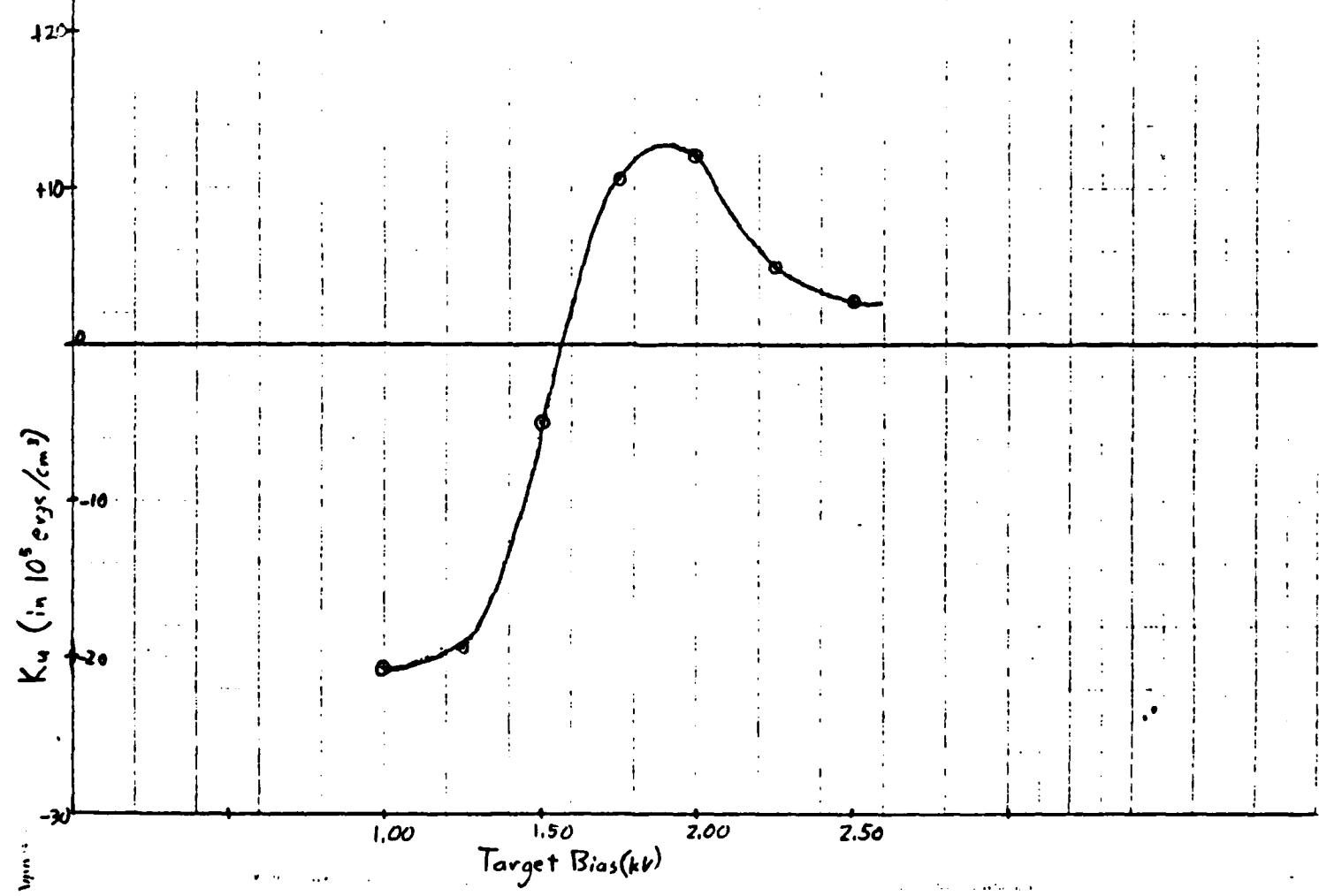
Figure 10 — Ku vs. Sputtering Rate - Both Sets with 3in. Table Height
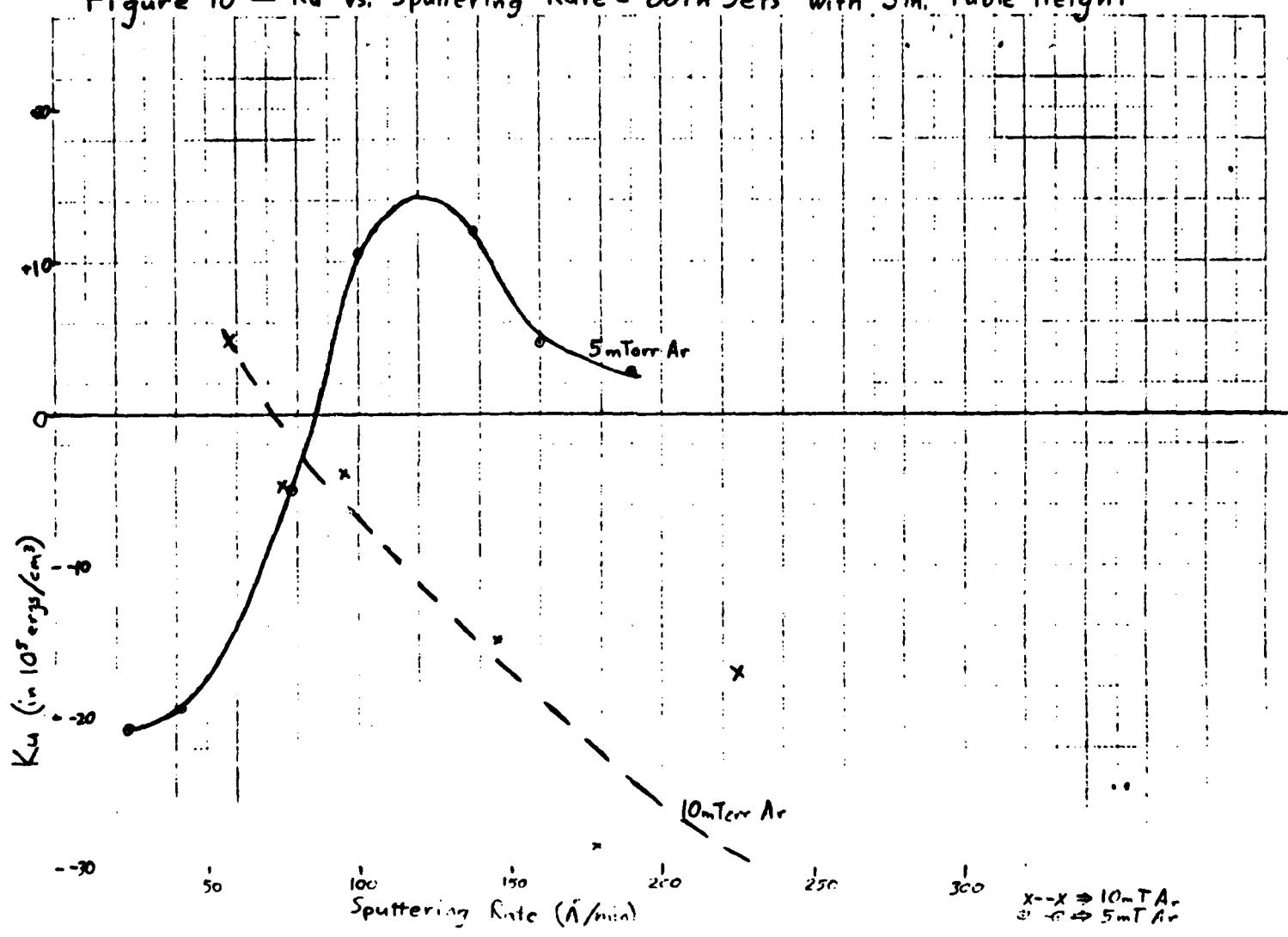
K_u (in 10^5 ergs/cm^3)

Sputtering Rate (Å/min)

5mTorr Ar

10mTorr Ar

x--x ⇒ 10mTAr
⊙--⊙ ⇒ 5mTAr

have been completed (because thickness measurements require breaking off and
destroying a part of the film). What data are available for these more
recent runs are summarized in Fig. 11.

DISCUSSION, CONCLUSIONS, AND PLANS

Results to date show good qualitative agreement with the literature.
Looking first at the graph for the 5 mTorr data (Fig. 8), one can see that
as r.f. voltage is increased, anisotropy rises, peaks at about 1.9 kV, and then
declines. The data of Uesaka and Judy show a similar characteristic (see Fig. 12).
They plot squareness of the hysterisis curve (which can be taken to be a measure
of anisotropy). Their graph shows a peak around 1.8 kv (Uesaka and Judy, 1981).
Note, however, that their table spacing might be different so perhaps sputtering
rate might be a better basis for comparison.

The 5 mTorr part of the sputtering rate graph (see Fig. 10) shows a very
similar trend to the target bias graph. This is to be expected, since sputtering
rate depends on target bias. The peak value of anisotropy corresponds to a sput-
tering rate of 120. $\overset{\circ}{A}$/min. This is exactly the optimal sputtering rate quoted by
Uesaka and Judy (Uesaka and Judy, 1981).

The graph of K_u vs. target bias for the 10 mTorr runs shows entirely dif-
ferent characteristics from that for 5 mTorr runs. This was somewhat of a sur-
prise. It is important to note that this difference is not explainable in terms
of differing sputtering rates, as shown by Fig. 10). Rather, there is a basic
difference in the anisotropy trends for the two different gas pressures. The
data taken at 10 mTorr Ar pressure agree with the contention of Iwasaki and
Ouchi that when working at 10 mTorr the slower one sputters, the higher will
be the perpendicular anisotropy. In particular, of the two rates which they
quote, sputtering at 55 $\overset{\circ}{A}$/min results in a substantially higher perpendicular

64

Figure. 11 - Parameters of CoCr Films Sputtered With New Target

Run Identifier	Argon Pressure (nTorr)	Target Bias (volts)	R.F. Power (watts)	Table Height (inch)	Film Thickness (μm)	Sputtering Rate (Å/min)	Atomic Composition (Co:Cr)	$K_u - 2\pi M_s^2$ (ergs/cm³)	estimated 4πM_s (Gauss)	K_u (ergs/cm³)
4/5/81-A	5	1500	180	3.00			78:21 *			
4/5/81-B	5	1750	250	3.00						
4/6/81-A	5	2000	330	3.00						
4/6/81-B	5	2250	420	3.00			79:21 *			
4/17/81-A	5	2500	540	2.50						
4/18/81-A	5	1250	120	2.50						
4/19/81-A	5	1000	80	2.50			77:22 *			

* films had 0.5-a7

Figure 12

(Uesaka ...)
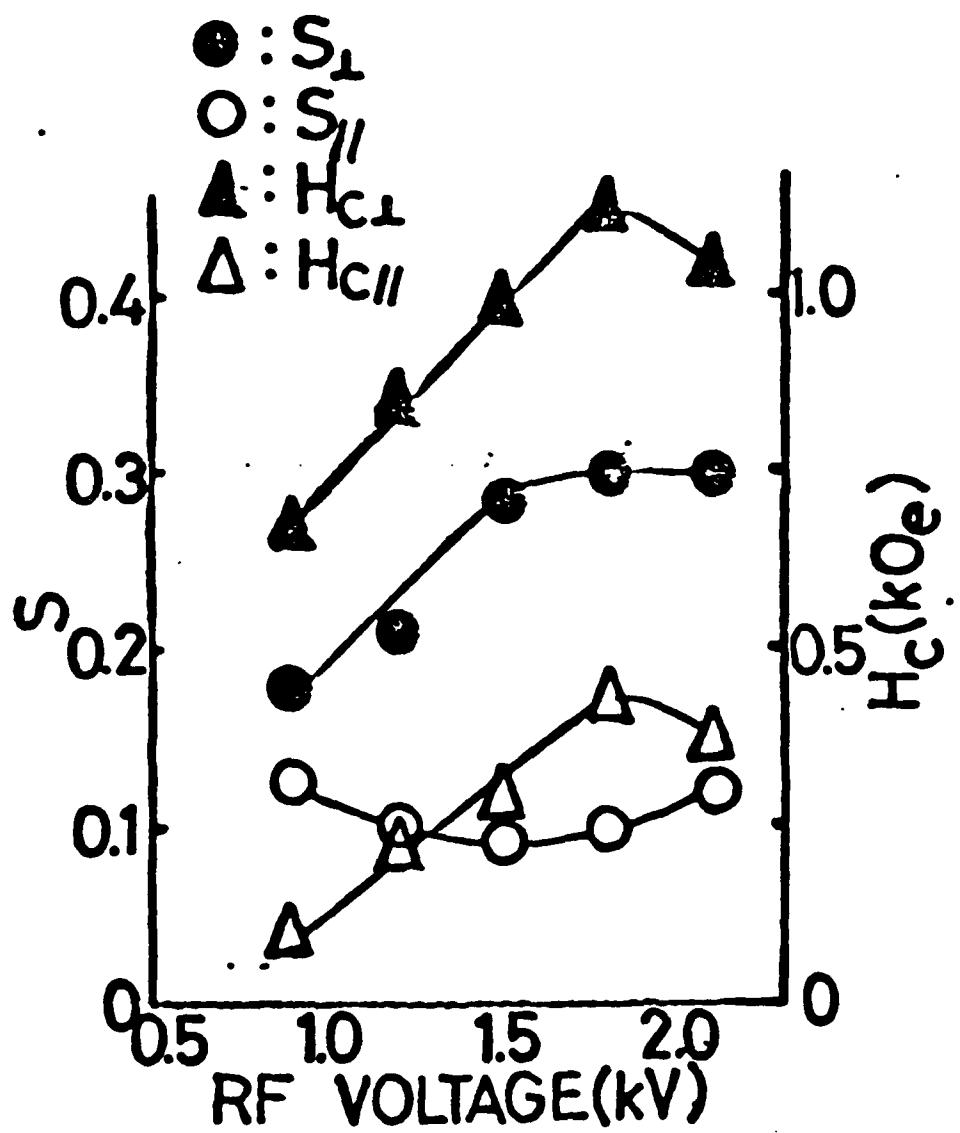
anisotropy than sputtering at 167 $\mathring{A}$/min (Iwasaki and Ouchi, 1978).

Comparison of the data for the two different Ar pressures would seem to indicate that 5 mTorr is the preferable one. Not only were films fabricated with higher values for K_u, but the high K_u films could be sputtered much faster. This is an important consideration when one thinks of practical application. Uesaka and Judy concluded that 5 mTorr was the optimal Ar pressure (Uesaka and Judy, 1981).

Although films have been fabricated with positive K_u, the effective perpendicular anisotropy ($K_u - 2\pi Ms^2$) for all films analyzed to date has been negative (see Fig. 7). This is due at least in large part to two major reasons. First, as discussed earlier, 10 a.t.% Cr is much too low. Optimum Cr percentage is about 18%. Increasing the Cr content will have the effect of decreasing the demagnetizing energy ($2\pi M_s^2$) relatively much more than the anisotropy energy K_u, and should make the balance much more favorable (Iwasaki and Ouchi, 1978). Secondly, the substrates must apparently be heated during sputtering. Uesaka and Judy show that peak hysteresis loop squareness results from heating the substrate table to 160°C (see Fig. 13), and in fact, claim that one can not fabricate films with positive $K_u - 2\pi M_s^2$ without heating the substrates (Uesaka and Judy, 1981).

The composition problem has probably been remedied, due to the new sputtering target mentioned earlier. Referring to Fig. 12 shows that Cr content varies from 20 a.t.% to 22 a.t.%, which should be a workable range. For the second problem, a heated substrate stage has been obtained. The heater has been tried in the system here, and a thermocouple for it has been fabricated and tested. Sputtering of films of the new composition at elevated temperatures has now been carried out, but characterization data are not yet available.

Figure 13
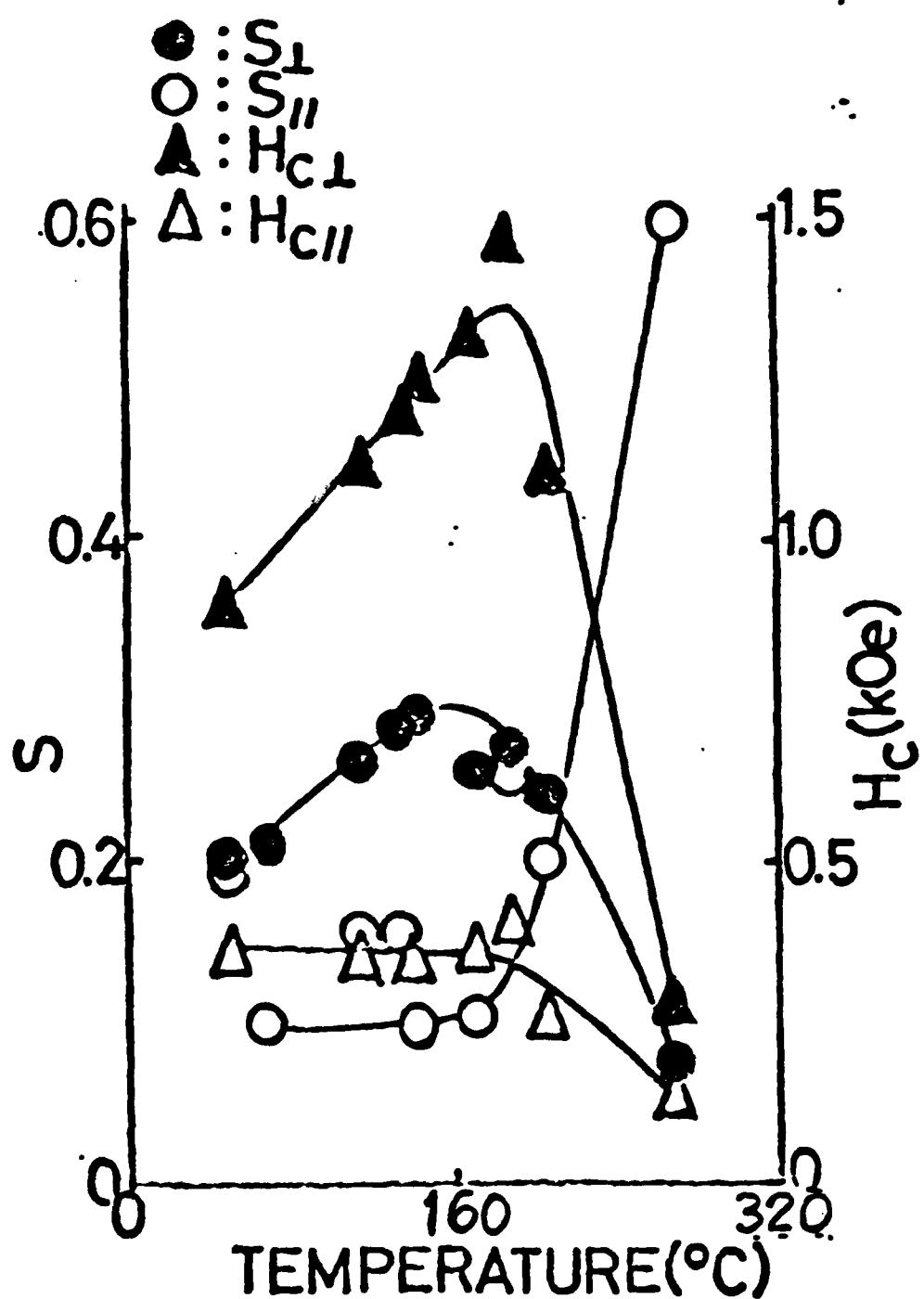
(Uesaka and J.J.)

Assuming that the new films have high perpendicular anisotropy, the next problem to be faced is that of coercive force. Preliminary data indicates that CoCr films are not coercive enough to stay saturated in a self-biasing situation. Solution of this problem will be attempted through the addition of Sm to the films. CoSm and CoCuSm have been studied for permanent magnet materials, and coercive forces as high as 20 to 30kOe have been reported for getter-sputtered Co_5Sm and $Co_{3.65}Cu_{1.35}Sm$. These exceptionally high values require substrate temperatures in the 500°C-600°C range (Theurer et. al., 1969). These temperatures could be harmful to the magnetic bubble storage layer. However, for self-biasing, a coercive force of a few thousand Oersteds is probably all that is needed, so considerably lower temperatures could be used.

If films can be fabricated with sufficient perpendicular anisotropy and coercive force, then they will be sputtered on actual magnetic bubble storage materials, for trials of the self-biasing effect.

LITERATURE CITED

Eschenfelder, Andrew H., Magnetic Bubble Technology, pp. 30-44
Springer-Verlag, Berlin (1980).

Iwasaki, S. and Ouchi, K., "Co-Cr Recording Films with Perpendicular
Magnetic Anisotropy," IEEE Transactions ⁊ Magnetics, vol. MAG-14
no. 5, 849-851 (1978).

— Kryder, Mark H., 1981. Personal Communication.

Liu, T. W. et al., "Thin Film Surface Bias on Magnetic Bubble Materials,"
Journal of Applied Physics, vol. 42 no. 4, 1360-1361 (1971).

Theurer, H. C. et al., "High-Coercive-Force Rare-Earth Alloy Films by
Getter Sputtering," Journal of Applied Physics, vol. 40 no. 7,
2994-2996 (1969).

chishiba, H. et al., 1974 Digests of the Intermag Conference, Toronto,
Canada, 14-17 May, IEEE, New York, 480-483 (1974).

— Uesaka, Y. and Judy, J. H., "Influence of RF Sputtering Conditions on
Co-Cr Films Having Perpendicular Magnetic Anisotropy," preprint -
as yet unpublished (1981).

Ref. on perpendicular recording

— D. D. Dressler and J. H. Judy, "A study of digitally recorded transitions in
thin magnetic films",   p674, 1974.

S. Iwasaki and K. Takemura, "An analysis for the circular mode of magnetization
in short wavelength recording", IEEE Trans. on Mag., Vol. MAG-11, N≗ 5, 1173 (1975)

S. Iwasaki and Y. Nakamura, "An analysis for the magnetization mode for high
density magnetic recording." IEEE Trans. on Mag., Vol. MAG-13, N≗ 5, 1222 (1977)

S. Iwasaki and Y. Nakamura, "The magnetic field distribution of a perpendicular re-
recording head", IEEE Trans. on Mag, Vol. MAG-14, N≗5, 436 (1978).

S. Iwasaki, Y. Nakamura and K. Ouchi, "Perpendicular magnetic recording with
a composite anisotropy film", IEEE Trans. on Mag., Vol. MAG-15, N26, 1456, 1979.

— S. Iwasaki, K. Ouchi and N. Honda, "Studies of the perpendicular magnetization
mode in Co-Cr sputtered films";

2c

INVESTIGATIONS WITH A MAGNETO-OPTIC PHOTOMETER

INTRODUCTION

The magneto-optic photometer is an instrument used to measure the magnetic properties of magnetization layers in magnetic materials and devices. Using this photometer, one may measure the coercivity and the anisotropies of a uniform, in-plane magnetization layer, as can be done by other methods - FMR, torque magnetometer, etc. However, the magneto-optic photometer, unlike other magnetometers, can be used to measure these same properties on a microscopic scale at any chosen area of a non-uniform, in-plane magnetization layer, such as is found in devices made using microfabrication techniques. This area selectivity makes it a powerful tool in analyzing magnetization processes and directly relating these processes to device performance. The photometer is thus far being used in analyzing magnetic bubble devices, and magnetic recording heads, but may also be applied to magneto-optics and microwave devices.

SYSTEM DESCRIPTION

The magneto-optic photometer consists of a polarizing microscope utilizing a laser light source and a photomultiplier (PMT) light detector along with electronics for applying magnetic fields and analyzing the PMT signal (see system diagram in accompanying journal article). The system relies on the Faraday magneto-optic effect for operation. The Faraday effect causes the polarity of light to rotate as the light beam passes through a magnetic material. The amount of rotation is proportional to the component of magnetization that is parallel to the light beam, i.e.

$$\text{angle of rotation} = F \ d \ m \ l \qquad (1)$$

where m is the direction of magnetization

l is the direction of the light beam

F is the Faraday coefficient of the
  magnetic material

d is the distance which the light travels
  through the material

The Faraday rotation angle is therefore an indicator of the direction of the magnetization and can be used to measure the reponse of the magnetization to applied fields. Knowing the response of the magnetization to applied fields is of utmost importance in understanding device performance. This response is dependent upon the magnetic anisotropies (favored magnetization directions) and the coercivity (initial resistance to magnetization change) of the material. The magneto-optic photometer can be used to measure these properties, not only in a uniform magnetic

film as most other types of magnetometers do, but also at specific points within a non-uniform film such as an ion-implanted bubble device.

In investigating the ion-implanted layer of magnetic bubble devices, the magneto-optic photometer works as follows: Laser light of wavelength 488nm is polarized transversely to the beam direction by the microscope polarizer (see Fig. 1). Using the microscope optics, the polarized light is made to be incident on the ion-implanted, in-plane magnetization layer at an angle of $20°$ from the film normal. The light travels through the in-plane magnetization layer (drive layer), and its plane of polarization is rotated about the light beam axis by an amount as described in Eq. 1. The light reflects at the drive layer/bubble layer interface and travels back up through the drive layer, its plane of polarization rotating further. The polarized light, now containing information about the magnetization in its polarization angle, passes back into the microscope optics and through another polarizer, the analyzer, set at about $90°$ to the first polarizer. Since the two polarizers are crossed, almost no light gets through except that light which has rotated polarization due to the Faraday effect. The intensity of the light passing through the analyzer is proportional to the Faraday rotation, and this intensity is detected by the photomultiplier, which converts it into an electrical signal.

To enhance the sensitivity of the system, the system is used in a time-varying mode as follows: An AC in-plane magnetic field is applied to the magnetic film at a specified frequency (the reference frequency). The AC magnetic field causes the in-plane magnetization to oscillate at the same frequency. Hence, the Faraday rotation also varies at the reference frequency, as does the light intensity to the PMT. A phase-locked amplifier is used to look at only the part of the signal from the PMT that is at the reference frequency. The magnitude and phase of the AC signal from the PMT, when compared to the applied field amplitude and phase, gives information about the magnetic anisotropies and coercivities.

MAGNETO-OPTIC MEASUREMENTS

Coercive Force - The coercive force is the magnetic field which when aplied to a magnetic material will cause a change in the magnetization. The larger the coercive force, the more "lossy" the material is, and more power is needed to operate a device using the material. This loss is known as hysterisis loss.

The magneto-optic photometer can be used to find the coercive force by plotting the derivative of the M-H hysterisis loop. This is done by applying a small AC reference field along the in-plant direction of the light beam (the y-axis), while slowly sweeping a large "DC" field along the same direction. The AC field varies the magnetization about a "DC" equilibrium position, the variation being proportional to the slope of the M-H curve at that position. By integrating the output, the M-H loop is formed.

Coercive forces of less than 5 Oe were measured as conveyed in the appended article. These are relatively small fields, and imply that domain wall movement may be the principal magnetization process at low fields.

<u>Determination of Crystalline Directions</u> - The garnet films typically used in ion-implanted devices have cubic crystalline symmetry and are oriented with a $\langle 111 \rangle$ crystal axis perpendicular to the film. When a perpendicular bias field is applied to the film so as to stabilize bubble domains, the in-plane magnetization of the drive layer is subject to the forces of the crystalline anisotropy which result in three favorable directions for the magnetization (see accompanying journal article). The magneto-optic photometer can be used to detect these directions.

A large AC reference field is rotated within the plane of the film as outlined in the journal article. When the sample is oriented with an easy magnetization direction along the y-axis, it is found that there is no phase difference between the reference field and the PMT signal.

<u>Crystalline Anisotropy</u> - The magnitude of the crystalline anisotropy, K_1, can be measured by fitting data from the magneto-optic photometer with a computer model of the system. A computer program has been written which simulates the behavior of the in-plane magnetization for a given crystalline anisotropy constant, K_1. The program calculates the response of the magnetization to applied fields and the resultant PMT signal. By varying K_1 in the computer program, the computer output is made to fit the actual experimental output. The K_1 which causes the best fit is taken as the anisotropy constant of the experimental film.

In one experiment, a large AC in-plane reference field is applied along the y-axis (see journal article). The sample is rotated in $10°$ increments and the magneto-optic photometer output is recorded at each increment. The computer program is used to simulate the same experiment. K_1 is varied in the computer program until the computer output and the actual output agree. The value of K_1 was found to be -3500 ergs/cm^3.

Further verification of the K_1 value was done by fitting the computer output to an experiment in which the reference field was applied along the x-axis. This gave K_1 = -2900 ergs/cm^3. Together, the two experiments gave K_1 = -3150 ergs/cm^3 with σ = 250 erg/cm^3.

The value of K_1 = -3150 ergs/cm^3 was found to fit well to the data of a third experiment in which a small reference field was applied in the y-direction while a large field was slowly swept in the x-direction. This method of curve fitting gives an accuracy of better than 10% in finding K_1.

SYSTEM ADDITIONS

Rotating Stage - A motor-driven, rotating sample stage has been added to the photometer system since the appended paper was written to allow K_1 measurements to be more easily and more quickly made. Now the sample is rotated automatically and with greater accuracy than can be achieved manually. Also, the resultant output is a continuous curve rather than a set of data points. Thus, an experimenter has a better picture of the actual response and is less likely to miss unusual behavior in the data.

Transmission Magneto-optic Photometry - Since magnetic garnet films and garnet substrates are transparent, it is possible to have the incoming polarized light enter through the bottom of the sample (the substrate) and exit through the top (the ion-implanted drive layer). This transmission type of photometry offers several advantages over the reflection mode explained previously (see Fig. 2):

(1) In transmission, all of the polarized light reaching the analyzer has travelled through the drive layer and hence has undergone Faraday rotation Thus, all of this light contributes to the PMT signal. In the reflection mode, much of the light reaching the analyzer has been reflected off the top air/drive-layer interface and contributes nothing to the signal, except possibly interference because of the Kerr effect.

(2) When the proper wavelength of light is used, more light is transmitted through the sample then is reflected at the drive-layer/bubble-layer interface. Therefore, a larger percentage of the incident light contributes to the signal in transmission mode than in reflection mode.

(3) In reflection mode, the light beam passes through the drive layer twice: once in incidence and once upon reflection. Because light changes phase upon reflection, the analysis of the data is complex. In the tansmission mode the light beam's single pass through the drive layer should make data analysis simpler.

Though the transmission mode offers the above advantages over the reflection mode, it is not a replacement of the reflection mode. The reflection mode has the advantages of needing access to only one surface of the sample, of being able to be used on non-transparent magnetic materials (the Kerr effect would be used instead of the Faraday effect), and of being more suitable for probing the surface only.

In preparation for transmitted light photometry, a lens-and-polarizer assembly has been designed and is being built to fit underneath the microscope stage. The assembly will direct and focus polarized laser light up through the bottom surface of the garnet sample, up through the drive layer, and out the top of the sample. The usual microscope optics receive the transmitted light beam and send it through the analyzer to the PMT. The lens-and-polarizer assembly is designed to allow for focussing, as well as x-y movement of the lens, rotation of the polarizer, and changing of the angle of incidence of the light.

Spot-Size Reduction - To look at small magnetic structure in the ion-implanted films, it is necessary to illuminate only the small area of interest. The magneto-optic photometer uses the optics of a microscope to achieve the necessary resolution. The data taken in the accompanying article were obtained with a spot-size of 5μm (the diameter of the illuminated area). This size is fine for finding uniform film properties, however structures in ion-implanted bubble devices are on the order of 1μm. Spot sizes of this magnitude can be realized with a careful arrangement of lenses between the laser source and the microscope objective lens (see system diagram in journal article). Painstaking alignment can result in a spot of about 1.5μm.

Increasing Resolution in Image Plane - Resolution of small magnetic structure can be further increased by decreasing the area of the image reaching the PMT. An image of the illuminated area of the sample is formed just before the PMT by the microscope optics. If an opaque sheet having a small aperture in to see placed in the plane where this image is focused, only that part of the image passing through the aperture will reach the PMT (see Fig. 3). Because the image of the sample area is about 100 times larger than the actual area, a 50μm aperture in the image plane can reduce the effective spot size seen by the PMT down to 0.5μm. Such a small effective spot size would make the magneto-optic photometer a powerful tool in probing local magnetic properties of devices.

A system for achieving this kind of reslution is being obtained from Leitz. The system allows the experimenter to see the actual spot size and the effective spot size simultaneously. Therefore, the experimenter knows exactly what area he is probing.

FIGURE I

FROM LASER   TO ANALYZER

Only small percentage of reflected light has passed through drive layer

Light passes through drive layer twice

AIR

DRIVE

BUBBLE

SUBSTRATE

TO ANALYZER

All light has passed through drive layer

AIR

DRIVE

Light passes through drive layer only once

BUBBLE

SUBSTRATE

FROM
LASER
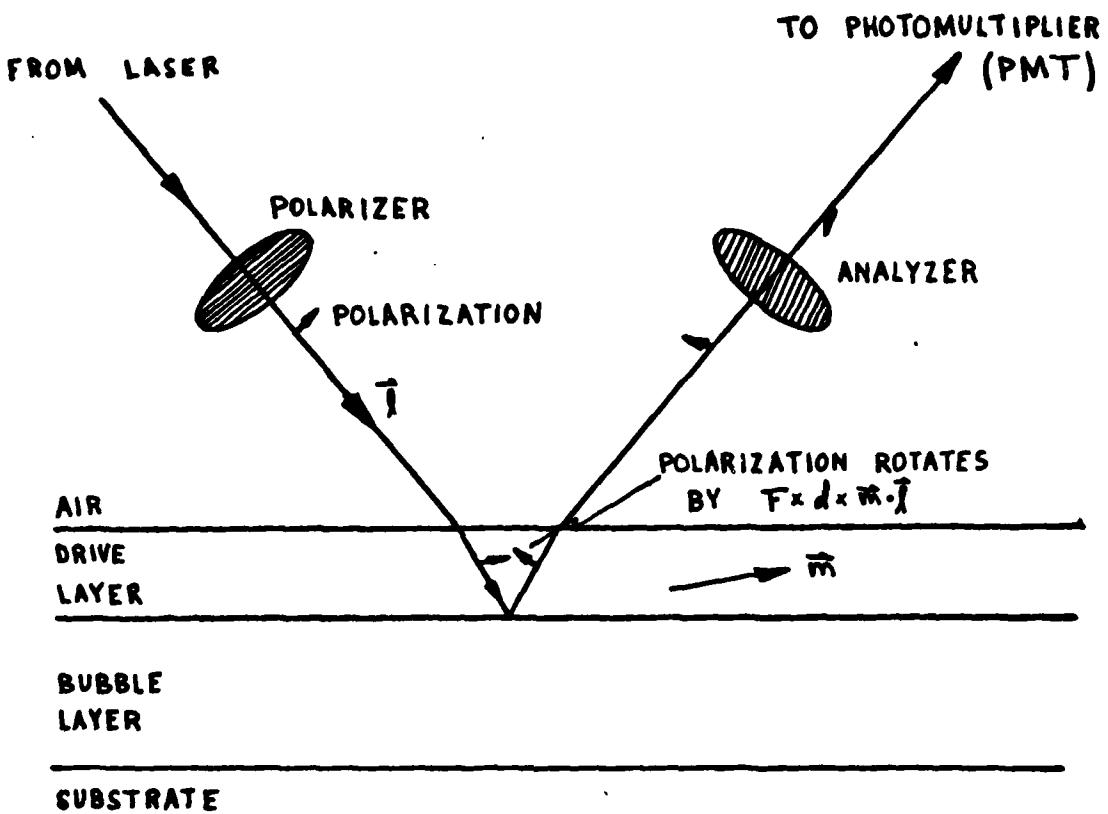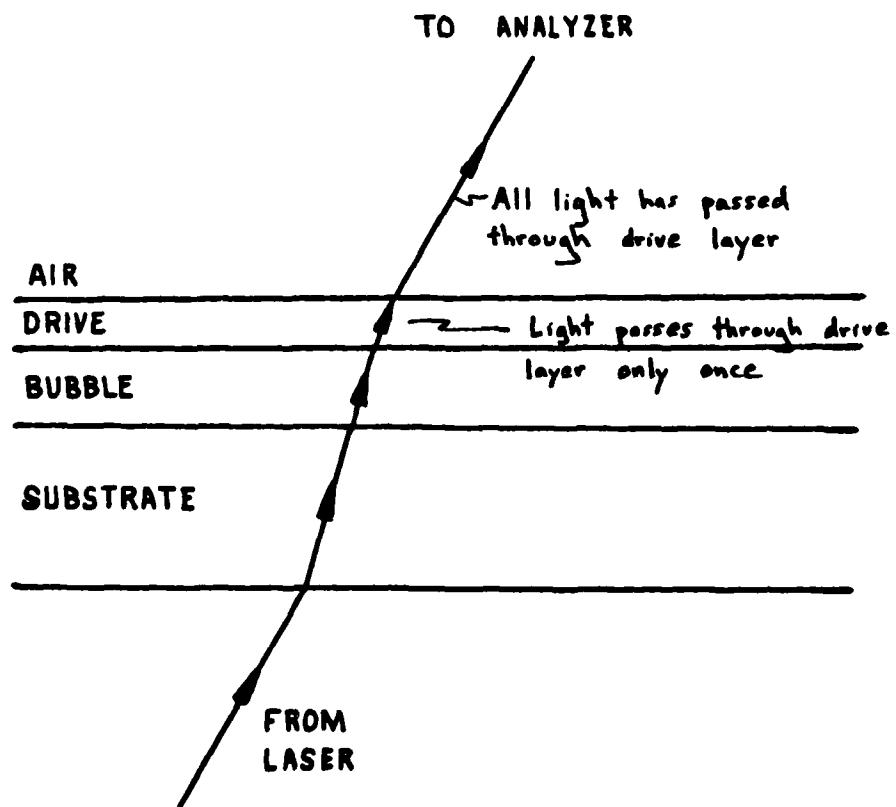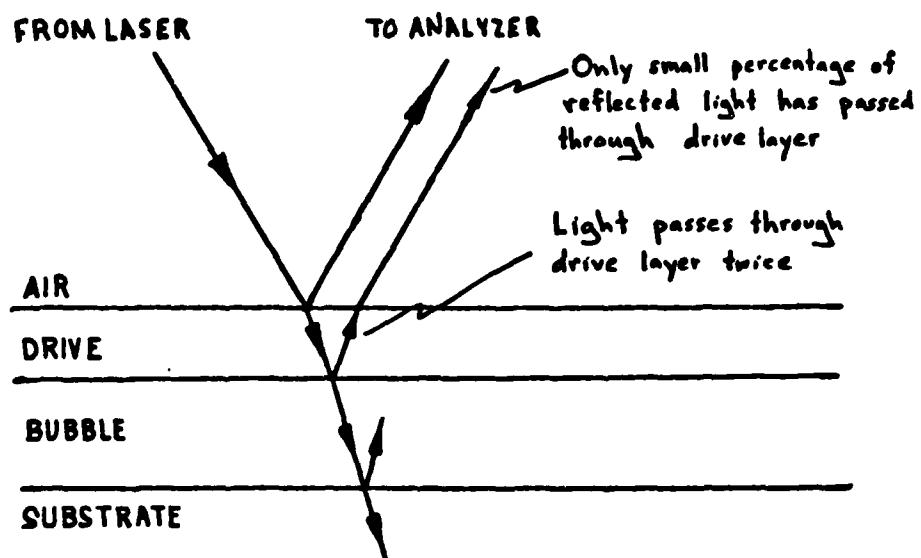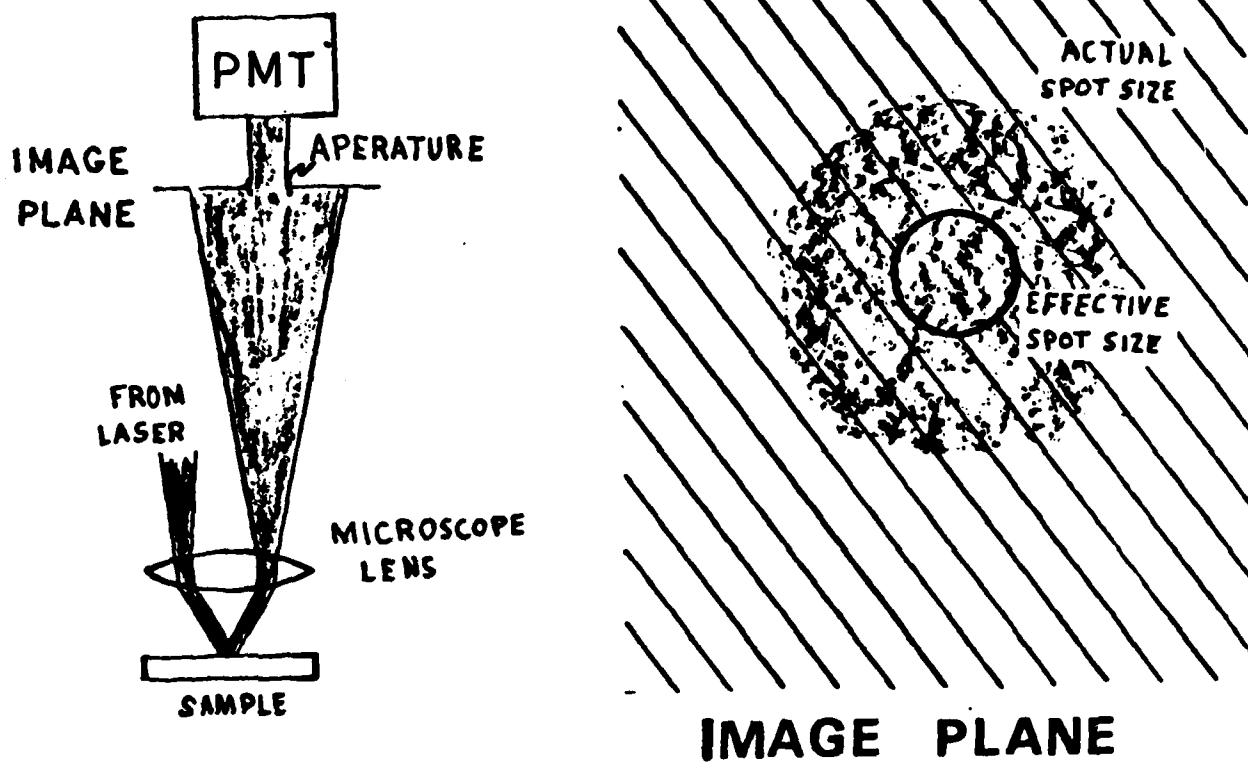
FIGURE II

FIGURE III

INVESTIGATIONS OF ION IMPLANTED LAYERS OF GARNET BY
TRANSMISSION ELECTRON MICROSCOPY

Transmission electron microscopy is being used to study the effects of ion implantation on single crystal garnet materials. Previous investigations of ion implanted garnets have used techniques such as X-ray diffraction and Mossbauer spectroscopy which do not offer high resolution and are thus not amenable to investigation of microfabricated structures with micrometer or smaller dimensions. The use of electronmicroscopy for these investigations has been hindered by the difficulty of thinning single crystal epitaxial materials. Although our yield of thinned samples has not been high we have been successful in making a sufficient number of samples to investigate the strain profile near boundaries between implanted and unimplanted areas in a garnet. Since magneto-striction effects at these boundaries are critical to the operation of ion implanted bubble and microwave devices, these investigations are expected to have a significant technological impact. We expect in the future to investigate the effects of annealing, different implantation conditions, etc., and to broaden the microscopy investigations to include studies of implantation-induced defects and Lorentz microscopy. Below are described the sample preparation procedures and measurements of the strain profiles at implanted boundaries which have thus far been performed using selected area transmission electron diffraction.

SAMPLE PREPARATION

Samples employed for examination are films of $(Sm\ Y\ GdTm)_3Ga_{0.4}Fe_{4.6}O_{12}$, epitaxially grown on 0.5 mm thick gadolinium gallium garnet substrates. A pattern of $8\mu m$ diameter disks on $16\mu m$ centers in a square lattice is defined on the film surface in AZ 1350J photoresist. Ion-implantation is done through the photolithographically defined mask at 120keV with 1×10^{14} O/cm^2 and at 80 keV with 4×10^{15} He/cm^2. This implantation is designed to produce a relatively uniform distribution of ions to a depth of about 3000A.

THINNING PROCEDURE

For examination by TEM, samples must be thin (<200nm) in order that the electrons pass through. The sample must also have a mirror-like surface so that the images obtained contain only information about the internal structure. The thinning procedure is described below.

After implantation, the photoresist was removed from the garnet and the wafer was diced into chips. Individual chips were then bonded to a polishing block using wax and the substrate was thinned by grinding with grit of decreasing particle size ($25\mu,15\mu,9\mu,6\mu,3\mu$). After thinning to approximately 60μ, thickness, the chips were cut into 3mm diameter disks and polished. The polished disks, which were about $30\mu m$ thickness, were removed from the polishing block using warm acetone and transferred into an ion-milling machine (Gatan, Model 600).

The ion miller is equipped with two ion guns for one sample and designed so that the center of the slowly rotating sample (0.5rpm) is removed by an Ar$^+$ beam and thinned until a small hole is formed at the center. The edge of the hole is usually thin enough to allow transmission of the electron beam for image formation. The rim of the sample, which is not thinned is used for handling the sample after ion milling. The photolithographically defined disks on the sample are approximately 8μm in diameter. For the investigation it is necessary that the thinned portion of the film, therefore be somewhat larger than 8μm. For this purpose, the following ion milling procedure was used. Prior to the start of ion milling, one of the two ion guns was aligned approximately 0.4mm off center so that a circular depression of 0.8 mm diameter was formed as the specimen rotated. The other gun was next aligned to ion-mill the center of the specimen. Thus, alternating between guns, a large relatively flat area, of 0.8 mm diameter, may be formed.

The ion milling was performed at the substrate side. An Ar$^+$ beam at 6kV with the gun current ranging from 0.1-0.3 mA was used at a glancing angle of 10-15°. These conditions were selected to accelerate the ion milling process and avoid formation of a rough surface. The ion milling time required to prepare one sample, typically, was 40 hours. At about 2 hours before the end of the process time, a small dimple will form due to the compressive stress in the implanted region. After this dimple was observed only the ion gun aligned at the center was used until a small hole was formed.

USE OF TEM

A transmission electron microscope JEM-100C, operated at an accelerating voltage of 120kV was used to locate unimplanted discs in the garnet and examine microstructural defects in the implanted area. However, as may be expected for garnet, which is ionic in character and possesses a large lattice constant (a=12.383A) and thus possesses a large Burgers vector, large scale lattice defects were not observed in the implanted region. Hence, it was determined to direct the efforts to experimental confirmation of the localized stress relaxation at pattern boundaries. It was very recently suggested by Hidaka and Matsutera (Appl Phys. Lett., 39, 116 (1981)) and Backerra et al. (Philips J. Res., 36, 112(1981)) that in ion implanted contiguous disc bubble devices, there should be a localized stress relaxation near to and normal to the boundary, leading to the localized uniaxial anisotropy necessary to form charged walls. However, there has previously been no experimental work reported which provides information on the localized strains introduced at pattern boundaries.

Electron microscopy may be used both for imaging and electron diffraction, and with the aid of an intermediate aperture, it is possible to obtain diffraction patterns from small portions of the sample, which is termed selected area diffraction (SAD). With the JEM-100C, the diameter of the smallest selectable area was 0.7μm. This

diameter of the diffracting area was employed throughout this investigation to obtain strain profiles by measurement of the variations of lattice constants. Fig. 1 shows the simplified geometry of selected area diffraction. The disc of 0.7 μm diameter corresponds to the diffracting area. On the viewing screen or photographic plate, the hkl spot appears at a distance r_{hkl} from the transmitted beam spot (000) in a direction perpendicular to the atomic plane in the real space, which has Miller indicates hkl and the interplaner spacing d_{hkl}, where $d_{hkl} = \lambda L/r_{hkl}$ is the wave length of the incident electron beam and L is a constant characteristic of a set of selected conditions of the microscope.

For cubic garnet crystal, the lattice constant $a=d_{hkl}[h^2+k^2+l^2]$. Therefore, the lattice constant in a direction perpendicular to the hkl plane may be obtained by measurement of r_{hkl}. Since the typical angle between transmitted and diffracted beam is small ($\leq$ 1 o 2°), the lattice constant measured in this way is the in-plane lattice constant.

The electron microscope image appears rotated with respect to the diffraction pattern. However, the rotation angle is a function of the electron microscope operating conditions and can be easily determined. Thus, after correction for image rotation, it was possible to measure in-plane lattice constants as a function of position with 0.7 micron spatial resolution.

A Siemens recording microphotometer was used in measurement of the distance between two spots in the photographed SAD pattern.

EXPERIMENTAL RESULTS

Fig. 2 shows an example of a diffraction pattern characteristic of the (111) plane and an electron microscope image of a non-implanted disc, which is surrounded by implanted region. The thin lines which run through the non-implanted region, were found to be diffraciton contours which occur because of curling of the sample in a direction perpendicular to the diffraction contours. These lines bend at the boundary of implanted and non-implanted region, suggesting that the lattice constants abruptly change at the boundary.

Before the actual measurement of lattice constants, calibration of the camera constant λ_L, which is a function of accelerating voltage and other operating conditions of the microscope, is needed. The λ_L ($=r_{hkl} \cdot d_{hkl}$) may be determined by measurement of r_{hkl} for a substance which has an accurately known interplaner spacing. For this purpose Au was used. Also, in order to avoid the possible difference in L, 100A of Au was deposited directly on some of the ion-milled garnet foils. The lattice constant of garnet, at the center of the non-implanted discs, invariably was found to be 12.43|0.01A, a value somewhat greater than those of usual garnet (a=12.383A). This larger value may have arisen because the lattice constant of Au is somewhat expanded by tensile stress introduced by deposition on

the garnet film. However, in this preliminary study, it was observed that the value of λ_L was constant with respect of time. Therefore, in subsequent measurements, Au was not deposited and the lattice strain $\Delta a/a$ was referenced to the lattice parameter at the center of the unimplanted discs.

Fig. 3 shows in-plane strain as a function of position along three directions which run through the center of the non-implanted discs. The lattice constants at each position were measured for diffraction spots which were aligned at or nearly normal to the disc edge. Thus, the in-plane strain was measured for directions normal to the boundary edge. Uncertainty in the measurement, which depends on sizes of the aperture and diffraction spots, was to within $\Delta a/a = 0.06\%$ To minimize the spot sizes, the intensity of the incident electron beam was minimized and a long exposure time, typically 1 minute, was employed. The locations of the individual diffracting areas, of 0.7 micron diameter, were frequently checked by photographing the image with pointer which indicates the diffracting area. An example of such a photograph is given in Fig. 4. In this way, a spatial accuracy of better than 0.2 μm is achieved for the data presented in Fig. 3.

DISCUSSION

The data in Fig. provide experimental evidence of the stress relief predicted in the models proposed by Hidaka and Matsutera (Appl. Phys. Lett., 39, 116(1981)), and Backerra et al. (Philips J. Res., 36, 112(1981)). These workers pointed out that, for a film on a thick substrate, there is no relaxation parallel to the boundary (the y-direction in Fig. 5), but that there is an elastic relaxation normal to the boundary causing the implanted region to expand and the unimplanted region to contract.

Although the films examined in this study had the substrate removed, thereby allowing stress relief in all directions, the data in Fig. 3 indicate that significant stress relaxation normal to and near to the boundary does occur in qualitative agreement with the above models. Figure 5 shows a model for the stress relaxation expected in films with no substrate. In Fig. 5a, a schematic cross-sectional diagram of the cubic lattice near the interface between the unimplanted and implanted areas is shown. In the far left hand edge of the diagram the lattice constant is uniform and equal to that of an unimplanted garnet film, while on the far right the lattice constant is also uniform, but equal to that of a uniformly implanted film. The area of interest is the transition region between the two uniform areas.

To understand why the strains indicated in Fig. 5a occur, consider the stresses on unit cells near to the boundary between the unimplanted and implanted areas. Figure 5b shows the cells and their distortions. The cell on the left lies in the unimplanted area and without any additional stresses would be cubic with a lattice constant smaller than that of neighboring implanted cells on the right. Due to bonding of the unimplanted cells to larger implanted cells, both the unimplanted and implanted cells feel stresses causing them to distort. The unimplanted cells feel tensile stresses in

the y and z directions, causing the lattice constant a, measured along x, the normal to the implanted boundary, to contract. Similarly, the implanted cells feel compressive stresses in y and z, causing the lattice constant measured normal to the implanted boundary to expand. A measurement of strain perpendicular to the boundary between unimplanted and implanted areas is thus expected to exhibit a minimum on the unimplanted side near the boundary and a maximum on the implanted side near the boundary as shown qualitatively in Fig. 5c.

The majority of data in Fig. 3 show evidence of minima and maxima in the strain normal to the boundary like that in Fig. 5c. In certain cases, however, the minima and/or maxima are not detected. It is possible that failure to detect the peaks in those cases is due to experimental difficulties, such as the fact that in very thin films the relaxation might occur over a very short distance, making it possible that the peaks in strain were located between positions where data points were taken. Alternatively, if the minima and maxima in strain are in fact absent, then one must conclude that the implantation induced stress is graded across the boundary in such a fashion that the tetragonal distortion indicated in Fig. 5 does not occur. This could be the case in samples which have an implantation mask profile which is chamfered at the edge and suggests that the charged wall structure may depend critically on the implantation profile normal to the boundary. Relaxation of the peaks in strain at the boundary could also occur as a result of annealing. Diffusion of the defect structure introduced by implantation and responsible for the stress would be promoted by the non-uniform stress fields existing at the boundary.

The non-uniform stresses at the boundary between implanted and unimplanted areas can be expected not only to produce significant magnetic anisotropies in the implanted layer, but also in the underlying bubble layer. To estimate the stress induced anisotropies in the bubble layer, an analysis of stress fields from patterned metal films performed by Dishman et al. (J. Appl. Phys. 45, 4076 (1974)) is used. Although contiguous disk devices use curved boundaries, the analysis may be simplified by assuming a straight boundary as in Fig. 6. This approximation is reasonable when the radius of curvature R of the boundary is large compared to the implanted film thickness t, which is typically fulfilled in practical devices. (With $1 \mu m$ bubbles, R = $4 \mu m$ and t = $0.4 \mu m$.) The stresses from the implanted layer are approximated by a line force $s = -\sigma_{xx} t$ acting at the surface of a semi-infinite solid, where $-\sigma_{xx}$ is the compressive stress in the implanted region. The line force is assumed to exist a distance t/2 above the surface of the bubble material and the space between the line force and the bubble layer is assumed to have elastic constants equal to those of the bubble material.

To obtain a value for σ_{xx} we use data from Fig. 3 and $\sigma_{xx} = Ye_{xx}/(1-2v)$ where Y is Young's modulus and v is Poissons's ratio. Choosing $e_{xx} = 0.5\%$ as a typical value in the uniformly implanted region far from the disk edge in Fig. 3, and using $Y = 2 \times 10^{12}$ dyne/cm^2 and $v = 0.32$ we find $\sigma_{xx} = 2.8 \times 10^{10}$ dyne/cm^2.

Taking the origin of coordinates at the point of application of the line force, the longitudinal stress in the z direction perpendicular to the film is given by

$$\sigma_z = -2s \times z^2/\pi(x^2+y^2)^2 \tag{1}$$

which has a maximum value of

$$\sigma_z(max) = -9s/8\sqrt{3}\pi z \tag{2}$$

when $x = z/\sqrt{3}$. This stress component gives rise to an anisotropic energy density which when added to the growth induced anisotropy of the film produces a total perpendicular anisotropy energy density

$$E_{Kz} = K_u \sin^2\theta + 1.5\lambda_{111}\sigma_z\sin^2\theta \tag{3}$$

where θ is the polar angle defined from the z-axis. In the region x>0 under the implanted layer σ_z is positive. Since λ_{111} is typically negative, the stresses from the boundary reduce the effective perpendicular anisotropy of the garnet.

Table I compares $1.5\ \lambda_{111}\ \sigma_{zz}$ with K_u for two garnets used in 1μm bubble ion implanted devices. Values are given both at the top (z=-t/2) and bottom (z=-h-t/2) surfaces of the bubble layer which is $h=0.8\mu$m thick and which has an implanted layer $t=0.4\mu$m thick on its surface. The SmGdTmYGa garnet, which is useful as a single layer ion implantable material, has high magnetostriction ($\lambda_{111} = -3.5\times10^6$) and moderate K_u. The EuTmYGa garnet, which has been used in double layer contiguous disk devices, has lower magnetostriction ($\lambda_{111} = -1.8\times10^{-6}$) and higher K_u. It is seen that $1.5\ \lambda_{111}\sigma_{zz}$ is comparable to K_u in the SmGdTmYGa garnet, but significantly less than K_u in the EuTmYGa garnet.

Since the net perpendicular anisotropy near an implanted boundary in SmGdTmYGa garnet films is much less than in EuTmYGa garnet films, the nucleation threshold for bubble domains is considerably lower when using the SmGdTmYGa garnet material. With identical nucleator designs current requirements for nucleation in SmGdTmYGa films is about one-half the current requirement in EuTmYGa materials.

The reduced perpendicular anisotropy at the implanted boundary edge also gives rise to a potential energy minimum for domain walls there. Thus the force necessary to pull a bubble domain from a boundary edge should depend linearly on the magnetostriction constants of the bubble material. One would expect, therefore, that devices using high magnetostriction materials would require higher transfer gate currents than devices using low magnetostriction materials.

CONCLUSIONS

Measurements of strain perpendicular to the edge of implanted boundaries in garnet films indicates that in most cases there is stress relaxation normal to the boundary. These data are in agreement with the predictions of researchers who have indicated that such stress relaxation is critical for the formation of charged walls. In some cases the data do not show the expected strains. Although experimental difficulties may have prevented their measurement, it is also possible that the stress profile

normal to the boundary is graded over a sufficiently large distance that the predicted relaxation does not occur. This could arise when the implantation profile normal to the boundary is graded, due to a chamfered mask edge, or when the non-uniform stresses at the boundary are annealed out.

Consideration of the stress induced anisotropy arising from an implanted boundary led to the conclusion that bubble layers with high negative magnetostriction constants can be expected to have low bubble nucleation thresholds and to require large field gradients to pull a bubble from an implanted boundary.

TABLE I

MATERIAL	$\frac{3}{-2} \lambda_{111} \sigma_z$(max) (erg/cm^3)		Ku(erg/cm^3)
	TOP SURFACE	BOTTOM SURFACE	
SmGdTmGaYIG	-4.5×10^4	-1.2×10^4	3×10^4
EuTmGaYIG	-2.3×10^4	-0.6×10^4	4.6×10^4
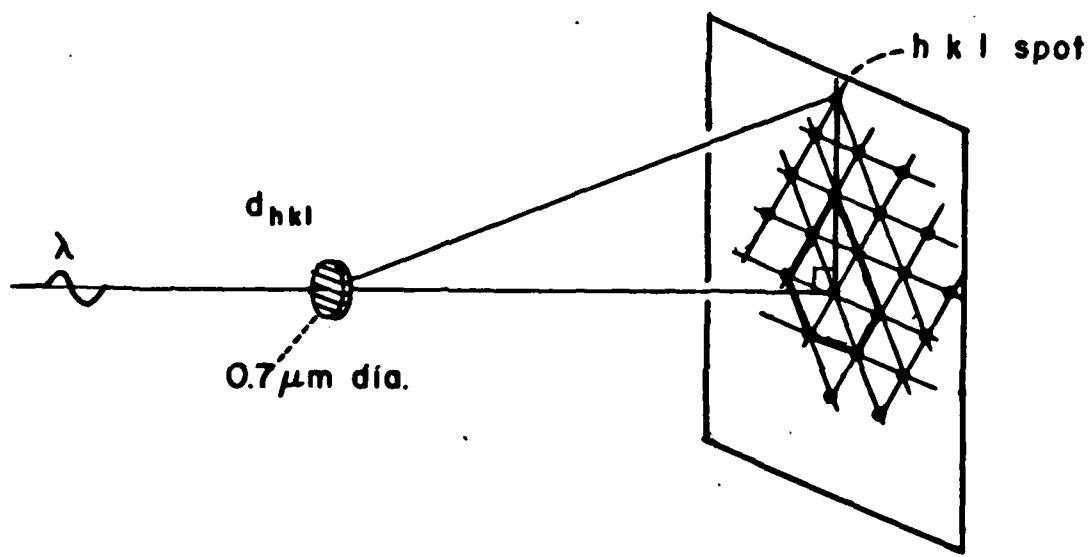
FIGURE 1
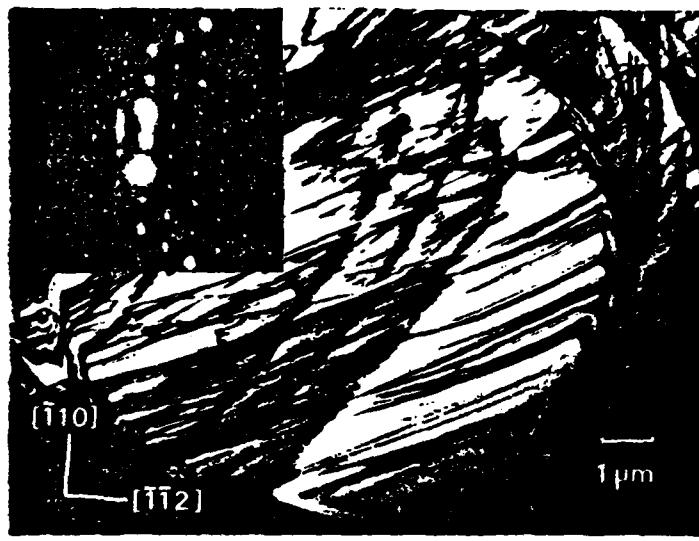
FIGURE II

FIGURE III

FIGURE IV

MASK

z

x

UNIMPLANTED REGION | IMPLANTED REGION

(a)

z

y

x

z

y

x

(b)

Δa/a

x

(c)
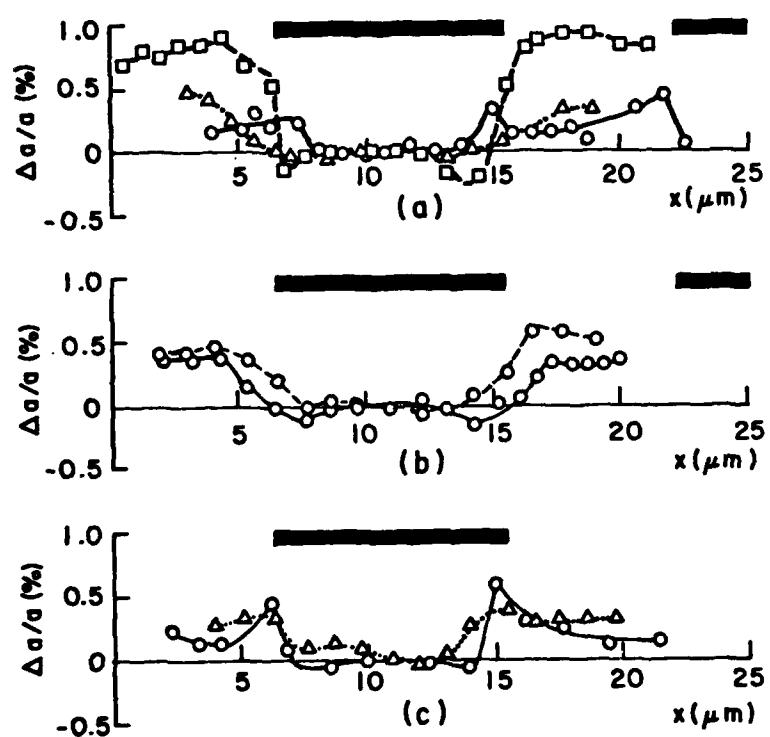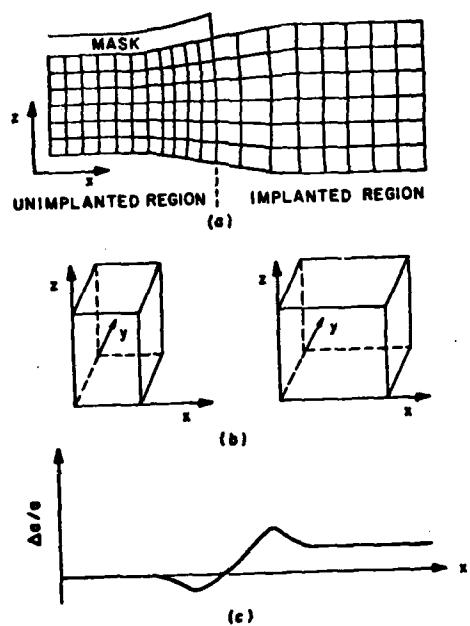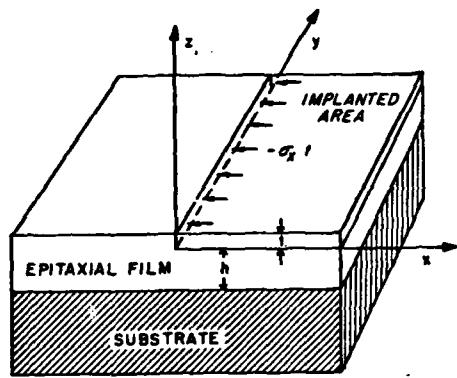
FIGURE V

FIGURE VI

FABRICATION OF CONTIGUOUS DISK MAGNETIC BUBBLE DEVICES

INTRODUCTION

Contiguous disk magnetic bubble devices offer order of magnitude higher bit densities than conventional field access permalloy devices which are now in manufacturing.

This report describes progress in fabricating submicron ion implanted magnetic bubble devices, which require 1 minimum line width. Electroplated gold was selected over photoresist as a propagation pattern implantation mask because photoresist patterns show rounding effects at pattern edges. Separate conductor masks are used, apart from the propagation pattern mask, to give wider design lattitude. A propagation pattern device for 1 μm bubbles was fabricated on a double layer garnet film with material characteristics shown in Tablє I. Its device structure and processing steps are shown in Fig. I and Table II, respectively. Test results show bias margin (Fig. 2, 14% for good track) comparable with published data. Other propagation devices for 1μm and 0.5μm bubbles are being fabricated.Masks for these devices were fabricated using electron beam lithography at the National Research and Resource Facility for Submicron structures and are shown in Fig. 3.

In the following section, the processing steps listed in Table II are discussed in detail and future research directions are indicated.

DEPOSITION OF RELFECTION LAYER, SPACER AND PLATING BASE

A reflection layer is deposited to facilitate the observation of bubbles with a polarized light microscope. Pellets of Cr were evaporated with a resistive vacuum evaporator with good results.

SiO2 was sputter-deposited as spacer with no difficulties. Typical deposition rate is 80 A/min at I50 W forward power and 10 mTorr Ar pressure using a Perkin Elmer 2400 series RF sputterer.

About 40 A of Mo and 80 A of Au were used as adhesion layer and electroplating base, respectively. They were sputter-deposited successively in one pumpdown without breaking vacuum so as to insure good adhesion of Au on Mo. Deposition rate of Mo was 120 A/min and that of Au was 240 A/min at 150 W forward power and 10 mTorr Ar pressure. Using this techique good adhesion was obtained, whereas when Mo and Au were deposited in separate pumpdowns, adhesion was poor.

PHOTOLITHOGRAPHY

The main advantage of contiguous disk devices is the ability to manipulate small bubbles with large circuit patterns (minimum features are twice the size of the bubble diameter). This allows the use of conventional optical lithography rather than electron beam or X-ray technology.

The mask designed by us (Fig. 3 and Fig. 4) contains both 1 μm and 0.5 μm propagation patterns with various shapes such as diamonds, symmetrical arrows and asymmetrical arrows. It was made at Cornell University's National Submicron Facilities with a Cambridge electron beam pattern generator and chemical etching of a Cr mask. Although this mask is quite good, sputter etching of the mask will be attempted in the future to obtain even better linewidth control.

The photolithography process is used to define the ion implantation mask and conductor patterns. AZ-1350Z photoresist with 1.0 μm-1.5 μm thickness was used. 1.5 μm of photoresist was used for 1 μm bubble devices with good pattern delineation, while 1 μ of photo resist (AZ 1400-27) is being used to fabricate 0.5 μm patterns.

A Kulick and Soffa contact printing mask aligner was used to print the mask. Patterns for 1 μ bubbles were very good, but only 30% of the 0.5 μm patterns fabricated thus far appear to be acceptable. We are trying to obtain a grant from the NSF to purchase a new contact mask aligner with submicron resolution and improved alignment tolerance (0.1 μm) to improve our yield on submicron structures.

ELECTROPLATING OF ION IMPLANTATION MASK

The electrodeposition of gold through a photolithographic pattern requires very simple equipment, but gives excellent pattern definition and a good implantation mask. The plating method used was a variation of barrel plating as shown in Fig. 5. The barrel is stationary and serves as the anode. The sample is clamped to the shaft of an agitating motor which is connected to the negative terminal of a constant current source. This plating cell was built along with a motor control unit which automatically changes the direction of the rotation of the agitating motor at desired intervals. Sel-Rex Corporation's gold bath BDT 510 was used with excellent results. Gold plating rate was 2,300 A/min. at 5 mA/cm^2 current density.

SPUTTER ETCHING OF PLATING BASE AND ADHESION LAYER

After gold plating, the plating base and adhesion layer outside the proagation patterns were removed by sputter etching. The etch rate of gold was 120 A/min at 150 W forward power and 10 mTorr Argon pressure, while that of Mo was 20 A/min at the same conditions.

ION IMPLANTATION

In devices fabricated thus far, triple implantation of He$^+$ with energy levels of 190 KeV, 90 KeV and 30 KeV and respective dosages of 3.5x10/cm^2, 1.96 x 10 /cm^2 and 1.15 x 10 /cm^2 was used. This implantation gives relatively uniform damage levels throughout the bubble driving layer thickness of about 0.35 μm. We are now experimenting with double implantations of deuterium and oxygen.

FUTURE RESEARCH

Many more propagation patterns for both 1 μm and submicron bubbles will be fabricated and tested to optimize garnet growth conditions, ion implantation conditions and overall device performance as well as to improve metal overlay fabrication techniques. Presently, masks are being designed for bubble memory chips containing all functions necessary for full read/write operation. The emphasis of our work is to gather experimental data on how ion implanted devices scale to higher density, to test out new submicron bubble materials, and to identify any unforseen problems of submicron-dimensioned ion-implanted devices. It is anticipated for example that the profile of the implantation at a boundary may be critical to submicron device performance as suggested in the section describing measurements of the strain profile at implanted boundaries. This as well as other potential problems will be studied.

TABLE I

TYPICAL ROOM TEMPERATURE PROPERTIES OF LPE LAYERS

Property	Storage Layer $(EuTmY)_3(FeGa)_5O_{12}$	Drive Layer $(GdTmY)_3(FeGa)_5O_{12}$
Thickness, $h(\mu m)$	0.83	0.43
Stripewidth, $Ws(\mu m)$	0.89	—
Bubble Collapse field, $H_o(Oe)$	322	—
Material Parameter, $\ell(\mu m)$	0.10	~0.12
Saturation Magnetization, $4\pi M_s(G)$	650	~520
Quality factor, Q	~2.5	~1.2

TABLE II

CONTIGUOUS DISK PROPAGATION PATTERN PROCESSING STEPS

Purpose of Step	Material	Process	Thickness
A. Spacer	SiO_2	Sputtering	200 Å
B. Reflection Layer	Cr	Evaporation	350 Å
C. Spacer	SiO_2	Sputtering	200 Å
D. Adhesion Layer	Mo	Sputtering	40 Å
E. Plating Base	Au	Sputtering	80 Å
F. Mask for Propgation Patterns	AZ-1350J		1.0-1.5 μm
G. Ion Implantation Mask (Propagation Patterns)	Au (BDT 510)	Electroplating	0.7 μm
H. Remove Plating Base	Mo/Au	Sputter etch	120 Å
I. Ion Implantation	He^+, Deuterium, Oxygen		
J. Anneal		Optional	

AN ION IMPLANTATION MASK
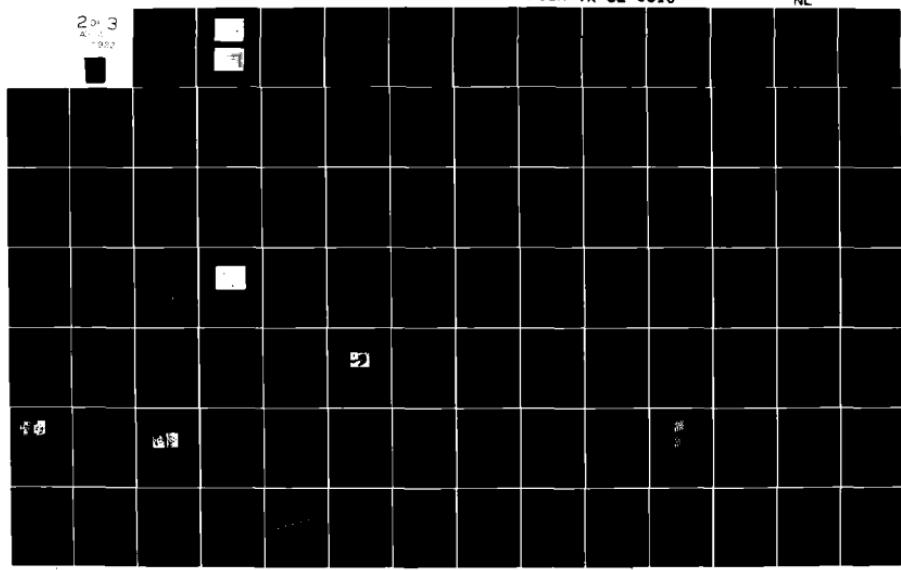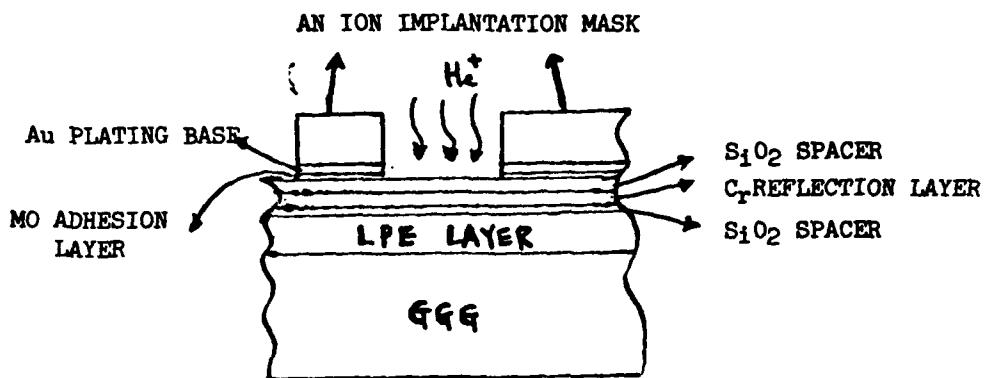
FIG 1 SIDE VIEW OF CONTIGUOUS BUBBLE DEVICE
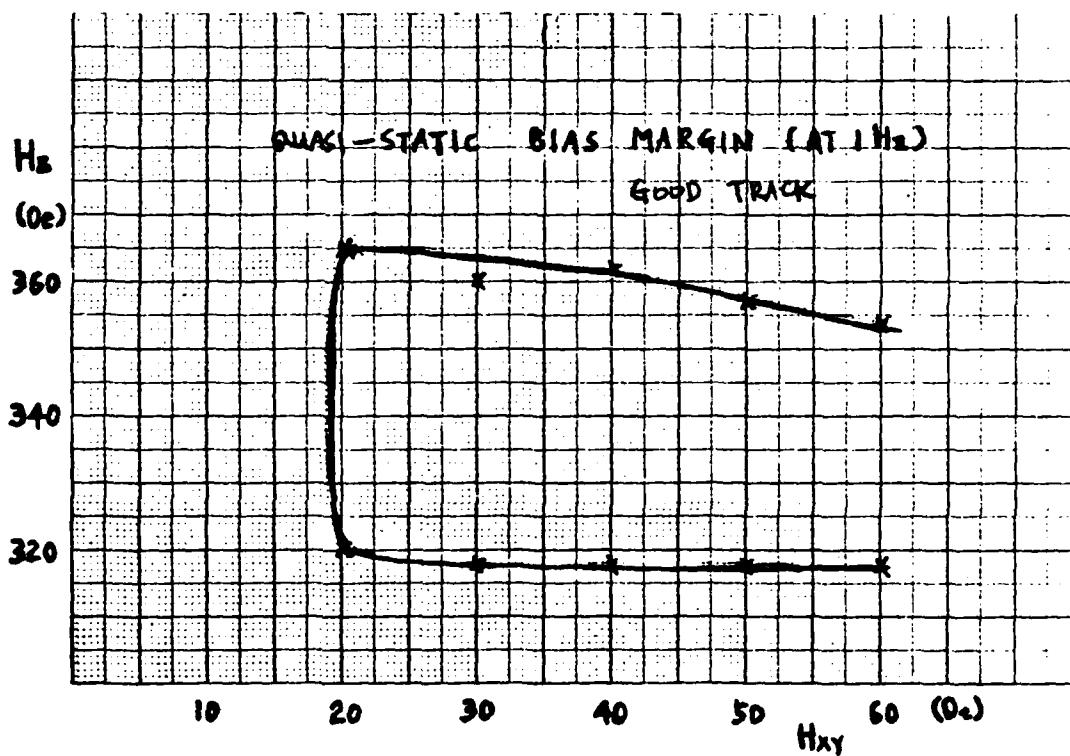
FIG. 2 BIAS MARGIN OF CONTIGUOUS DISK
PROPAGATION PATTERN S1603

FIG. 3 MASK FOR 0.5μm and 1μm BUBBLE DEVICES

2.2μm
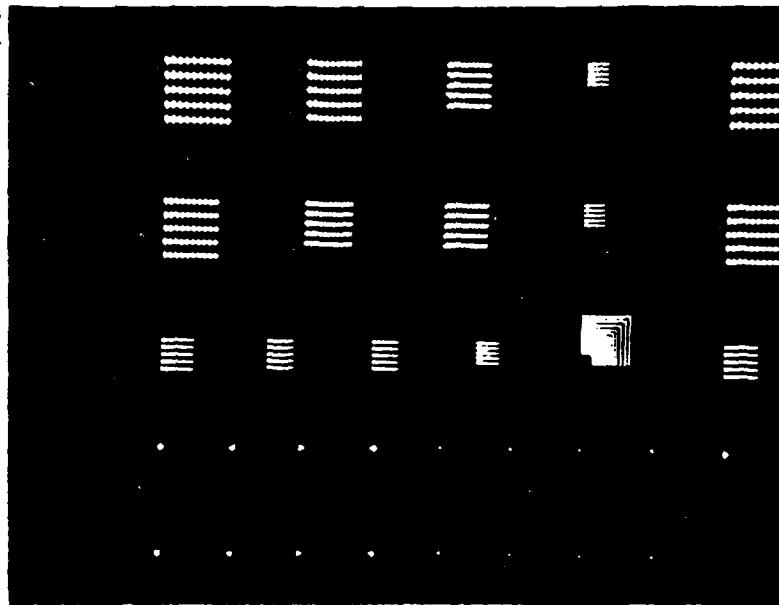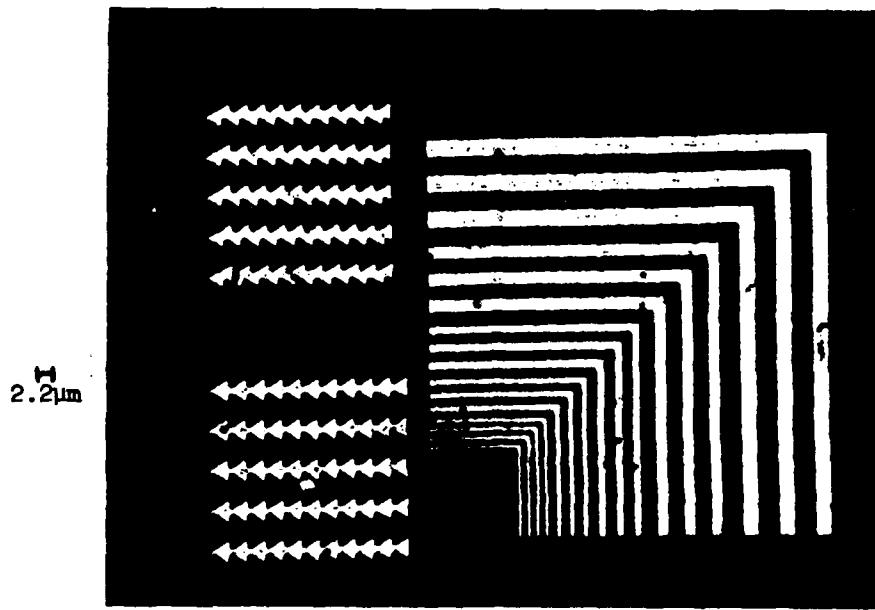
X 1333   4/22/81 at Cornell

FIG. 4   BLOW UP OF THE ABOVE MASK
1μm CD AND RESOLUTION PATTERN

CONSTANT CURRENT
SOURCE

SYNCHRONOUS
MOTOR

MOTOR CONTROL

PLATING BATH (BDT 510)

CATHODE CLIP

SAMPLE

STAINLESS STEEL
ANODE
(TYPE 316)

BEAKER
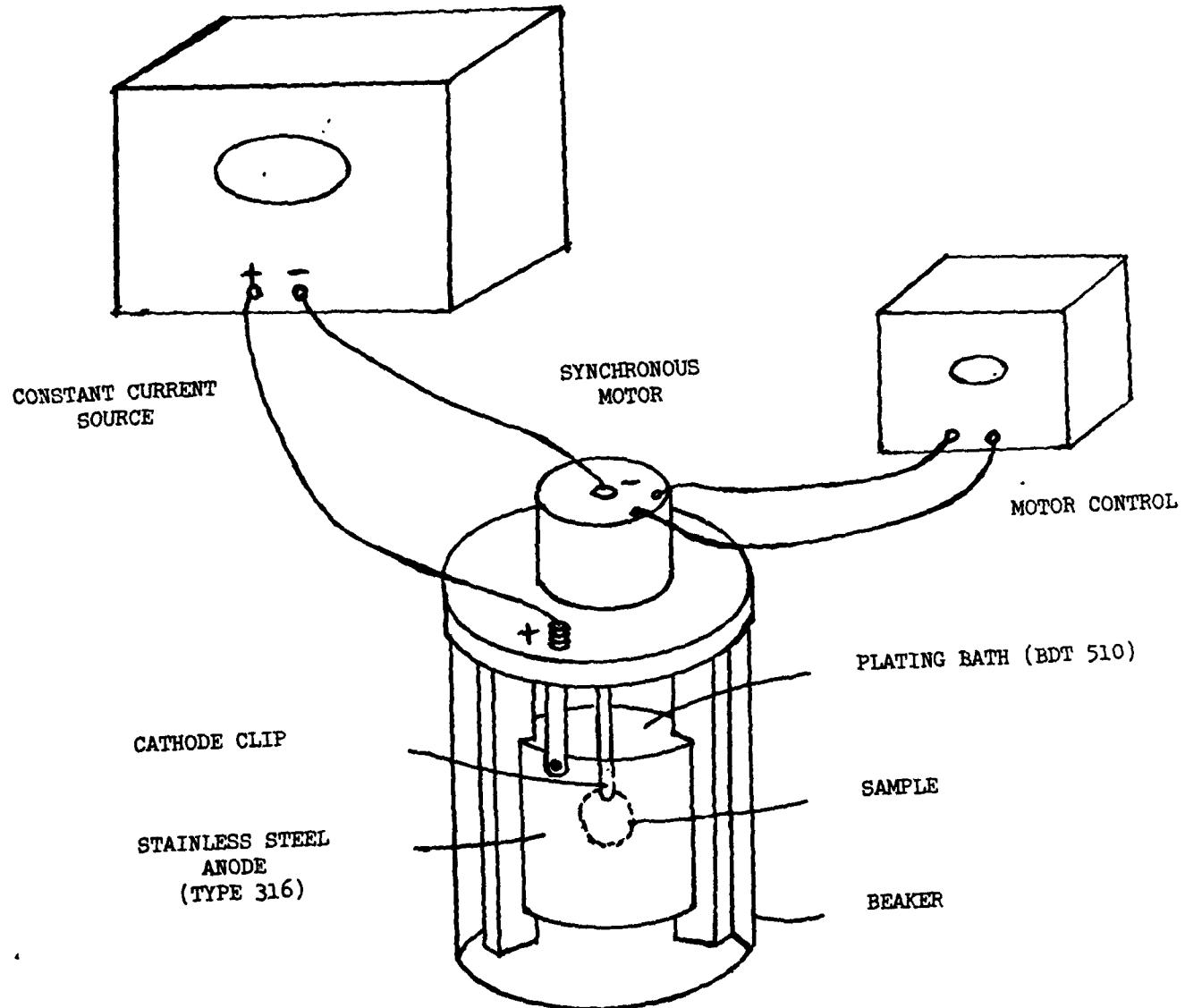
FIG. 5 A SCHEMATIC DIAGRAM OF GOLD ELECTRO-
PLATING APPARATUS

Optical Investigation of Ion Implanted Garnet Epilayers

To give a better understanding of stoichiometric and crystal field deviations present with and without ion implantation, a spectroscopic study of rare earth epilayers has been initiated. Optical examination of ion implanted layers doped with a rare earth probe has not been previously tried by us or groups familiar to us. Conventional absorption and reflection spectroscopy on such samples seems likely to expand the understanding of the damage to the microscopic structure of the epilayer. Preliminary investigations of gadolinium gallium garnet (GGG) substrates and representative epilayers have determined tentative sample parameters (i.e. substrate and epilayer thickness) best suited to the optical measurements. Design of a low temperature magnetoptical measurement system has been finished with construction of the system expected to be completed by mid-December, 1981. To gain familiarity with the substrate and to ready the spectrophotometer, a sample of pure GGG was tested.

The absorption spectrum of GGG illustrates some of the unique features of rare earths in crystals (Figure 1). From the comparison of the energy levels of gadolinium (Gd) in $LaCl_3$ (Figure 2) with the energy levels of GGG (Figure 3), it is obvious that the absorption pattern is due to the fine structure of Gd^{3+}. Even though the local crystal structure is quite different (dodecahedral (D_2) in GGG and hexagonal (D_{6h}) in Gd^{3+} doped $LaCl_3$) the fine structure levels remain approximately the same. The tightly bound 4f electrons are shielded from the crystal field by the 5s and 5p electrons in the Gd^{3+} (Figure 4) and exhibit basic atomic transitions. The crystal field comes in as a small correction to the Hamiltonian and gives a Stark splitting of the fine structure levels. At room temperature this splitting is not resolved for GGG. In the case of Gd^{3+} doped $LaCl_3$ it is known that the splitting is very small and borders on the resolution of our spectrophotometer.

The resolution difficulty, as well as the absence of absorption in the visible and infrared, makes Gd^{3+} a poor probe of local crystal fields. A possible rare earth probe is erbium (Er) having been successfully used by Ashurov et al.[1] under similar circumstances. A small percentage doping of an epilayer with Er^{3+} should allow the measurement of rare earth substitution (rare earths other than Er^{3+}) into octahedral sites. Normally the Er^{3+} would go into a dodecahedral site and be surrounded by non-rare earth neighbors (i.e. Al^{3+}, Fe^{3+}, Ga^{3+}) in the octahedral and tetrahedral sites (Figure 5). This predominant absorption is known as an N-center. However, if a rare earth is substituted into an octahedral site, there is a distortion in the regular arrangement of adjacent oxygen atoms. The local crystal field surrounding the Er^{3+} in the nearest neighbor dodecahedral site is altered producing a shift of the absorption peak from the N-center. This is known as a P-center.

Figure 6 shows some examples of P-centers in non-mixed garnets. The number of P-centers varies depending on the symmetry of the distortion and the number of adjacent dodecahedral sites. In the garnets there are six nearest neighbor dodecahedral sites to each octahedral site (Figure 7). In the completely non-symmetric case a maximum of six P-centers is possible. Figure 6 has examples with one, two, and three P-centers resolved. Using the number and relative integral intensity of P-satellite lines, the amount of rare earth substitution into octahedral sites can be calculated giving the stoichiometric deviation of the epilayer of garnet.

Four samples will be necessary to do the experiment. The first sample must be a carefully grown (and perhaps thinned) epilayer without any Er^{3+} as a probe. A portion of this sample is then ion implanted, giving the second sample. The third sample is a duplication of the first sample but with a small amount of erbium present. Again, a portion of this third sample is implanted with the same ion dose as the second sample, giving the fourth sample. The first and second

samples will be references for the third and fourth samples.

Since the probe will constitute only a small fraction of the epilayer, background absorption must be kept to a minimum so that the spectrometer's sensitivity can best be utilized. A substrate thickness of about 10 microns seems workable. With a strong absorption beginning around 5000 Ångstroms, the Fe^{3+} in the epilayer causes a major difficulty (Figure 8). To allow maximum flexibility and access to most rare earth probe levels, going below 5000 Ångstroms is desirable. Several possibilities exist for obtaining a thin epilayer - growing a thin layer, sputter etching a thick layer - but the best way is not known. Presently a thinly grown layer is being tested on a thinned substrate. Pushing below 5000 Ångstroms was easily accomplished with the new sample; however, the limiting factor is now a strong ultraviolet absorption (characteristic of the GGG substrate) beginning at around 2300 Ångstroms (Figure 9).

The spectra from the samples will be recorded with attention focused to the N-center satellites. Ion implantation may induce a shift in P-center absorption frequencies, a change in the number of resolved P-centers, an increase or decrease in relative intensity, or a new type of center (call it an I-center) associated with a damaged local environment. I-centers are a general class which may run from a displaced oxygen atom to an unexpected implanted ion (i.e. H, He, Ne). Through careful analysis the experiment will hopefully resolve many questions concerning the satellite lines. Preliminary results from this experiment are expected in late January when the low temperatures of the magnetoptical system become fully available. With more data and a clearer understanding of the microscopic nature of ion implanted epilayers, an attempt will be made to explain macroscopic behavior (i.e. rotation of magnetization into the plane) in terms of this new knowledge.

[1]M. K. H. Ashurov, Yu. K. Voranko, V. V. Osiko, A. A. Sobol, and M. I. Timoshechkin, phys. stat. sol. (a) 42, 101 (1977).

Distinct Absorption Lines Produced by Gd^{3+} in GGG at 300 K

Wave length in Angstroms
(Figure 1)

Level Structure of Gd³⁺ in LaCl₃ (Hexagonal) at 1.7 K

Electron Volts

4.7
4.6
4.5 — $^6I_{15/2}$ $^6I_{13/2}$ $^6I_{11/2}$ $^6I_{17/2}$ $^6I_{9/2}$ $^6I_{7/2}$
4.4
4.3
4.2
4.1 — $^6P_{3/2}$
4.0 — $^6P_{5/2}$
3.9 — $^6P_{7/2}$

$^6I_{15/2}$	4.5432 – 4.5759 eV
$^6I_{13/2}$	4.5368 – 4.5415
$^6I_{11/2}$	4.5242 – 4.5270
$^6I_{17/2}$	4.4967 – 4.4985
$^6I_{9/2}$	4.4900 – 4.4924
$^6I_{7/2}$	4.4475 – 4.4488
$^6P_{3/2}$	4.1298 – 4.1314
$^6P_{5/2}$	4.0579 – 4.0608
$^6P_{7/2}$	3.9831 – 3.9871

(Figure 2)

GGG Preabsorption Edge Structure

(Figure 3)

Radial Distribution of Electrons in Gd⁺
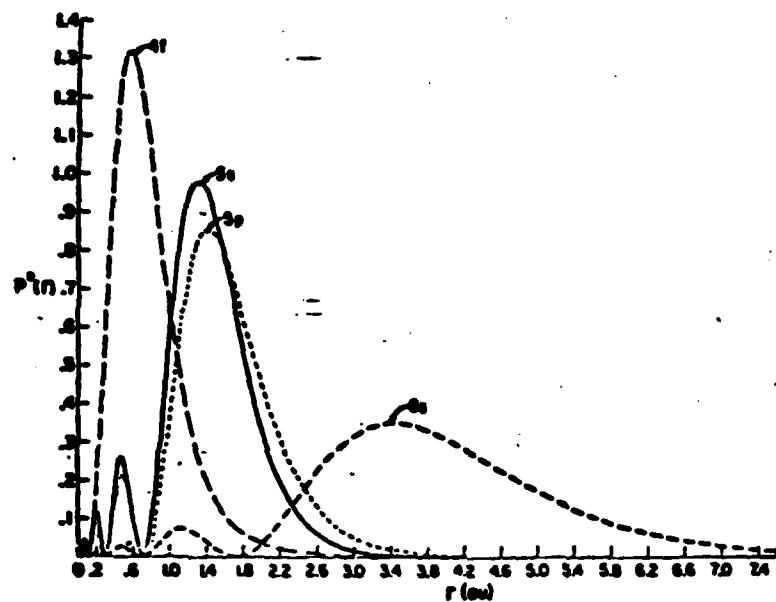
Fig. 7. Square of the radial wavefunction times the squared radius for the 4f, 5s, 5p, and 6s electrons in Gd⁺ [FrWa62]. For RE³⁺ ions this picture will be contracted somewhat because of the larger effective nuclear charge.

Taken from Optical Spectra of Transparent Rare Earth Compounds by S. Hüfner.

(Figure 4)
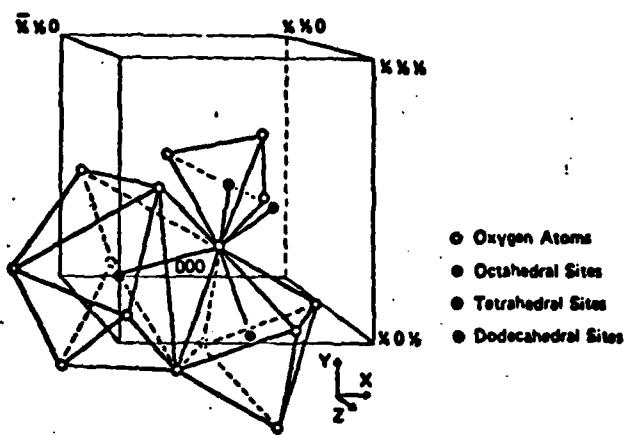
Fig. 6.8. Crystal structure of magnetic garnets. [6.1]

Figure 5

Examples of P and N Centers in Several Crystals
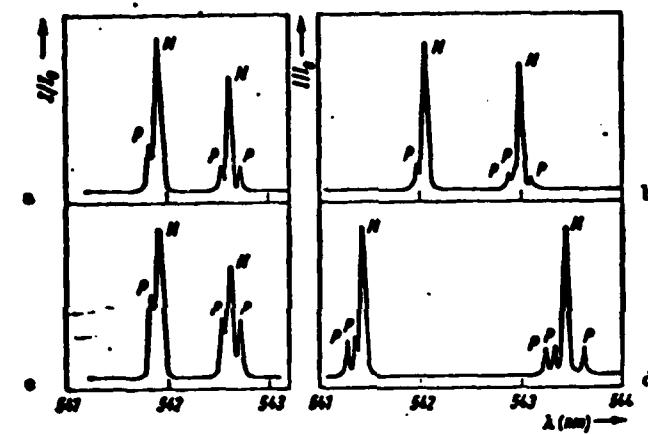
Fig. 2. Absorption spectra of Er^{3+} ions ($^4I_{15/2} \rightarrow {}^4S_{3/2}$ transition) at 4.2 K for crystals grown from the melt with compositions: a) $Y_3Ga_5O_{12}$, b) $Gd_3Ga_5O_{12}$, c) $Y_3Ga_5O_{12}$ with Y_2O_3 (10%; excess), d) $Y_3Al_5O_{12}$

Figure 6

Typical Local Enviroment About AN
Octahedral Site

○ tetrahedral site
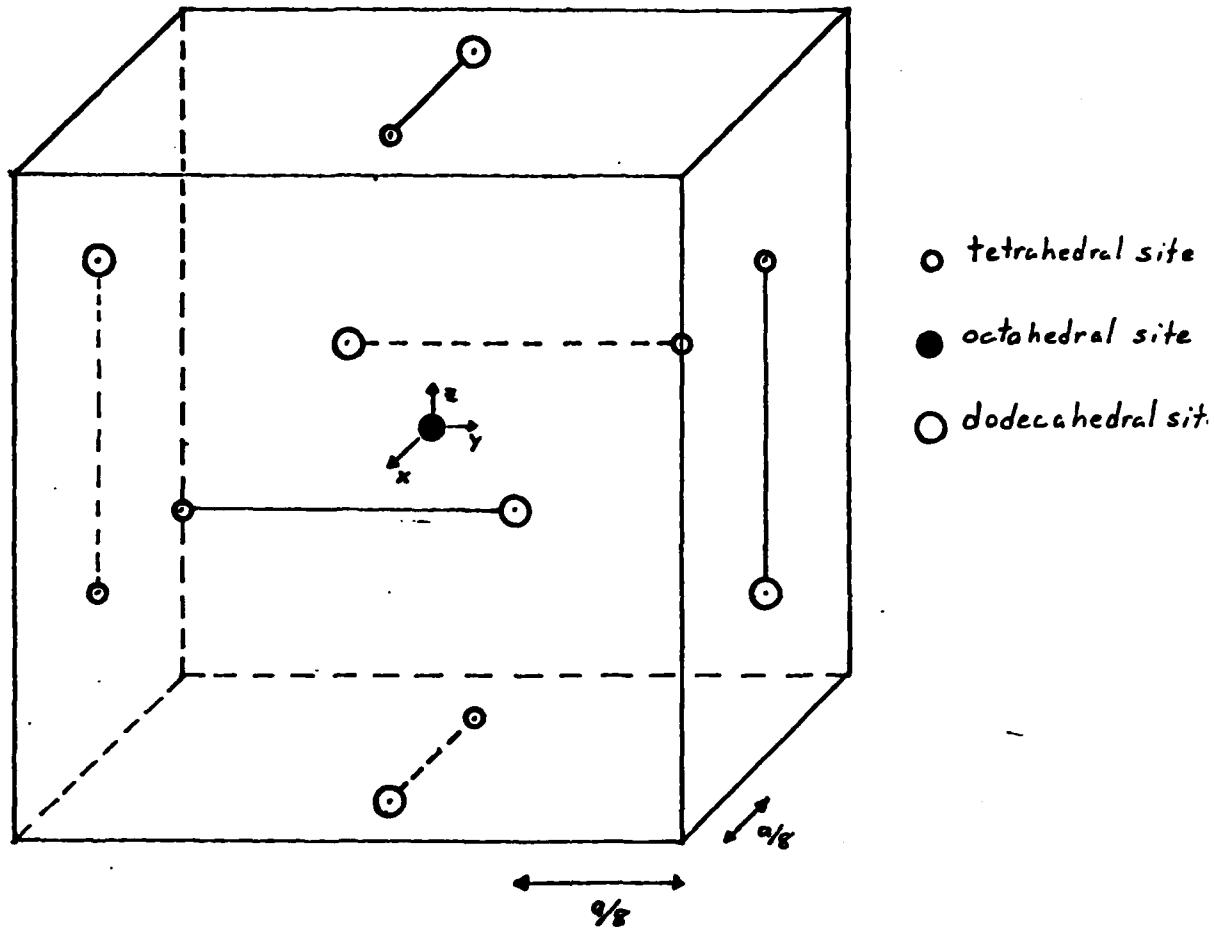
● octahedral site

◎ dodecahedral sit.

Tetrahedral Sites	Dodecahedral Sites ($\times$ a/8)
(1, 0, 2)	(-1, 0, 2)
(-1, 0, -2)	(1, 0, -2)
(2, -1, 0)	(2, 1, 0)
(-2, 1, 0)	(-2, -1, 0)
(0, 2, 1)	(0, 2, -1)
(0, -2, -1)	(0, -2, 1)

Figure 7

First Strong Absorption in Epilayer (Figure 8)
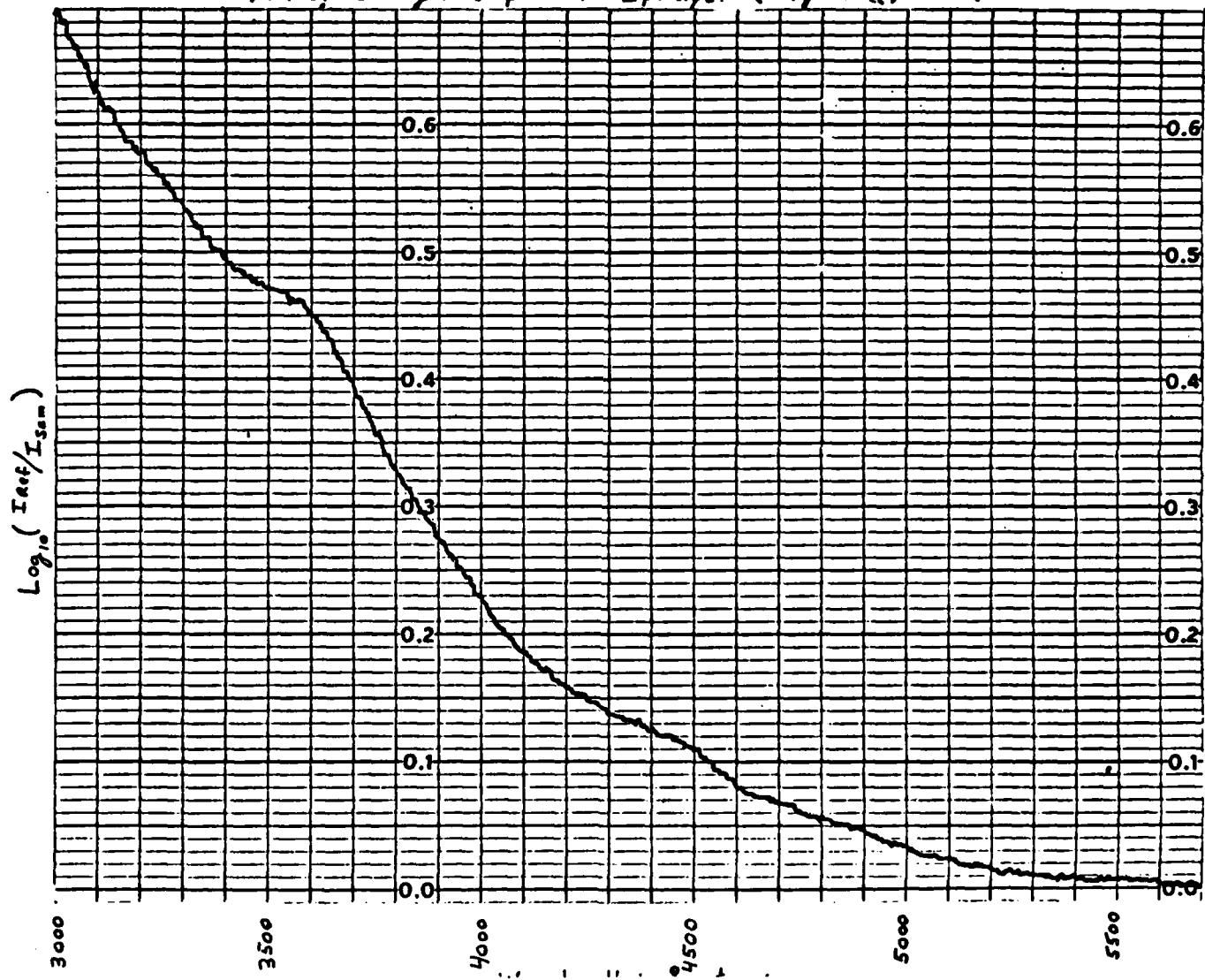
Very Strong Absorption in Ultraviolet
Sample: GGG with epilayer
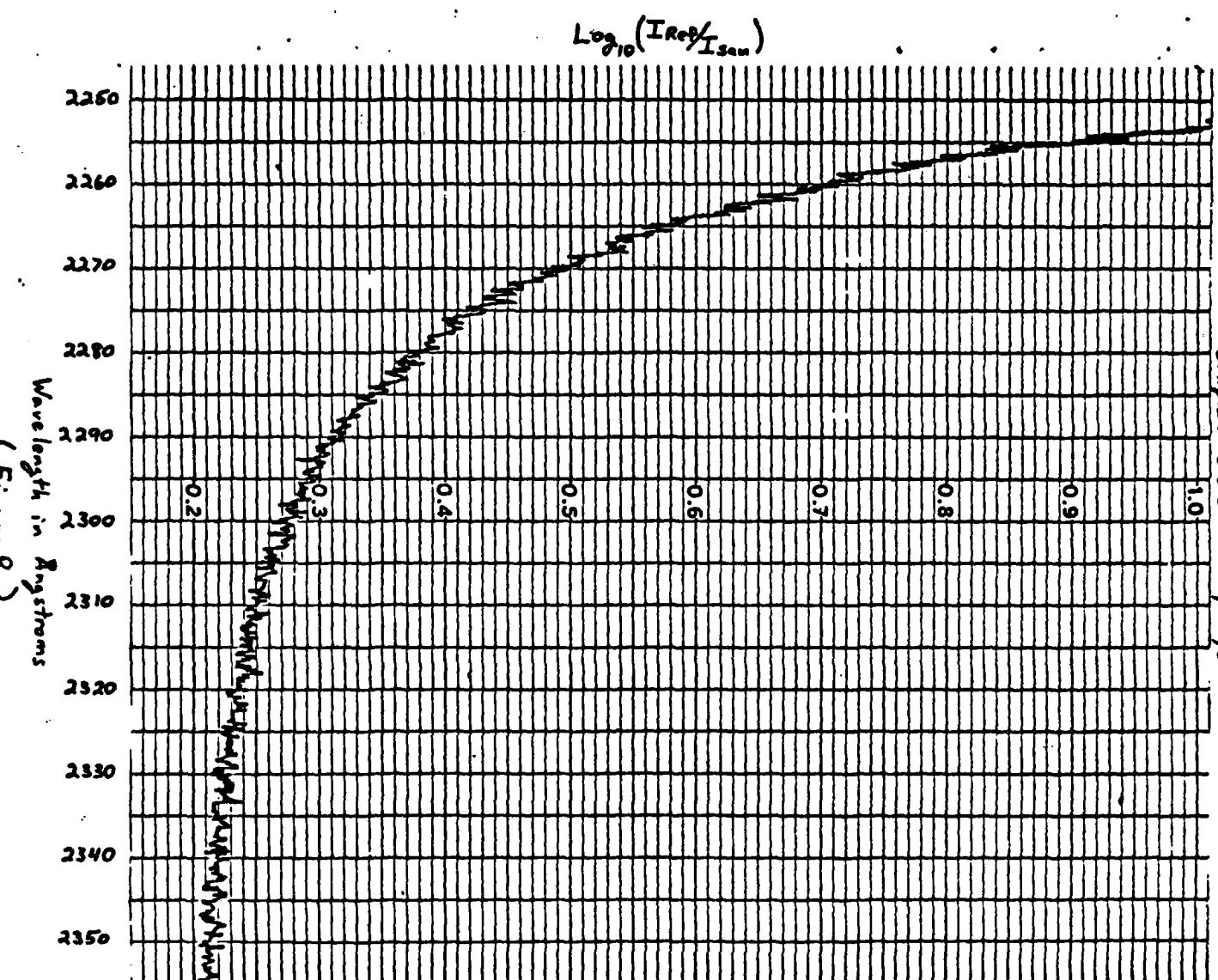
"MAGNETO-OPTIC MEASUREMENTS

OF THE EFFECTS OF CRYSTALLINE ANISOTROPY

IN ION-IMPLANTED LAYERS OF GARNETS"

J. J. Fernandez de Castro

M. H. Kryder

ABSTRACT

A magneto-optic photometer system was designed, constructed and used to
characterize in-plane magnetization in magnetic bubble memory devices. The
system was based on the Faraday magneto-optic effect. A model of the in-
plane driving layer was developed and used to explain the experimental re-
sults. Data were taken on the magnitude, orientation and symmetry of the
magneto-crystalline anisotropy for threefold symmetric (111) films. The
experimental results were correlated with a theoretical model from which
computer solutions were obtained. The crystalline anisotropy constant
(K_1) of 3150 ergs/cm^3 was determined for the (111) oriented film. Hys-
teresis loops with very low coercive force (H_c < 5 Oe) were measured,
indicating that magnetic domain wall motion was responsible for the mag-
netization process when the in-plane field was applied inside the criti-
cal curve.

INTRODUCTION

Contiguous disk magnetic bubble devices typically have a Gadolinium
Gallium Garnet (GGG) substrate and one or two eiptaxial layers of garnet
(1,2,3). After the growth of the epitaxial layers by liquid phase epi-
taxy, a pattern of contiguous disks is deposited and the surface is ion-

implanted, (see Fig. 1). If the implanted layer has a negative magneto-
striction constant, anisotropic stress caused by the ion-implantation
causes the magnetization to lie in the plane of the film in the ion-im-
planted layer. When an in-plane field H_{xy} is applied to the device,
the in-plane magnetization of the driving layer creates magnetic charged
walls near the disks which attract and propagate the bubbles in the stor-
age layer (4,5).

Lin et al. (2) used the coordinate system of Fig. 2 and a total
energy equation to describe the driving layer. This energy equation
for the (111) driving layer may be expressed as

1) $E = K_u \cos^2\theta + K_i \sin^2\theta - M_s H_z \sin\theta - M_s H_{xy} \cos\theta \cos(\phi_H - \phi)$
     $+ 2 \pi M_s^2 \sin^2\theta$

     $- |K_1| [\frac{1}{4} \cos^4\theta + 1/3 \sin^4\theta + (\sqrt{2}/3) \cos^3\theta \sin\theta \cos3\phi]$

Where K_u is the uniaxial anisotropy constant, K_i is the implantation in-
duced anisotropy constant, K_1 is the crystalline anisotropy constant, M_s
is the saturation magnetization, H_z is the bias field, H_{xy} is the in-plane
field, ϕ_H is the azimuthal angle of H_{xy} and ϕ and θ are the azimuthal and
inclination angles of the magnetization, respectively.

Shir and Lin et al., (6) assumed θ constant and then found the stable
directions of the magnetization in the plane of the film by minimizing the
total energy with respect to $\phi (\partial E/\partial\phi = 0)$. Then to find the critical val-
ues of the applied field at which the magnetization became unstable he
used $\partial^2 E/\partial\phi^2 = 0$. The simultaneous solution of $\partial E/\partial\phi = 0$ and $\partial^2 E/\partial\phi^2 = 0$
leads to the following parametric equations which describe the three-fold
symmetric critical curve shown in Fig. 3:

2) $\quad h_x = H_x/H_{k1} = -\cos 3\phi \cos\phi - 1/3 \sin 3\phi \sin\phi$

$h_y = H_y/H_{k1} = -\cos 3\phi \sin\phi + 1/3 \sin 3\phi \cos\phi$

$H_x = H_{xy} \cos\phi_H$

$H_y = H_{xy} \sin\phi_H$

$H_{k1} = (|K_1| 3 (2)^{\frac{1}{2}} / M_s) \cos^2\theta \sin\theta$

As Lin pointed out, the slope of a line from a point tangent to the critical curve to the applied in-plane field gives the stable direction of the magnetization. Furthermore, it can be shown that the distance from the point of tangency to the field vector corresponds to the magnitude of the effective field for that direction of magnetization. Thus, the most energetically favorable magnetization direction has the largest vector.

However, Chang (7) demonstrated that θ is not ϕ independent and, therefore, θ can not be considered constant. Figure 4 shows the graph which describes the relation θ vs ϕ (applying Chang's procedure) for the film used in the experiments described here. The film parameters are presented in Table I.

SYSTEM DESCRIPTION

A special magneto-optic photometer system was designed and constructed for the characterization of the in-plane magnetization. This system is based on the Faraday magneto-optic effect (8,9,10,11) which causes plane polarized light to rotate by an amount proportional to the component of magnetization in the direction of the light propagation as the light passes through a sample.

Figure 5 shows a simplified schematic block diagram of the magneto-optic photometer system. Here, the light source for the microscope is a laser. Due to the small dimensions of the magnetic features in the device, the light beam was focused to a small spot (~5um). In order to obtain this small spot of light on the garnet film, an optical microscope and two external lenses were used. Two external mirrors and an X-Y micrometer stand were used between the two lenses and the microscope to control the beam direction. The optical microscope uses a Berek compensation prism to direct the beam into the objective lens. The Berek compensation prism illuminates only one half of the objective lens, hence the light is incident on the sample at an angle to the normal. After the light beam has passed into and been reflected from the magnetized film, it is analyzed with a dichroic polarizer. This transforms the rotation of the plane polarization into a change in light intensity. This light intensity change is detected by a photomultiplier (RCA-8644). The PMT transforms the change in light intensity to an electrical signal which is filtered and amplified by the phase lock loop amplifier (PLLA). The output of the PLLA tuned amplifier is observed with an oscilloscope while the PLLA output after phase sensitive detection is recorded by the X-Y plotter.

The sample to be tested was placed on a holder which allows rotation of the sample in its plane. Three orthogonal coils generated the bias field (H_z) and the in-plane field in the X and Y directions (H_x, H_y). A variable DC power supply (100 volts, 10 Amps) created the H_z field (- 850 Oe to + 850 Oe). Two phase locked signal generators and a DC coupled dual channel amplifier (300 Watts) created the H_x and H_y fields (-200 Oe to +200 Oe).

The signal detected by the PMT is linearly dependent on the rotation of the polarization of the light (12,13). Since the rotation of the polarization of the light is small, the signal to noise ratio must be carefully considered. To optimize the signal to noise ratio it is critical that the laser wavelength be appropriately chosen. In garnet films, both the magneto-optic coefficient describing the rotation of the plane of polarization and the absorption coefficient of the light are wavelength dependent (10). Consider first the absorption coefficient, α. When the laser beam reaches the garnet sample, some of the light is absorbed as it passes through the film. The ratio of absorbed intensity (I) to incident intensity (I_0) is;

$$3) \qquad I/I_0 = 1 - e^{-\alpha t}$$

where t is the light path in the film and α is the absorption coefficient for the film. Next considering the magneto-optic rotation, the Faraday rotation of the plane of polarization is given by,

$$4) \qquad \rho = F \; t \; M$$

where t is the light path in the film, M is the magnetization component in the direction of the light propagation, ρ is the Faraday rotation angle and F is the Faraday magneto-optic coefficient.

As pointed out by Mac Donald et al., (10), the signal detected at the PMT cathode is given by

$$5) \qquad \Delta I_L = I_T \; 4 \; \xi \; \rho$$

where ξ is the polarizer to analyzer angle measured from extinction and I_T is the photo-current in the PMT cathode.

The two most important fundamental sources of noise in the magneto-

optic photometer system (14) are shot noise due to the electron multiplication and thermal noise. These two contributions give a noise current of:

$$I_N = [2 q B I_T + 4 k T B / R]^{\frac{1}{2}}$$

where q is the electron charge, B is the PMT bandwidth, k is Boltzmann's constant, R is the PMT load and T is the PMT temperature. The signal to noise ratio may then be expressed as,

$$\frac{S}{N} = \left[\frac{8 \eta^2 q^2 P_L^2 e^{-2\alpha t} \xi^2 F^2 t^2 \lambda^2 R}{h c q^2 B \eta R P_L e^{-\alpha t} \lambda + 2 K T Z h^2 c^2} \right]^{\frac{1}{2}}$$

where c and λ are the speed and wavelength of the light. For this magneto-optic system, the light beam of an Argon laser (4880 A$^\circ$) was chosen and used in the experiments since the signal to noise ratio is nearly optimum for detecting the magnetization in the 0.4 µm thick ion-implanted layer at that wavelength.

DESCRIPTION AND DISCUSSION OF EXPERIMENTS

To obtain an increased understanding of the effects of crystalline anisotropy in (111) oriented films and to verify the models described earlier, a number of experiments were performed on the available samples. In this section these experiments and the data obtained will be presented and discussed.

Figure 2 shows the cartesian coordinate system used. Here, the magnetization, the in-plane field and the light beam vector are all shown. As before, θ and ϕ are the inclination and azimuthal angles of the magnetization, respectively, while θ_L and ϕ_L are the inclination and azimuthal angles of the light beam, respectively, and ϕ_H is the azimuthal angle of

the in-plane field. In general the applied in-plane field is of the form $H_{xy}(\omega t) = H_x + H_y + \Delta H_x + \Delta H_y$ where H_x and H_y are the DC components of the field and ΔH_x and ΔH_y are the AC components of the field. For all the experiments, the frequency used was 35 Hz. The inclination angle (θ_L) of the light beam was equal to 70 degress and the azimuthal angle (ϕ_L) of the light beam was equal to 90 degress (the Y axis). The characteristics for the (111) storage and driving layers are given in Table I. A bias field (H_z) larger than the collapse field was used in all the experiments so that the storage layer was saturated, eliminating unwanted signals from bubble domains.

To determine the crystalline orientation of the (111) oriented film, a rotating in-plane field of $H_{xy} = 120\ e^{j\omega t}$ Oe was applied to the sample. The signal from the PMT was amplified by an amplifier tuned to the frequency of the in-plane field and compared with the AC in-plane field ΔH_y. A phase difference between the in-plane field ΔH_y and the PMT signal was observed (see Fig. 6). It was found that, as the sample was rotated around the Z axis (the light beam was incident in the Y-Z plane), the phase difference between the PMT signal and the drive field ΔH_y varied. For the (111) film, this phase difference decreased to zero at three equally spaced orientations of the sample relative to the Y axis.

To understand why the phase shift changes with the sample orientation, it is necessary to realize that the Faraday magneto-optic rotation angle ϕ is a maximum when the magnetization component parallel or anti-parallel to the direction of the light propagation is a maximum. Thus, zero phase difference is measured between the PMT signal and the drive field (ΔH_y) when the easy direction lies parallel with the y axis. This measurement, however,

does not uniquely determine the easy direction unless it is known whether a positive Faraday rotation σ causes the light intensity through the polarizer / analyzer pair to increase or decrease. This depends upon the relative orientation of the polarizer / analyzer pair. Indeed by rotating the analyzer through extinction, the phase of the PMT signal is made to change by 180 degrees.

In order to determine whether the maximum signal occurred when the easy direction was aligned with the +Y or -Y direction, the bubble stripe out positions were located. This was done by reducing the bias field and slowly rotating a small in-plane field, so bubbles which formed in the storage layer striped out in three places around the disk. As Lin et al. (15) showed, these stripe out directions correspond to hard directions of aniso-tropy as the charged wall extends far from the disk when the field is ap-plied in a hard direction. For this experiment, it was found that when the polarizer to analyzer angle was set at $\xi = +1.5$ degrees from extinction, the PMT signal was in phase with the ΔH_y field signal when one easy direc-tion lay in the -Y direction. On the other hand, when the polarizer to analyzer angle was set at $\xi = -1.5$ degrees from extinction, the PMT signal was in phase with the ΔH_y field signal when an easy direction lay in the +Y direction.

The hysteresis loops of the driving layers were also measured and used to determine the crystalline orientation and coercivity of the film. Here, the in-plane field (see Fig. 7(a)) consisted of a DC component (H_y) and a small amplitude ($\Delta H_y = 10$ Oe) AC component at 35 Hz. The DC component of the field (H_y) was swept very slowly (0.01Hz) from +200 Oe to -200 Oe and back again to +200 Oe. Examples of the PLLA output are shown in Figs. 7(b)

and 8(b). These signals which represented the slope or derivative of the
hysteresis loops can be integrated to obtain the actual hysteresis loops.
Figures 7(c) and 8(c) were obtained by graphically integrating Figs. 7(b)
and 8(b), respectively. As can be seen, the hysteresis loop in Fig. 7(c)
is symmetric with respect to H_y, while the hysteresis loop in Fig. 8(c)
is not. The symmetric loop is obtained when a hard or easy direction is
in the H_x axis because in those cases the critical curve is symmetric a-
bout the H_x axis (see Fig. 7(a)). In these experiments, as in those des-
cribed in Fig. 6, the easy direction can only be determined to modulo 180
degrees. The hysteresis loops also indicated that the coercive force (H_c)
is very small (<5 Oe) in these samples. This measured low coercivity in-
dicates that the samples switched by domain wall motion processes. If
the samples had remained in a single domain state, the measured coercive
force should have been comparable to the anisotropy field and predictable
from the critical curve of Fig. 3.

To determine the crystalline anisotropy constant (K_1) and verify the
models developed by Shir (6) and Chang (7), another experiment was per-
formed. In this case, an in-plane field (see Fig. 9(a)) consisting of an
AC component (ΔH_y) with an amplitude equal to 40 Oe and a frequency of 35
Hz was applied. The sample was then rotated 10 degrees at a time and the
DC output from the PLLA, which corresponded to the amplitude of the signal
with the same phase and frequency as ΔH_y was measured. Examples of these
data are shown in Fig. 9(b) for the (111) oriented film. Figure 9(b) in-
dicates that the threefold crystalline response is directly observable.
By comparing the sample orientation for maximum signal with the previously
determined hard axis directions, it was found that the maxima occurred

when an easy direction of magnetization lay in the +Y direction.

To understand the response in Fig. 9(b), consider Fig. 10 where four different sample orientations are presented with an in-plane field applied parallel and anti-parallel to the Y axis. As was explained before, the signal detected by the PMT is proportional to ρ, where ρ is the Faraday rotation angle. In general, the Faraday rotation angle may be expressed as the sum of the rotation due to the magnetization component in the plane of the film (ρ_i) and of the component of the rotation due to the magnetization component perpendicular to the plane of the film (ρ_p). Therefore, the signal in the PMT is proportional to $\rho_i + \rho_p$. When the field in Fig. 10(a) is applied parallel to the Y axis, the signal in the PMT is proportional to $\rho_{1i} + \rho_{1p}$, where $\rho_{1i} (>0)$ is the rotation due to the magnetization component in the +Y direction and $\rho_{1p} (>0)$ is the rotation due to the magnetization component in the +Z direction. When the field in Fig. 10(a) is applied anti-parallel to the Y axis, the signal in the PMT is proportional to $-\rho_{2i} + \rho_{2p}$, where $-\rho_{2i} (<0)$ is the rotation due to the magnetization component in the -Y direction and ρ_{2p} is the rotation due to the magnetization component in the +Z direction. (Since the bias field is always along +Z, the rotations ρ_p are always positive, whereas the rotations ρ_i due to in-plane components of magnetization may have either positive or negative signs). Now, the AC component of the signal which is detected by the PMT and amplified by the PLLA is found as the difference between those values or $\rho_{1i} + \rho_{2i} + \rho_{1p} - \rho_{2p}$.

Considering now Fig. 10(c), the PMT output signal due to the field applied parallel to the Y axis is proportional to $\rho_{2i} + \rho_{2p}$ while the signal in the PMT due to the anti-parallel field is proportional to $-\rho_{1i} + \rho_{1p}$ and the PLLA output signal is proportional to $\rho_{1i} + \rho_{1i} - \rho_{1p} + \rho_{2p}$. Comparing the

PLLA output signal from Figs. 10(a) and (c), the resultant graph is a

curve with a maximum for the crystalline orientation in Fig. 10(a) and

a minimum for the one in Fig. 10(c). The resultant curve has an offset

given by $\rho_{1i} + \rho_{2i}$ (the Faraday rotation due to the magnetization compon-

ent in the plane of the film) and an oscillatory component with a peak-to-

peak amplitude given by $2(\rho_{1p}-\rho_{2p})$ (the Faraday rotation due to the magne-

tization component perpendicular to the plane of the film). Therefore,

the curve presented in Fig. 9(b) has an offset and an oscillatory peak-

to-peak amplitude with three maxima which represent the three easy direc-

tions (in the (111) film) oriented parallel to the Y axis. It is worth-

while to note here that, as indicated in Fig. 4, the changes in the angle

of inclination θ are of the order ot 2°. Yet, these small changes are

readily observable as the oscillations in Fig. 9(b) with the magneto-

optic photometer.

An experiment, similar to the one explained above, was performed

with an in-plane field consisting of an AC component (ΔH_x) with an amp-

litude equal to 40 Oe and a frequency of 35 Hz (see Fig. 11(a)). Here

again, the sample was rotated 10 degrees at a time while the DC output

from the PLLA was recorded by the plotter. Examples of these data are

shown in Fig. 11(b) for the (111) oriented film. Figure 11(b) also in-

dicates that the threefold crystalline response is directly observable.

Here as before, the Faraday rotation angle may be expressed as the sum

of the component of the rotation due to the magnetization projection in-

plane (ρ_i) and perpendicular to the plane (ρ_p) of the film. However,

when the sample is oriented as in Fig. 12(b), there is no Y-component

of the magnetization. Thus, the rotation for an applied field of

$+\Delta H_x$ comes entirely from the Z-component of magnetization ρ_{3P}; whereas for $-\Delta H_x$, the rotation is proportional to ρ_{4P}. Therefore, the signal detected by the PLLA is $\rho_{3P}-\rho_{4P}$. Considering now Fig. 12(d), the PMT output signal due to the field applied parallel to the X axis is proportional to ρ_{4P} while the signal in the PMT due to the anti-parallel field is proportional to ρ_{3P} and the PLLA output signal is proportional to $-\rho_{3P}+\rho_{4P}$. Comparing the PLLA output signal from Figs. 12 (b) and (d), the resultant graph is a curve with a positive maximum for the crystalline orientation in Fig. 12(b) and a negative maximum for the crystalline orientation in Fig. 12(d). The resultant curve has no offset level, but an oscillating component with a peak to peak amplitude given by $2(\rho_{3P}-\rho_{4P})$ (the Faraday rotation due to the magnetization component perpendicular to the plane of the film). Therefore, the curve presented in Fig. 11(b) has an oscillatory response with three positive maxima which represent the three easy directions in the (111) film oriented parallel to the X axis.

Another experiment which was performed was to sweep one component of the in-plane field [H_x or H_y] very slowly (0.01 Hz) from -200 Oe to +200 Oe while an oscillating in-plane field [ΔH_y or ΔH_x] of 10 Oe amplitude and 35 Hz frequency was applied to the sample (see Figs. 13 and 14). The DC output of the PLLA, which corresponded to the amplitude of the signal with the same phase and frequency as the in-plane field [ΔH_y or ΔH_x] was measured. Examples of the data are shown in Figs. 15 (a) and (b) for the in-plane fields and crystalline orientations of Figs. 13 and 14, respectively. To understand the responses in Figs. 15 (a) and (b), consider first Fig. 13 where seven values for the DC component of the applied in-plane field are presented. As was explained earlier, the signal detected by the PMT is proportional to the difference between the polarization rotations caused by

the magnetization components due to the positive and negative values of the oscillating in-plane field $[\Delta H_y]$. When the in-plane field $[H_x]$ is applied outside the critical curve (see Fig. 13(a)), the components of the magnetization in the direction of the light beam propagation due to the positive and negative values of the in-plane field $[\Delta H_y]$ are very nearly equal, so the difference between the two rotations is very small (see $|H_x| > |H_1|$ in Fig. 15(a)). Furthermore, when $|H_x|$ decreases from $|200\ Oe|$ to $|H_1|$ (see Fig. 13 (b) and (d)), the difference between the two rotations increases in magnitude since the difference between the components of the magnetization due to the positive and negative values of the in-plane field $[\Delta H_y]$ increases. When Fig. 13(c) is considered and H_x has a value between $+H_1$ and $-H_1$, the signal detected by the PLLA decreases again. To understand this behavior, let us assume, as before, that ρ_i and ρ_p are the polarization rotations due to the magnetization components in-plane and perpendicular to the plane of the film. As the in-plane field ΔH_y is oscillatory, the PLLA signal is proportional to the difference between the rotation at the positive ΔH_y and the rotation at the negative ΔH_y. Therefore, when H_x is close to $+H_1$ or $-H_1$, the rotational difference may be expressed as $\rho_{i0} - \rho_{i1} + \rho_{P0} - \rho_{P1}$ (see Figs. 13 (e) and (f)). However, when H_x is close to the origin, the rotational difference is expressed as $\rho_{i2} + \rho_{i3} + \rho_{P2} - \rho_{P3}$ (see Fig. 13(c)). Knowing that the perpendicular component of M is greatest near an easy direction, it can be seen in Fig. 13 that $\rho_{i0} - \rho_{i1} > 0$, $\rho_{P0} - \rho_{P1} > 0$, $\rho_{i2} + \rho_{i3} > 0$ and $\rho_{P2} - \rho_{P3} < 0$. Therefore, $\rho_{i0} - \rho_{i1} + \rho_{P0} - \rho_{P1}$ can be larger than $\rho_{i2} + \rho_{i3} + \rho_{P2} - \rho_{P3}$ (this, in fact, is confirmed by computer calculations described in the next section). The amplitude near the origin in Fig. 15(a) is, therefore, smaller than the amplitude near $+H_1$ or $-H_1$.

Similarly, for the experiment in Fig. 14, the PLLA amplitude is small when H_y is large. In Fig. 14, when H_y passes through the origin, the PLLA signal oscillates near zero amplitude (see Fig 15(b)). For H_y larger than $+H_1$, the rotational difference can be expressed as $c_{i4}-c_{i5}+c_{p4}-c_{p5}$, where $c_{i4}-c_{i5} > 0$ and $\rho_{p4}-\rho_{p5} < 0$ (see Fig. 14(b)). For some value of H_y less than $+H_1$, positive ΔH_x causes ρ_8 as shown in Fig. 14(e), and the rotational difference is given by $c_{i8}-c_{i9}+\rho_{p8}-\rho_{p9}$, where $c_{i8}-c_{i9} < 0$ and $\rho_{p8}-\rho_{p9} < 0$. Therefore, there must be a sign change in the rotational difference due to the in-plane magnetization. The result is that the PLLA signal changes sign too (this was also verified by computer calculations).

As H_y nears the origin (see Fig. 14(c)), the magnetization present for positive ΔH_x is closer to an easy direction than the magnetization for the negative ΔH_x and, hence, $\rho_{p6}-\rho_{p7} > 0$, $\nu_{i6}-c_{i7} < 0$ for $+H_y$ and $c_{i6}-c_{i7} > 0$ for $-H_y$ in Fig. 14(c), where the PLLA signal is proportional to $\rho_{i6}-c_{i7}+\rho_{p6}-\rho_{p7}$. However, since ρ_{i6} and ρ_{i7} are very close to the easy direction, as can be seen in Fig. 14(c), $\rho_{p6}-\rho_{p7}$ and $\rho_{p6}-\rho_{p7}$ is almost zero and can be neglected. Therefore, the rotational difference due to the in-plane component of the magnetization changes sign as H_y sweeps through the origin and the PLLA signal changes sign again. Due to the symmetry of the experiment, the PLLA output signal becomes an odd function for which AMPLITUDE($+ H_y$) = $-$AMPLITUDE($- H_y$), as is shown in Fig. 15(b).

THEORY AND DISCUSSION

A numerical analysis was used to verify the accuracy of the proposed model and to provide an experimental measure of the magneto-crystalline

anisotropy constant (K_1). In this analysis, a computer was used to calculate the magnetization direction (ϕ and θ), the components of magnetization in the direction of the light beam propagation, the Faraday rotation, the signals in the PLLA and PMT and the least squares fit to the experimental data. Here, theoretical graphs were obtained by solving $\partial E/\partial \phi = 0$ and $\partial E/\partial \theta = 0$ simultaneously and calculating the total Faraday rotation caused by the magnetization acting on the light beam. As noted by Lin et al. (5), when the in-plane field (H_{xy}) is inside the critical curve, there are three possible stable directions for the magnetization in the (111) oriented films. However, due to the low coercive force of the sample, here the magnetization switched into the one direction having the lowest energy.

To calculate the changes in the intensity of the detected light beam, the total Faraday magneto-optic rotation is calculated as the sum of the Faraday rotation of the incident and reflected light beams, (see Fig. 2). This Faraday rotation is proportional to the projections of the magnetization M_I and M_R in the direction of the incident and reflected light beam, respectively. By substituting the magnetization component in the light beam propagation direction into Eq. 4 and considering that the light beam travels from air to the driving layer and vice versa, one may find:

8) $\quad M_R = \tan^{-1}\{\tan[Ft(\sin\phi \cos\theta \sin\phi_L \cos\phi_L + \sin\theta \sin\theta_L)]T_N/T_P\}$

9) $\quad M_I = -\tan^{-1}\{\tan[Ft(-\sin\phi \cos\theta \sin\phi_L \cos\theta_L + \sin\theta \sin\theta_L)]T_P/T_N\}$

Where θ and ϕ are the inclination and azimuthal angles of the magnetization (see Fig. 2), θ_L and θ_L are the inclination and azimuthal angles of the light beam, F is the Faraday magneto-optic coefficient, t is the light path length in the driving layer and T_N and T_P are the normal and in-plane

transmitted components of the light beam (16). Those transmitted coefficients may be expressed as,

10) $\qquad T_N = n_0 \cos\theta_0 \, / \, [n_0 \cos\theta_0 + n_1 \cos\theta_1]$

11) $\qquad T_P = n_0 \cos\theta_1 \, / \, [n_0 \cos\theta_1 + n_1 \cos\theta_0]$

Where n_0 and n_1 are the refractive indices in air and in the driving layer ($n_0 = 1$ and $n_1 = 2.368$) (17,18), θ_0 and θ_1 are the light beam angles with respect to the normal to the film plane in air and in the driving layer and may be obtained by using Snell's law as;

12) $\qquad \theta_1 = \sin^{-1}[n_0/n_1 \sin\theta_0]$

$\qquad\qquad \theta_0 = 90^\circ - \theta_L$

It must be pointed out that more than one reflection is not considered because absorption in the garnet film makes multiply reflected beams very small in intensity. This absorption was earlier discussed and Eq. 3 gave the ratio of absorbed to incident intensity. Here $\alpha = 10^{-4}\,\mathrm{cm}^{-1}$.

When an oscillating AC in-plane field as in Fig. 9(a) is applied to the sample, the signal detected by the PLLA is proportional to the difference between the total Faraday rotations when the oscillating field has its positive and negative values, (see Fig. 9(a)). The solution for the signal detected by the PLLA may then be expressed as,

$\qquad\qquad S_R \propto M_{RP} - M_{RN} + M_{IP} - M_{IN}$

Where M_{RP} and M_{RN} are the magnetization components parallel to the reflected light beam when the AC field has its maximum positive and negative values, respectively, and they are calculated using Eq. 8. Similarly, M_{IP} and M_{IN} are the magnetization components parallel to the

incident light beam when the AC field has its maximum positive and negative values, respectively, and they are calculated using Eq. 9. These theoretical predictions of the signal recorded by the plotter are shown in Figs. 9(b) and 11(b) along with the experimental data for the two respective experiments.

A least squares fit to the data of Fig. 9(b) yielded $K_1 = 3500$ erg/cm^3, while a least squares fit to the data in Fig. 11(b) yielded $K_1 = 2900$ erg/cm^3. A least squares fit to both sets of data simultaneously yielded $K_1 = 3150$ erg/cm^3 with a standard deviation of 250 erg/cm^3 (8%). Thus, the theoretical results fit the experimental data quite well, yielding a measured value of K_1 in the ion-implanted layer with better than 10% accuracy.

The numerical results presented above took into account only the effects of the driving layer on the PMT signal; however, some signal may, in theory, also be created by the storage layer. In order to determine how big the signals from the storage layer were, $\partial E/\partial \phi = 0$ and $\partial E/\partial \theta = 0$ were solved simultaneously for the case when the implanted anisotropy constant (K_i) was equal to zero. The resultant PMT signals were projected to be 100 times less than those from the driving layer. The reason for the small effect of the storage layer is that the uniaxial anisotropy constant (K_u) is so large that the small in-plane fields used in these experiments had only a small effect on the magnetization. Thus, it appears well justified that the effects of the storage layer on the signals can be ignored.

For additional verification of the value of K_1 which was determined from fitting the data in Figs. 9(b) and 11(b) and to further verify the

validity of the model used, the same method of analysis was used to fit the data in Fig. 15. The numerical results are shown as dots in Fig. 15, whereas the solid curve is the experimental data recorded on the X-Y recorder. The value of K_1 used to generate the dots was that determined above ($K_1 = 3150$ erg/cm^3). As may be seen in Fig. 15, the fit of the numerical results to the experimental data is quite good even near $H_x = 0$ where the curves have a peculiar shape due to switching of the stable magnetization directions.

SUMMARY AND CONCLUSION

In this research (19), a magneto-optic photometer system based on the Faraday magneto-optic effect was built for detecting in-plane magnetization. The system used a laser as the light source for an optical polarized light microscope. The light beam reflected from the magnetized sample was plane polarized but in a direction slightly away from the direction in the incident light beam because of the Faraday magneto-optic effect. A dichroic polarizer (the analyzer) transformed the change in polarization direction to intensity changes which were detected and converted to an electrical signal by the photo-multiplier, (PMT). The electrical signal from the PMT was filtered and amplified by the phase lock loop amplifier (PLLA) in order to improve the signal to noise ratio.

Experimental data were collected on the coercivity and the magnetic anisotropy of the in-plane layers of (111) oriented films. A low coercive force ($H_c < 5$ Oe) in the hysteresis loops was measured, indicating that magnetic domain wall motion was responsible for the magnetization process when the in-plane field was applied inside the critical curve. The magnetic anisotropy data from the in-plane layers of (111) films clearly

showed threefold anisotropy symmetry. Theoretical models were developed

to describe the anisotropy and shown to be in good agreement with the

experimental results. It was found that although the angle of inclina-

tion of the magnetization out of the plane of the ion-implanted layer

varied by only 2°, that this effect could be measured and shown to have

a significant influence on the data. The crystalline anisotropy con-

stant was determined to be 3150 erg/cm^3 $\doteq$ 250 erg/cm^3 by fitting the

theoretical curves to the experimental data. This value is well within

the range of expected values.

ACKNOWLEDGEMENTS

The authors are grateful to their many colleagues and friends at

Carnegie-Mellon University for their help and encouraging comments.

J. J. Fernandez de Castro also thanks the Mexican Government (CONSEJO

NACIONAL DE CIENCIA Y TECNOLOGIA) for the funds that it gave him dur-

ing the two years while this research was being done.

FOOTNOTES

† The authors are with the Electrical Engineering Department, Carnegie-
  Mellon University, Pittsburgh, PA 15213.

REFERENCES

1. Y. S. Lin, G. S. Almasi, G. E. Keefe. "Manipulation of 1_m Bubbles with Coarse (>4um) Overlay Patterns." J. Appl. Phys., 48, 5201 (1977).

2. Y. S. Lin, G. S. Almasi, G. E. Keefe. "Contiguous-Disk Bubble Domain Devices." IEEE Trans. on Magnetics, Mag-13, 1744, (1977).

3. T. J. Nelson, R. Wolfe, S. L. Blank, P. I. Bonyhard, W. A. Johnson, B. J. Roman and G. P. Vella-Caleiro. "Design of Bubble Device Elements Employing Ion-Implanted Propagation Patterns." Bell Sys. Tech. J., 59, 229 (1980).

4. D. B. Dove, Y. S. Lin, S. Schwarzl. "Domain Wall Behavior in Ion-Implanted Garnet Layers for 1um Bubble Devices." J. Appl. Phys., 50, 5906, (1979).

5. Y. S. Lin, D. B. Dove, S. Schwarzi, C. C. Shir. "Charged Wall Behavior in 1um Bubble Implanted Structures." IEEE Trans. on Magnetics, Mag-14, 494 (1978).

6. C. C. Shir and Y. S. Lin. "Critical Curves for Determining Magnetization Directions In Implanted Garnet Films." J. Appl. Phys., 50, 4246 (1979).

7. C. T. Chang. "The Effect of Material Parameters and Drive Field on the Magnetization Angles of Implanted Garnet Films." IEEE Trans. Magnetics, Mag-16, 952 (1980).

8. M. Prutton. Thin Ferromagnetic Films. Washington Butter Worths, Chapter 5, 132, 1964.

9. M. Prutton. Thin Ferromagnetic Films. Washington Butter Worths, Chapter 3, 54, 1964.

10. R. E. MacDonald, J. W. Beck. "Magneto-Optics." J. Appl. Phys, 40, 1429 (1969).

11. R. Carey, E. Isaac. Magnetic Domains and Techniques for their Observation. Academic Press, Chapter 5, p. 62, 1966.

12. G. Fan, E. Donath, E. Barekette, A. Wirgin. "Analysis of a Magneto-Optic Readout System." IEEE Trans. Elec. Computers, EC-12, 3 (1963).

13. N. Goldberg. "A High-Density Magneto-Optic Memory." IEEE Trans. on Magnetics, Mag-3, 605 (1967).

14. RCA. "Phototubes and Photocells." Radio Corporation of America, Chapter 2, 29, 1963.

15. Y. S. Lin, G. S. Almasi, D. B. Dove, G. E. Keefe, C. C, Shir. "Orientation Dependence of Propagation Margin of 1μm Bubble Contiguous Disk Devices." J. Appl. Phys., 50, 2258 (1979).

16. O. S. Heavens. Optical Properties of Thin Solid Films. Butterworths Scientific Publications, Chapter 4, 46, 1955.

17. B. C. McCollum, W. R. Bekebrede, M. Kestigian, A. B. Smith. "Refractive Index Measurements on Magnetic Garnet Films." Appl. Phys. Letters, 23, 702 (1973).

18. M. Wohlecke, J. Suits. "Refractive Index of Garnet Films Containing Ca and Ge." Appl. Phys. Letters, 30, 8 (1977).

19. J. Fernandez de C. "Detection of the In-Plane Magnetization in Ion-Implanted and Non-Implanted Garnet Films." Masters Thesis, Elect. Eng. Dept., Carnegie-Mellon University, Pittsburgh, PA, 1980.

FIGURE CAPTIONS

Fig. 1.   Cross-section of an ion-implanted contiguous disk device

Fig. 2   Coordinate system used to describe the magnetic film

Fig. 3   The three-fold critical curve for the magnetization in the
          ion-implanted layer

Fig. 4   The angle of inclination θ as a function of azimuthal angle
          ϕ defined from a $(11\bar{2})$ direction.

Fig. 5   A block diagram of the magneto-optic photometer system

Fig. 6   An oscillogram showing the phase difference between the PMT
          signal and the in-plane field ΔH_y

Fig. 7   (a) The critical curve and the applied fields used to sweep
          out the differentiated hysteresis loop shown in (b). (c) The
          hysteresis loop obtained by integration of (b).

Fig. 8   (a) The critical curve and the applied fields used to sweep
          out the differentiated hysteresis loop shown in (b). (c) The
          hysteresis loop obtained by integration of (b).

Fig. 9   (a) The applied fields used to obtain the data in (b) as the
          sample was rotated relative to the light beam and applied
          fields.

Fig. 10   The critical curve, applied field, and resulting magnetization
          directions which produce the data in Fig. 9b.

Fig. 11   (a) The applied fields used to obtain the data in (b) as the
           sample was rotated relative to the light beam and applied
           fields.

Fig. 12   The critical curve, applied field, and resulting magnetization
           directions which produce the data in Fig. 11b.

Fig. 13   The critical curve, applied field, and resulting magnetization
           directions which produce the data in Fig. 15

Fig. 14   The critical curve, applied field, and resulting magnetization
           directions which produce the data in Fig. 16

Fig. 15   The amplitude of the sinusoidal magneto-optic signal produced
           by the applied fields in Fig. 13 as a function of B_x.

Fig. 16   The amplitude of the sinusoidal magneto-optic signal produced
           by the applied fields in Fig. 14 as a function of B_y.

TABLE I

PARAMETER	(111) DRIVING LAYER	(111) STORAGE LAYER
FILM THICKNESS	0.4 μm	1.0 μm
FILM COMPOSITION	Gd Tm Y Ga Fe GARNET	Eu Tm Y Ga Fe GARNET
SATURATION MAGNETIZATION $(4\pi Ms)$	585 Gauss	650 Gauss
IMPLANTED ANISOTROPY ANISOTROPY CONSTANT (Ki)	−30,000 ergs/cm	Not Measured
UNIAXIAL ANISOTROPY CONSTANT (Ku)	+ 14,500 ergs/cm^3	————
COLLAPSE FIELD	N.A.	340 Oe
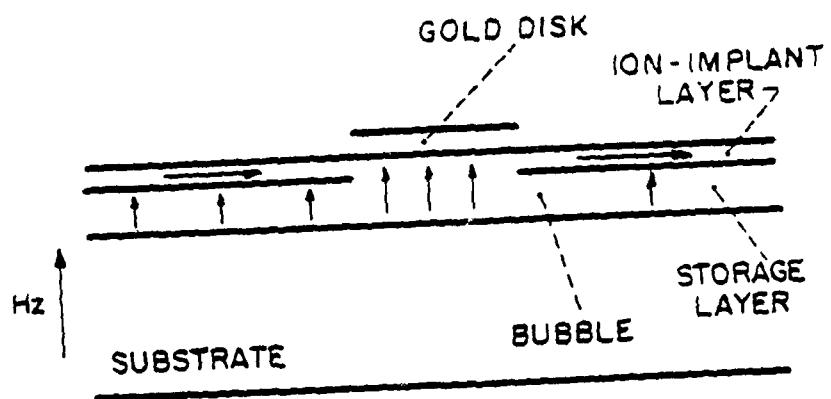
FIG. 1

FIG. 2

FIG. 3

FIG. 4

FIG. 5

FIG. 6

H_y

90 0e

80 0e

H_x

(a)

Amplitude

1

$-10\ 0e$ $10\ 0e$ H_y

(b)

Amplitude

1

H_c

$-10\ 0e$ $10\ 0e$ H_y

(c)

FIG. 7

FIG. 8

Light Beam Axis

h_y

H_{xy}

M

h_x

M

H_{xy}

(a)

Amplitude

1

0.25

0°   120°   240°   360°

Sample Orientation

(b)

FIG. 9

FIG. 10

Light Beam Axis
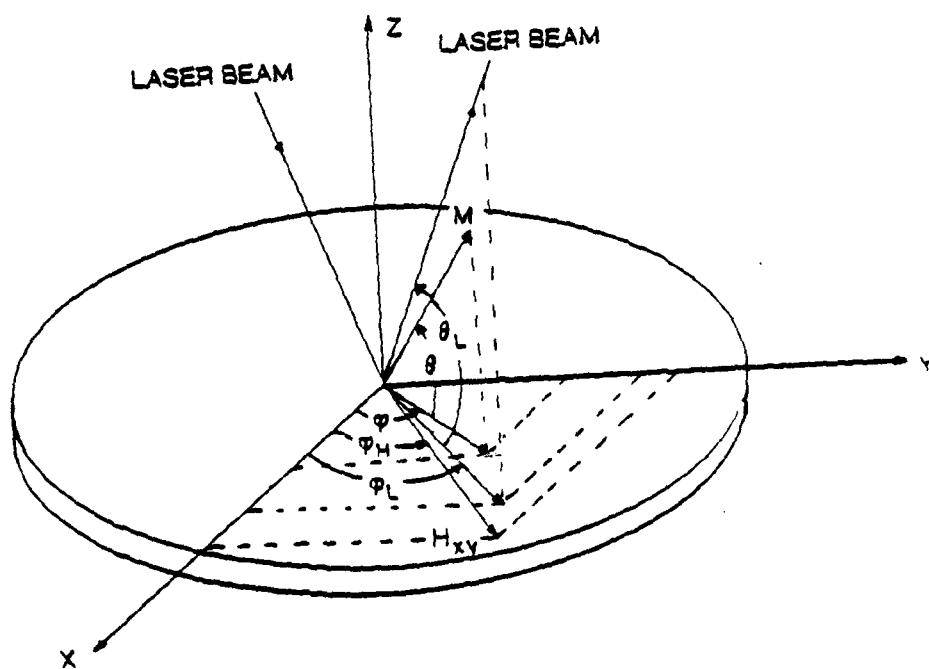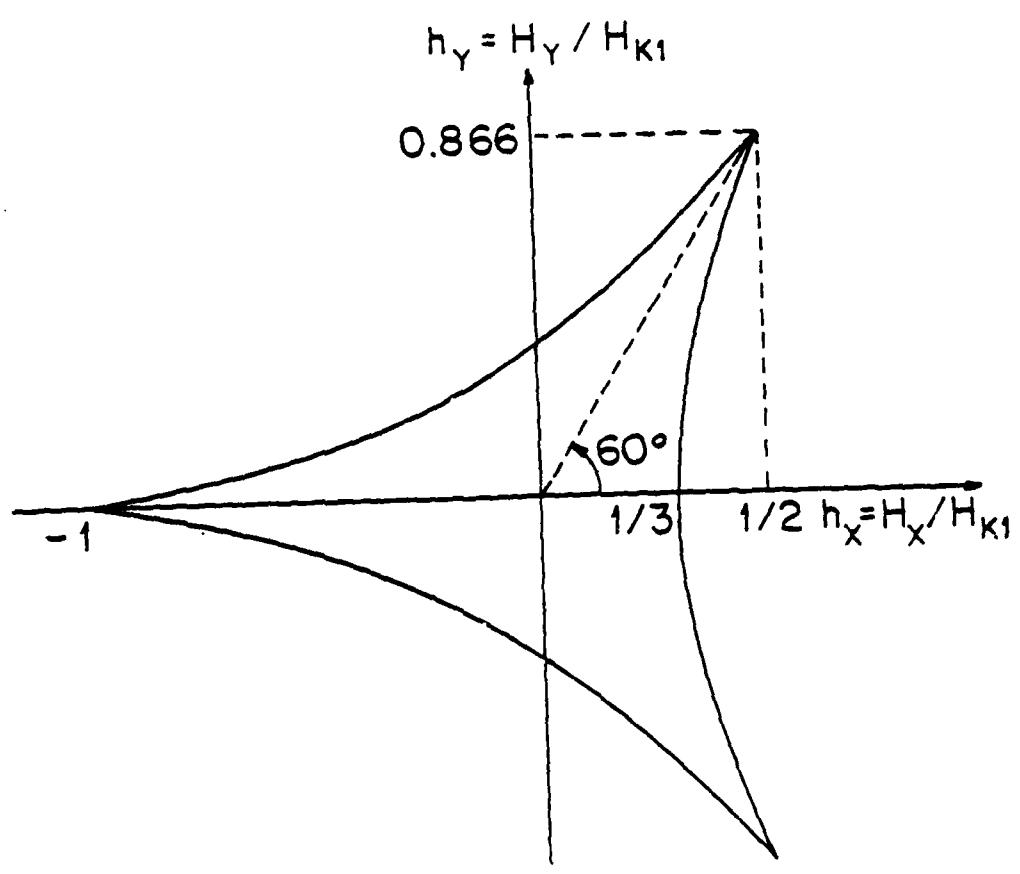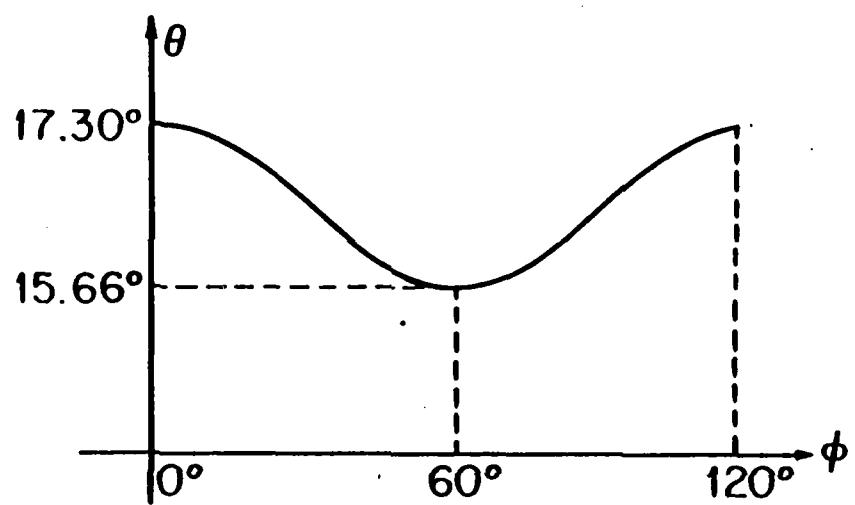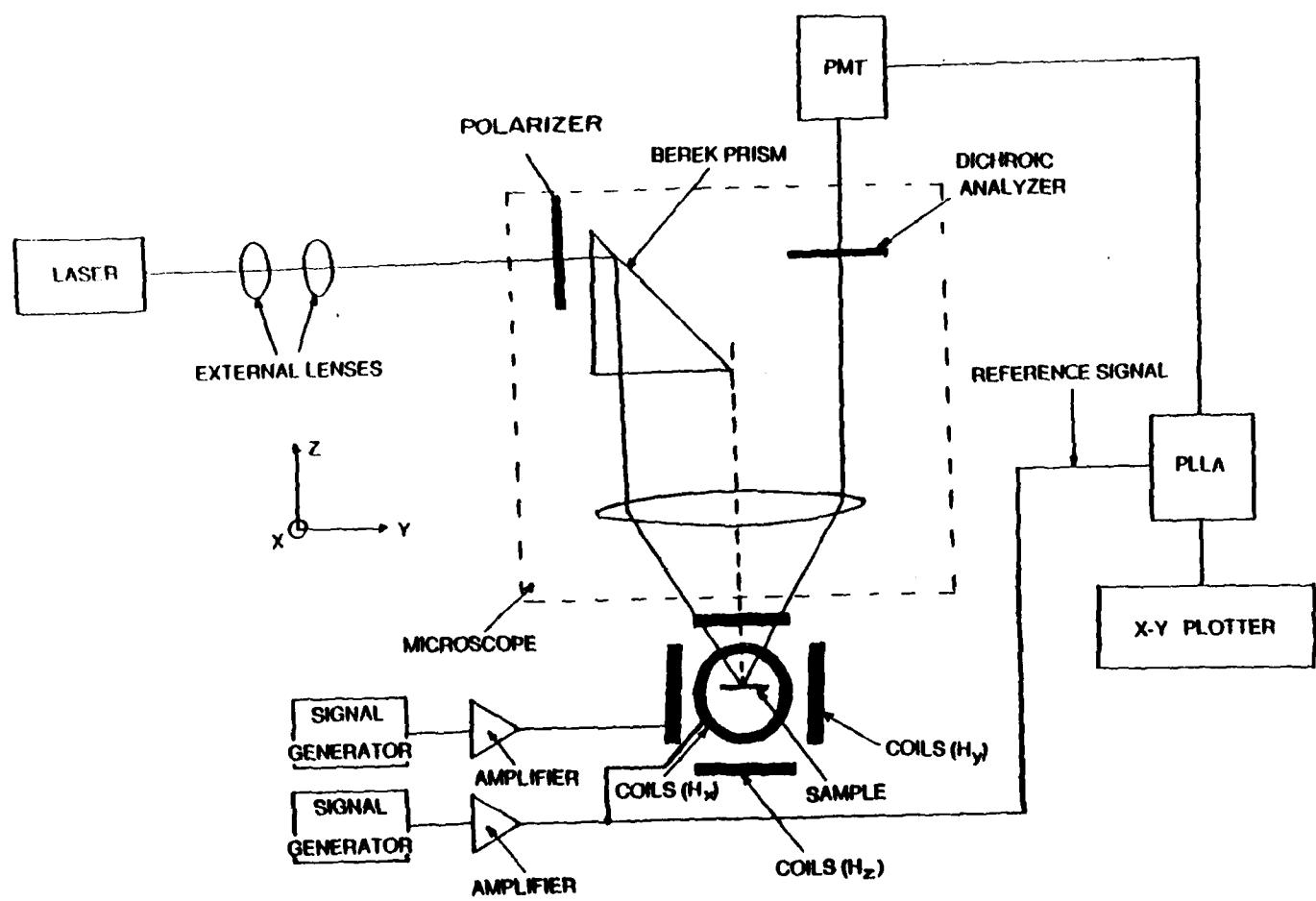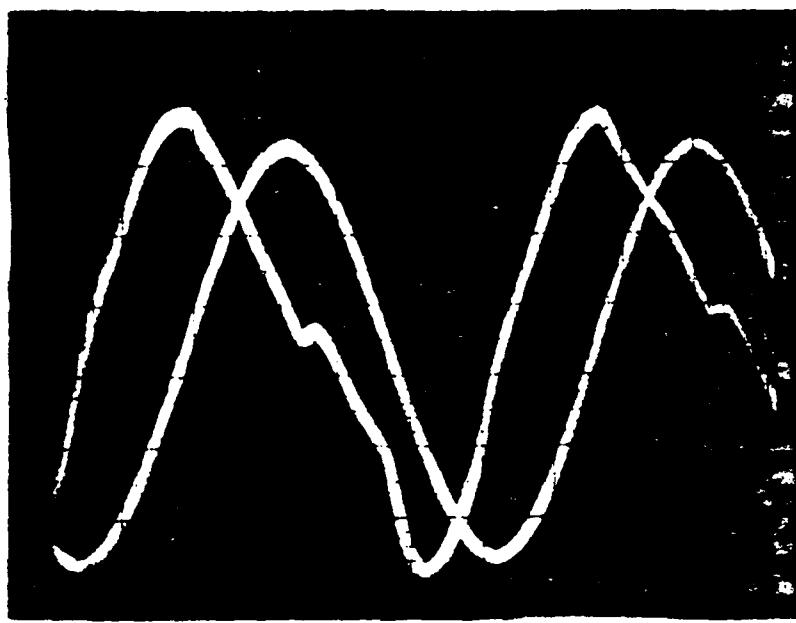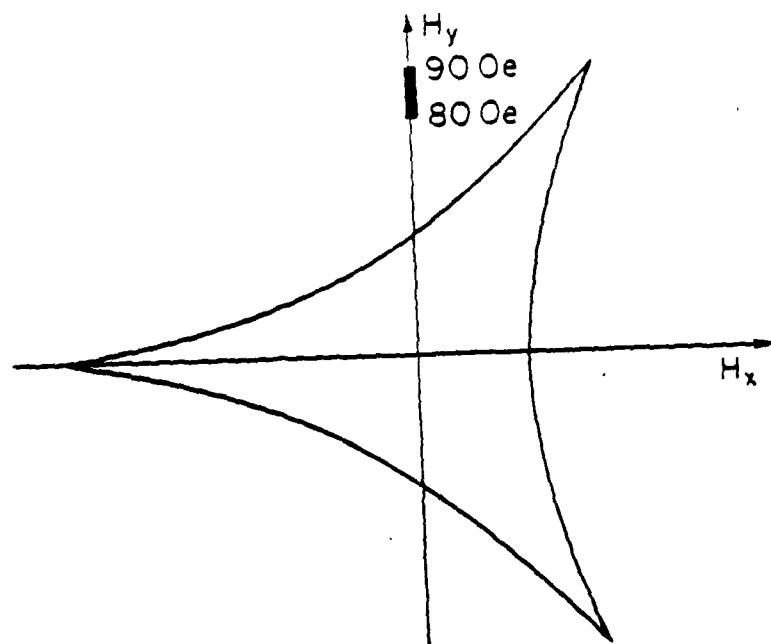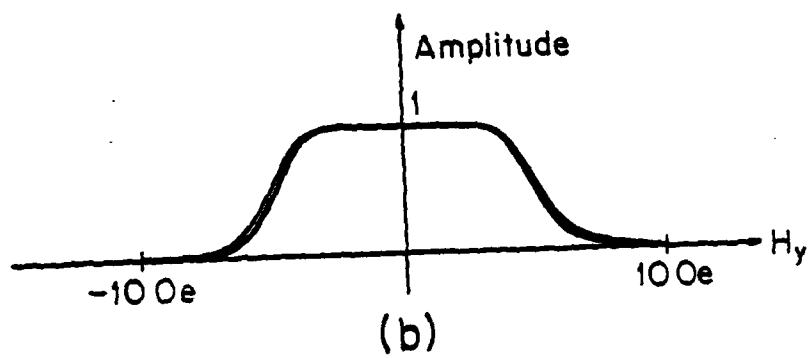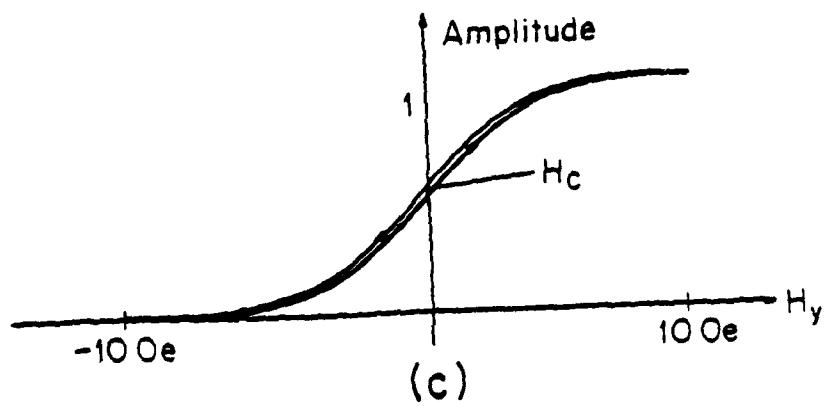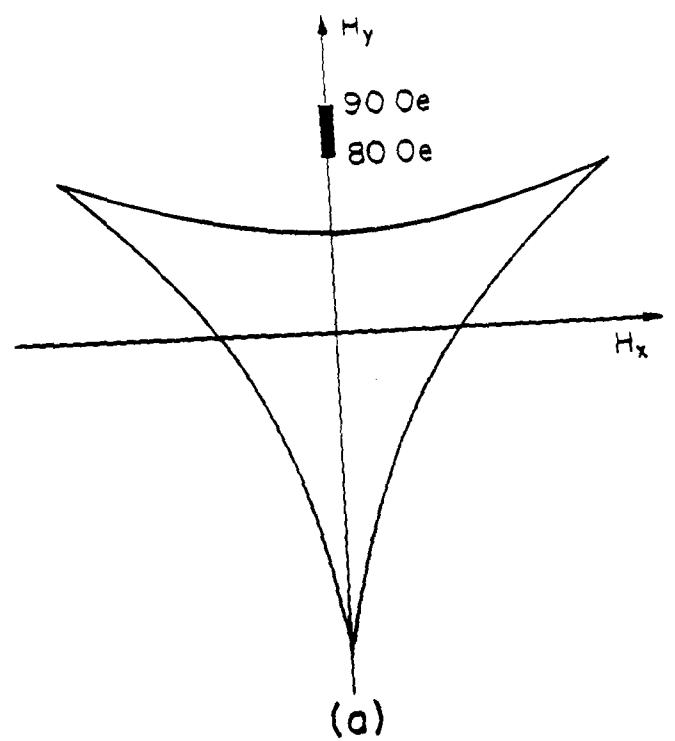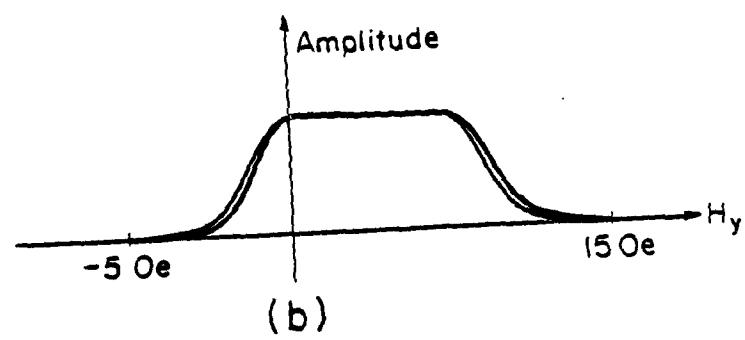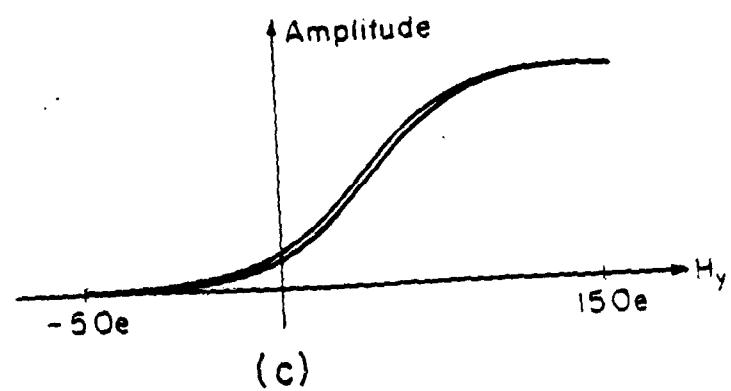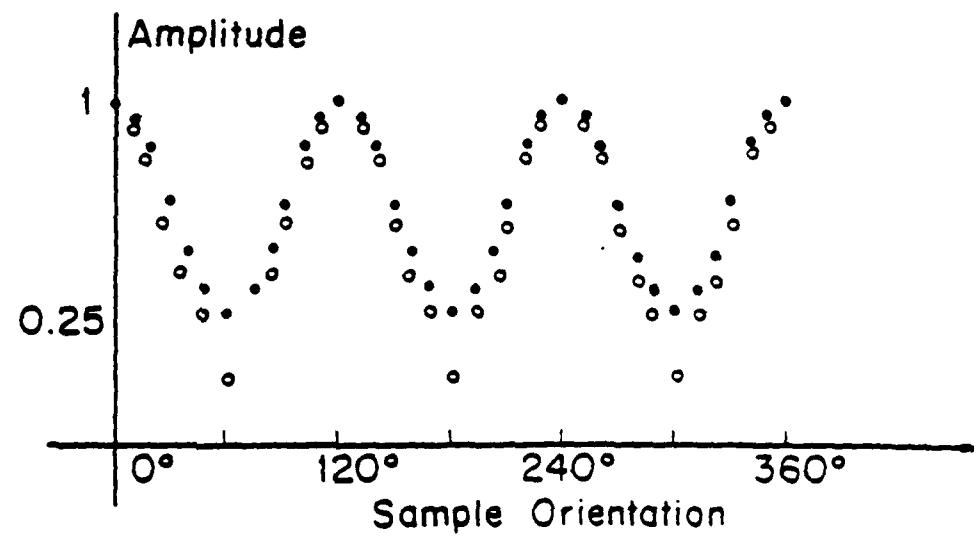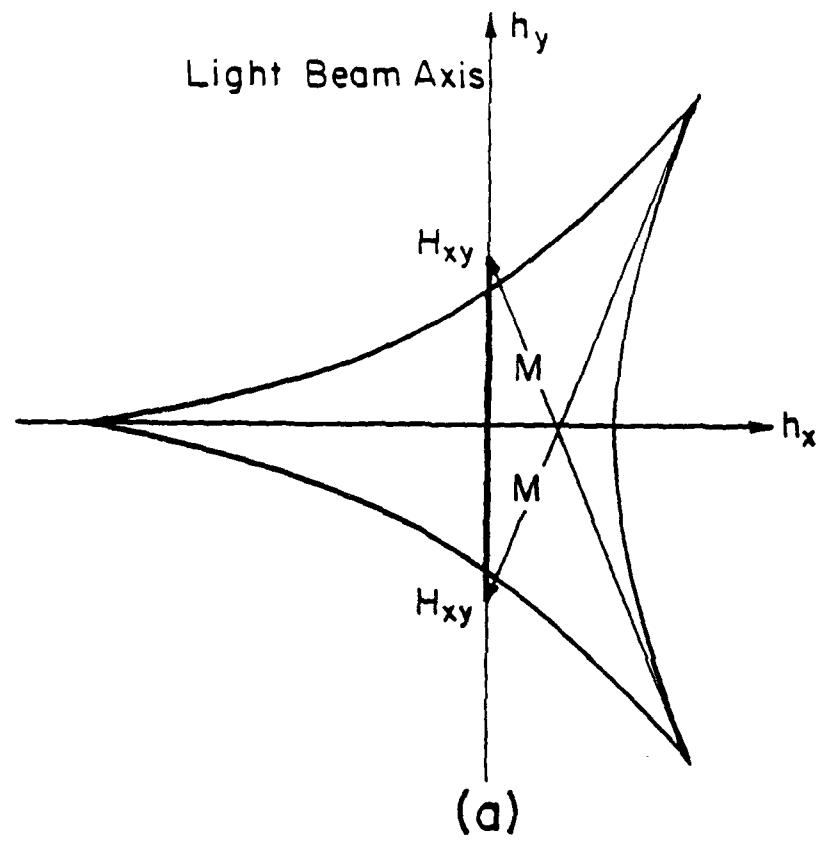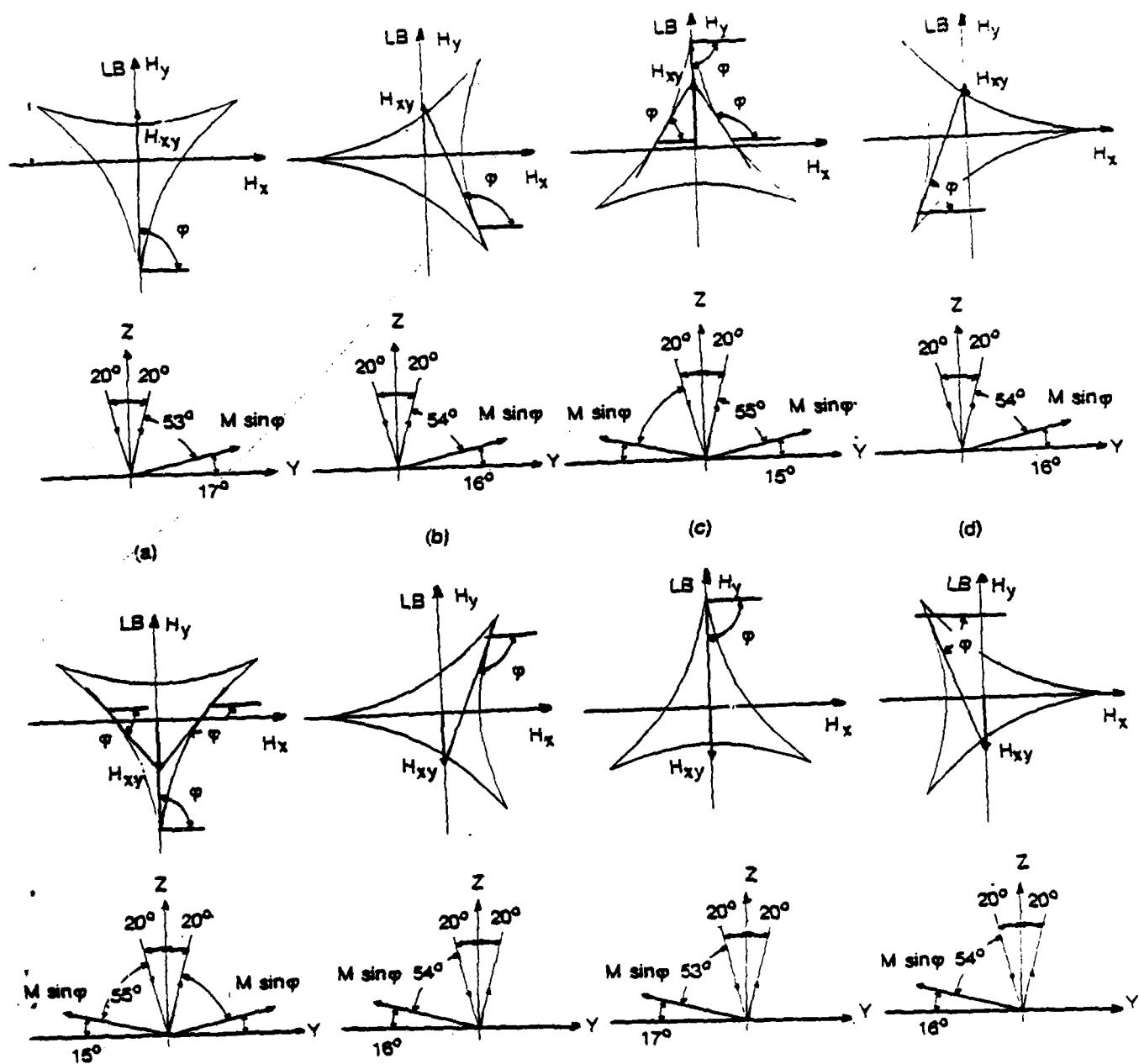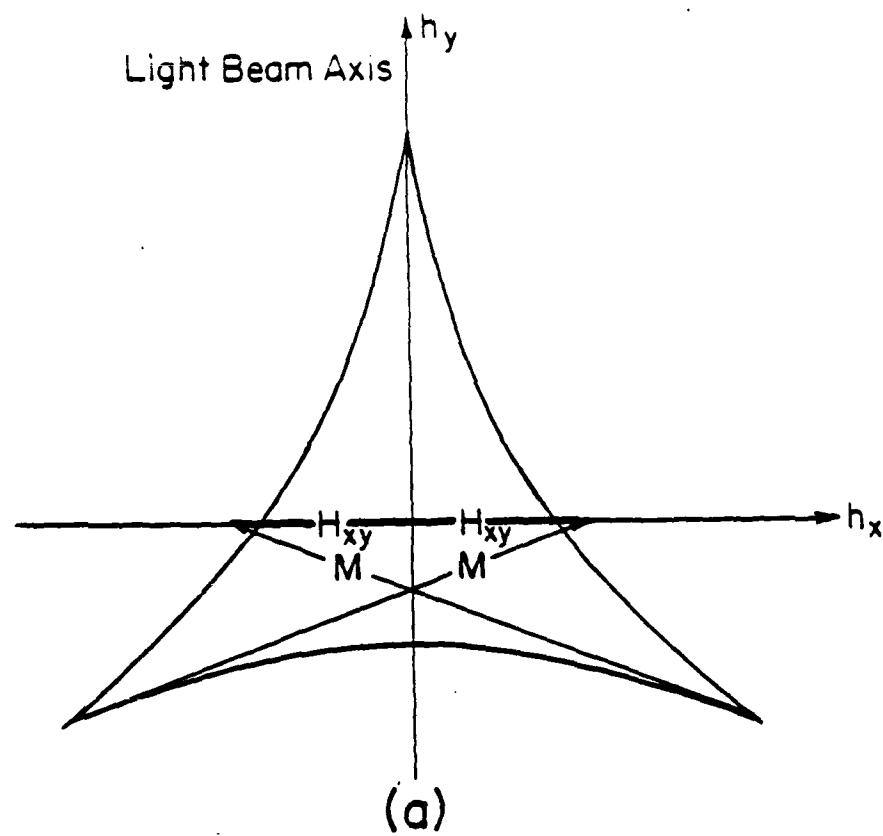
(a)
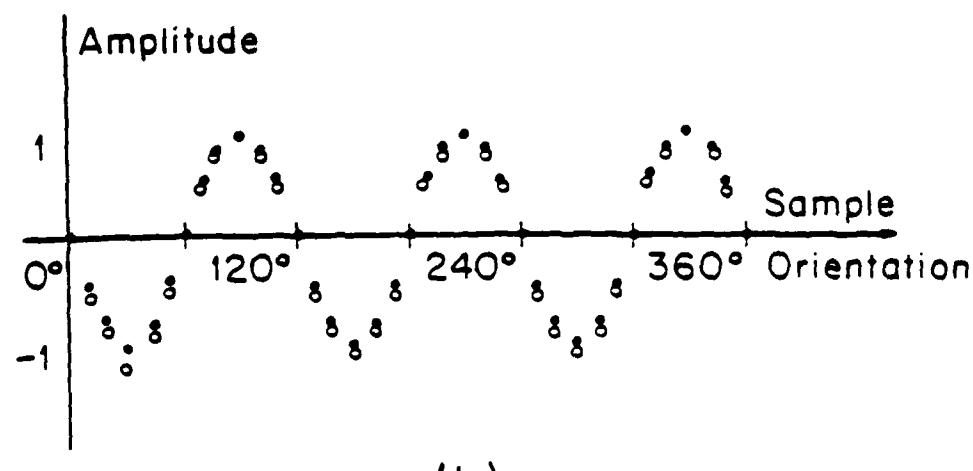
(b)

FIG. 11
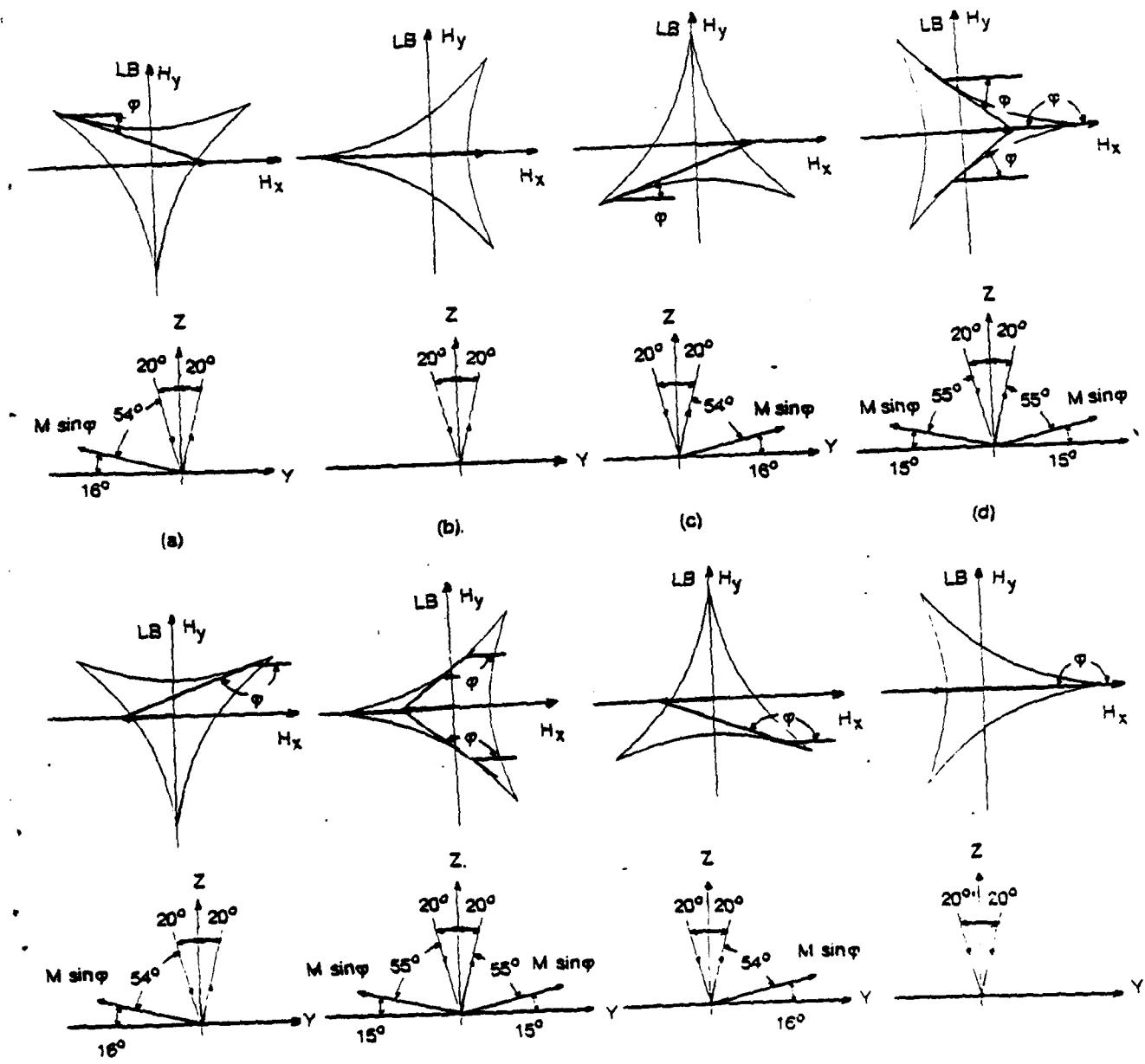
FIG. 12
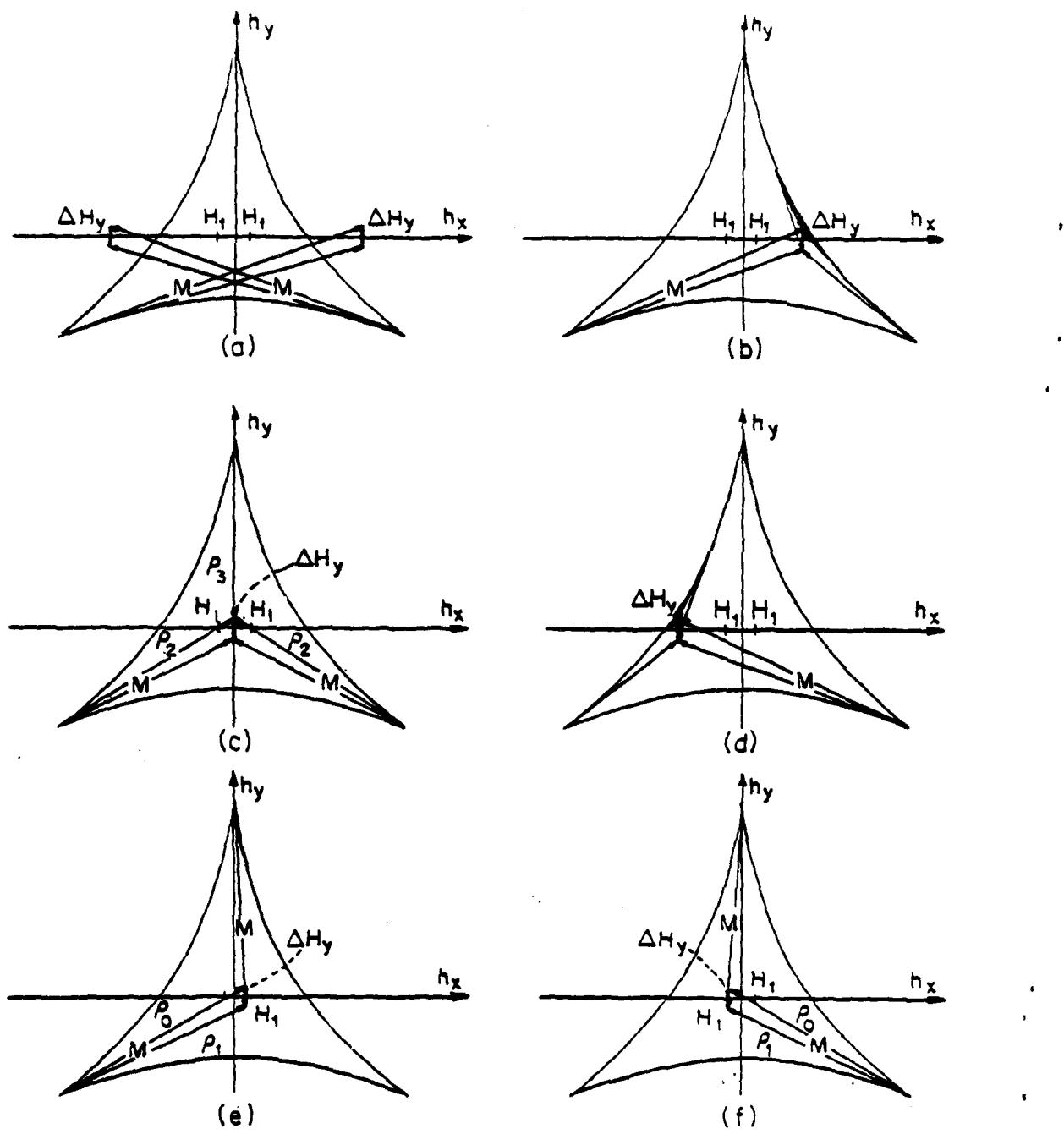
FIG. 13
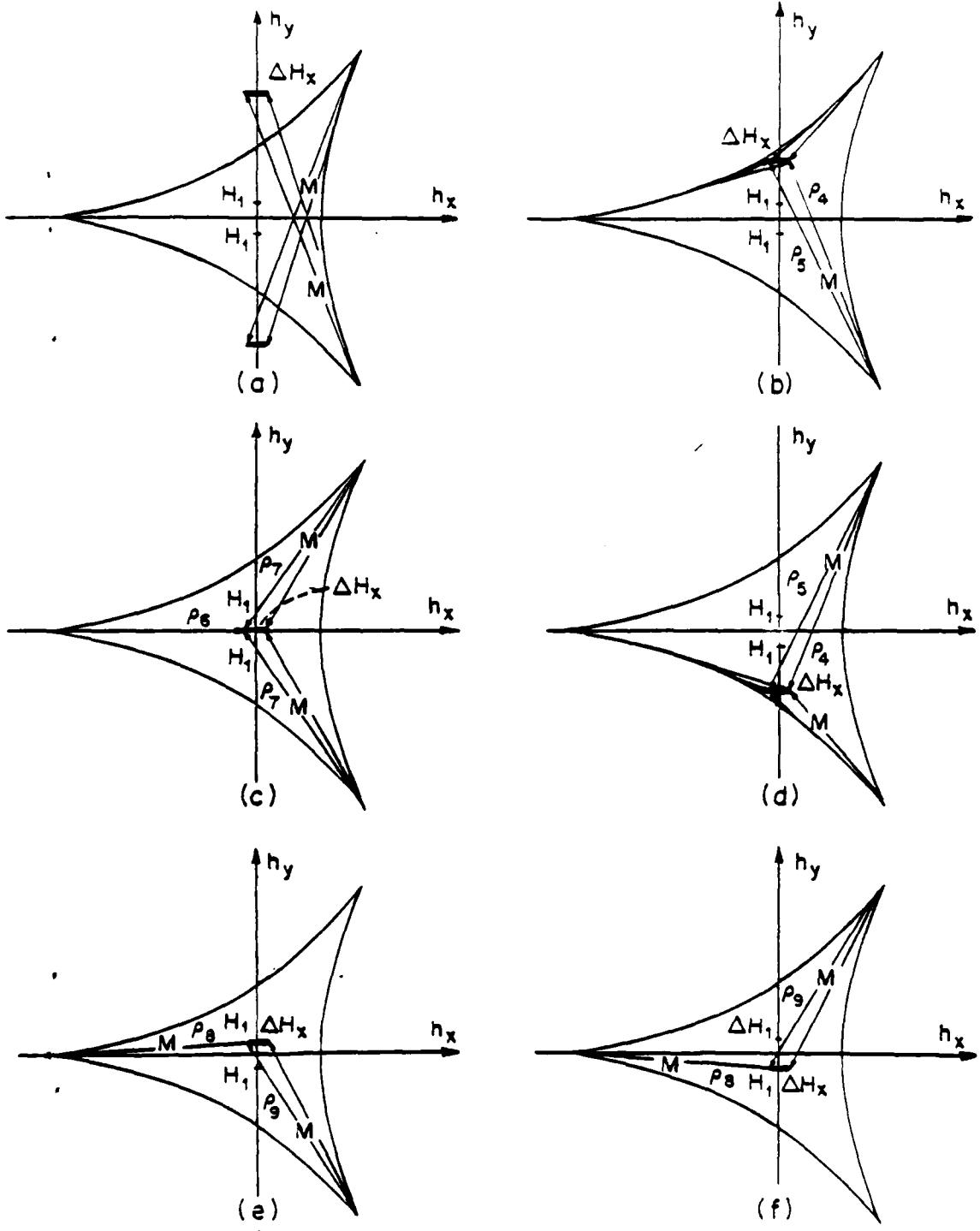
FIG. 14
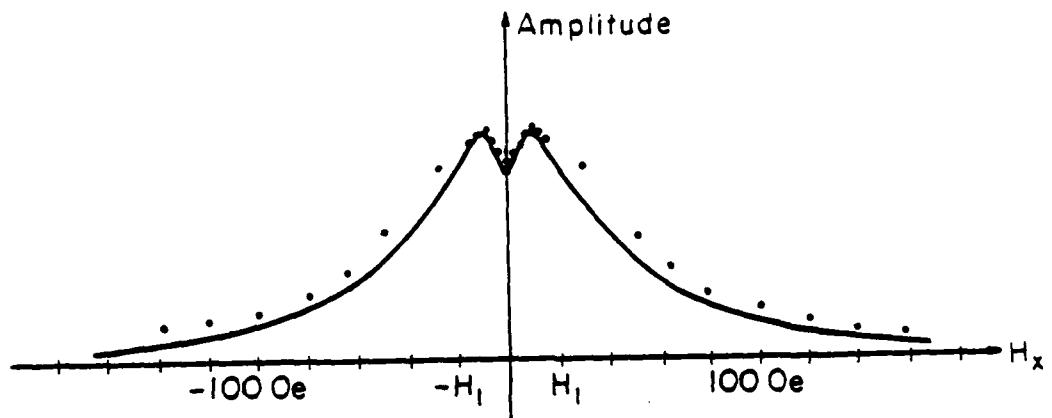
FIG. 15
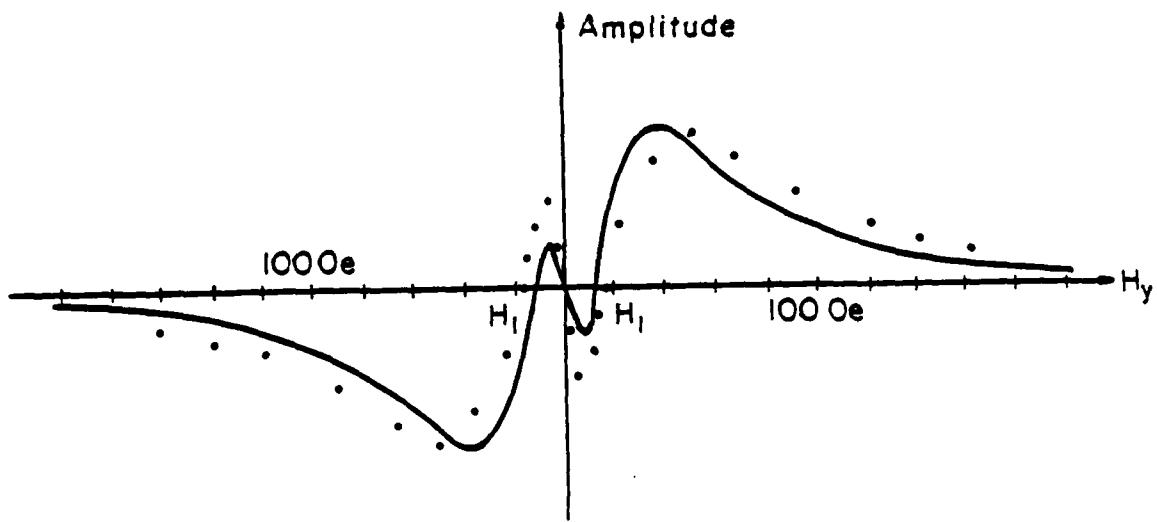
FIG. 16

STRAIN PROFILES IN ION IMPLANTED BUBBLE DEVICES INVESTIGATED

BY TRANSMISSION ELECTRON DIFFRACTION

T. Omi, C. L. Bauer, and M. H. Kryder[a]

Carnegie-Mellon University, Pittsburgh PA 15213

ABSTRACT

Selected area electron diffraction has been used to obtain strain profiles around unimplanted disks in thin ($<2000\text{Å}$) films of (111) oriented garnets. Measurements of in-plane lattice constant were made as a function of position in $(SmYGdTm)_3 Ga_{0.4}Fe_{4.6}O_{12}$ films implanted with oxygen (120 keV, $1 \times 10^{14}/cm^2$) and helium (80 keV, $4 \times 10^{15}/cm^2$). In most cases the data show a relaxation of stress normal to and near to the implanted boundary. These results are consistent with models suggesting that stress relaxation normal to an implanted boundary is critical to the formation of charged walls.

In addition, effects of the non-uniform stress field on the local anisotropy in the underlying bubble layer of an ion implanted contiguous disk device are considered. It is shown that under the edge of an implanted region, there is a tensile stress perpendicular to the film plane which reduces the perpendicular anisotropy, causing reduced bubble-nucleation thresholds in bubble materials with large negative values of λ_{111}.

PACS numbers: 61.14 -x, 61.80.Jh, 81.40.Rs, 85.70Ge

INTRODUCTION

Contiguous disk bubble devices employ ion implantation to create planar stress induced anisotropy in magnetic garnet thin films (1). The implantation is done through a photolithographically defined mask, and charged walls (2) appear in the implanted region near boundaries between implanted and unimplanted areas. There have been a significant number of experimental studies of the strains introduced by uniform implants; however, there has previously been no experimental work reported which provides information on the localized strains introduced at pattern boundaries. Recently, Hidaka and Matsutera (3), Backerra et al. (4), and Hubert (5) have suggested that there should be a localized stress relaxation near to and normal to the boundary, leading to the localized uniaxial anisotropy necessary to form the charged walls.

In this paper measurements of the local lattice strains near boundaries between implanted and unimplanted areas of garnets by selected area electron diffraction are described. These measurements provide experimental confirmation of localized stress relaxation near the boundary edges predicted by the above researchers. It is also shown that the stress field from the boundary is expected to cause lower bubble nucleation thresholds and higher gradient drive field requirements to pull a bubble from the boundary.

SAMPLE PREPARATION AND DIFFRACTION MEASUREMENT TECHNIQUES

Films of $(SmYGdTm)_3 Ga_{0.4}Fe_{4.6}O_{12}$ were epitaxially grown on 0.5mm thick gadolinium gallium garnet substrates. A pattern of $8\,\mu m$ diameter disks on $16\,\mu m$ centers in a square lattice was then

defined in AZ 1350J photoresist. The wafer was next implanted at 120keV with 1×10^{14} oxygen/cm^2 and at 80 keV with 4×10^{15} helium/cm^2. This implant is designed to produce a relatively uniform implant to a depth of about 3000Å. After implantation, the photoresist was removed from the garnet and the wafer was diced into chips. Individual chips were then bonded to a polishing block and the substrate was thinned by grinding with grit of decreasing particle size (25μm down to 3μm). After thinning to approximately 60μm thickness, the chips were cut into 3mm diameter disks and polished. The polished disks which were about 30μm thickness were removed from the polishing block and ion milled from the substrate face using an Ar beam at 6kV acceleration with the gun current ranging from 0.1 to 0.3mA. Successfully thinned samples had regions measuring 10-40μm with thicknesses less than 3000Å.

A transmission electron microscope (JEM-100C) which operated at an accelerating voltage of 120kv was used to detect unimplanted discs in the garnet and measure inplane lattice constants across the unimplanted disk edge, by selected area diffraction (SAD). A Siemens recording microphotometer was used in measurement of photographed SAD patterns.

EXPERIMENTAL RESULTS

Figure 1 shows an example of a SAD pattern as well as a TEM image of an unimplanted disk. A SAD aperture, which yields a diffracting area of 0.7μm diameter, was used throughout this research.

In a preliminary study, 100Å of Au was deposited on some of the ion-milled garnet foils in order to calibrate the resultant SAD patterns and thereby increase the precision of measured interplanar spacing and lattice constant. The lattice constant of garnet, at the center of the unimplanted discs (cf.Fig. 1), invariably was found to be 12.43±0.01Å, a value somehwat greater than those of usual garnet. This larger value may be due to stress introduced by deposition of the Au(6) onto the thin garnet film. In subsequent measurements Au was not deposited and the lattice strain was referenced to the lattice parameter in the unimplanted disks.

Figure 2 shows in-plane strain as a function of position along three directions which run through the center of the unimplanted disks. The lattice constant at each position had been measured for diffraction spots which were aligned at or nearly normal to the disk edge. Uncertainty in the measurement, which depends on the spot sizes, was to within $\Delta a/a = \pm 0.06\%$.

The three thick solid curves in Fig. 2 were measured for a disk which was located in a region of relatively uniform thickness. Each of the curves show a peak in strain at or near the disk edge and a shallow negative strain inside. The strain in areas far outside the disk is approximately constant at +0.25±0.1% although stress fields from adjacent disks are seen to affect the measurements outside a disk to some extent. The remaining curves show data taken on a variety of other disks on films of various thicknesses, some with significant thickness gradients and some with large holes formed during the ion-milling process near to or intersecting with the edge of the disk. Film thicknesses are estimated to be less than 0.2μm,

which is less than the implanted depth.

DISCUSSION

The data in Fig. 2 provide experimental evidence of the stress
relief predicted in the models proposed by Hidaka and Matsutera (3);
Backerra et al. (4) and Hubert (5). These workers pointed out that,
for a film on a thick substrate, there is no relaxation parallel to the
boundary (the y-direction in Fig. 3), but that there is an elastic
relaxation normal to the boundary causing the implanted region to
expand and the unimplanted region to contract.

Although the films examined in this study had the substrate
removed, thereby allowing stress relief in all directions, the data in
Fig. 2 indicate that significant stress relaxation normal to and near
to the boundary does occur in qualitative agreement with the above
models. Figure 3 shows a model for the stress relaxation expected
in films with no substrate. In Fig. 3a, a schematic cross-sectional
diagram of the cubic lattice near the interface between the
unimplanted and implanted areas is shown. In the far left hand edge
of the diagram the lattice constant is uniform and equal to that of
an unimplanted garnet film, while on the far right the lattice
constant is also uniform, but equal to that of a uniformly implanted
film. The area of interest is the transition region between the two
uniform areas.

To understand why the strains indicated in Fig. 3a occur,
consider the stresses on unit cells near to the boundary between the
unimplanted and implanted areas. Figure 3b shows the cells and their
distortions. The cell on the left lies in the unimplanted area and
without any additional stresses would be cubic with a lattice constant
smaller than that of neighboring implanted cells on the right. Due to
bonding of the unimplanted cells to larger implanted cells, both the
unimplanted and implanted cells feel stresses causing them to distort.
The unimplanted cells feel tensile stresses in the y and z directions,
causing the lattice constant a, measured along x, the normal to the
implanted boundary, to contract. Similarly, the implanted cells feel
compressive stresses in y and z, causing the lattice constant measured
normal to the implanted boundary to expand. A measurement of
strain perpendicular to the boundary between unimplanted and
implanted areas is thus expected to exhibit a minimum on the
unimplanted side near the boundary and a maximum on the implanted
side near the boundary as shown qualitatively in Fig. 3c.

The majority of data in Fig. 2 show evidence of minima and
maxima in the strain normal to the boundary like that in Fig. 3c. In
certain cases, however, the minima and/or maxima are not detected.
It is possible that failure to detect the peaks in those cases is due to
experimental difficulties, such as the fact that in very thin films the
relaxation might occur over a very short distance, making it possible
that the peaks in strain were located between positions where data
points were taken. Alternatively, if the minima and maxima in strain
are in fact absent, then one must conclude that the implantation
induced stress is graded across the boundary in such a fashion that
the tetragonal distortion indicated in Fig. 3 does not occur. This
could be the case in samples which have an implantation mask
profile which is chamfered at the edge and suggests that the charged

wall structure may depend critically on the implantation profile normal to the boundary. Relaxation of the peaks in strain at the boundary could also occur as a result of annealing. Diffusion of the defect structure introduced by implantation and responsible for the stress would be promoted by the non-uniform stress fields existing at the boundary.

The non-uniform stresses at the boundary between implanted and unimplanted areas can be expected not only to produce significant magnetic anisotropies in the implanted layer, but also in the underlying bubble layer. To estimate the stress induced anisotropies in the bubble layer, we make use of an analysis of stress fields from patterned metal films performed by Dishman et al. (7). Although contiguous disk devices use curved boundaries, we simplify the analysis by assuming a straight boundary as in Fig. 4. This approximation is reasonable when the radius of curvature R of the boundary is large compared to the implanted film thickness t, which is typically fulfilled in practical devices. (With $1\,\mu$m bubbles, R= $4\,\mu$m and t=$0.4\,\mu$m.) We approximate the stresses from the implanted layer by a line force $s = -\sigma_{xx}t$ acting at the surface of a semi-infinite solid, where $-\sigma_{xx}$ is the compressive stress in the implanted region. We assume that the line force exists a distance t/2 above the surface of the bubble material and that the space between the line force and the bubble layer has elastic constants equal to those of the bubble material.

To obtain a value for σ_{xx} we use data from Fig. 2 and $\sigma_{xx} = Ye_{xx}/(1-2v)$ where Y is Young's modulus and v is Poisson's ratio. Choosing $e_{xx}= 0.5\%$ as a typical value in the uniformly implanted region far from the disk edge in Fig. 2, and using $Y=2x10^{12}$ dyne/cm^2 and $v=0.32$ we find $\sigma_{xx}=2.8x10^{10}$ dyne/cm^2.

Taking the origin of coordinates at the point of application of the line force, the longitudinal stress in the z direction perpendicular to the film is given by (7)

$$\sigma_z = -2s \times z^2/\pi(x^2+y^2)^2 \qquad (1)$$

which has a maximum value of

$$\sigma_z(max) = -9s/8 \quad 3\pi z \qquad (2)$$

when $x = z/3$. This stress component gives rise to an anisotropic energy density which when added to the growth induced anisotropy of the film produces a total perpendicular anisotropy energy density

$$E_{Kz} = K_u\sin^2\theta + 1.5\lambda_{111}\sigma_z\sin^2\theta \qquad (3)$$

where θ is the polar angle defined from the z-axis. In the region x>0 under the implanted layer σ_z is positive. Since λ_{111} is typically negative, the stresses from the boundary reduce the effective perpendicular anisotropy of the garnet.

Table 1 compares $1.5 \lambda_{111} \sigma_z$ with K_u for two garnets used in $1\,\mu$m bubble ion implanted devices. Values are given both at the top (z=-t/2) and bottom (z=-h-t/2) surfaces of the bubble layer which is h=$0.8\,\mu$m thick and which has an implanted layer t=$0.4\,\mu$m thick on its surface. The SmGdTmYGa garnet, which is useful as a single layer ion implantable material, has high magnetostriction ($\lambda_{111} = -3.5x10^6$) and moderate K_u. The EuTmYGa garnet, which has been used in double layer contiguous disk devices, has lower

magnetostriction ($\lambda_{111} = -1.8 \times 10^6$) and higher K_u. It is seen that $1.5 \lambda_{111} \sigma_{zz}$ is comparable to K_u in the SmGdTmYGa garnet, but significantly less than K_u in the EuTmYGa garnet.

Since the net perpendicular anisotropy near an implanted boundary in SmGdTmYGa garnet films is much less than in EuTmYGa garnet films, the nucleation threshold for bubble domains is considerably lower when using the SmGdTmYGa garnet material. With identical nucleator designs current requirements for nucleation in SmGdTmYGa films is about one-half the current requirement in EuTmYGa materials.

The reduced perpendicular anisotropy at the implanted boundary edge also gives rise to a potential energy minimum for domain walls there. Thus the force necessary to pull a bubble domain from a boundary edge should depend linearly on the magnetostriction constants of the bubble material. One would expect, therefore, that devices using high magnetostriction materials would require higher transfer gate currents than devices using low magnetostriction materials.

CONCLUSIONS

Measurements of strain perpendicular to the edge of implanted boundaries in garnet films indicate that in most cases there is stress relaxation normal to the boundary. These data are in agreement with the predictions of researchers (3,4,5) who have indicated that such stress relaxation is critical for the formation of charged walls. In some cases the data do not show the expected strains. Although experimental difficulties may have prevented their measurement, it is also possible that the stress profile normal to the boundary is graded over a sufficiently large distance that the predicted relaxation does not occur. This could arise when the implantation profile normal to the boundary is graded, due to a chamfered mask edge, or when the non-uniform stresses at the boundary are annealed out.

Consideration of the stress induced anisotropy arising from an implanted boundary led to the conclusion that bubble layers with high negative magnetostriction constants can be expected to have low bubble nucleation thresholds and to require large field gradients to pull a bubble from an implanted boundary.

ACKNOWLEDGEMENT

REFERENCES

a) This work was suported by the Air Force Office of Scientific Research under Grant AFOSR-80-0284.

1) R. Wolfe, J. C. North, W. A. Johnson, R. R. Spiwak, L. J. Varnerin, and R. F. Fischer, AIP Conf.Proc., 10, 339 (1973).

2) G. S. Almasi, E. A. Giess, R. J. Hendel, G. E. Keefe, Y. S. Lin, and M. Slusarczuk, AIP Conf. Proc., 24, 630 (1975).

3) Y. Hidaka and H. Matsutera, Appl Phys. Lett., 39, 116 (1981).

4) S. C. M. Backerra, W. H. DeRoode and U. Enz, Philips J. of
   Res., 36, 112 (1981).
5) A. Hubert, private communication to be published.
6) K. Kinoshita, K. Maki, K. Nokamizo, and K. Takeuchi, Jap. J.
   Appl. Phys., 6, 42 (1967).
7) J. M. Dishman, R. D. Pierce, and B. J. Roman, J. Appl. Phys.,
   45, 4076 (1974).

TABLE I

Figure 1. Transmission electron micrograph of the (circular) un-
implanted region of (111) garnet, measuring about $8 \mu m$
in diameter, and typical selected-area electron diffraction
pattern.

Figure 2. Fractional variation of lattice parameter ($\Delta a/a$) as a
function of distance x along (a) [112], (b) [110] and (c)
$45°$ from [110]. Solid (o), dashed ( ) and dotted (Δ)
curves denote results obtained from different specimens and
the solid (horizontal) bars denote position of circular masks
which shield the underlying material from implantation.

Figure 3. (a) Schematic representation of lattice distortions expected
near the boundary separating unimplanted and implanted
garnet. (b) Tetragonal distortion of cells in the unimplanted
material. (c) Expected strain profile normal to the boundary
plane.

Figure 4. A model for calculating the stress field as a function of
distance from the implanted boundary.

FIG. 1

FIG. 2

MASK

z

x

NIMPLANTED REGION   IMPLANTED REGION

(a)

z   y
x

z   y
x

(b)

Δa/a

x

(c)
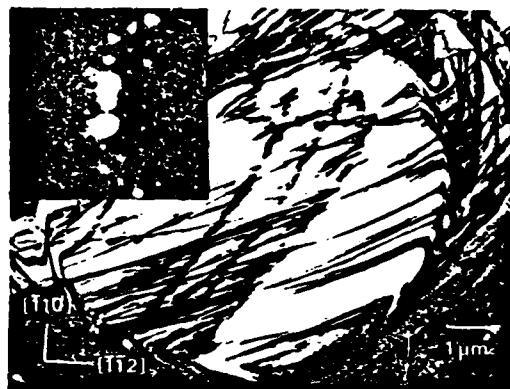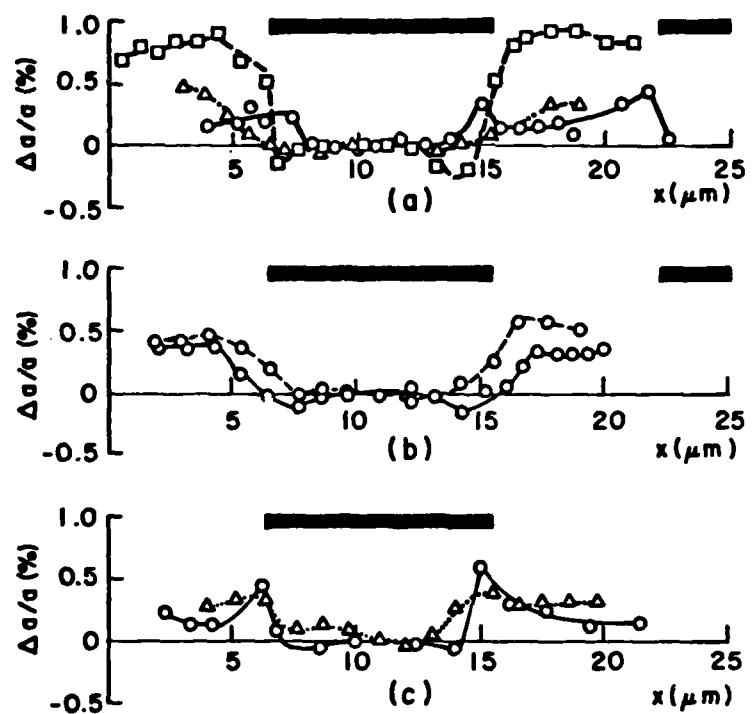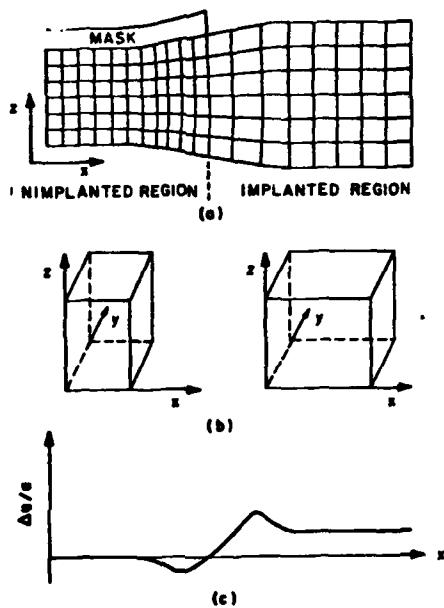
FIG. 3
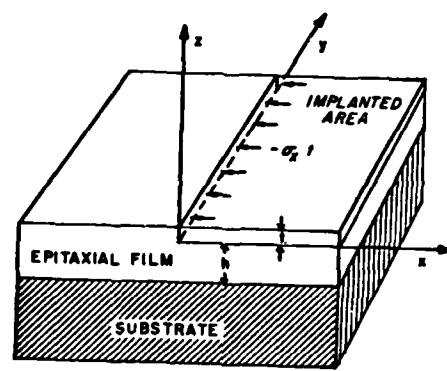
FIG. 4

THE INFLUENCE OF STRESS RELAXATION ON CHARGED WALLS IN A
100   ORIENTED GARNET FILM

D. A. Saunders and M. H. Kryder[a),b)]

ABSTRACT

Planar domain configurations in a (100) garnet film [1] are explained in terms of
inverse magnetostrictive anisotropies present at boundaries between implanted and
unimplanted regions of the film. Stress relief at such boundaries has been cited as
an important factor in the formation of charged walls in (111) films [2],[3],[4]. The
domains seen in this (100) film illustrate dramatically the effect of this stress relief.
The stress is modeled as a uniaxial stress along the boundary which gives rise to
uniaxial anisotropies along the boundary. Because λ_{100} and λ_{111} are of different
sign, the easy axis of magnetization is found to alternate perpendicular to and
parallel to the boundary around an implanted disk. It is conjectured that (100) films
with λ_{100} and λ_{111} of the same sign may successfully support charged walls
suitable for bubble propagation.

INTRODUCTION

In a paper presented at the 1980 Intermag Confernce [1], we described the
formation of charged walls in a (100) garnet film with planar magnetization. The film
was investigated with the interest that (100)-oriented films might be used in ion-
implanted contiguous-disk bubble devices. However, the planar domains and
associated charged walls seen around ion-implanted patterns in this (100) film were
unlike those typicaly seen in (111)-oriented drive layers. Recent investigations
[2],[3],[4] of the influence of the stress at boundaries between implanted and
unimplanted regions of a drive layer have pointed to the reason for this difference.

Hidaka and Matsutera [2]; Backerra, De Roode, and Enz [3], and Hubert[4] have
suggested that magnetic anisotropies are present at pattern boundaries due to the
anisotropic relief of stress at these boundaries. Away from the boundaries,
compressive stress due to ion-implantation is relieved by lattice expansion only
perpendicular to the film. At the implanted/unimplanted boundaries, there is additional
stress relief normal to the boundary - the expansion perpendicular to the film allows
the lattice near the boundary to stretch normal to the boundary [2] and there is
mutual relief of the tensile stress of the unimplanted region and the compressive
stress of the implanted region [3]. However, there is no relief for stress parallel to
the boundary. Indeed, the stress may be increased by the implanted region trying to
expand while the unimplanted region trys to contract, each pulling on the other.

EXPERIMENTAL

The (100) film was $Sm_{1.16}Tm_{1.34}Ca_{0.5}Ge_{0.5}Fe_{4.5}O_{12}$ grown on a samarium-gallium-garnet substrate. Its characteristics were as follows: $\lambda_{100} = 8.7\times10^{-6}$, $\lambda_{111} = -5.6\times10^{-6}$, $4\pi M = 550G$, $2K_u/M = -5000G$ (as-grown), $2K_1/M = -280G$, thickness $1\mu m$. In this film with planar magnetization and positive λ_{100}, contiguous-disk patterns were created by ion-implantation of the patterns themselves with two dosages of 2×10^{15} He^+/cm^2 at 240 KeV and 120KeV.

Typical domain patterns seen by modified Bitter technique [8] around implanted patterns after a.c. demagnetization are shown in Figs 1a and 1b with the magnetization directions indicated by arrows. Because of the negative crystalline anisotropy and the large planar anisotropy, the domain magnetization directions are approximately along the <110> crystalline axes. As can be seen in Fig. 1, the magnetization actually seems to flow into and out of the implanted patterns, creating magnetic charge at the boundaries - a magnetostatically unfavorable configuration. These observations can be explained by the variation in the stress-induced anisotropy at the boundaries.

THEORY

In analysis, we adopt a simple model where the stress, σ, is a uniaxial tension (compression being negative tension) parallel to the boundary and in the film plane. Choosing the crystalline axis as the coordinate system with the [001] axis perpendicular to the film, the inverse magnetostrictive energy expression [5] becomes

$$E = -(3\sigma/8)\sin^2\{2\lambda_{100}+(\lambda_{100}+\lambda_{111})\cos[2(\phi-4)]$$
$$+(\lambda_{100}-\lambda_{111})\cos[2(\phi-4)+4\psi]\} \qquad (1)$$

where

θ	is the polar angle of the magnetization from the [001] axis
ϕ	is the in-plane angle of the magnetization from the [100] axis (Fig. 2)
ψ	is the in-plane angle of the uniaxial stress from the [100] axis, i.e. the angle of the boundary (Fig. 2)

The first term is a uniaxial anisotropy perpendicular to the film. The second term is a uniaxial anisotropy parallel to the boundary. The third term is a uniaxial anisotropy at an angle of 4ψ with respect to the boundary. Therefore, around an implanted disk, the third term causes the stress-induced anisotropy to vary with fourfold symmetry. For boundaries parallel with <100> axes,

$$4\psi = 2n\pi \qquad n = \text{integer} \qquad (2)$$

Thus, the energy expression becomes (ignoring the first term)

$$E = -.75\sigma\lambda_{100}\sin^2\theta\cos 2(\phi-\psi) \quad\quad\quad (3)$$

For the experimental film, σ is positive and λ_{100} is positive, so that expression (3) represents an anisotropy with an easy axis <u>parallel</u> to the boundary. For boundaries parallel with $\langle 110\rangle$ axes,

$$4\psi = (2n+1)\pi \quad\quad n = \text{integer} \quad\quad\quad (4)$$

Expression (1) becomes, in these cases,

$$E = -.75\sigma\lambda_{111}\sin^2\theta\cos 2(\phi-\psi) \quad\quad\quad (5)$$

Expression (5) is of the same form as (3); however, λ_{111} is negative and hence expression (5) represents an anisotropy with an easy axis <u>perpendicular</u> to the boundary. Therefore, around an implanted disk, the easy magnetization axis is found to be alternately parallel and then perpendicular to the disk edge, as shown in Fig. 1c.

DISCUSSION

The effects of the stress-induced anisotropies shown in Fig. 1c can be clearly seen in the domain configuration of Fig. 1b. The stress-induced easy magnetization directions perpendicular to the pattern edge (the $\langle 110\rangle$ directions) correspond to the easy directions in the bulk of the film. Consequently, the domains in the bulk of the film terminate perpendicular to the edge. This is seen at the immediate top, bottom, and sides of the disk in Fig. 1b. Because the magnetization is perpendicular to the pattern edge at these points, large collections of magnetic charge are created at the boundary - these are especially evident at the disk edges to the right and to the bottom of Fig. 1b. and along the edges of the bar in Fig. 1a.

In order for the magnetization to be normal to the boundary, the stress-induced anisotropy must be larger than the demagnetizing effect at the boundary, i.e.

$$|1.5\sigma\lambda_{111}| > 2\pi M^2 \quad\quad\quad (6)$$

In this film, the planar stress far from the implanted region is due to lattice mismatch between the magnetic film and the substrate. The uniaxial stress along the implanted region boundary is the residual of the planar stress left after relief of the stress component normal to the boundary. Hence, this uniaxial stress is caused by the same lattice mismatch and can be written [6]

$$\sigma = 2.82 \times 10^{12} \, \Delta a \text{ (dynes.cm}^{-2}) \quad\quad\quad (7)$$

where $\Delta a/a$ is the lattice mismatch between the SGG substrate (a=12.437A) and the magnetic film (a=12.411A)[7]. For these lattice constants,

$$\sigma = +5.9\times 10^9 \text{ (dynes.cm}^{-2})$$

With $\lambda_{111} = -5.6\times 10^{-6}$, the stress-induced anisotropy energy is

$$|1.5\lambda_{111}\sigma| = 5.0 \times 10^4 \text{ (ergs.cm}^{-3})$$

Whereas, the demagnetizing energy is only

$$2\pi M^2 \approx 1.2 \times 10^4 \quad (ergs.cm^{-3})$$

Thus, the stress-induced anisotropy is the dominant effect at the boundary.

Further evidence of the presence of the stress-induced anisotropy at the boundary is the fading of the 90° walls near to the disk shown to the upper-right, upper-left, lower-right, and lower-left of the disk in Fig. 1b. The easy axes are parallel to the disk in these areas and favor the spins in the center of the 90° walls. Thus, the walls are widened near to the disk.

The walls in Fig. 1b. are dipolar in nature and have no net charge. As was reported in our previous paper [1], charged walls can be formed by applying in-plane fields to the sample. When a sufficiently large in-plane field (>25 0e) is applied along a hard magnetization direction, <100>, only domains having two of the four easy magnetizaiton direct ns are present. Charged walls then form at the disk along the <100> directions parallel to the in-plane field (Fig. 3a). For smaller fields (<25 0e), closure domains form at the charged wall so as to distribute the charge over a larger area (see Fig. 3a, reference [1]). When the in-plane field is applied along an easy magnetization direction, <110>, closure domains with magnetization perpendicular to the in-plane field form so as to evenly distribute the charge on the walls (Fig. 3b). Consequently, the charged walls in Fig. 3a become the dipolar 180° walls along the <110> directions in Fig. 3b. That is, strongly charged walls form around a disk only where the uniaxial anisotropy is parallel to the disk edge.

In this (100) film, λ_{100} and λ_{111} are of different signs, causing the stress-induced anisotropy to change signs for boundaries along different crystalline directions. This sign variation can be avoided by using a material with λ_{100} and λ_{111} of the same sign - the third term in expression (1) then becomes smaller than the secnd. Indeed, by having λ_{100} equal to λ_{111}, one may eliminate altogether the variation caused by the third term in expression (1). The result would be a uniaxial anisotropy parallel to the boundary and having equal magnitude for any boundary orientation. However, it may only be necessary to have λ_{111} and λ_{100} of the same sign in order that charged walls suitable for bubble propagation will form.

CONCLUSION

The domain structure exhibited by this (100) film provides direct experimental evidence for the models of Hidaka and Matsutera [2]; Backerra, De Roode, and Enz [3]; and Hubert[4], in which the stress-induced anisotropies of an implanted/unimplanted boundary allow the formation of strongly charged walls. The domain configurations around an implanted disk demonstrate that the stress relief at the boundary is the dominant effect, even more so than demagnetizing effects, and that charged walls form only where there is a stress-induced uniaxial anisotropy with

an easy axis parallel to the boundary. A (100) film having $\lambda_{100}, \lambda_{111}$ and σ all of the same sign will have a stress-induced easy axis parallel to the boundary for any boundary orientation and, hence, should be able to support charged walls suitable for bubble propagation. Additionally, similar to Hubert's findings in (111) films, if $\lambda_{100} = \lambda_{111}$, the effect on the charged wall of the fourfold symmetry due to the (100) orientation should be largely eliminated, and charged walls would propagate isotropically around a disk.

REFERENCES

a) The authors are with the Electrical Engineering Department,
    Carnegie Mellon University, Pittsburgh, PA 15213.
b) This work was supported by the National Science Foundation under
    Grant ECS-7912677 and by the IBM Corporation.

1. D. A. Saunders, M. H. Kryder, and T. J. Gallagher, *Charged Walls in a Fourfold Symmetric (100) Garnet Film,* IEEE Trans. Magnet. Mag - 16, 955 (1980).

2. Y. Hidaka and H. Matsutera, *Charged Wall Formation Mechanism in Ion-Implanted Contiguous Disk Bubble Devices,* Applied Physics Letters, 39, 116 (1981).

3. S. C. M. Backerra, W. H. De Roode and U. Enz., *The Influence of Implantation-Induced Stress Gradients in Magnetic Bubble Layers,* Philips J. of Res., 36, 112 (1981).

4. A. Hubert, *The Role of Cubic Magnetostrictive Ansisotropy in Ion-Implanted Garnets used for Magnetic Bubble Devices,* to be published.

5. S. Chikazumi, S. H. Charap, Physics of Magnetism, Chapter 8, p. 183, Huntington, New York: Robert E. Krieger Publishing Co.

6. K. Komenou, I. Hirai, K. Asama, and M. Sakai., *Crystalline and Magnetic Properties of an Ion-Implanted Layer in Bubble Garnet Films,* J. Appl. Phys., 49, 5816 (1978).

7. A. H. Eschenfelder, Magnetic Bubble Technology, Chapter 6.2.1, Springer-Verlag, New York, 1980.

8. Y. S. Lin, D. B. Dove, S. Schwarzl, and C. C Shir, *Charged Wall Behavior in 1-μm Bubble Implanted Structures,* IEEE Trans. Magnet., MAG-14, 494 (1978).
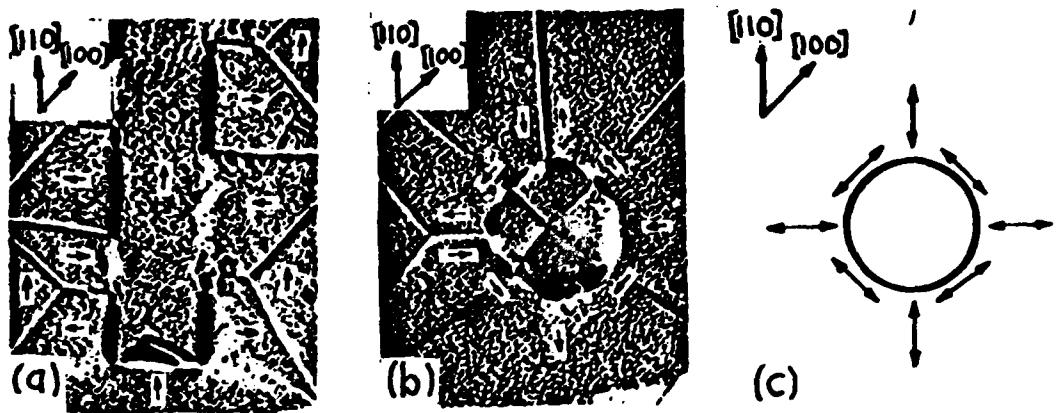
FIGURE 1

FIGURE 11

FIELD   FIELD
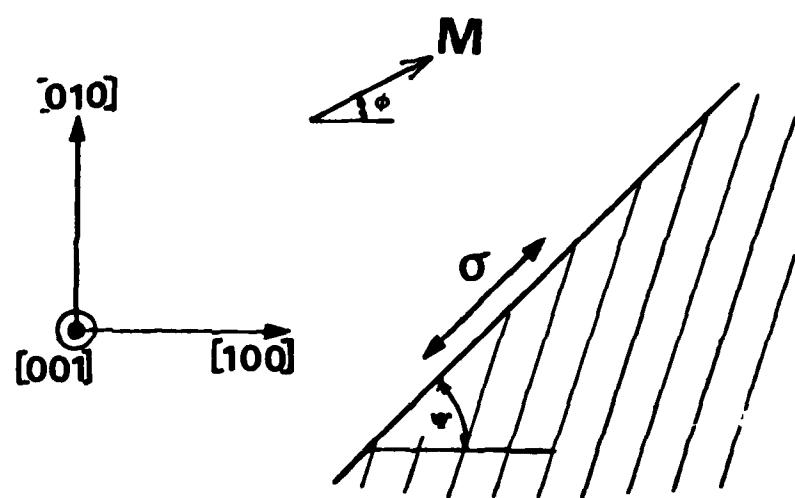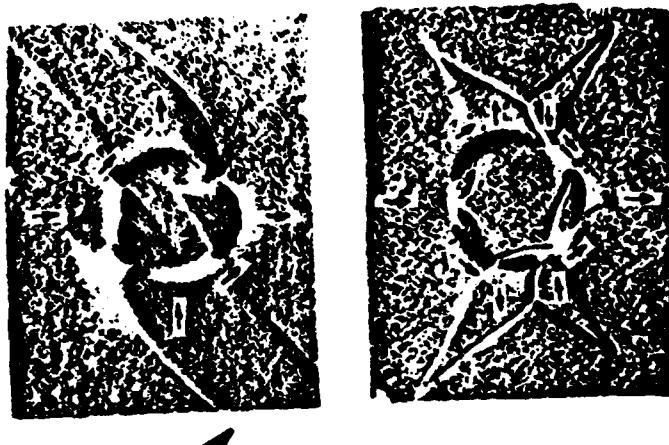
(A)   (B)

FIGURE 1 1 1

THE FABRICATION OF DUAL CONDUCTOR CURRENT
ACCESS MAGNETIC BUBBLE DEVICES

M.S. Thesis
Department of Electrical Engineering
Carnegie-Mellon University

April 1981

Michael J. Alex

ABSTRACT

A procedure for fabricating dual conductor current access magnetic bubble devices is established. These devices, which consist of overlapping apertures in a pair of conducting sheets separated by a dielectric, have 2 micron minimum features that are defined by a wet chemical etch process which yields vertical sidewalls. RF sputtered SiO_2 is used to isolate the two aluminum current sheets, where good step coverage of the aperture sidewalls is obtained by sputtering with no bias applied to the substrate. Due to argon ion bombardment of the growing step when bias voltages are applied to the substrate, step coverage is seen to deteriorate; these results are verified through the use of scanning electron microscopy. Wet chemical etching of thin (1500 - 2500 angstrom) evaporated aluminum films is a suitable means of etching fine (2 micron) features using patterns delineated by standard contact print photolithography. In the first dual conductor devices, plasma etched apertures were covered with a plasma deposited SiO_2 dielectric.[2] Compared to the processes used by Bobeck et. al.[2], the methods of aperture delineation and insulator deposition performed by chemical etching and RF sputtering, respectively, are seen to be more easily implemented while excellent pattern definition and good step coverage are obtained.

i

TABLE OF CONTENTS

iii

LIST OF FIGURES

LIST OF TABLES

CHAPTER 1

INTRODUCTION AND THEORY OF OPERATION

1.1 Magnetic Bubbles

A bubble is a small region of magnetization in a thin magnetic platelet with its direction of magnetization antiparallel to the direction of magnetization of the platelet. When viewed with a polarizing microscope the cylindrical domains appear as dark (light) circular islands in a light (dark) sea. (By adjustment of a polarizing filter the bubbles can be made to appear dark or light.)

Fig. 1-1 depicts the formation of bubbles in a thin film of single crystal magnetic material.[1] With no external magnetic field applied, the direction of magnetization in the film is perpendicular to the plane of the film; the domains are serpentine and occupy equal areas of opposite magnetization. This domain configuration is such that the magnetic energy of the film is minimized (Fig. 1-1). When a small bias field is applied perpendicular to the plane of the wafer, the domains whose polarities are opposite to that of the bias field shrink (Fig. 1-1b). Increasing the bias field further causes shrinkage of the domains into cylindrical configurations called bubbles (Fig. 1-1c).

Typically, bubble films are grown by a technique called Liquid Phase Epitaxy (LPE). In this method of film growth, a 10 - 20 mil. thick substrate of Gadolinium Gallium Garnet (GGG) is dipped into a molten flux of lead oxide containing constituents of the film one wishes to grow. The substrate can be rotated during film growth, enhancing compositional and thickness uniformity. The film growth rate is a strong function of temperature; typical films are one to three microns in thickness.

Physical and magnetic properties of the epitaxially grown films can be tailored by the melt composition. For most bubble devices some desireable characteristics are:

1. High bubble domain mobility

2. Small bubbles for high storage densities
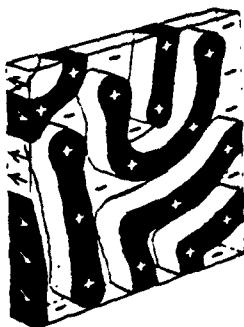
(a) No applied field
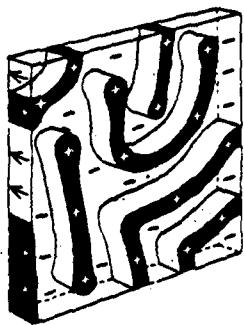
(b) Small applied field
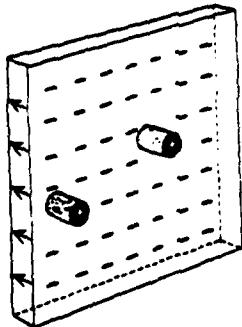
(c) Larger applied field

Figure 1-1: The formation of bubbles under the influence of an externally applied bias field

After Bobeck et. al.[1]

3. A low number of film defects

4. Temperature stability over a wide temperature range

5. Perpendicular uniaxial anisotropy

The last property is a requirement for the existence of serpentine domains at zero and low bias fields and the existence of bubbles at higher bias fields.

1.2 Field Access Devices

Bubbles may be moved about in the plane of the film by a magnetic field gradient. Several schemes are employed to create this magnetic field gradient, or drive field. The most familiar method employs perm..lloy (NiFe) patterns that are deposited on the film surface. A field in the film plane is used to orient the magnetization in the permalloy patterns and the bubble is attracted to the portion of the permalloy which has the opposite polarity. This situation is depicted in Fig.1-2.[2] By proper configuration of the permalloy patterns and the use of a rotating in-plane field, bubbles may be propagated. Devices that employ a rotating in-plane field to produce bubble motion are known as field access devices.

Another type of field access device utilizes ion-implantation to create the propagation structure. These types of devices are called contiguous disc or ion-implanted devices. They are fabricated as follows (refer to Fig. 1-3): An epitaxial film with magnetic anisotropy perpendicular to the film plane is masked in certain areas using photoresist, gold etc. After ion-implantation, the stress induced in the implanted areas causes the magnetization there to lie in the plane of the film whilst the magnetization in the masked areas remains perpendicular to the plane of the film. Under the influence of an in-plane field, the in-plane magnetization is oriented in the same direction as the externally applied in-plane field. However, at the implanted/unimplanted boundary, the magnetization is forced to diverge, causing the formation of "charged walls", one positive (converging) and one negative (diverging). As the in-plane field is rotated, the in-plane magnetization and charged walls also rotate. Since the charged walls provide flux closure, bubbles will couple to them and rotate along with the drive field. As with permalloy devices, judicious selection of the ion-implantation mask will allow the fabrication of a bubble propagation pattern.

In-plane field

Bias field

Bias field

In-plane field
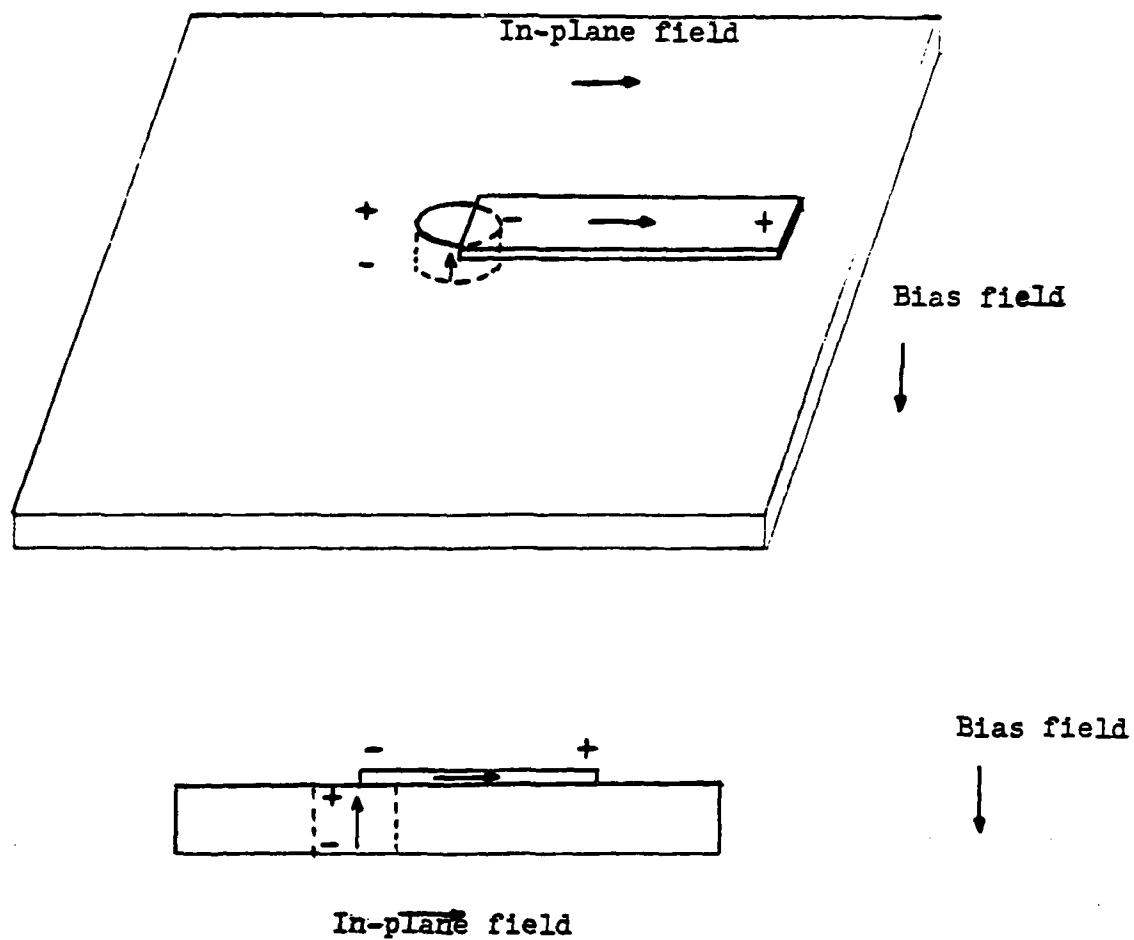
Figure 1-2: Bubble being attracted to permalloy bar immersed in external
field

Adopted from Chang[3]
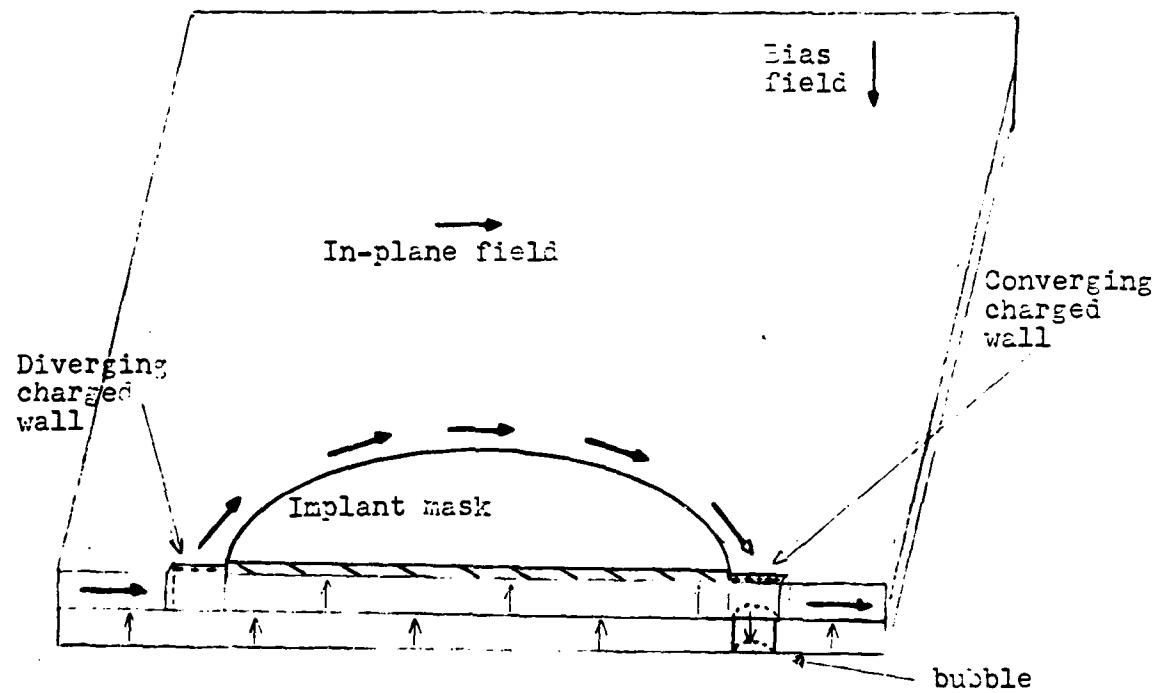
Figure 1-3: Bubble coupled to charged wall formed around unimplanted disc

1.3 Current Access Devices

In current access devices, a field gradient is provided by a conductor on top of the bubble film. It is interesting to note that the first bubble devices were of this type.[3,4] Current loops and meandering conductors in conjunction with etched grooves or ferrite patterns on the film surface were used to propagate bubbles.

In 1974 Walsh and Charap suggested that a perforated conducting sheet and a rotating current could be used to drive bubbles.[5] In 1979 Bobeck et. al.[6] proposed using two overlapping apertures in a pair of parallel conducting sheets; a bipolar current in each sheet provided the drive field gradient needed for bubble propagation. It is this dual conductor current access device that this thesis describes in detail.

1.4 Dual Conductor Current Access Devices

1.4.1 The Permalloy/Conductor Analogy

Before discussing the dual conductor device, it will be helpful at this point to compare the aforementioned permalloy device structure and the propagation structure of the current access device of this study: the aperture.

In Fig. 1-4 is shown a permalloy bar in an in-plane field as well as an aperture in a current carrying conductor sheet. The figure also depicts a bubble in a rest position in each of these structures. Note that in the aperture sheet device the magnetic field lines are obtained simply from the right hand rule. If the current is reversed, the opposite end of the aperture becomes attractive and the bubble is repelled from its previous position of rest.

1.5 The Dual Conductor Device

1.5.1 Normal Propagation

We may extend the concept of the aperture described in Fig. 1-4 by using two conductor sheets, separated by an insulator, having overlapping apertures as shown in Fig. 1-5.[6] The cross-hatched aperture is in the first conducting sheet, nearest the epitaxial film, while the open aperture is in the top conductor; this notation will be used throughout the thesis to describe the aperture levels.
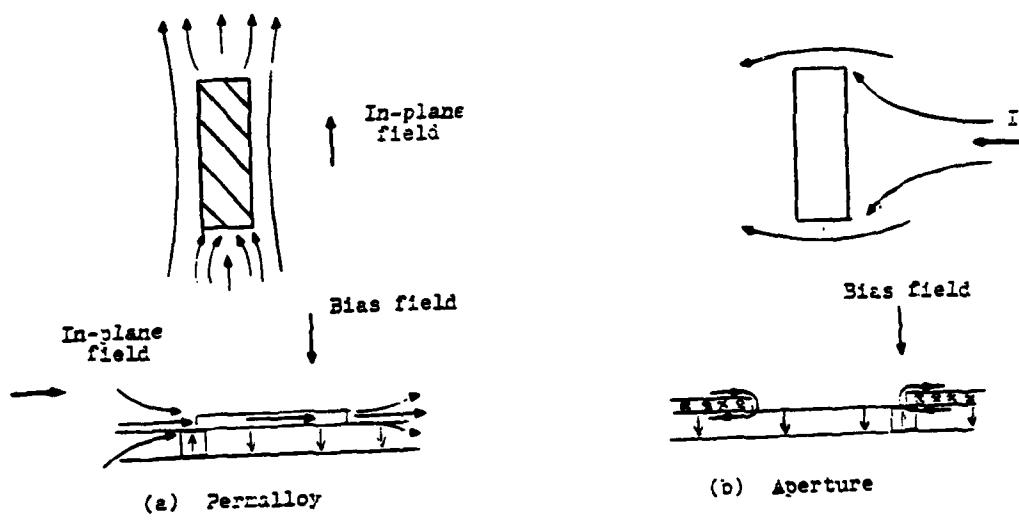
Figure 1-4: Permalloy/Conductor Analogy

Adopted from Bobeck et. al.[2]

Also seen in this figure are numbered rest positions and the currents necessary to create these positions on the ends of the apertures. Cross-hatched currents I_1 and I_3 flow through the first level conductor whilst currents I_2 and I_4 flow through the top conducting sheet. By pulsing currents I_1 through I_4 in sequence, a bubble will propagate from position 1 to position 4, the propagation direction being normal to the direction of current flow. In essence, Fig. 1-5 depicts a one step bubble shift register. By connecting pairs of apertures, a longer propagation track is made. With a circuit period λ, the length of each aperture is 0.5λ with 0.25λ being the overlap length. In this study, apertures of dimension $0.5\lambda \times 0.3\lambda$ were used with $\lambda = 8$ microns. Fig. 1-6 shows the operation of a shift register and the current sequences necessary for successful operation.[6] Reversal of the current sequences will return the bubble to its original position. In Fig. 1-7 is seen the current pulse sequence used by Bobeck et. al.[6] to drive bubbles in the dual conductor shift register. Pulse overlap insures smooth propagation as well as quantizing the propagation field.

1.5.2 Parallel Propagation

Bubbles may be propagated parallel to the direction of current flow as seen in Fig. 1-8.[6] The apertures are staggered so as to maintain a uniform current density along the length of the propagation path. The apertures are also lengthened to prevent bubbles from jumping to adjacent attractive poles that aren't on the propagation path. Attractive pole positions are numbered according to the currents needed to create these attractive poles.

1.5.3 Stretching and Sensing

Fig. 1-9 shows the stretcher design of Bobeck et. al.[6] used in their dual conductor devices. As the bubble propagates upwards, it first stretches along the length of the elongated apertures under the influence of the magnetic field due to the diverging current, then contracts as the apertures are reduced in length. A permalloy sense element may be deposited and used to detect bubbles as in the field access devices, but this would require a permalloy processing level. In their paper, Bobeck et. al.[6] give sense signals obtained by using RF detection with the expander of Fig. 1-9 used to stretch the bubble. (In RF detection, a conductor loop senses the change in a strip's flux when driven by an RF field.)
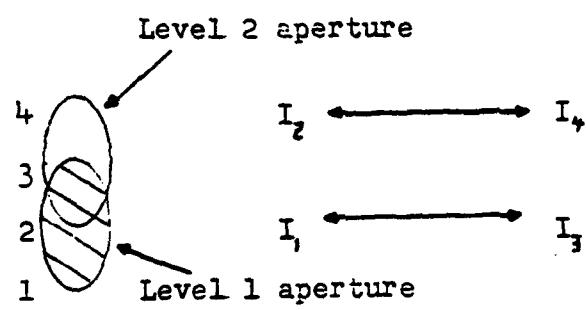
Figure 1-5: Overlapping Apertures in Parallel Conducting Sheets
From Bobeck et. al.[2]
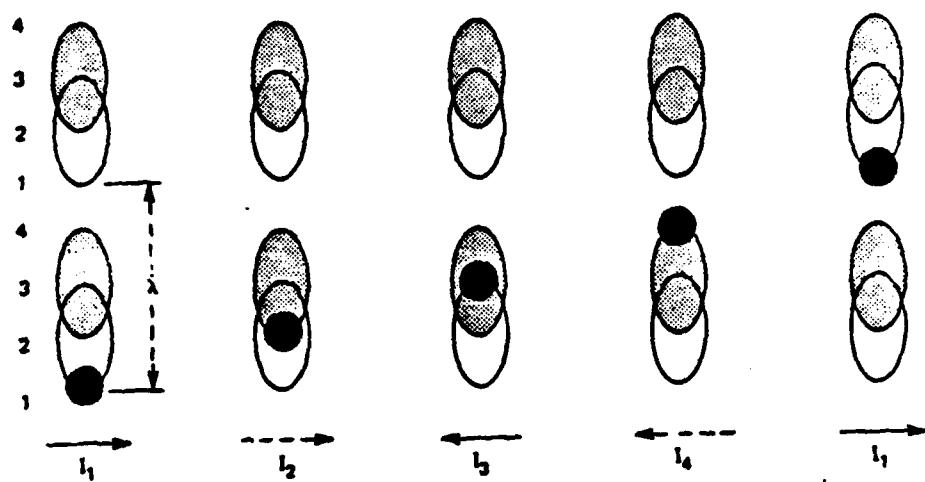
Figure 1-6: Normal Propagation in The Dual Conductor Device
From Bobeck et. al.[2]
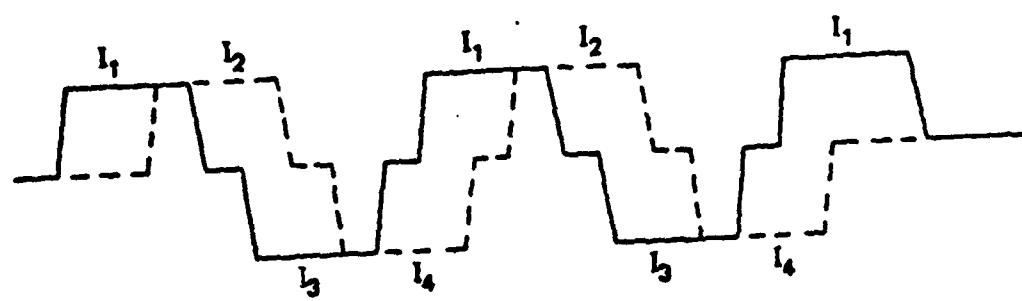
Figure 1-7: Current Pulse Sequence for Propagation
From Bobeck et. al.[2]
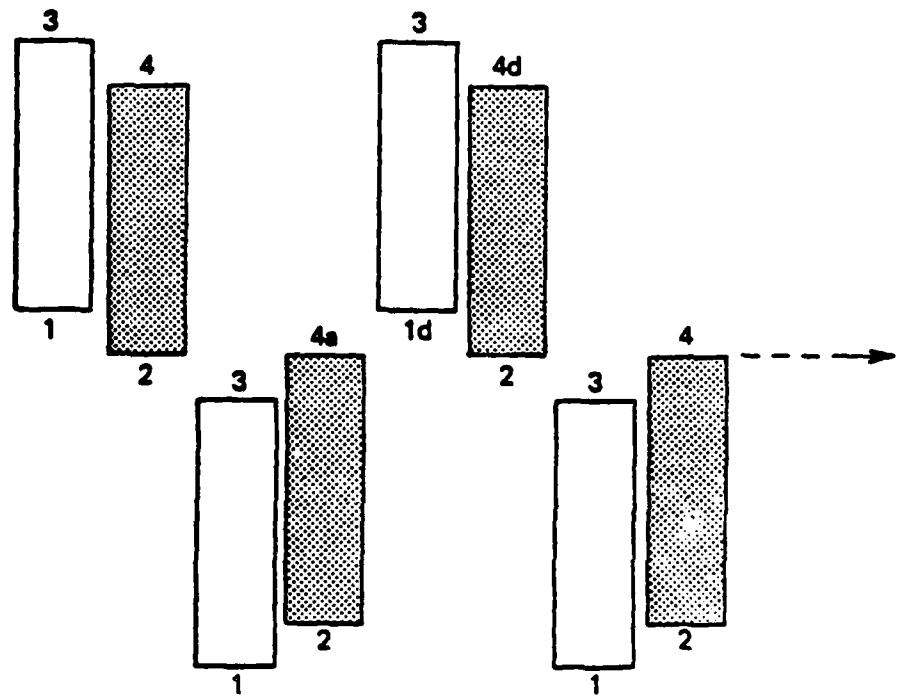
Figure 1-8: Parallel Propagation in the Dual Conductor Device
From Bobeck et. al.[2]
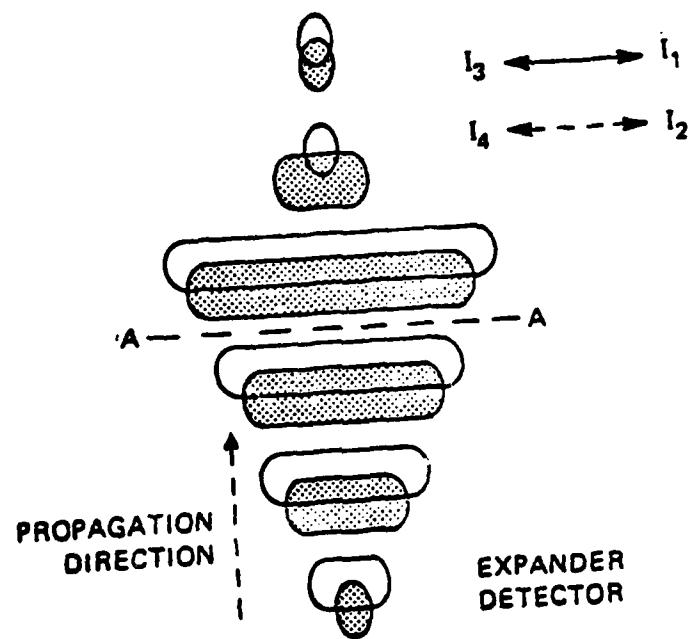
Figure 1-9: Current Access Device Stretcher
From Bobeck et. al.[2]

1.5.4 Nucleation

Bobeck et. al. designed a bubble generator that was patterned in the bottom conductor level.[6] This design eliminated an extra processing step and minimized nucleation current. It is depicted in Fig. 1-10.[6] Current is funnelled into the generator by slots #2 and #4. Because of the high resistance formed by slots #1, #3 and #4, nucleate current I_f concentrates at the tip of slot #2 as shown, creating a bubble. Note that the bubble is on a propagation path and may be readily shuttled out of the generator after nucleation.

1.5.5 Transfer

Bobeck et. al.[6] implemented bubble transfer without adding a third conductor level by using nested apertures in conjunction with a modified propagating pulse sequence. Such a transfer gate is seen in Fig. 1-11.[6] In the figure, the numbered locations designate the current pulse sequences needed to attract bubbles to these positions. Also given are two pulse sequences. The 12341234 sequence propagates bubbles in clockwise fashion around the minor loop, while the 123412141234 sequence transfers out a bubble that is at position 1a at the beginning of the transfer sequence.
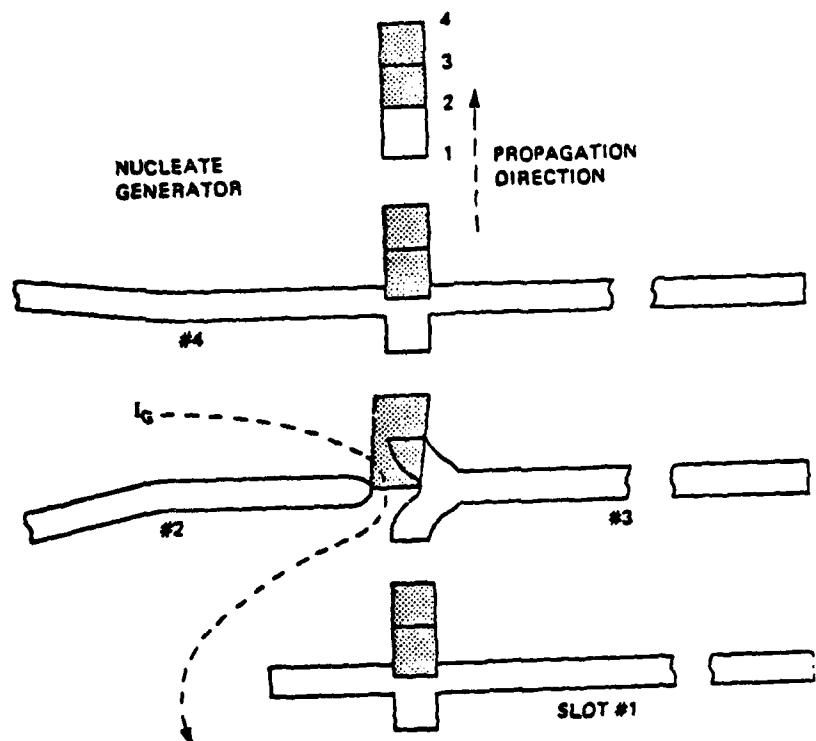
Figure 1-10: Current Access Device Nucleator

From Bobeck et. al.[2]
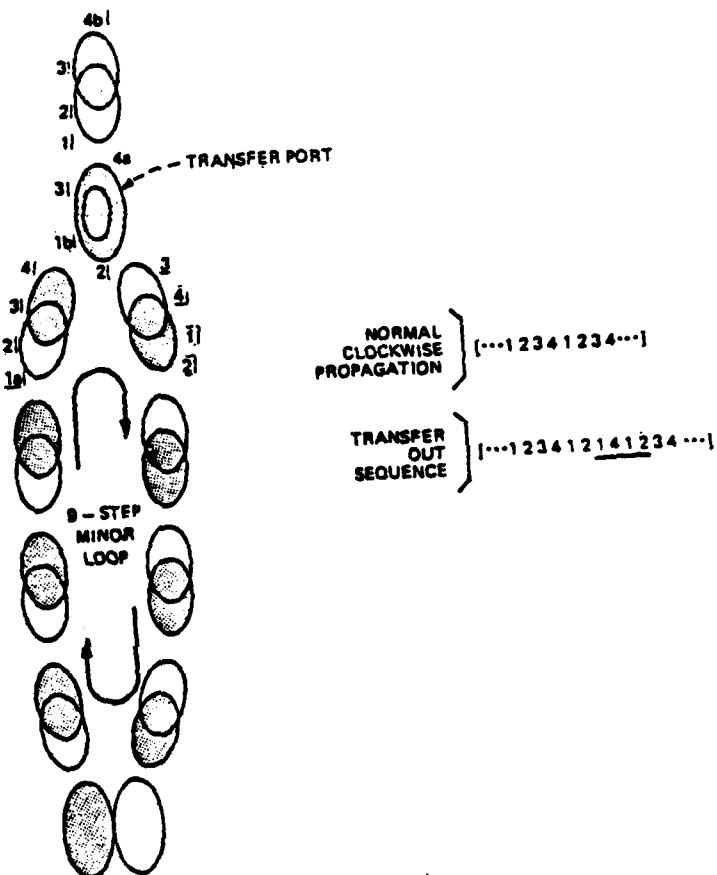
Figure 1-11: Dual Conductor Transfer Gate
From Bobeck et. al.[2]

CHAPTER 2
THEORY OF DEVICE PROCESSING

In this section will be discussed the various processes utilized in the fabrication of the dual conductor current access device as described by Bobeck et. al.[6] Some alternate methods which can be used in the fabrication procedure will also be discussed.

2.1 Conductors

The conducting sheets may consist of aluminum, gold, AlCu or some other highly conductive metal. Gold is the best choice from a reliability standpoint due to its low electromigration rates.[7] However, one important criteria for conductor selection is the method and ease of patterning. Au sputter etches readily but small features may not chemically etch reproducibly due to excessive undercutting.[8] Al is not undercut as severely by the isotropic etch process and so small features may be chemically etched in it.[9] Also, the sloped edges usually obtained by chemically etching aluminum are desireable in non-planar processing since step coverage is enhanced.[10] In their current access devices, Bobeck et. al.[6] used evaporated AlCu for the conducting sheets; the apertures were patterned using RF plasma etching which yielded vertical sidewalls.

All the above conductors may be deposited by a variety of techniques. All may be sputteped or evaporated; the lowest temperature technique is preferred to avoid the buildup of stress which may be deleterious to bubble propagation.[11] If gold is to be used, it is first necessary to deposit a few hundred angstroms of an adhesion base such as Cr or TiW.[12]

18

2.2 Insulators

The most commonly used insulator in device processing is probably SiO_2 and it may be deposited by a number of techniques, the most common being rf sputtering or Chemical Vapor Deposition-CVD. No matter how it is deposited the SiO_2 must have high dielectric strength and be relatively free of pinholes. A necessary requirement of the insulator between the two conducting sheets is that it must provide a conformal coating of steps to eliminate shorting between the conductors. Plasma deposition of SiO_2 was used to conformally coat the vertical sidewalls in the first dual conducting devices.[6]

A common method of relieving conductor stress is the deposition of an SiO_2 prespacer at the outset of processing.[13] This thin layer also protects the epitaxial film from subsequent etching and processing. Since the film is planar, it is not critical how the prespacer is applied if one is even used at all.

2.3 Pattern Delineation

The conducting sheet patterns can be defined by contact print photolithography, which was done in the first dual conductor devices.[6] In this technique, photoresist is spun on the film to be etched, exposed to UV light through a 1:1 mask in intimate contact with the photoresist and developed. This leaves a photoresist mask through which etching may be done to define a pattern in the film. After etching, the photoresist is removed chemically or by reaction in an O_2 plasma.

Contact printing, where the mask is held against the substrate by vacuum, is used to minimize aberration. Since the exposure light source is divergent, any gap between the resist and the mask will allow undesireable spreading of the exposed region, causing pattern distortion. The gap and distortion are minimized by holding the mask and substrate in intimate contact during exposure.

Another common method of pattern delineation is projection printing. In this technique, an intermediate transparency of the pattern is projected onto the resist-coated substrate. Usually, the intermediate transparency (mask) is larger than the final size pattern by as much as 10X. Since the mask does not physically contact the resist coated substrate in projection printing, pattern defects are minimized and mask life is extended indefinitely.

Projection printing does have its drawbacks however. To obtain the highest possible line resolution, lenses for projection exposure must be designed to yield minimum

aberrations so that their performance is diffraction limited. This requires the use of monochromatic light and lenses which are corrected for the particular wavelength chosen. If very high resolution is desired, field size has to be sacrificed. Lenses capable of resolving 1 micron wide or narrower lines have depths of focus of 1 micron or less. This requires that the substrate be flat within 1 micron or better and the resist coat be uniform and less than 1 micron thick. Finally, the most serious problem in producing fine patterns occurs because of interference effects. Reflections of the monochromatic light at the resist/air, resist/substrate interfaces produce light intensity variations in the resist, causing nonuniform exposure of the resist and subsequent pattern distortion.[14]

The most common methods for etching thin films are wet chemical etching, rf sputter etching or reactive ion etching. During sputter etching, the sample to be etched is bombarded by ionized Ar atoms and the film area which is not protected with photoresist is etched due to the momentum transfer of the impinging ions. Photoresist removal is difficult after sputter etching due to the cross linking of the resist that occurs at the elevated temperatures reached by the sample during the etching process. Reactive ion etching is similar to sputter etching except for the gas species used in the process. In plasma etching the working gas reacts chemically with the material to be etched. This allows for high etch selectivity depending upon the gas used and the material being etched.

Dry etching techniques such as plasma and sputter etching are preferred over wet chemical etching because of the good controlability of the dry processing parameters which result in minimal dimensional variation in etched patterns. As mentioned previously, Bobeck et. al.[6] used plasma etching to etch apertures in their AlCu films and reported minimal dimensional variations in their patterns.[6] In their radial RF system, aluminum was reacted with a chlorine plasma.

2.4 The Device Structure

In this section will be discussed the step-by-step procedure Bobeck et. al.[6] used to fabricate their dual conductor devices. Diagrams of the device structure cross-section are shown for each of the processing steps.

a) Sputtered directly upon the epitaxial film is the aforementioned SiO_2 stress absorbing layer which also protects the film surface during processing. This prespacer is on the order of a few hundred angstroms in thickness. Afterwards, the first conducting layer of AlCu is deposited by evaporation. This first layer is approximately 1500 angstroms thick. At this point the device appears similar to the one seen in Fig. 2-1a.

20
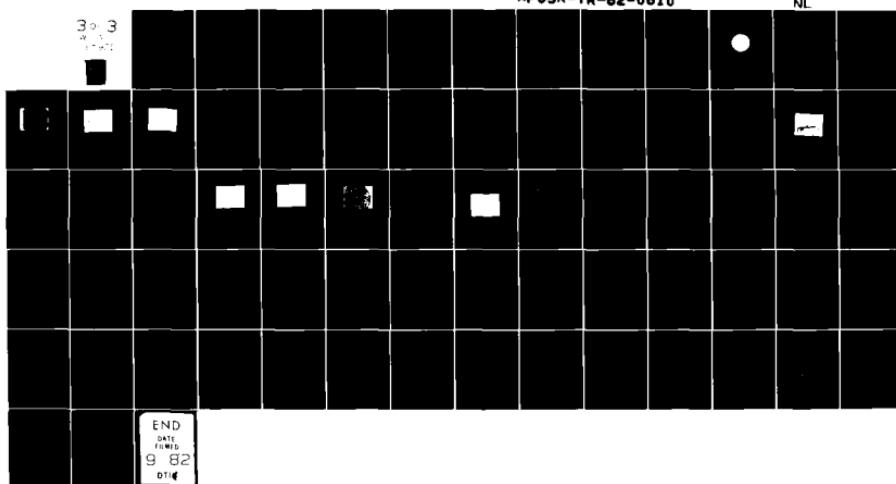
b) After spinning on photoresist, exposing it through the first level mask and developing it, we have the structure seen in Fig. 2-1b.

c) The device is now etched in a chlorine plasma. It is necessary to remove all the AlCu in the apertures without undercutting the photoresist which would result in deformed patterns. After etching the apertures, the photoresist is stripped away with solvents or oxygen plasma, resulting in the device seen in Fig. 2-1c. The first conducting sheet has now been completed.

d) The next step is probably the most critical: the deposition of the insulator between the two conducting sheets. The sidewalls of the apertures must be coated to prevent shorting of the conductors. The dielectric used in the first devices was plasma deposited SiO_2, which conformally coated the vertical aperture walls. Fig. 2-1d shows the device after deposition of the insulator which is about 1500 angstroms thick.

e) Now, the steps used to construct the first conducting sheet are merely repeated. A 2500 angstrom thick AlCu film is deposited, photoresist is applied and exposed through the precisely aligned second level mask and the apertures are defined. After etching the conductor and stripping of the photoresist as described above, the device structure is complete. These processes are seen in Figs. 2-1e and 2-1f.

aluminum →   ← silicon dioxide

Epitaxial layer →

GGG

(a)

photoresist →

aluminum →   silicon dioxide ←

Epitaxial layer

GGG

(b)

silicon dioxide

aluminum →

GGG

Epitaxial layer

(c)
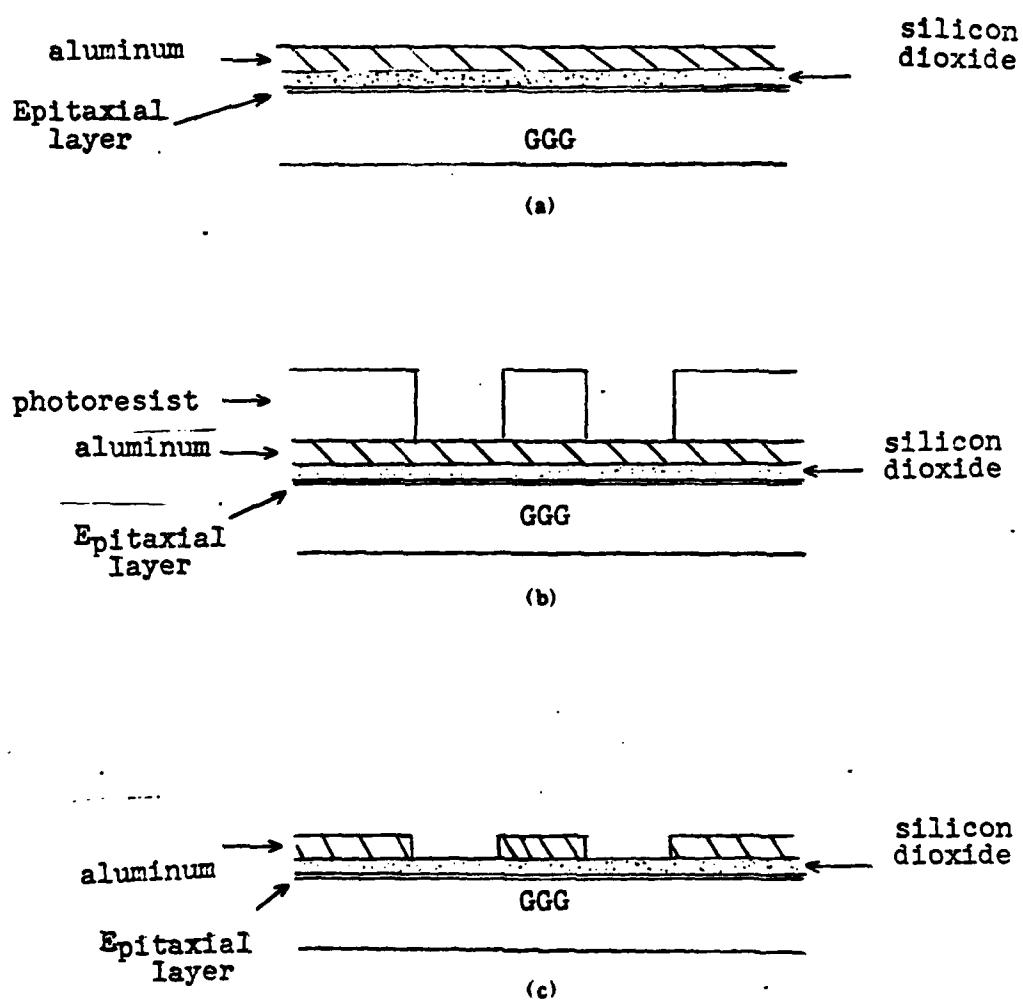
Figure 2-1: Processing the *Dual Conductor Device*

aluminum → ... ← silicon dioxide

GGG

Epitaxial layer

(d)

photoresist →

aluminum →

silicon dioxide ←

Epitaxial layer

GGG

(e)

aluminum →

silicon dioxide ←

Epitaxial layer

GGG

(f)
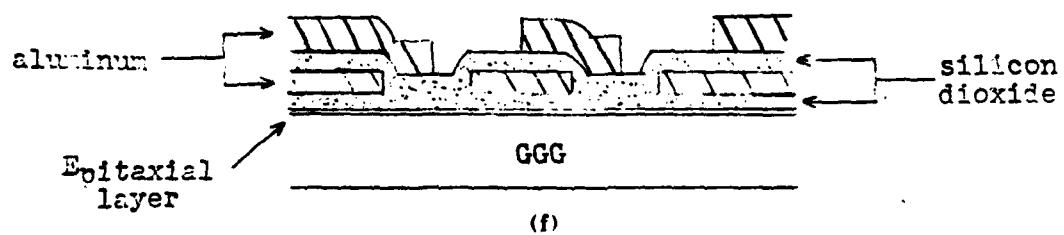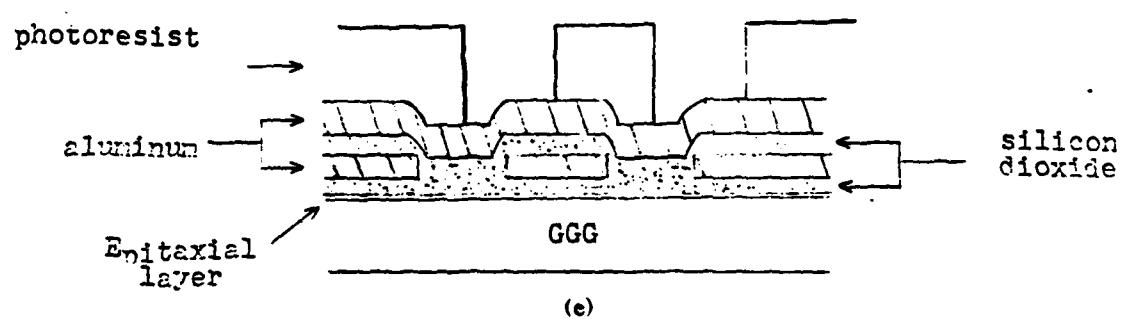
Figure 2-1, continued

CHAPTER 3
EXPERIMENTAL DEVICE PROCESSING

In this section the experimental details of the fabrication of the dual conductor device as performed at Carnegie-Mellon University will be described and presented. First, the calibration of the various systems will be described and finally the step-by-step fabrication procedure of the device will be given with the results shown when possible.

3.1 Conductors

In this project the conducting sheets consist of evaporated aluminum. Films were deposited using a Veeco-400 resistive heating evaporator.[15] A general configuration of the system is depicted in Fig. 3-1. Al staples, precleaned in a mild acetic acid solution. are draped over the tungsten filament and the system is evacuated to roughly 2×10^{-7} torr. The substrates. suspended face down over the filament. are protected from contamination by a manually controlled shutter, which is opened after the staples have melted and wet the filament. Typical current used was 70 amperes for 30-60 sec.· yielding films in the 1500-2500 angstrom range. The evaporated film thickness was monitored through use of a Sloan DTM-3 thickness monitor.[16] This instrument utilizes a quartz crystal oscillator and the piezoelectric properties of quartz to monitor evaporated mass deposition upon the thin quartz crystal wafer. The change in frequency caused by an evaporated deposit on the quartz crystal is read directly from a frequency meter, and is directly proportional to the deposit thickness.

The system was calibrated by depositing several Al films over a wide range of frequencies and by measuring the thickness using a Sloan Dektak[16], yielding a plot of frequency versus thickness as seen in Fig. 3-2.

to frequency
meter

Thickness
Monitor

Substrates
(face down)

Shutter
Access

Filament
Current

Tungsten filament draped
with aluminum staples
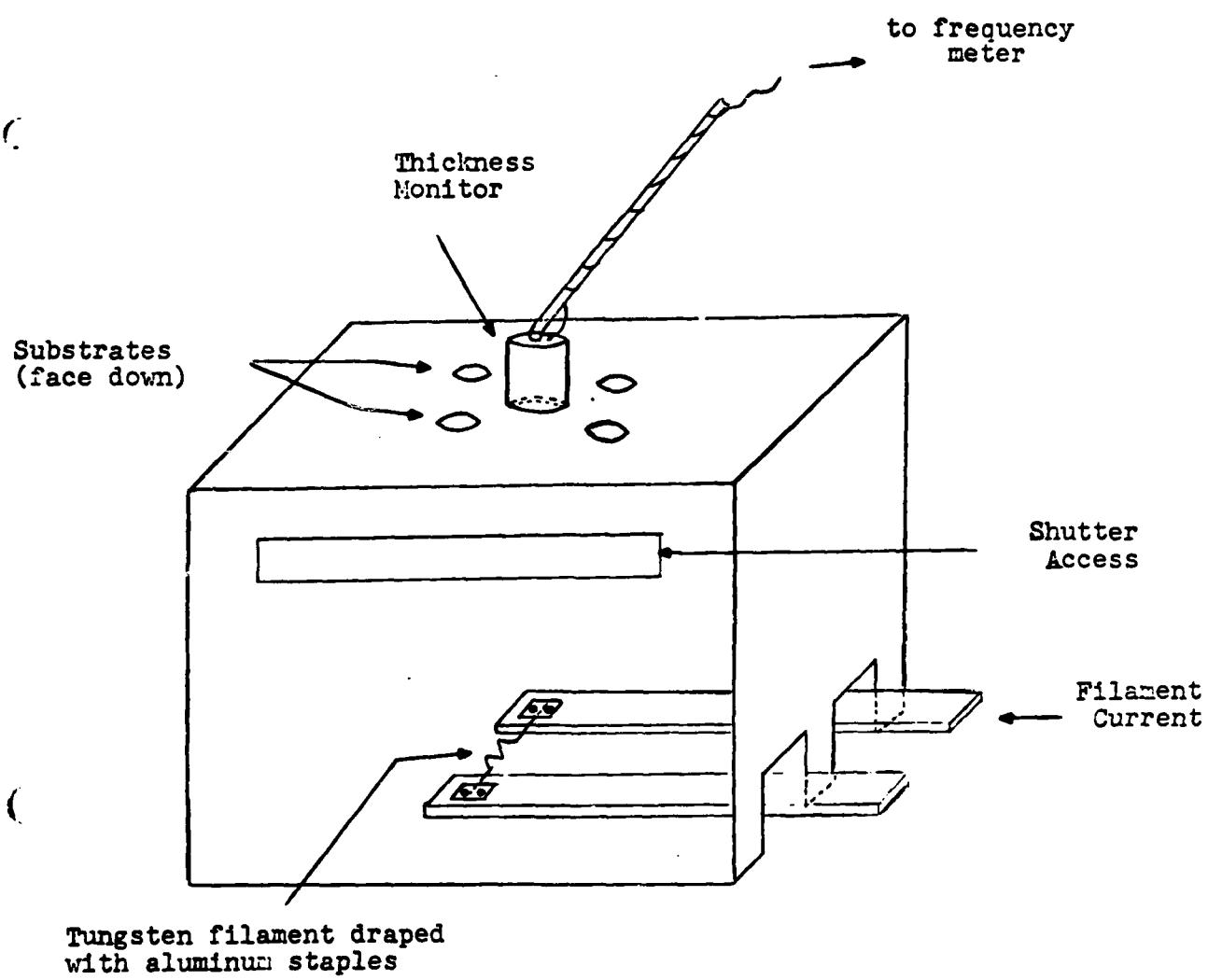
Figure 3-1: Configuration of Al Evaporation Substrate Assembly
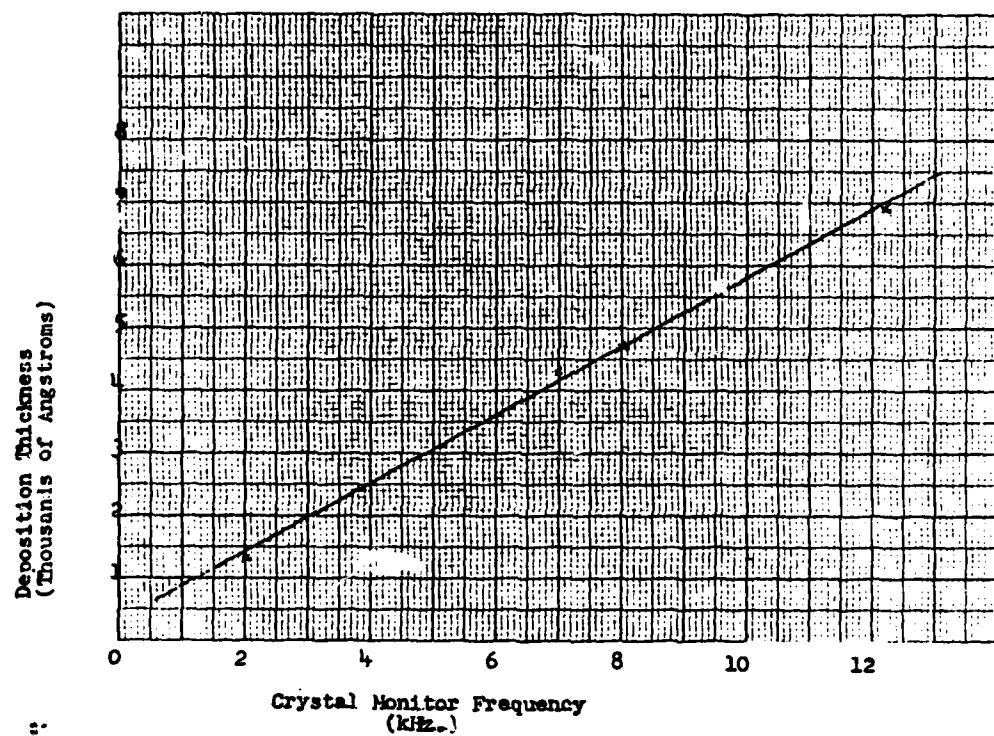
Figure 3-2: Evaporated Al Thickness Versus Monitor Frequency

3.2 Insulators

Sputtered SiO_2 was used as the insulating material in this work. The SiO_2 was deposited in a Perkin Elmer 6-J RF sputtering system using argon as the working gas.[17] The deposition rate was determined by sputtering SiO_2 onto Si wafers, etching a stripe in the oxide across the diameter of the wafer with buffered HF and using a Sloan Dektak to ascertain the film thickness. Recording the deposition time yielded the sputtering rate. The deposition rate for bias sputtered SiO_2 as found by this worker is given in Fig. 3-3 along with the important system parameters.

A device structure was devised to ascertain the optimum bias sputtering voltage. It is fabricated as follows (see Fig. 3-4): 5,000 angstroms of aluminum are evaporated on a glass wafer, and apertures are etched to a depth of 1500 angstroms, as in the final device. The reason for such a thick base layer is so that electrical contact can be made easily. After the pattern is etched and the photoresist is removed, SiO_2 is sputtered on the film at the desired bias voltage. Next, Al is evaporated over the SiO_2 to form a capacitor like structure and the resistance between the sheets is measured to ascertain the presence of shorts or electrical isolation.

Fig. 3-5 is a photograph of a glass wafer with a number of the devices depicted in Fig. 3-4 on it. Each top electrode is 2000 x 2000 microns of 3500 angstrom thick aluminum; a micromanipulator probe was used to make contact to these electrodes. The resistance between the large base electrode (at the top of the picture) and each top electrode was measured with a digital ohmmeter.

Test structures were built for SiO_2 sputtered at 0, -25, -50 and -75 volts bias and the results are tabulated in Table 3-1, with the Electrode/SiO_2 Resistance being the figure-of-merit for the insulator. The SiO_2 thickness for these samples ranged between 1,840 to 2,375 angstroms. Both probes were also placed on the bottom electrode to find out the probe/contact resistance; this value is called Probe Resistance in the table. Also, with one probe on the bottom electrode the other probe was placed directly on the SiO_2 layer to make sure the probe was not punching through the dielectric when the Electrode/SiO_2 Resistance measurements were being made. This is seen as SiO_2/Probe Resistance in Table 3-1. Fig. 3-6 shows a plot of Log (Electrode/SiO_2 Resistance) as a function of the bias sputtering voltage.

From the data shown it appears that the best step coverage is obtained when SiO_2 is sputtered at 0 bias voltage. This is also seen from the scanning electron micrographs of
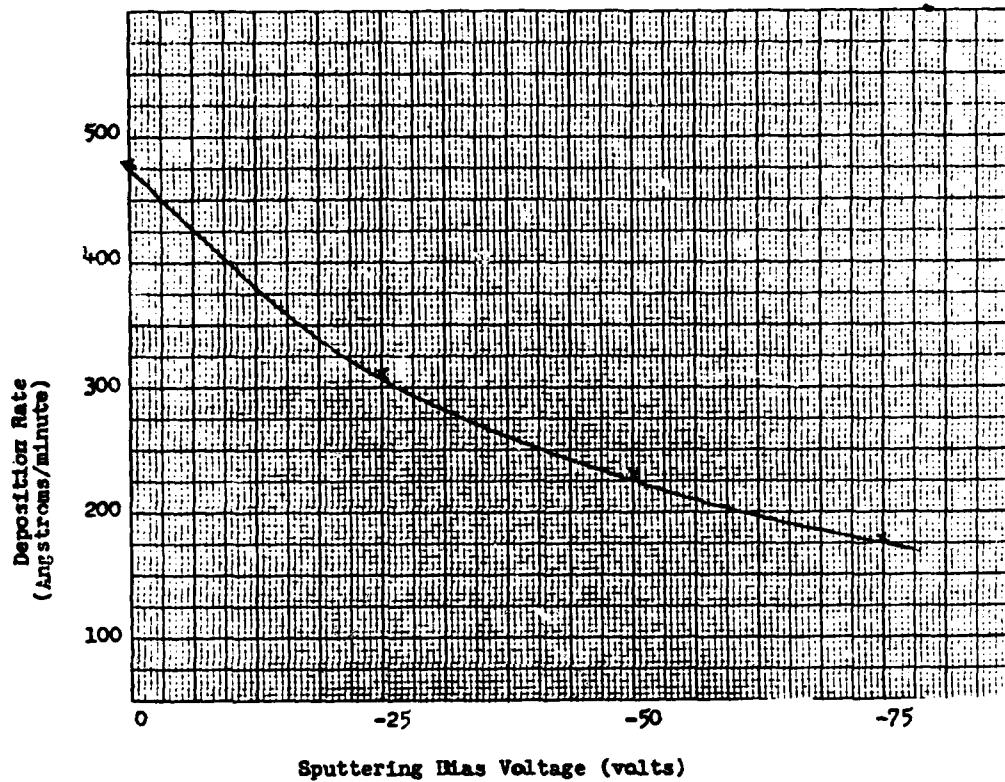
Figure 3-3: SiO$_2$ Sputtering Rate as a Function of Bias Voltage
R.F. power: 250 watts; Ar pressure: 10 mt.
Target/substrate spacing: 1.25 inches.

aluminum

aluminum

silicon
dioxide

glass
substrate
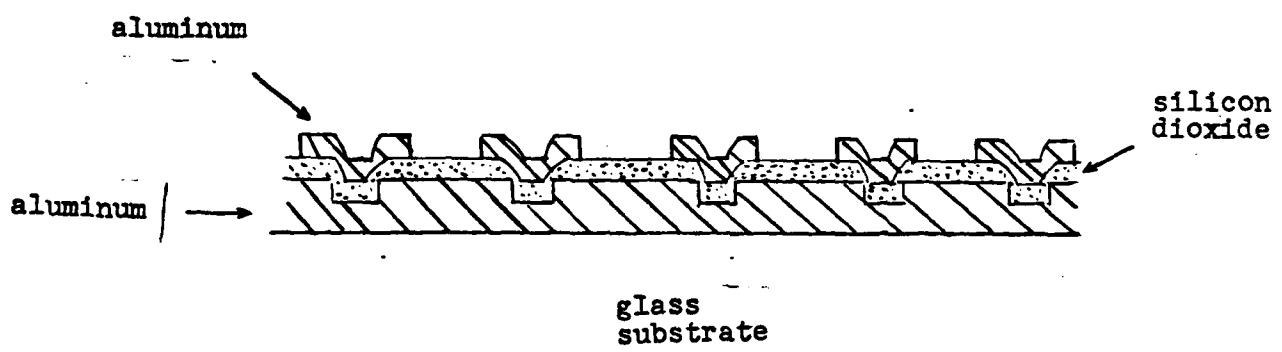
Figure 3-4: Structure used to optimize bias sputtering voltage

Figure 3-5: Photograph of bias sputtering test structure

Table 3-1: Ascertaining the optimum bias sputtering voltage.

Bias Voltage Volts	Electrode/SiO Resistance (avg. of 20 readings)	Probe Resistance	SiO /Probe Resistance
0	15.6 megΩ *	8.7 Ω	20 megΩ
-25	2.84 megΩ	5.8 Ω	20 megΩ
-50	329 Ω	4.4 Ω	20 megΩ
-75	42.7 Ω	9.2 Ω	14 megΩ

* 14 of the 20 readings were greater than 20 megΩ,
  which was the maximum the meter could read.

Fig. 3-7 which show SiO_2 sputtered at various bias voltages on chemically etched apertures in 1500 angstrom thick aluminum. Step coverage appears best at a bias of 0 volts where the oxide has built up along the aperture perimeter. At higher bias voltage values, step coverage is seen to diminish.

3.3 Pattern Delineation

In Chapter 2 it was mentioned that photoresist was used to define the apertures in the conducting sheets for etching. In this work AZ 1350J photoresist was used for pattern delineation.[18] AZ 1350J is a positive working resist which means that UV exposed regions of the resist dissolve in the appropriate developing solution whilst the unexposed regions remain intact, reproducing the mask pattern.

The basic procedure for the application of AZ 1350J resist and its proper use is given as follows:[19]

a) The photoresist is spun on a clean dry wafer for 30 seconds at an appropriate spin speed which is chosen from Fig. 3-8 once the desired resist thickness is known.[20]

b) The wafer is allowed to stand for 10-15 minutes to enhance step coverage.

c) The wafer is prebaked in air for 30 min. at 90 degrees C.

d) The wafer is allowed to cool for 15-20 min.

e) In contact with the mask pattern desired, the wafer is exposed to UV light using the contact printer. The exposure time required is determined by the time which gives the
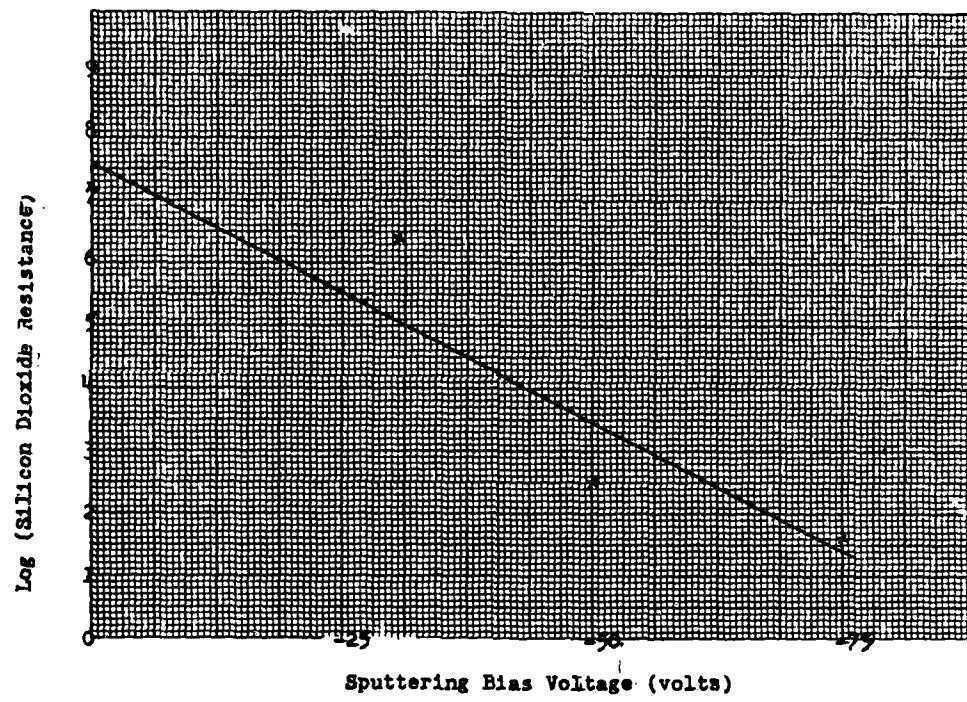
Figure 3-6: SiO$_2$ Resistance as a Function of Bias Sputtering Voltage

(a) Bias voltage = 0 v.

Figure 3-7: Micrographs of SiO_2 Covering Aperture Sidewalls

33
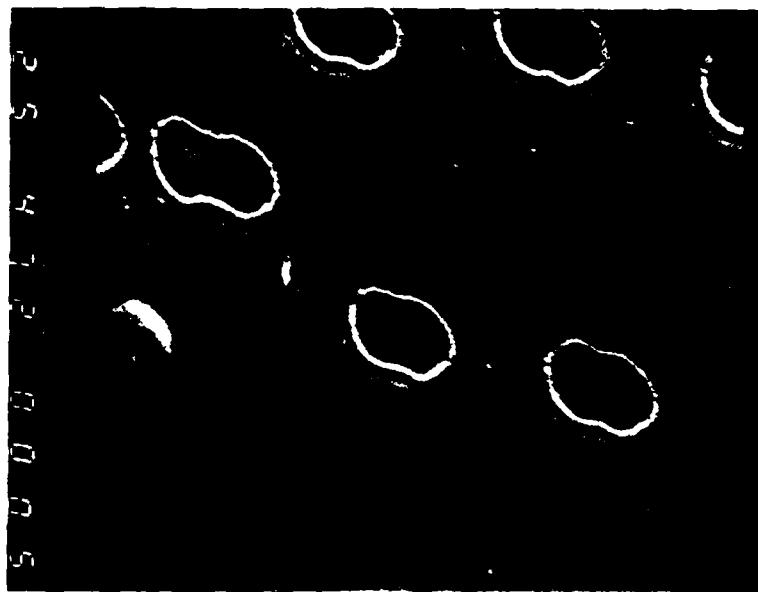
(b)   Bias voltage = -12 v.

Fig. 3-7, continued

(c) Bias voltage = -38 v.

Fig. 3-7, continued

best pattern resolution when developed for 60 sec. This is found empirically by observing the photoresist pattern and comparing it with the original mask pattern.

f) The wafer is developed for 60 sec. in a solution of AZ 351 developer and water in the ratio of 1:3.5 and then rinsed thoroughly in water.[18]

g) To promote adhesion of the photoresist the wafer is postbaked for 20 min. in air at 125 deg. After cooling, the pattern may be etched in the appropriate etching solution. In this work, evaporated aluminum films were etched in a solution of phosphoric acid, acetic acid, water and nitric acid in the volume ratios of 80:5:10:1. The films were etched at room temperature in a beaker with no agitation in order to minimize undercutting. Results will be shown in the next section.

When etching is complete, the photoresist may be removed by stripping in acetone and using an ultrasonic bath. A Plasmaline plasma asher was used to remove photoresist residues and overbaked photoresist which are relatively inert and resistant to chemical stripping.[21] The asher is a barrel type unit and the plasma is maintained by bleeding oxygen into the system. Typical ashing conditions to remove photoresist residues are 300 watts power for 5 min. and only 1-2 minutes if one wishes to preserve existing photoresist patterns and remove residues on the same wafer.

Photoresist patterns were exposed and masking levels were aligned using a Cobilt contact printer.[22] Masks used were Electron Beam Generated chromium on 4" glass plates that were designed by the author at I.B.M. Research Center in San Jose, California. Appendix I describes in more detail the types of propagation elements and chips that were designed.

3.4 Fabricating The Device Structure

In this section the details of fabricating the entire device structure will be given, with illustrative diagrams and photographs shown for clarity. The reader should refer to Fig. 3-9 as the processes are described.

a) On a clean dry wafer is evaporated 1500 angstroms of aluminum as described previously. If a prespacer is desired, 100 - 200 angstroms of SiO_2 may be sputtered first.

b) AZ 1350J is spun on at 8000 R.P.M. for 30 sec., yielding a coat approximately 1.3 microns thick. The wafer is allowed to stand for 10-15 minutes, after which it is prebaked in air for 30 min. at 90 degrees C.
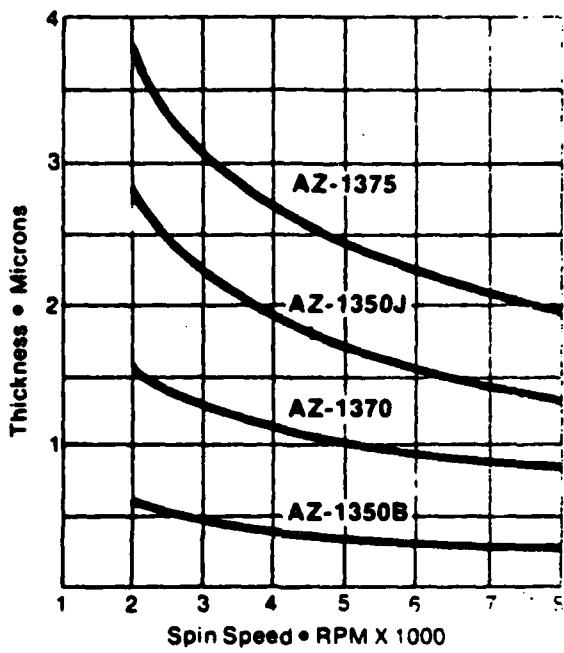
Figure 3-8: AZ-1350J Thickness as a Function of Spin Speed From Shipley Photoresist Data[20].

aluminum

(a)

photoresist

aluminum

(b)

photoresist

aluminum

(c)
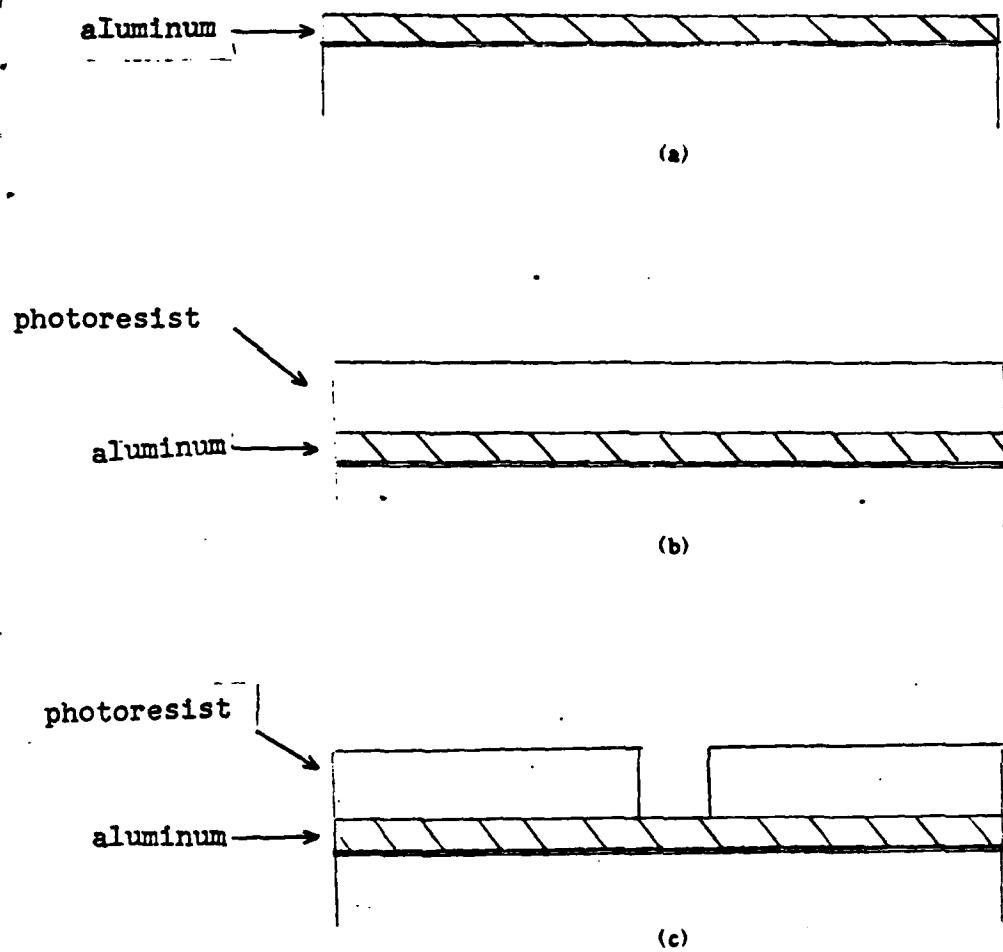
Figure 3-9: Processing of the Device

aluminum

(d)

silicon
dioxide

aluminum

(e)

photoresist

silicon
dioxide

aluminum
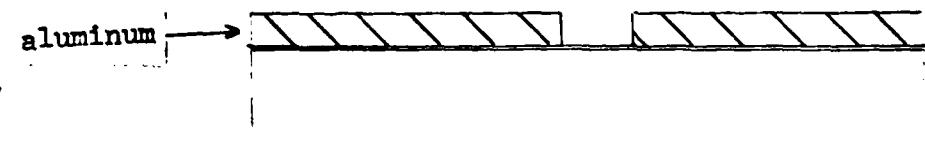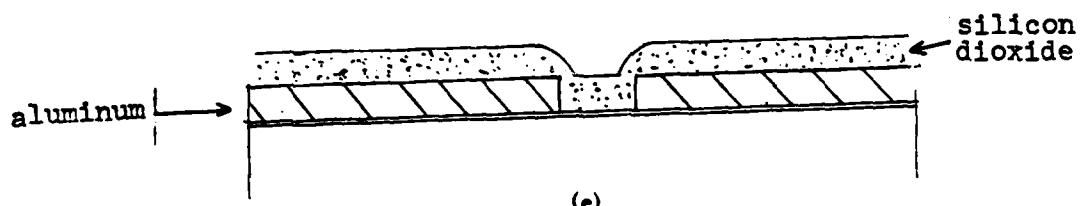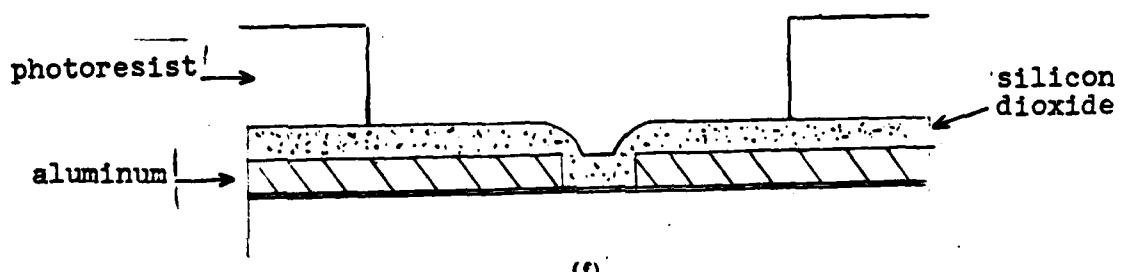
(f)

Figure 3-9, continued

(g)

(h)

(i)

(j)
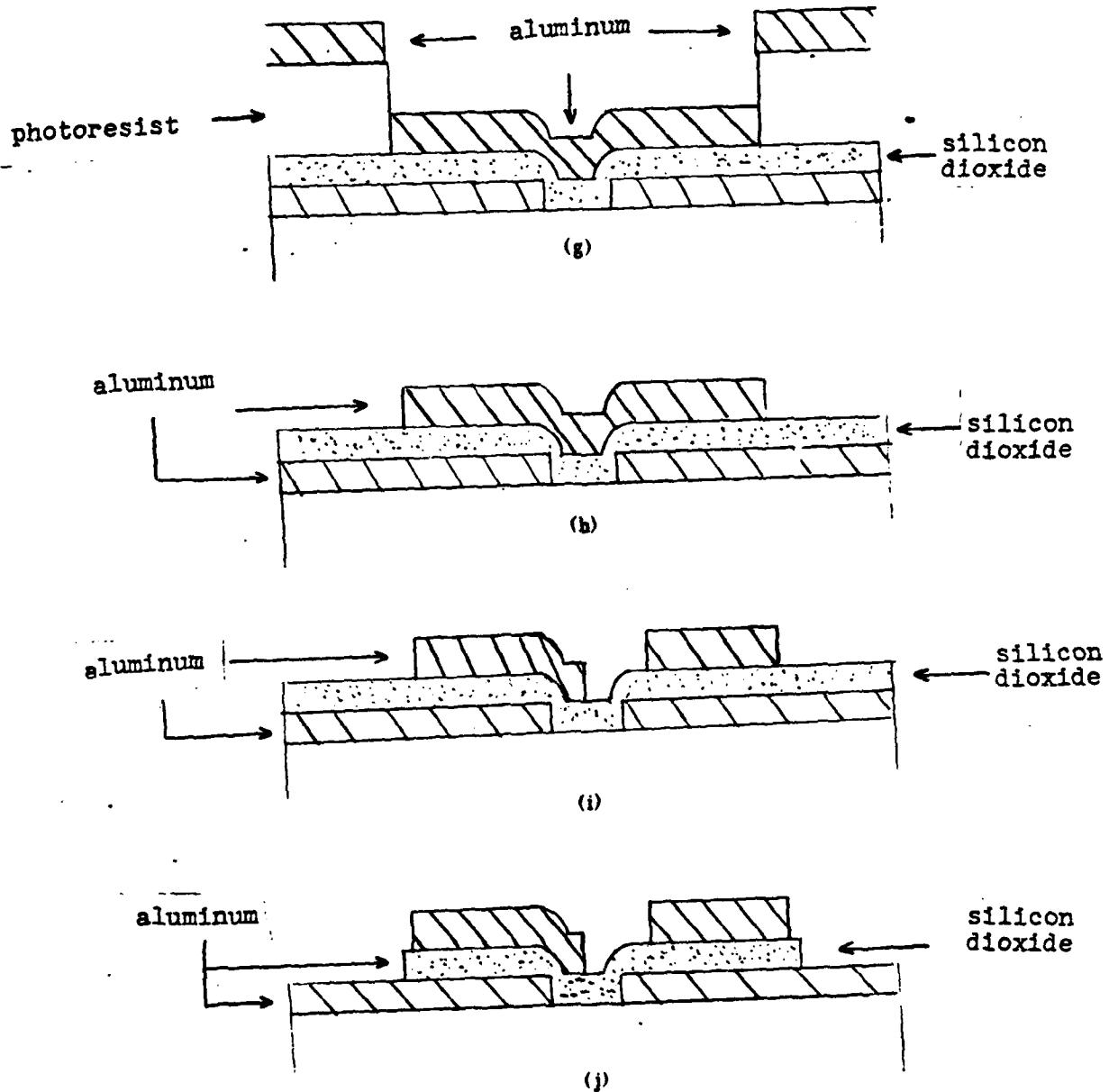
Figure 3-9, continued

c) After a 20 min. cooling period, the wafer may be exposed to the first level aperture mask. Exposure time is 11 sec., after which the wafer is developed for 60 sec. in a 3.5:1 mixture of water and AZ 351 developer at room temperature. The wafer is then rinsed well in water, dried with nitrogen, and ashed in oxygen for 1-2 minutes, yielding the structure of Fig. 3-9c.

d) The pattern is now etched in the aluminum etchant for roughly 3 min. After removal from the acid, the wafer should be rinsed immediately in water so that etching is promptly terminated. During the etching procedure, frequent microscopic inspection is necessary so over- and under-etching are avoided. When etching is complete, the photoresist is removed in an ultrasonically agitated acetone bath for 5 min. and ashed in O_2 plasma for 5 min.

e) Now, SiO_2 is sputtered to isolate the two conducting sheets. A 1750 angstrom layer is deposited using the parameters of Fig. 3-3. As mentioned earlier, no bias voltage is applied.

f) To facilitate making electrical contacts to the bottom sheet, the top level conductor is applied as follows. Photoresist is deposited and prebaked as in b) above. Using the SiO_2 VIA mask, the photoresist is exposed, developed and ashed as in c) above, resulting in the structure shown in Fig. 3-9f.

g) 2500 angstroms of Al are now evaporated on top of the photoresist and the SiO_2.

h) The wafer is now placed in acetone and ultrasonically agitated for 5 min., causing the photoresist to undercut and liftoff the aluminum on top. Recall that the photoresist is 1.3 microns thick; vertical sidewalls allowed easy implementation of this technique, which is known as liftoff.

i) Photoresist is again spun on at 8,000 R.P.M. and the VIA Level 2 mask is used to pattern the resist, as in c) above. After postbaking, the aluminum is etched for 5 min. and the photoresist is again removed.

j) Finally, using negative photoresist and the SiO_2 VIA mask, the entire device is covered with photoresist except for the SiO_2 covering the areas of level 1. This SiO_2 is etched in buffered HF providing vias to the bottom level and the device is ready for bonding.

It should be noted that steps a) through j) were performed, but due to the fact that

VIA Level 1 and VIA Level 2 masks were found to be identical, a complete working device was not possible to fabricate.

CHAPTER 4

RESULTS AND DISCUSSION

4.1 Conductors

As mentioned previously, chemical etching reproduces fine lithographic features in aluminum with minimal pattern variations, in contrast to the deleterious effects of wet chemical etching on thin gold films. On the other hand, sputter etching does not undercut the mask material due to the normal bombardment of the etching species.

Sputter etching does have drawbacks however. The photoresist mask is sputtered away at highly variable rates, depending upon the substrate temperature and the residual gases in the plasma.[23] In particular, the integrity of photoresist masks is difficult to maintain in the sputter etching of aluminum.[24] Also, the removal of photoresist masks after sputtering may be difficult due to the crosslinking of the resist that may occur during the etch process.[23] RF sputtered SiO_2 may react with aluminum to form insoluble residues which may require damaging over-etching to insure complete removal; this would impede or prevent complete sputter etching of the second level apertures.[25] High temperatures, such as those that might be reached during sputter etching, may increase the chemical reaction between the aluminum and the SiO_2.[26]

Since aluminum is easily evaporated, readily obtainable and much more cost-efficient to use than gold is, it is a prime candidate to consider when selecting a conductor material. In addition, aluminum is presently being used as a conductor in commercial bubble device processing where fine features in it are being chemically etched.[27] Chemical etching of aluminum is preferable to sputter etching as mentioned above, and the former is more easily implemented. For these reasons, aluminum was chosen by the author as the conductor used in this project.

In Fig. 4-1 is seen a chemically etched aperture in 1,500 angstrom thick aluminum. (The aperture was defined using a poorly exposed photoresist pattern, which accounts for the rounded edges.) The important feature to note however is the vertical walls of the

aperture, giving evidence of an anisotropic etch process. This is not the case in relatively thick aluminum films, where sloped edges are usually obtained in the wet etch process.[27] Fig. 4-1 emphasizes the fact that the ability of the interlevel insulating layer to cover steps conformally is critical in the dual conductor current access device.

4.2 Insulators

Sputtering of insulators has the advantage of being a low temperature process, which is preferred in magnetic bubble device processing because of the possible deleterious effects of annealing on device performance; a typical CVD. deposition temperature could be greater than 300 deg. C as opposed to 200 deg. C which might be reached in sputtering of SiO_2.[28] SiO_2 may be sputtered on a device after a previous deposition if a multiple target system is used; this technique has been shown to improve the performance of permalloy bubble detectors.[29] Finally, sputtering is a more versatile process than CVD; bias sputtering in particular can be used to influence virtually any property of a film.

The effects of substrate bias and other parameters upon the step coverage of sputtered SiO_2 over conductor steps has been previously researched; the results of some more recent investigations will be discussed and compared with those obtained by the author.

During bias sputtering, a voltage is applied to the substrate to make it negative with respect to the plasma. This negative substrate voltage causes the depositing film to be bombarded by the working gas ions, which can affect film purity, resistivity, and structure, among other things.[30]

In his study, Serikawa[31] found that for SiO_2 sputtered at 0 bias, step coverage was a function of substrate-target spacing (at constant Ar pressure) and Ar pressure (at constant substrate-target spacing). If the Ar pressure or substrate-target spacing were increased step coverage decreased. It was concluded that at the shorter distances and lower gas pressures, a high percentage of the sputtered material arrived at the substrate having oblique or normal incidence which enhances step coverage (Fig. 4-2a). Increasing either of these two parameters results in a fraction of the material having horizontal incidence, yielding negative step coverage (Fig. 4-2b). He also found that a positive voltage applied to the substrate gave positive step coverage and that negative bias voltages resulted in negative step coverage.

Kennedy[32] reactively sputtered SiO_2 in an Ar/O_2 atmosphere and studied the effect of negative substrate bias voltage on step coverage. He reported increasing step coverage as
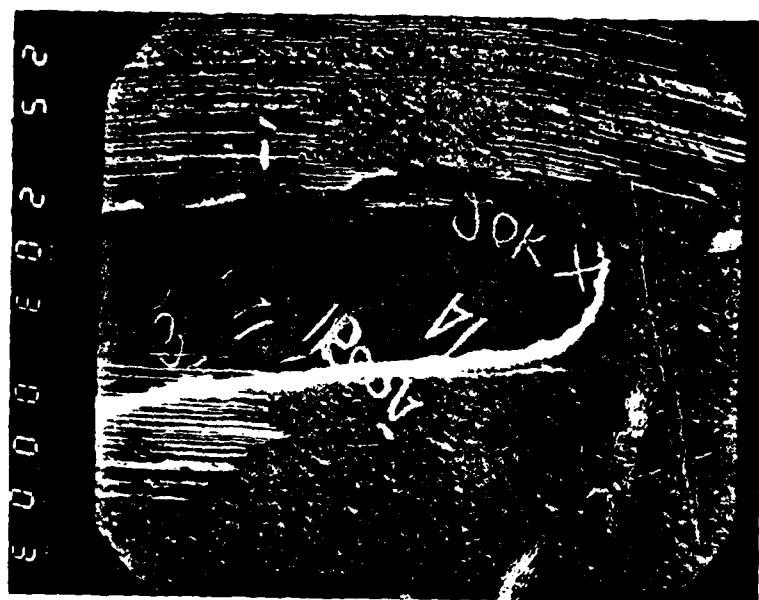
Figure 4-1: 20,000X micrograph of chemically etched aperture. The aluminum thickness is 1,500 angstroms.
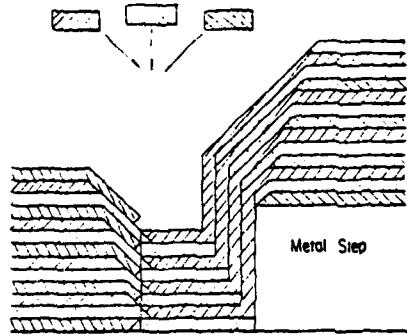
(a) Oblique and normal incidence enhances step coverage
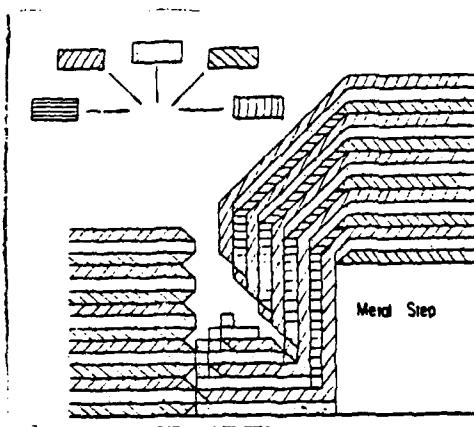
(b) Increasing horizontal incidence yields negative step coverage

Figure 4-2: Step coverage of SiO$_2$

From Serikawa[31].

the voltage was increased negatively, but the effect saturated and at high enough voltages negative step coverage was obtained. This can be explained by referring to Fig. 4-3, which depicts a metal step being covered by a bias sputtered insulator. As the gas ions bombard the film, the sloped regions are etched at higher rates because ions strike them obliquely, removing more material from them than regions that are struck by ions with normal incidence. Hence, the angle between the horizontal step surface and sloped insulator is the angle where an obliquely incident ion removes the maximum amount of material. At low voltages, the film is resputtered at low angles, being deposited at the steep sidewall and base. At equilibrium, the amount of deposition and etching of the sloped regions are equal, resulting in positive step coverage. If the voltage is increased, the sloped surface will have a negative deposition rate, resulting in poor step coverage. The two sloped surfaces will move in the direction indicated by the arrows; the step will actually be exposed if this process is continued.

In their computer simulation of deposition processes, Neureuther et. al.[33] modelled unbiased RF sputtering of SiO_2 as an isotropic process which coated steps uniformly. Their decision to model it as such was based upon Scanning Electron Micrographs of SiO_2 sputter deposited on steps of aluminum. These results are similar to those obtained by Serikawa when he sputtered the insulator using low working gas pressures and short substrate/target spacing. Unfortunately however, Neureuther et. al.[33] gave no sputtering parameters or system geometry details in their report.

In order to explain these apparently conflicting results, the mechanism by which a sputtered atom reaches a substrate must be briefly explained. In the sputtering process, an atom is removed from a target by momentum transferred from an impinging ion. The angular distribution of atoms sputtered from an amorphous target by normally incident ions can be approximated to first order by a cosine distribution.[34] Once sputtered atoms travel a few mean free paths from the target, scattering causes them to be thermalized, after which their energies are reduced to the average energy of the sputtering gas. Once thermalized, transport of the sputtered atoms is controlled by diffusion through the plasma, and the atoms no longer travel normal to the target surface.[35] This results in an increasing percentage of the sputtered atoms having horizontal incidence. If relatively high working gas pressures are used in the sputtering process or if the target/substrate spacing is large, sputtered atoms reach the sample by diffusion, with subsequent poor step coverage resulting.[31]

In this work the sputtering gas pressure was 1.33 Pa (10 millitorr) whilst the target/substrate spacing was 1.25 inches. It was estimated from data given by Westwood
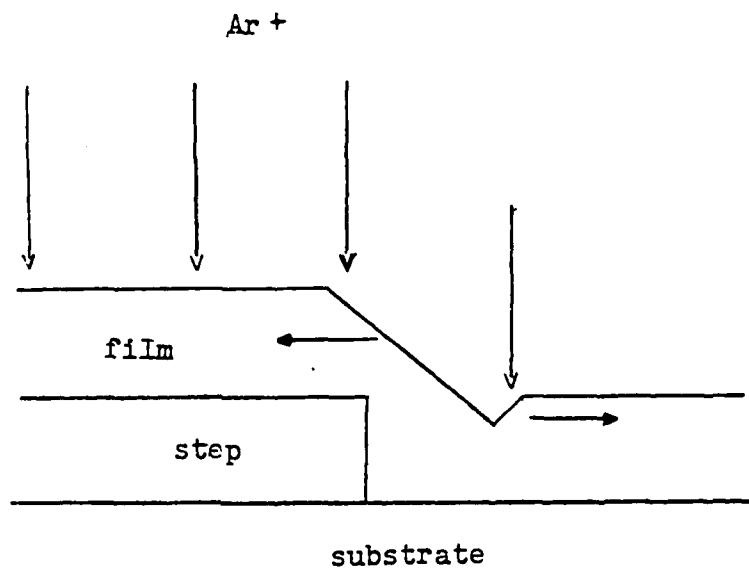
Figure 4-3: Step coverage as a function of bias voltage
Increasing the substrate voltage increases ion bombardment.
High enough voltages will etch and expose step.
Adopted from Kennedy[32].

that the minimun thermalization distance of an SiO_2 molecule at a pressure of 1.33 Pa (10 millitorr) is approximately 1.5 inches.[35] Hence, the majority of SiO_2 molecules sputtered reached the sample having normal or oblique incidence, yielding positive step coverage. However, when a negative voltage is applied to the substrate, the aperture sidewalls are preferentially etched, resulting in negative step coverage. Referring to Table 1, this accounts for the fact that the SiO_2/Probe Resistance was relatively high independent of bias voltage while the figure-of-merit of step coverage, namely Electrode/SiO_2 Resistance, decreased with increasing bias voltage.

It should be recognized that many factors influence step coverage of sputtered materials. The amount of bias voltage needed to obtain good step coverage has been shown to be a function of:[32]

1. the system electrical design

2. sputter efficiency of the film material with the sputtering gas

3. capacitive impedance of the substrate and film

4. step geometry

5. deposition rate

4.3 Pattern Delineation

It was mentioned previously that proper UV exposure times were ascertained empirically by comparing the mask and photoresist patterns. A typical result is given in Fig. 4-4. Seen are photoresist aperture patterns on aluminum at a magnification of 1020X. All patterns have been developed for 60 sec. in an AZ 351 developing solution but have been exposed to the contact printer's UV source for different lengths of time. The sample of Fig. 4-4a was exposed for 8 sec. Note the underdevelopement of the apertures; the insufficient exposure has left behind an insoluble veil of photoresist. Fig. 4-4b was exposed for 14 sec.; note the rounding of the pattern edges yielding ovally shaped apertures. Diffuse light scattering into the photoresist has exposed areas underneath the mask, causing pattern distortion. Finally, in Fig. 4-4c, is seen a pattern exposed for 11 sec. The aperture corners are relatively square, indicating good resolution in the pattern definition.

Fig. 4-5 is a photograph of the first level chromium mask taken with reflected light at a magnification of 1020X. Seen is an array of small propagating loops, where bubbles traverse the perimeter of the loops in clockwise or counterclockwise fashion. The smaller
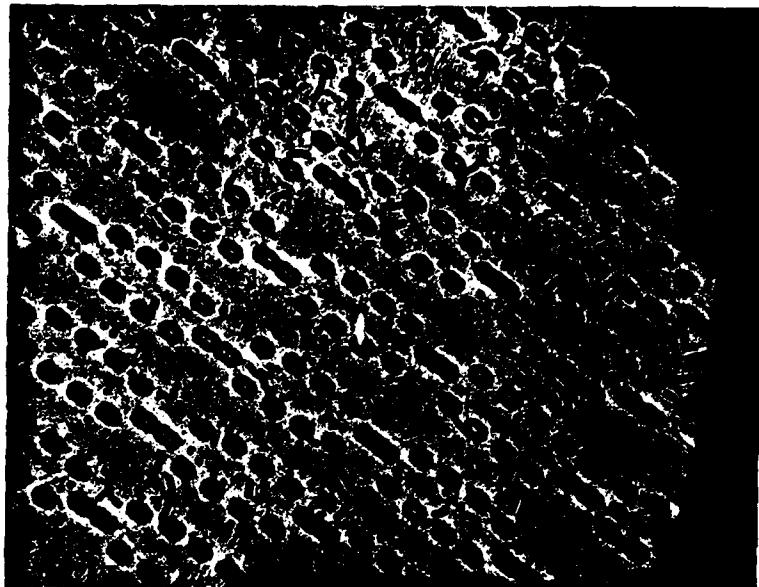
(a) AZ 1350J photoresist pattern

Exposure time: 8 sec.

Figure 4-4: Ascertaining the Optimum Exposure Time
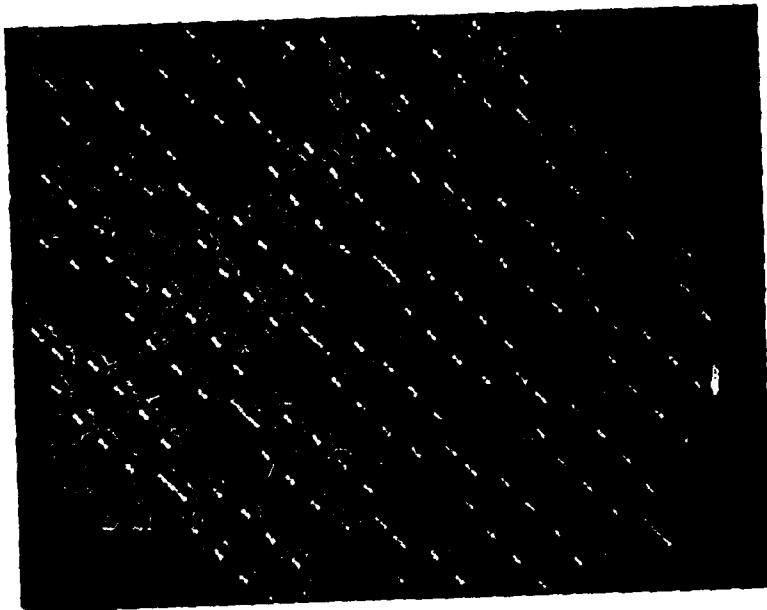
(b) AZ 1350J photoresist pattern

Exposure time: 14 sec.

Fig. 4-4, continued

52
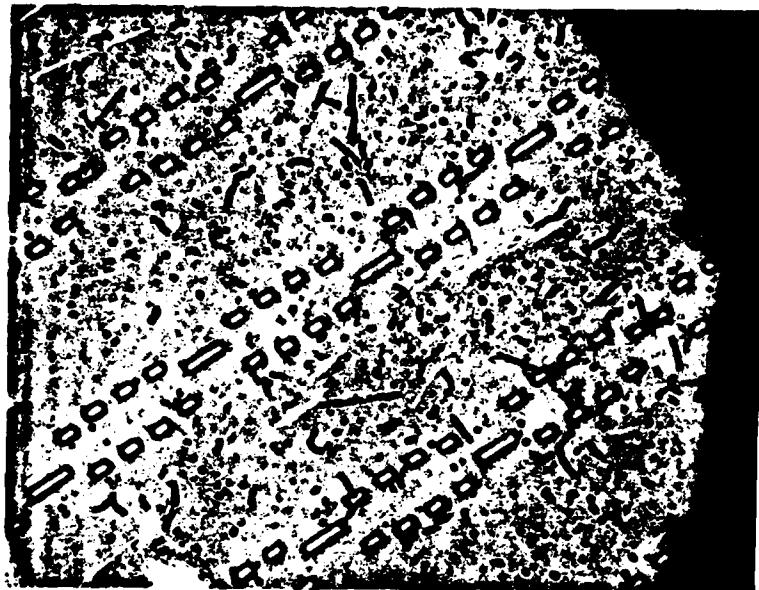
(c) AZ 1350J photoresist pattern
Exposure time: 11 sec.

Fig. 4-4, continued

apertures are 2.4 x 4.0 microns, spaced 2.0 microns apart. Fig. 4-6 shows loops of similar dimensions, but these are AZ 1350J photoresist patterns on an aluminum film. Note the relatively square corners of the apertures, implying good reproduction of the mask pattern. The magnification here is 1020X as in Fig. 4-6. The dark apertures imply photoresist residues are present or that the photoresist is incompletely developed. These residues were removed by ashing the sample in oxygen; this can be seen from Fig. 4-7, which is a 1020X magnification photograph of chemically etched apertures in aluminum. If the apertures contained photoresist residues, the etch process would not have completely removed the aluminum from the interior of the apertures. Note that the apertures are not rounded and compared with Fig. 4-5 it appears that the mask pattern is reproduced fairly well.

4.4 Conclusions

Some of the fabrication processes used in this project were markedly different than those used by Bobeck et. al.[2] in the fabrication of the first dual conductor devices. For example, in this author's work, chemical etching was used to define patterns in aluminum conductors, and sputtered SiO_2 was used as an insulator. In their devices, Bobeck et. al.[2] used plasma etching to define patterns in AlCu films and plasma deposited SiO_2 was used as a dielectric. It is seen that different materials, deposition and etching techniques, and systems may be used in a particular fabrication step and yield similar results, as long as the appropriate processing parameters are used and equipment characteristics are understood.

Even though plasma etching allows high etch selectivity depending upon the working gas used, chemical etching is more easily implemented, requires less capital investment and allows accurate endpoint detection of the etch process since the substrates are not confined to a vacuum chamber. Although probably not the concern of a university laboratory, wafer throughput is higher for chemical etching compared to plasma etching. This is certainly an important consideration in a production environment.

Since mostly any material may be sputtered, depending upon the availability of target material, sputtering is a popular method of film deposition. Most sputtering systems contain more than one target position so that multiple depositions may be made in one system pumpdown. On the other hand, plasma deposition may be performed only with a limited number of chemically reactive species. Also, plasma systems are usually dedicated to the deposition of one type of material so that film contamination is minimized. Hence, the investment in a sputtering system gives one the ability to deposit a variety of

54

**Figure 4-5:** 1020X photograph of chromium mask
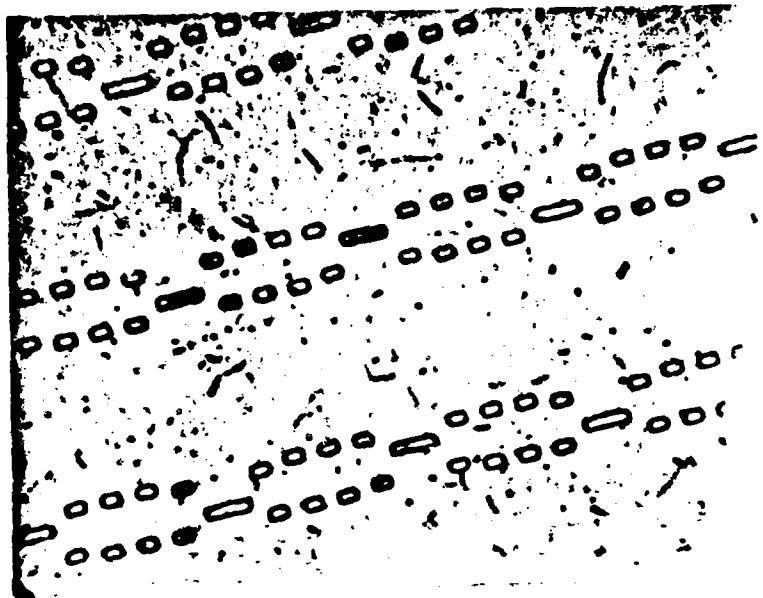
**Figure 4-6:** 1020X photograph of apertures in photoresist
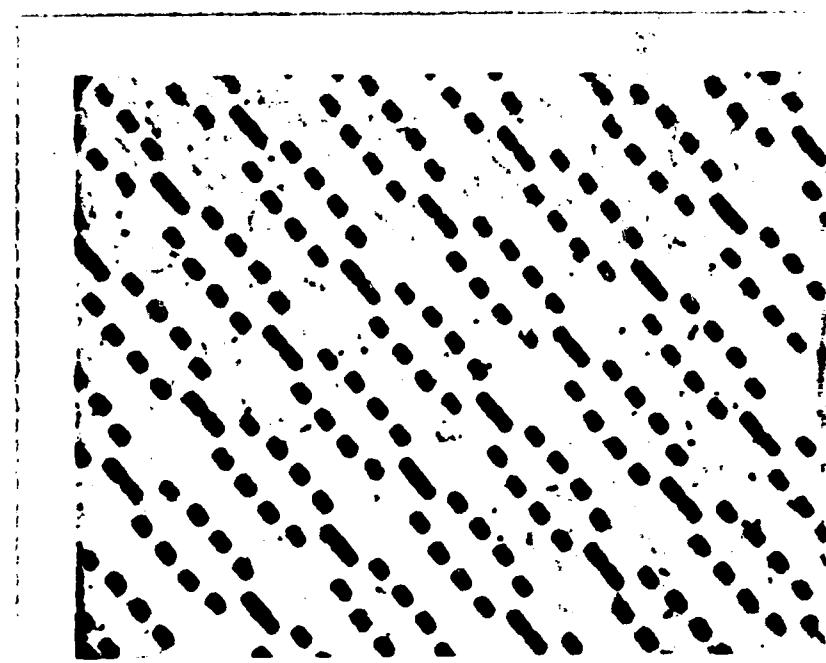
Figure 4-7: 1020X photograph of apertures etched in 1500 angstrom Al

57

materials, allows control of film parameters and structure through the application of substrate bias and provides greater flexibility than a plasma deposition system since sputter etching is available as a processing option.

In this thesis is described the fundamental groundwork needed for the successful fabrication of dual conductor devices. Apertures, defined by contact print photolithography, were chemically etched in thin aluminum films which were isolated by an rf sputtered SiO_2 dielectric. Oxygen ashing of photoresist patterns prior to etching was shown to be important for good pattern definition due to photoresist residue removal in the oxygen plasma. In addition, several processing procedures were developed, studied. and optimized. These include:

1. The developement of a contact print photolithographic process which allowed reproducible definition of current access device propagation structures in photoresist with minimal pattern variation.

2. It was discovered that chemical etching is a suitable means of delineating fine lithographic patterns in thin evaporated aluminum films.

3. Even though the anisotropic etch process yields vertical sidewalls in these films, sputtered SiO_2 can be used to conformally coat the conductor sidewalls under the appropriate sputtering conditions.

4. Negatively increasing the bias sputtering voltage degrades the step coverage of SiO_2 due to oblique incidence of the working gas ions which etches material deposited on the sidewalls.

5. As seen in Appendix I, a device library was constructed which contained various propagation elements, minor loop arrays and structures used to study the effects of adjacent aperture spacing on bubble propagation.

59

APPENDIX A
DEVICE LIBRARY

The following is a library of elements used to create propagation structures in the devices that were fabricated for this project. The patterns were laid out on a grid with 1/8 micron spacing on an Interactive Graphics System (IGS) at I.B.M. Research Laboratory in San Jose, California. Figures were created, manipulated and modified using a light pen and once defined, elements could be repeated in the X or Y direction in the plane of the C.R.T. screen a user-specified integral number of times. For example, with PE-1 displayed on the screen (Propagation Element PE-1 seen in Fig. 4-8), a command to repeat the element 50 times in the Y direction would create a 50 step propagation pattern.

For each element, the dimensions are given in microns and the aperture nearest the bubble supporting film is shown cross-hatched. Some of the elements appear more than once, implying that variations were made in subsequent designs such as aperture spacing, orientation, etc.

Chips were laid out using the following elements to create propagation paths, bubble stretchers and arrays of minor (storage) loops. Arrays of propagation paths were made with a variety of spacings between adjacent paths to test the interaction of bubbles traversing these paths.

Fig. 4-22 through Fig. 4-25 are photographs of an electron beam generated mask showing various features in detail. Fig. 4-22 shows a major loop containing an array of minor loops. Actually, this major/minor loop array occupies only one fourth of the chip area. Each chip (there is a 9 X 9 array of chips on each 4" mask plate) typically contains four different types of propagation structures. Also seen in this photograph are a pair of bubble stretchers, which expand bubbles traversing the outer major loop track. Fig. 4-23 is a 320X detail of the dense array of minor loops.

In Fig. 4-24 is seen a major/minor loop array as well as a pair of structures devised to test the interaction of bubbles as they traverse adjacent parallel propagation paths. Note that in the structure seen on the upper left hand side of the figure that the adjacent

apertures are staggered or offset by roughly 1.5 microns as opposed to those on the lower right hand side of the figure. This was done to see the effects, if any, of current density uniformity on bubble propagation. Fig. 4-25 is a 320X detail of the lower right hand side structure of Fig. 4-24.

Fig. 4-26 is a 320X photograph of the stretcher seen in Fig. 4-19. This design was modelled after the stretcher described by Bobeck et. al.[6] in their report.
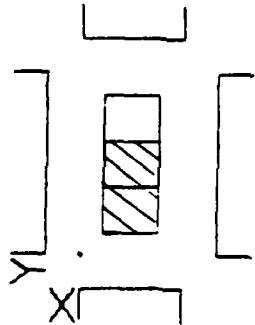
Figure 4-8: Propagation Element PE-1. X = 4.375 μm, Y = 9.0 μm.
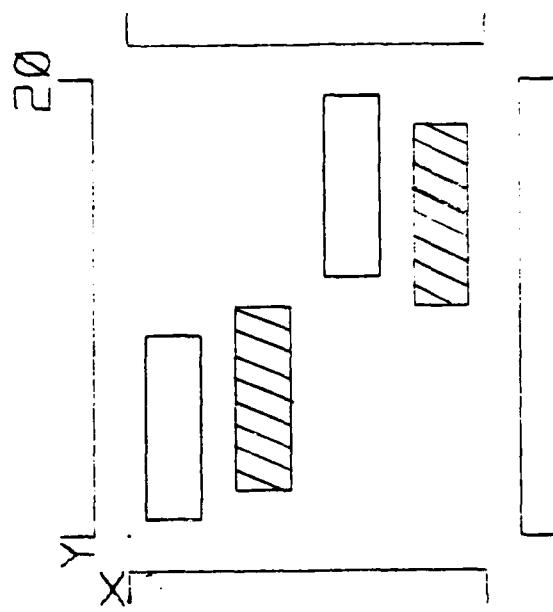
Figure 4-9: Propagation Element PE-2. X = 15.5 μm, Y = 20.0 μm.
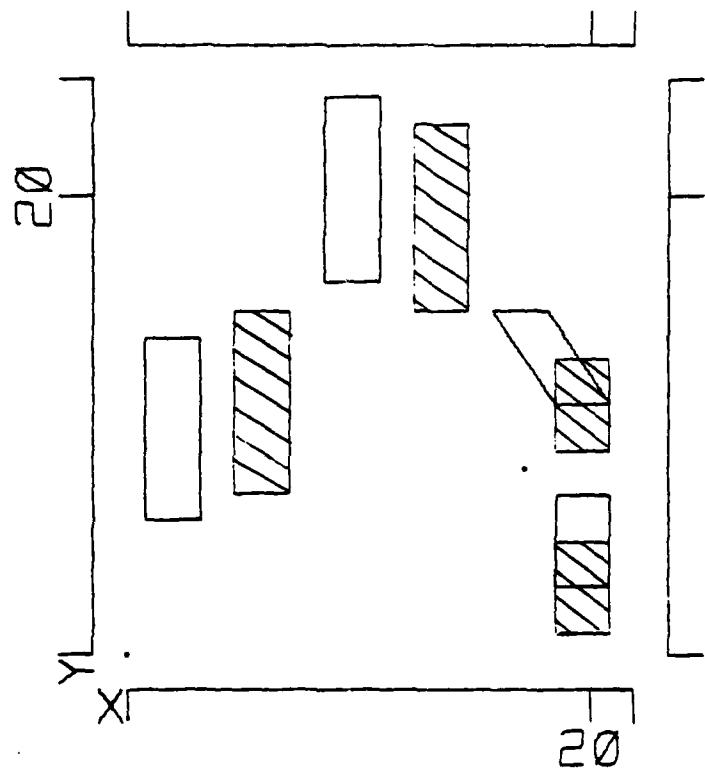
Figure 4-10: Turn Element LT-1. X = 21.875 µm, Y = 25.125 µm.
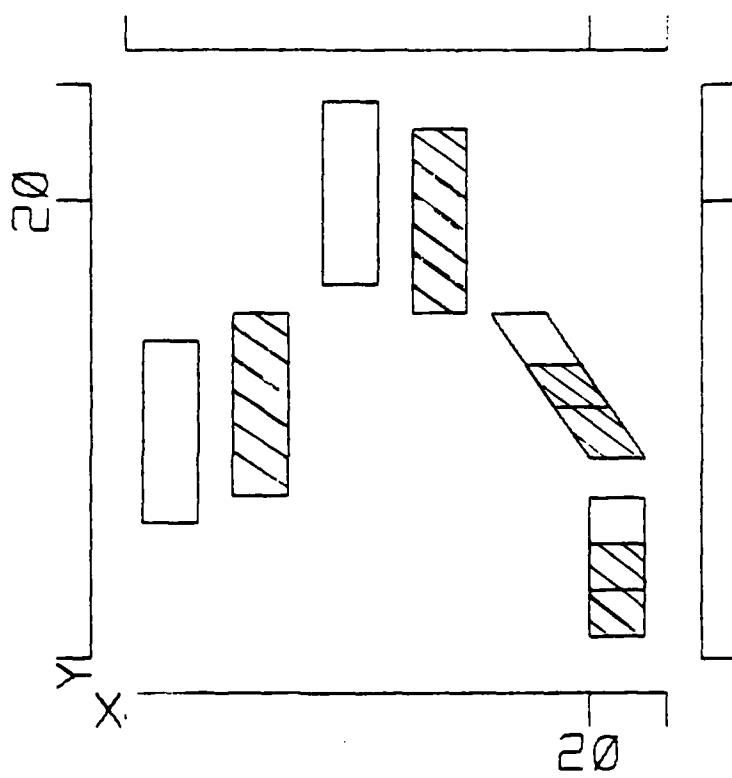
Figure 4-11: Turn Element LT-1A. X = 23.375 μm, Y = 25.125 μm.
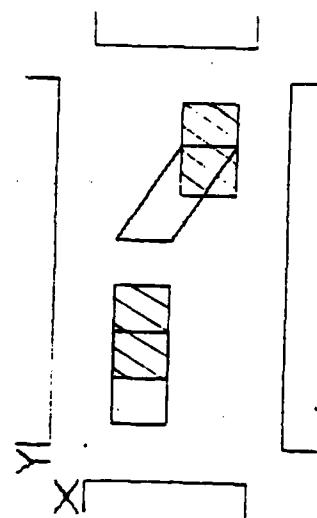
Figure 4-12: Turn Element LT-2. X = 7 μm, Y = 16 μm.
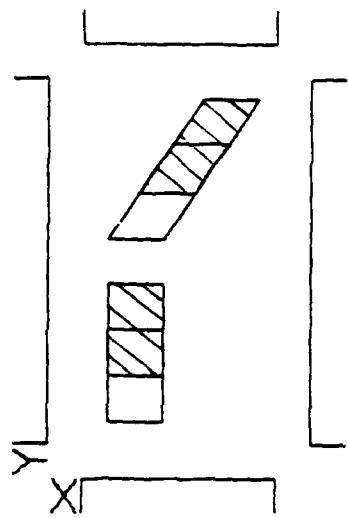
Figure 4-13: Turn Element LT-2A. X = 8.375 μm, Y = 16 μm.
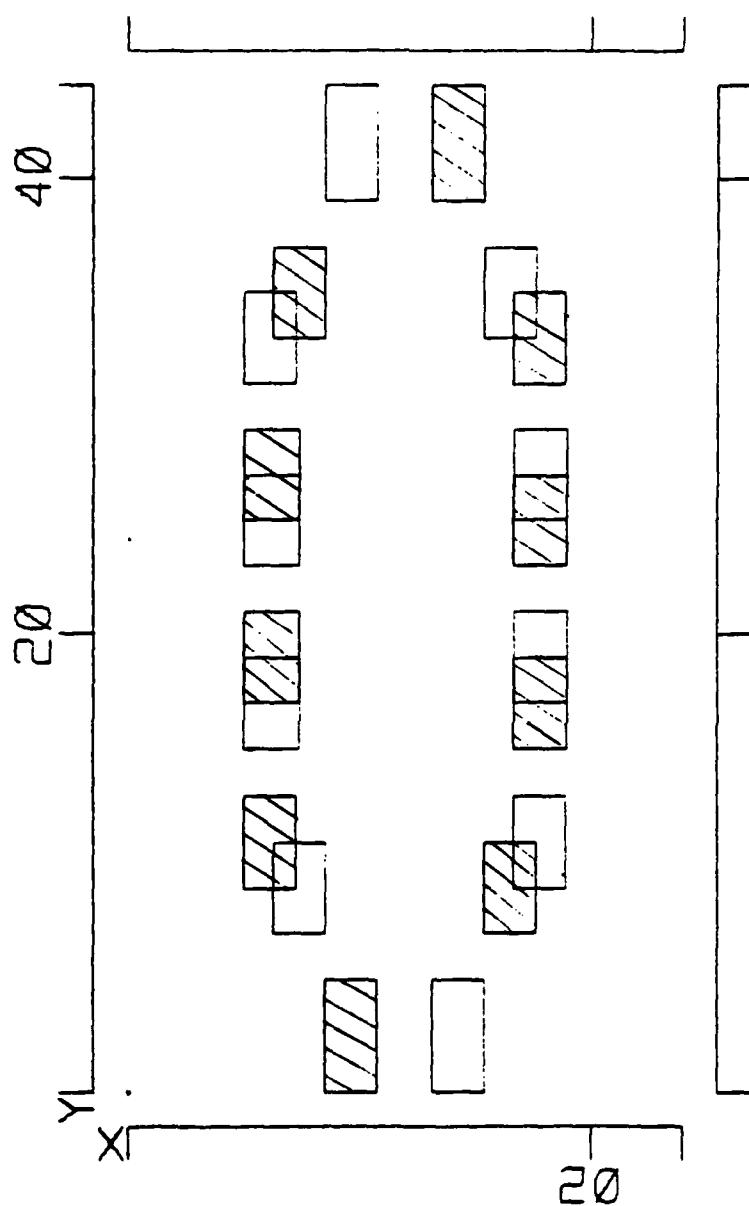
Figure 4-14: Minor Loop TL-1. X = 24.0 μm, Y = 44.0 μm.
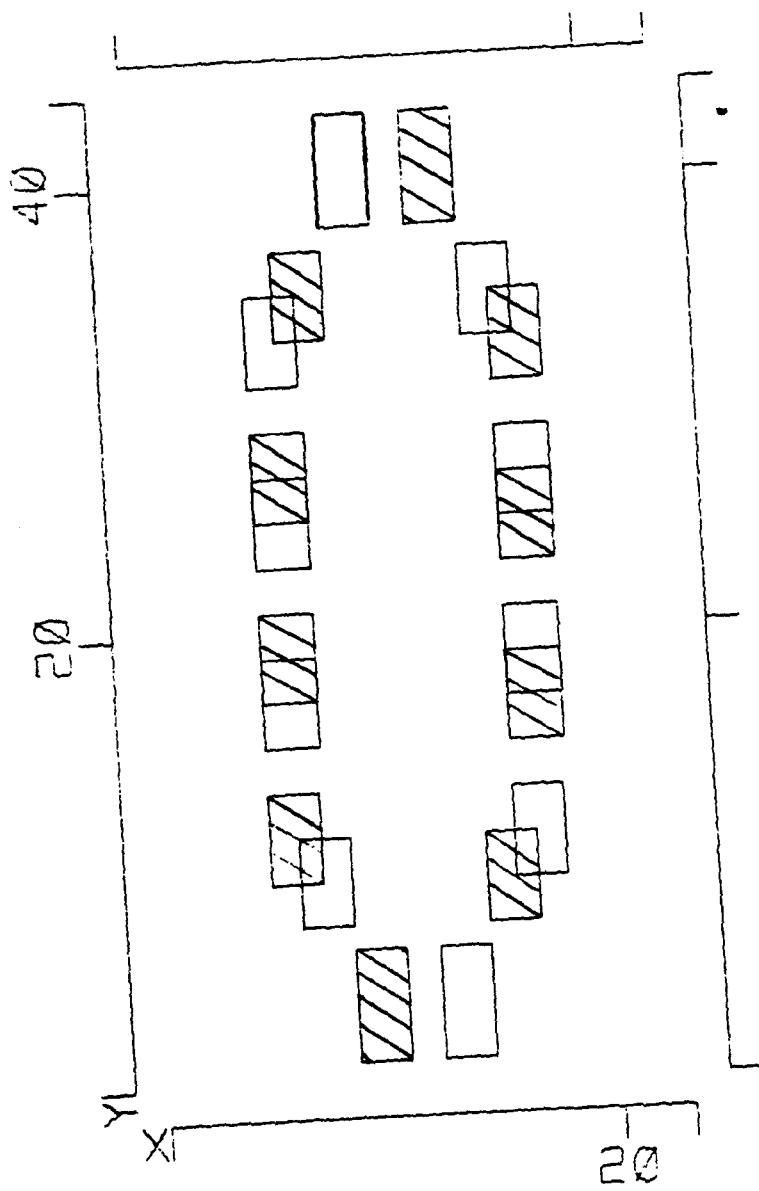
Figure 4-15: Minor Loop TL-1A. X = 23.125 μm, Y = 44.0 μm.
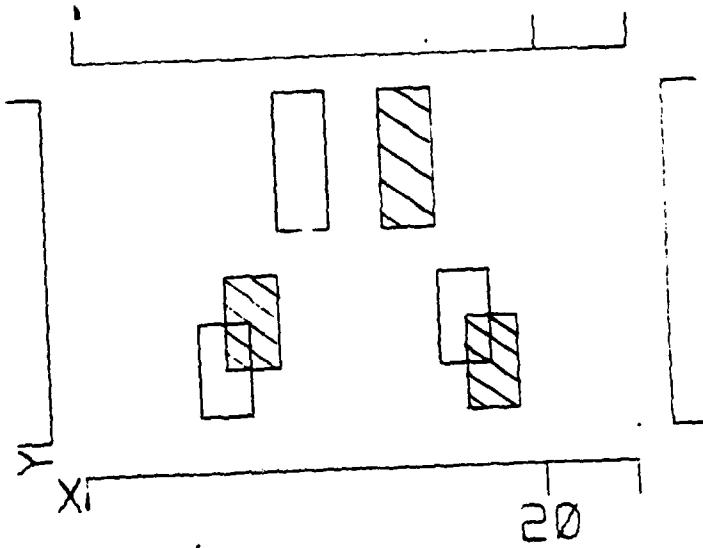
Figure 4-16: Minor Loop Turn MLT-1. X = 24 μm, Y = 15 μm.
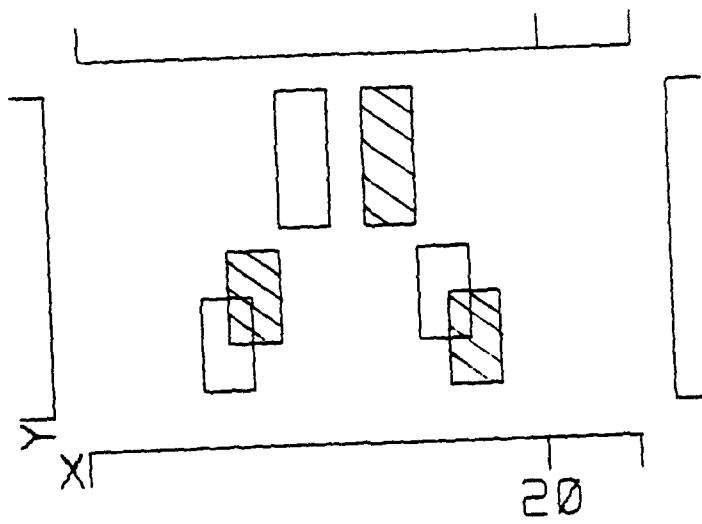
Figure 4-17: Minor Loop Turn MLT-1A. $X = 24 \ \mu m$, $Y = 14 \ \mu m$.
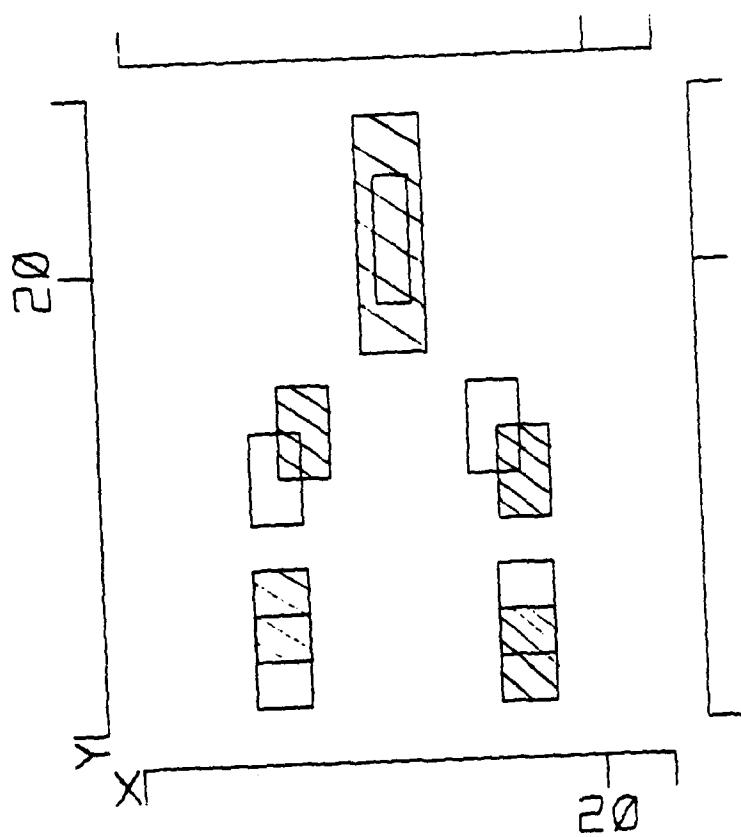
Figure 4-18: Transfer Port TP-1. X = 23 μm. Y = 27.75 μm.
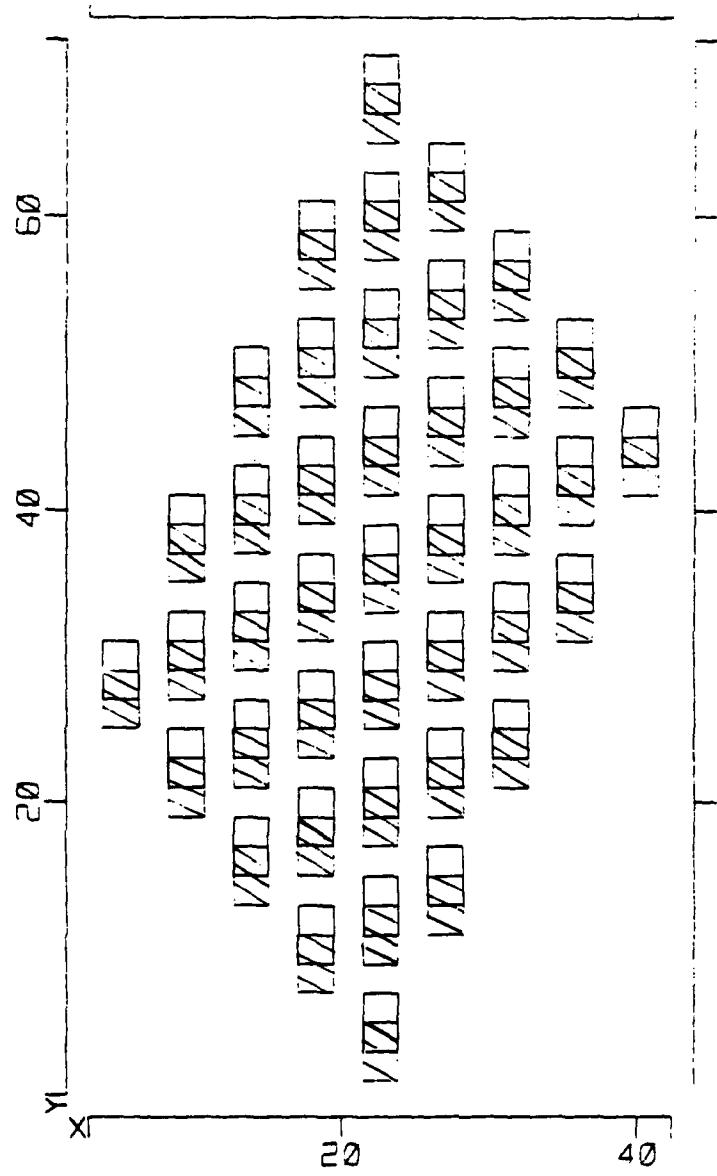
Figure 4-19: Stretcher ST-1. X = 42.375 μm. Y = 72 μm.
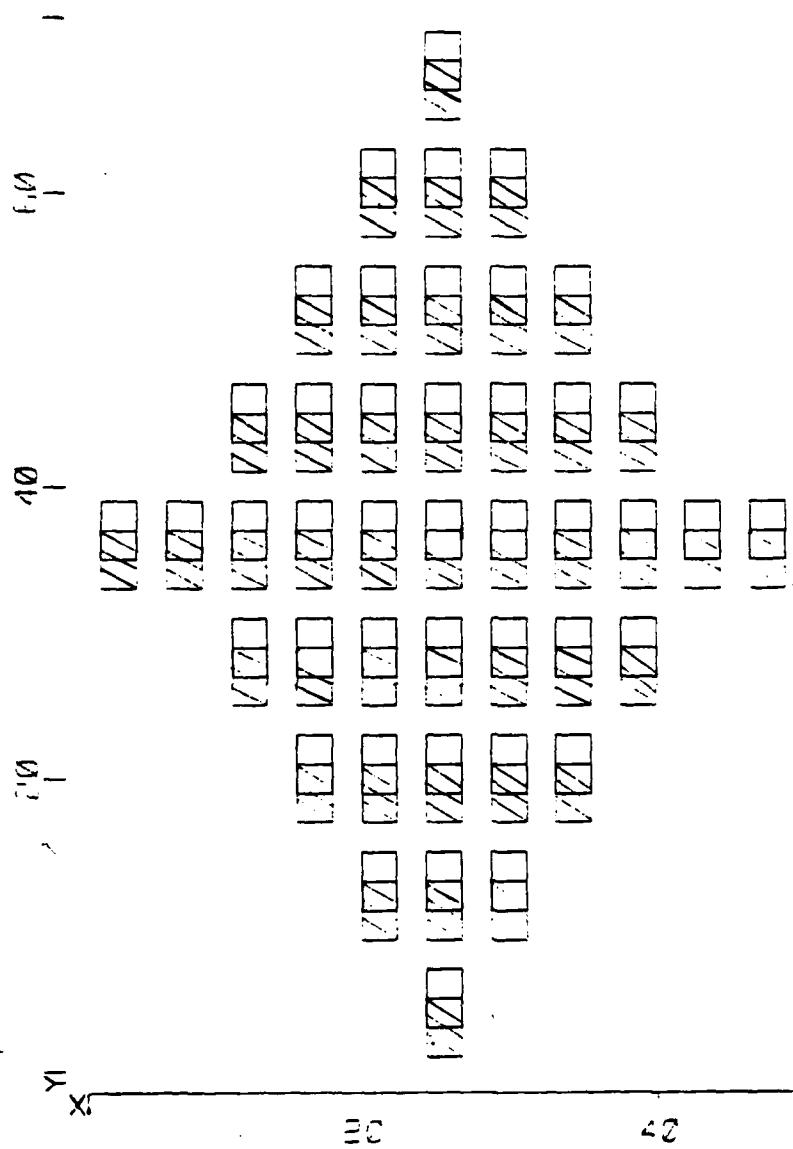
Figure 4-20: Stretcher ST-2. X = 49.625 μm. Y = 72 μm.
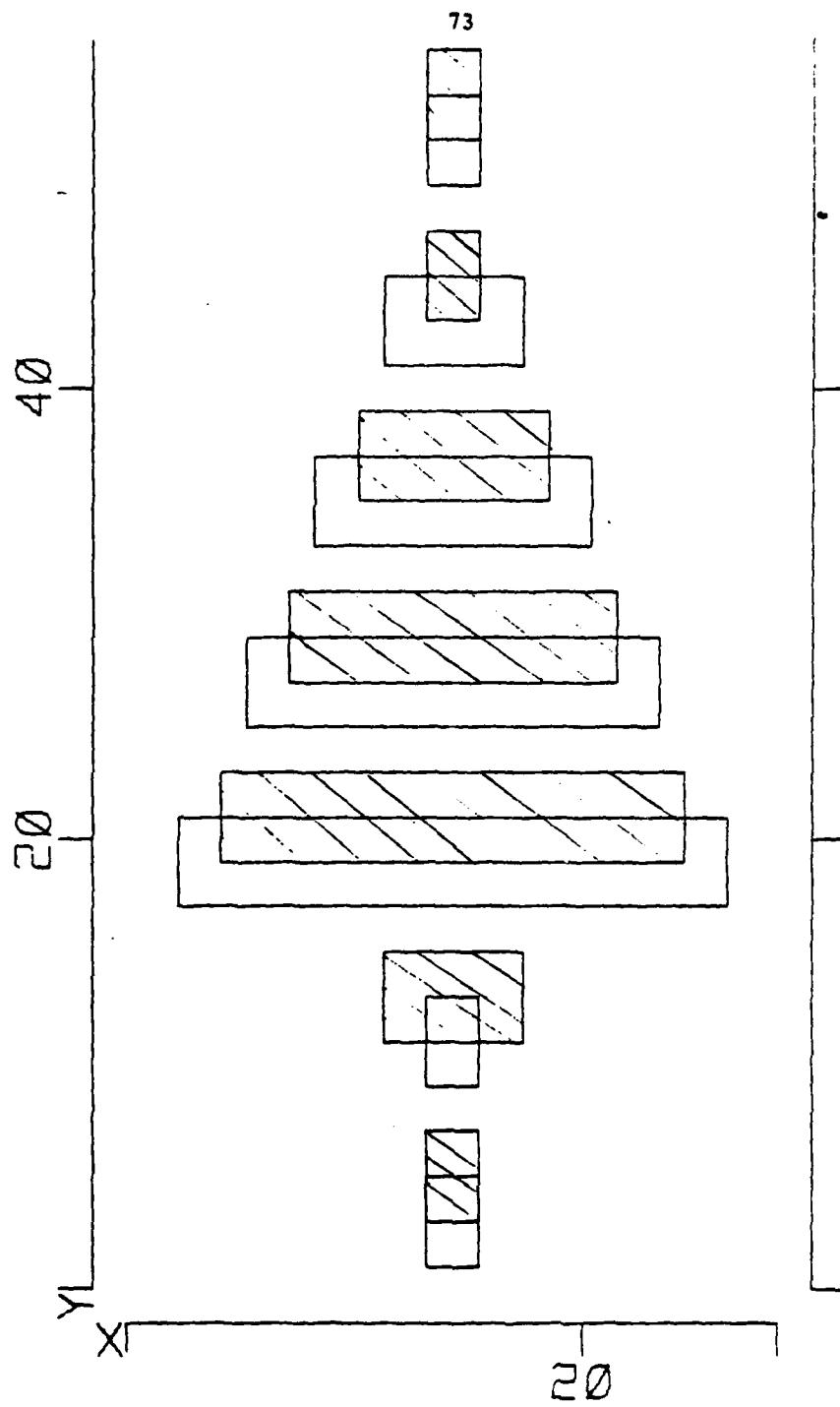
Figure 4-21: Stretcher ST-3. X = 28.625 μm, Y = 56 μm.
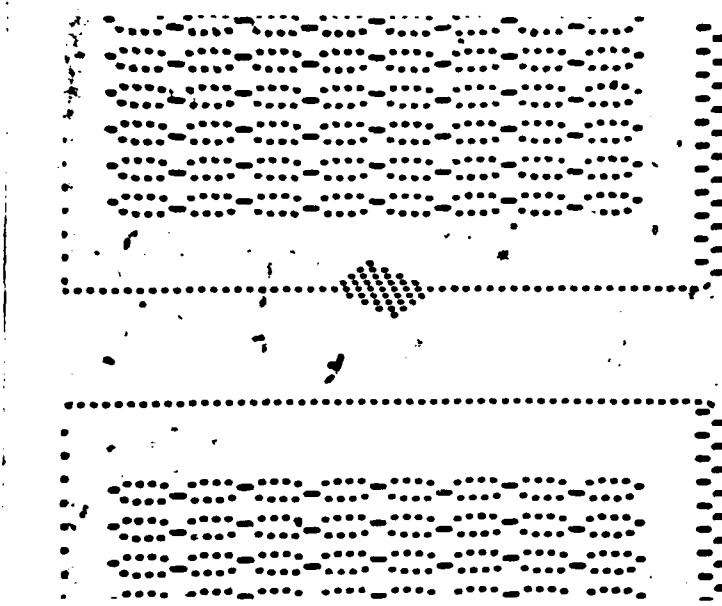
Figure 4-22: 160X photograph of portion of mask. Seen are a
major/minor loop array and stretcher designed by
author.
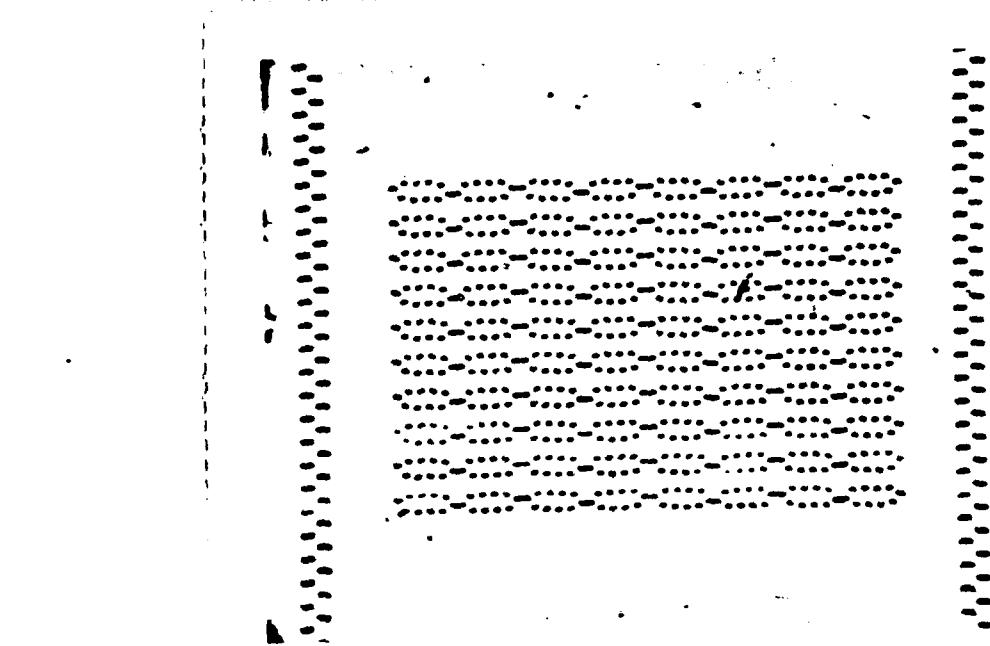
**Figure 4-23**: 160X photograph of minor loop array
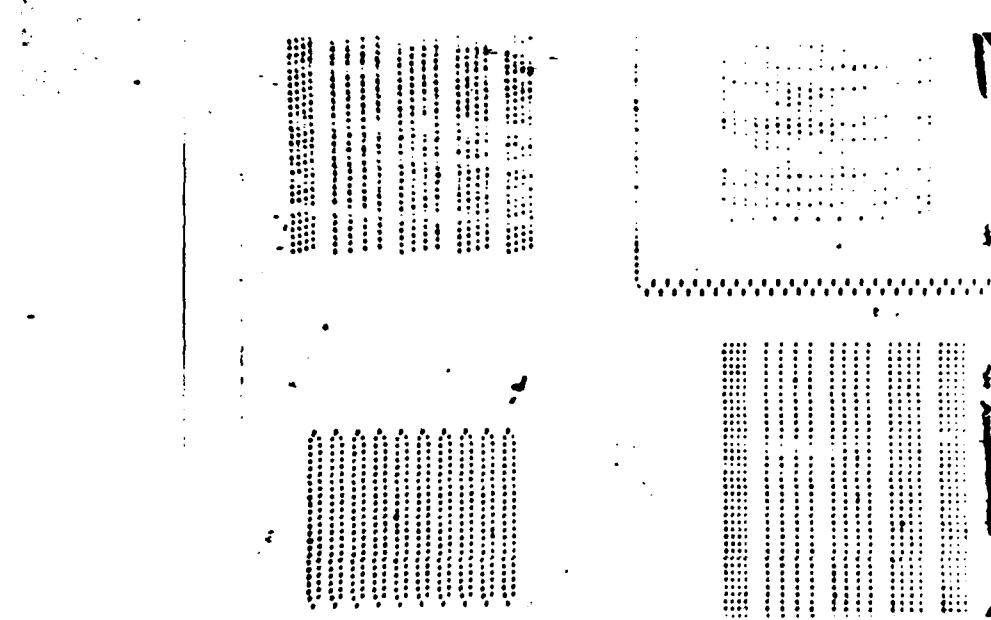
Figure 4-24: Major/minor loops and interaction test structures.
Magnification: 80X
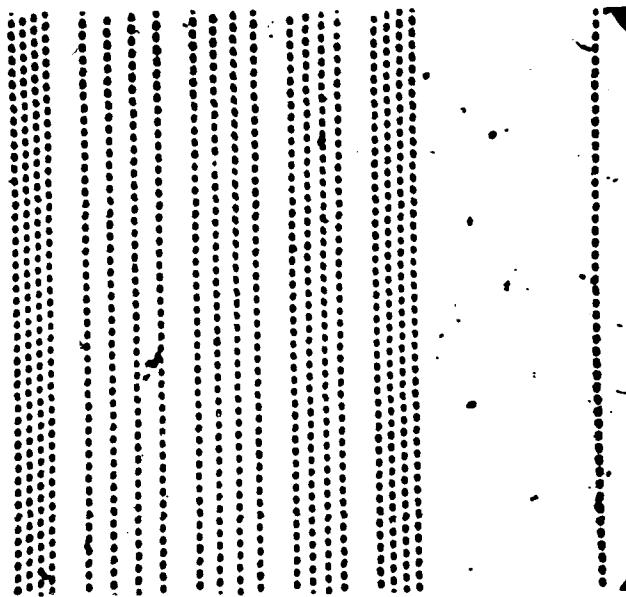
Figure 4-25: 160X photograph of interaction test structure
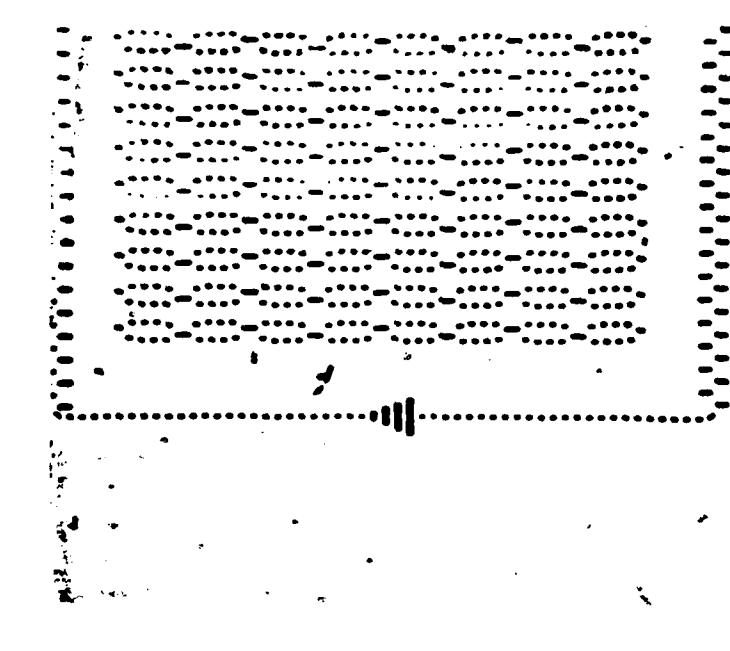
Figure 4-26: 160X photograph of stretcher design of Bobeck et. al.

79

References

1. A.H. Bobeck and H.E.D. Scovil, ""Magnetic Bubbles," *Scientific American*, Vol. 224, No. 6, June 1971, pp. 78 - 90.

2. Chang, Hsu, *Magnetic Bubble Technology*, IEEE Press, 1975, pp. 20.

3. Bobeck, A.H., Fischer, R.F., Perneski, A. J., Remeika, J.P., and Van Uitert, L.G., ""Application of Orthoferrites to Domain Wall Devices," *IEEE Transactions on Magnetics*, Vol. MAG-5, No. 3, September 1969, pp. 544 - 553.

4. Copeland, J.A., Elward, J.P., Johnson, W.A., and Ruch, J.G., ""Single-Conductor Magnetic-Bubble Propagation Circuits," *The Journal of Applied Physics*, Vol. 42, No. 4, March 1971, pp. 1266 - 1267.

5. Walsh, T.J. and Charap, S.H., ""Novel Bubble Drive," *A.I.P. Conference Proceedings*, No. 24, 1974, pp. 550-551.

6. Bobeck, A.H., Blank, S.L., Butherus, A.D., Ciak, F.J., and Strauss, W., ""Current Access Magnetic Bubble Circuits," *The Bell System Technical Journal*, Vol. 58, No. 6, July-August 1979, .

7. Braun, L., ""Electromigration Testing-A Current Problem," *Microelectronics and Reliability*, Vol. 13, 1974, pp. 215-228.

8. Nemirovsky, Y., Blech, I.A. and Yahalam, J., ""Abnormal Undercutting in Etched Cr/Au Films," *The Journal of the Electrochemical Society*, Vol. 125, No. 7, 1978, pp. 1177-1179.

9. Maissel, L.I. and Glaing, R., *Handbook of Thin Film Technology*, McGraw-Hill, New York,N.Y., 1970, pp. 7-35.

10. Reekstin, J.P. and Kowalchuk, R., ""Fabrication of Large Bubble Circuits," *IEEE Transactions on Magnetics*, Vol. MAG-9, No. 3, September 1973, pp. 485-488.

11. Sinha, A.K. and Sheng, T.T., ""The Temperature Dependence of Stresses in Aluminum Films on Oxidized Silicon Substrates," *Thin Solid Films*, Vol. 48, No. 2, February 1978, pp. 117-126.

12. Terry, L.E. and Wilson, R.W., ""Metallization Systems for Silicon Integrated Circuits," *Proceedings of the IEEE*, Vol. 57, No. 9, September 1969, pp. 1580-1586.

13. Dishman, J.M., Pierce, R.D., and Roman, B.J., ""Interaction of Domain Walls With Localized Stress Fields in Magnetostrictive Films," *Journal of Applied Physics*, Vol. 45, No. 9, September 1974, pp. 4076-4083.

14. Maissel, L.I. and Glaing, R., *Handbook of Thin Film Technology*, McGraw-Hill, New York,N.Y., 1970, pp. 7-53 - 7-56.

15. Vacuum Electronic Engineering Company, New Hyde Park, New York

16. Sloan Technology Corporation, Santa Barbara,CA

17. Perkin-Elmer Inc., Mountain View, CA

18.   Shipley Co. Inc.,Newton, Mass.

19.   Shipley Photo Resist Process Developement Guide

20.   Shipley Photo Resist Technical Manual

21.   Tegal Corporation, Novato, CA

22.   Cobilt Corporation, Sunnyvale, CA

23.   Maissel, L.I. and Glang, R., *Handbook of Thin Film Technology*, McGraw-Hill, New York,N.Y., 1970, pp. 7-52.

24.   Sol Krongelb, private communication

25.   Maissel, L.I. and Glang, R., *Handbook of Thin Film Technology*, McGraw-Hill, New York,N.Y., 1970, pp. 23-10.

26.   Kinsborn, E., Mc Iliar-Smith, C.M., and English, A.T., ""Failure of Small Thin-Film Conductors Due to High Current-Density Pulses," *IEEE Trans. on Electron Devices*, Vol. ED-26, No. 22, 1979, pp. 22-26.

27.   Anthony Tuxford, private communication

28.   Taft, E.A., ""Films From the Low Temperature Oxidation of Silane," *The Journal of The Electrochemical Society*, Vol. 126, No. 10, October 1979, pp. 1728-1731.

29.   Hammer, W.N. and Ahn, K.Y., ""Effects of Oxygen on Properties of R.F. Sputtered NiFe Films," *The Journal of Vacuum Science and Technology*, Vol. 17, No. 4, July-August 1980, pp. 804-807.

30.   Maissel, L.I. and Schaible, P.M., ""Thin Films Deposited By Bias Sputtering," *Journal of Applied Physics*, Vol. 36, No. 1, January 1965, pp. 237-242.

31.   Serikawa, T., ""Step Coverage of RF-Diode Sputtered SiO_2 Films," *The Journal of Vacuum Science and Technology*, Vol. 17, No. 2, March/April 1980, pp. 582-586.

32.   Kennedy, T.N., ""Sputtered Insulator Film Contouring Over Substrate Topography," *The Journal of Vacuum Science and Technology*, Vol. 13, No. 6, Nov./Dec. 1976, pp. 1135-1137.

33.   Neureuther, A.R.,Ting, C.H. and Liu, C-Y., ""Application of Line-Edge Profile Simulation to Thin Film Deposition Processes," *IEEE Transactions on Electron Devices*, Vol. ED-27, No. 8, August 1980, pp. 1449 - 1455.

34.   Jones, R.E., ""Theories of the Distribution of Deposit from Sputtered Disk and Rectangular Electrodes," *IBM Journal of Research and Developement*, Vol. 27, No. 16, January 1972, pp. 27 - 34.

35.   Westwood, W.D., ""Calculation of Deposition Rates in Diode Sputtering Systems," *The Journal of Vacuum Science and Technology*, Vol. 1, No. 15, Jan./Feb. 1978, pp. 1 - 9.

ACKNOWLEDGEMENTS

CURRENT-ACCESS ION-IMPLANTED BUBBLE DEVICE STRUCTURE

H. Ohta[a] and M. H. Kryder[b]

Carnegie-Mellon University, Pittsburgh, PA 15213

ABSTRACT

A hybrid current-accessed ion-implanted bubble device structure has been demonstrated to circulate bubbles around disk shaped structures using currents in apertured conductor sheets to access charged walls in ion-implanted layers of garnet. Measurements of the collapse field of bubbles indicate that with the new structure, magnetic poles produced by charged walls are made to add to the poles produced by currents flowing around apertures in conductor sheets, increasing the potential well of the bubble domains. As a result of the increased potential well the new structure requires less drive. Measurements show that, to circulate $1 \mu m$ bubbles in a double layer GdTmGaYIG/EuTmGaY G garnet around $6 \mu m$ disks, a linear current density of about $1.4 mA/\mu m$ is required, whereas more than $2.6 mA/\mu m$ was required in a conventional current-access apertured-sheet device fabricated on the same chip. This difference in minimum drive corresponds to a reduction in power dissipation per unit area by about a factor of four in the current-access ion-implanted structure.

PACS numbers: 85.70.-w, 85.70.Ge

INTRODUCTION

Field accessed magnetic bubble devices employing permalloy elements defined on a chip and a globally applied rotating magnetic field are presently being manufactured and marketed. Field accessed ion implanted contiguous disk devices presently appear to be the most promising successor to the permalloy devices because they offer up to a sixteen- fold gain in bit density on a chip with no change in minimum lithographic resolution (1). Both of these field accessed devices have relatively low on-chip power dissipation, but also a relatively low bit rate due to the fact that the coils used to produce the magnetic fields present a high inductance load to the current drivers.

Current accessed bubble devices using on-chip conductor lines to propagate bubbles present a low impedance load to current drivers and are potentially capable of being operated at much higher drive frequencies. However, recent past attempts to develop current accessed devices (2) have been impeded by high on-chip power dissipation (3).

Here we report on a new device structure which has potential to offer the density of ion implanted contiguous disk devices and the high data rate of current accessed devices with reduced on-chip power dissipation. This structure employs currents in apertured conductor sheets to access charged walls in an ion implanted layer of magnetic garnet thin films.

EXPERIMENTAL DEVICE STRUCTURE

To test and demonstrate the current accessed charged wall device structure and to provide meaningful comparisons to the field accessed contiguous disk structure and the current accessed apertured

sheet structure, all three structures were fabricated together on a two layer garnet (GdYTmGaIG on EuYTmGaIG) recently employed for ion implanted contiguous disk devices supporting $1 \mu m$ diameter bubbles (1). A diagram of the three structures investigated is shown in Fig. 1. In (a), a conventional field-accessed ion implanted device structure is shown. An external drive field produces charged walls at the positions shown and the bubble is attracted to the positively charged wall as indicated. In (b), a conventional current accessed apertured sheet device structure is shown. Currents diverge around the aperture in the conductor sheet creating an attractive potential energy well for the bubble domain at the position indicated. In (c), the new current-accessed charged-wall device structure is shown. Here an apertured conductor sheet coincides with the ion-implanted pattern. Currents in the apertured sheet of Fig. 1c have two effects: [1] as in Fig. 1a, due to the divergence of the current around the aperture, an attractive H_z field is created for the bubble at the edge of the disk and [2] the currents produce an in-plane component of field in the same direction (H_x) as the externally applied field in Fig. 1b which accesses the charged walls in the ion implanted layer around the aperture. To circulate a bubble domain around the disk, a rotating current density is applied to the conductor sheet. This may be accomplished by attaching four orthogonal leads to the sheet and driving with currents $J_x = J \sin \omega t$ and $J_y = J \cos \omega t$.

The three structures were fabricated on the same wafer with no critical mark alignments by using photoresist as an ion implantation mask and also as a mask for electroplating of gold metallurgy into areas containing a Cr/Au plating base. Figure 2 shows the process used to fabricate the current accessed ion implanted structure in Fig. 1c. After vacuum deposition of a plating base of 150Å Cr and 200Å Au, photoresist was spun onto the wafer, masked and developed so that photoresist remained only in the disks which were not to be implanted (Fig. 2a). The entire wafer was then ion-implanted with helium (80 keV, $3.5 \times 10^{15}/cm^2 + 30 keV, 1.2 \times 10^{15}/cm^2$). The ion energy was sufficiently high to penetrate the thin plating base, whereas the photoresist was sufficiently thick that it acted as an implantation mask. After implantation gold was electroplated through the photoresist mask creating the 4000Å thick conductor metallurgy with apertures over the unimplanted disks. The photoresist could then be removed and the entire pattern sputter etched to remove the plating base from the apertures (Fig. 2b); however, for the experiments described here, the Cr/Au plating base was left on. The thin Cr/Au plating base provides a uniform reflecting layer for observation of the magnetic bubbles in a reflected light microscope, and distorts the current flow in only a minor way since the thin Cr/Au offers a much higher resistance path than the thicker electroplated Au.

EXPERIMENTAL RESULTS

To compare the three structures in Fig. 1, the potential well of bubbles on the three structures was measured as a function of applied field and current. Figure 3 shows a plot of the collapse field

of a bubble on 6μm and 8μm diameter ion-implanted disks as a function of the in-plane field used to stabilize the bubble location. Data are given for the in-plane field oriented along a stable-bubble position (easy stripe-out direction (4)) and along an unstable-bubble position. As can be seen, the bubble collapse field in a stable-bubble position is a decreasing function of applied field indicating that the charged wall has its maximum strength at zero or slightly negative applied fields. On the other hand, when the field is applied in the unstable-bubble direction, the collapse field first increases approximately linearly with in-plane field, before reaching a maximum and decreasing.

The initial increase in collapse field of a bubble in an unstable-bubble position with in-plane field is presumably due to the fact that the unstable-bubble position corresponds with a normally weak charged wall. By increasing the applied field the charged wall can be strengthened until further increases in the field cause the magnetization on both sides of the wall to begin aligning with the field, reducing the strength of the wall. It is noted that to drive a bubble completely around a disk it is necessary to circulate a bubble through both stable and unstable positions. Hence, although the collapse field in the stable position decreases with increasing field, the collapse field observed during circulation around a disk can be expected to increase initially, since for low inplane field, the lowest collapse field occurs in the unstable position.

Data on the collapse fields of bubbles in the current accessed structures as a function of applied linear current density J (in ma/μm) are shown in Fig. 4. To perform these measurements a d.c. bias field was first applied to stabilize the bubble, and a current in the conductor sheet was used to position the bubble in the desired location. Then to avoid ohmic heating, the current was removed. To measure the collapse field without significant temperature changes both the current in the conductor sheet and a supplemental bias field were then pulsed. The current pulse width was about 10μsec and the supplemental bias pulse, which was applied near the center of the current pulse, was about 5μsec in width. By adjusting the magnitude of the total bias field, the collapse field of the bubble could be determined without significant ohmic heating of the device. Unfortunately in using this technique it was not possible to hold the bubble in an unstable-bubble position. Therefore data are shown in Fig. 4 only for the stable-bubble position. In the conventional current-accesed structure of Fig. 1b, the collapse field of the bubble is seen to increase linearly with current density, as would be expected. The collapse field of bubbles on the current-accessed ion-implanted device also increase with current density, but non-linearly and somewhat slower than in the current accessed device.

To understand why the hybrid device structure has a slower increase in collapse field in the stable-bubble position with current density than the conventional apertured-sheet device, it is only necessary to note in Fig. 3 that the bubble collapse field of a bubble in a stable-bubble location decreases with increasing in-plane field. The linear sheet current density produces a field

$$H(oe) = 2\pi \ J(mA/\mu m) \tag{1}$$

just below the conductor sheet. Thus, with J=2mA/μm, H=12.6Oe. In

Fig. 3 the collapse field for a bubble in a stable-bubble position on an $8\mu m$ disk is reduced by about 4 Oe at $H_{in} \approx 12.6$ Oe. This corresponds with the 4 Oe decrease in collapse field shown in Fig. 4 at $J=2mA/\mu m$. The non-linearity in the data of Fig. 4 at $J \gtrsim 3mA/\mu m$ is not understood and exhibits hysteresis. It may be due to a hysteretic charged wall structure which forms as a result of the combined inplane and perpendicular fields at the aperture edge.

It should be emphasized that, although the rate of increase of collapse field with drive current in the hybrid structure in Fig. 5 is somewhat slower than that of the conventional apertured sheet structure, the magnitude of the collapse field and therefore the potential well in the hybrid device is much higher throughout the range of practical measurement. In Fig. 4 the hybrid device is seen to have a minimum collapse field of 391 Oe at $J=0$, whereas the maximum collapse field in the apertured sheet structure is 367 Oe at $J=4mA/\mu m$. Furthermore, it can be expected that, for current densities up to at least $2mA/\mu m$, the collapse field of a bubble in the unstable position would increase faster in the hybrid structure than in the conventional structure, as indicated by the initial positive slope of data in Fig. 3.

The bias field margins for circulation of a bubble around a disk in the hybrid structure were found to be significantly better than those for the conventional apertured sheet structure. Figure 5 compares the bias field margins for circulation around a $6\mu m$ disk using the hybrid structure and the conventional apertured sheet structure. The minimum drive current in the hybrid structure is less than 1.4 $mA/\mu m$, whereas the minimum drive current for the apertured sheet structure is more than $2.6mA/\mu m$. Since the power dissipation per unit area varies as the square of the current density, the hybrid structure requires about one-fourth the power of the apertured sheet structure.

CONCLUSIONS

The data in the previous section show the hybrid ion-implanted current-accessed structure to offer significantly lower power dissipation than a conventional apertured sheet structure, because not only fields from the current, but also fields from the current-accessed charged-wall act on the bubble domain. In the structure discussed here a minimum drive current of $1.4mA/\mu m$ was achieved for circulating $1\mu m$ diameter bubbles around $6\mu m$ diameter disks. We believe this minimum drive current density may be decreased further by use of lower coercive force bubble materials and improved fabrication techniques. The bubble materials chosen here are standard materials used for field accessed contiguous disk devices, and no attempt has been made to reduce coercivity to a minimum. Additionally, the deposition of Cr onto the surface of an ion-implanted garnet has been shown to have detrimental effects on the margins of field-accessed contiguous disk devices (5). Hence a thin layer of SiO_2 between the garnet and plating base may reduce the drive current requirements below those obtained here.

5

ACKNOWLEDGEMENT

The authors would like to thank Dr. Y. S. Lin at IBM Corporation for having the samples used in this study ion implanted.

REFERENCES

a) H. Ohta is now with Mobara Works, Hitachi Ltd, Chiba, Japan
b) This work was supported by the Air Force Office of Scientific Research under grant AFOSR-080-0284 and the National Science Foundation under grant ECS-7912677.
1) Y. S. Lin, G. S. Almasi, G. E. Keefe, and E. W. Pugh, IEEE Trans. Magnet., MAG-15, 1642 (1979).
2) A. H. Bobeck, S. L. Blank, A. D. Butherus, F. J. Ciak, and W. Strauss, Bell Sys. Tech. J., 58, 1453 (1979).
3) M. H. Kryder, IEEE Trans. Magnet., MAG-17, 2392 (1981).
4) Y. S. Lin, D. B. Dove, S. Schwarzl, and C. C. Shir, IEEE Trans. Magnet., MAG-14, 494 (1978).
5) K. Y. Ahn and G. E. Keefe, IEEE Trans. Magnet., MAG-16, 553 (1980.

Figure 1. Diagrams of three bubble device structures: (a) ion-implanted contiguous disk (b) current-accessed perforated sheet and (c) hybrid current-accessed, ion-implanted structures.
Figure 2. The process used to fabricate the hybrid current-accessed, ion-implanted structures.
Figure 3. A plot of collapse field as a function of in-plane field for ion implanted devices.
Figure 4. A plot of collapse field as a function of linear current density for the apertured sheet and hybrid structures.
Figure 5. Operating margins for the hybrid structure and the apertured sheet structure.

FIGURE 1

| Ion – Implanted Contiguous Disk	Current – Accessed Perforated Sheet	Current – Accessed Ion – Implanted Contiguous Disk
(a)	(b)	(c)
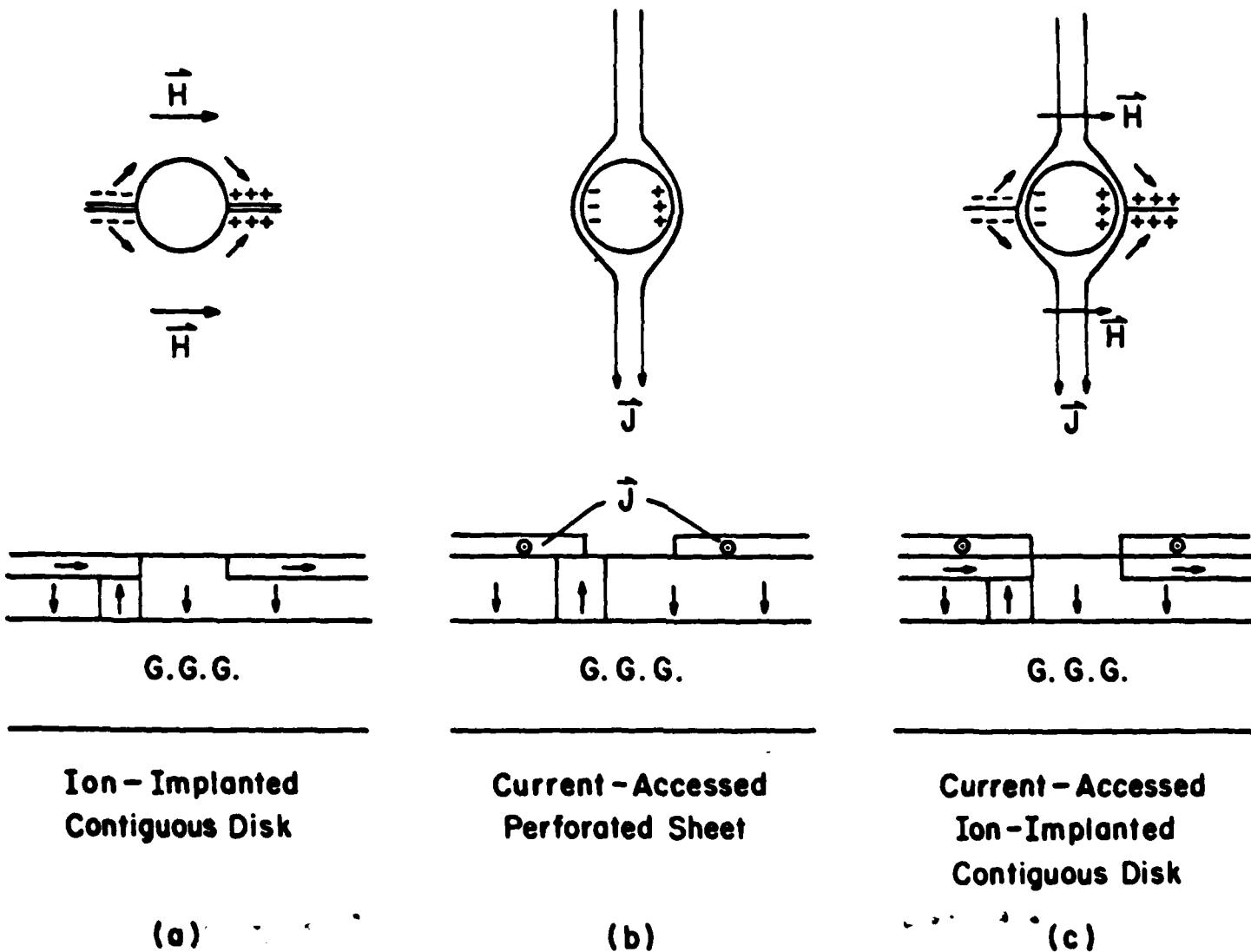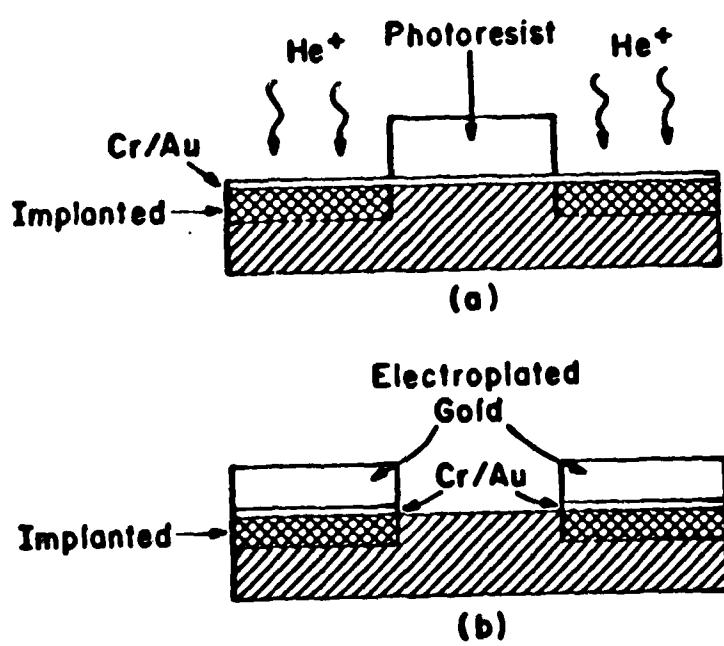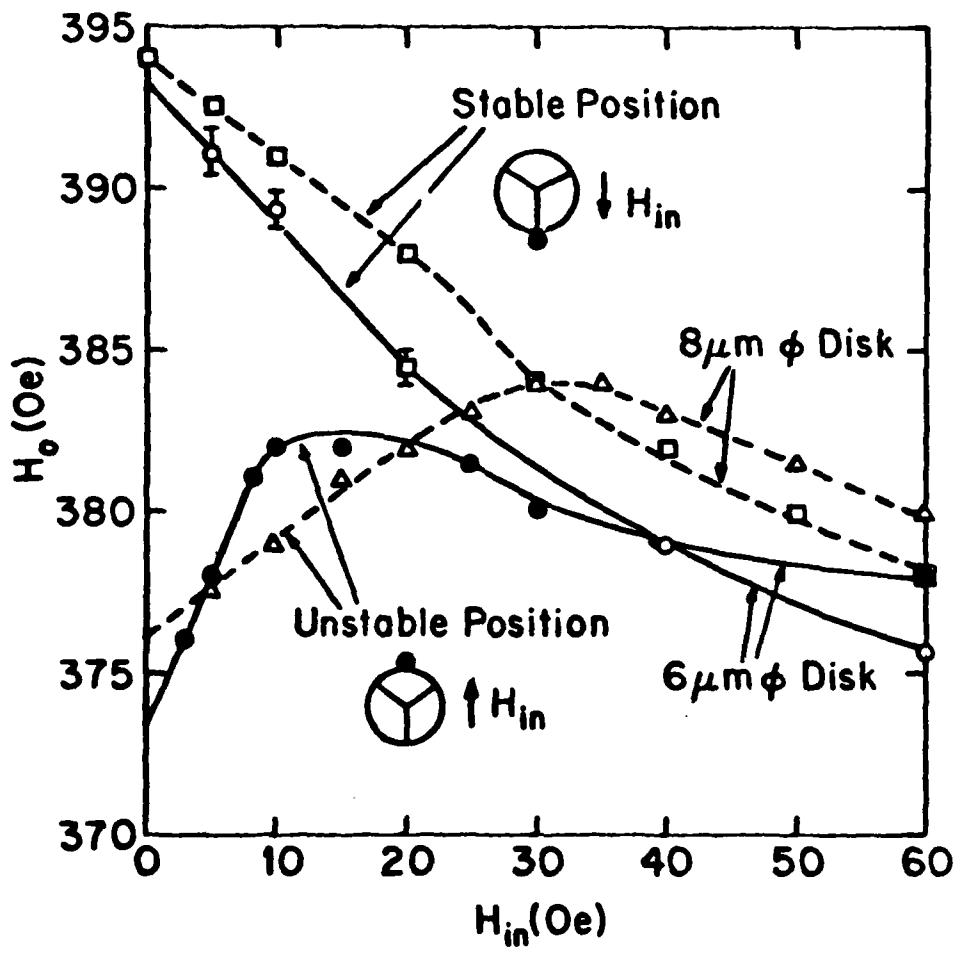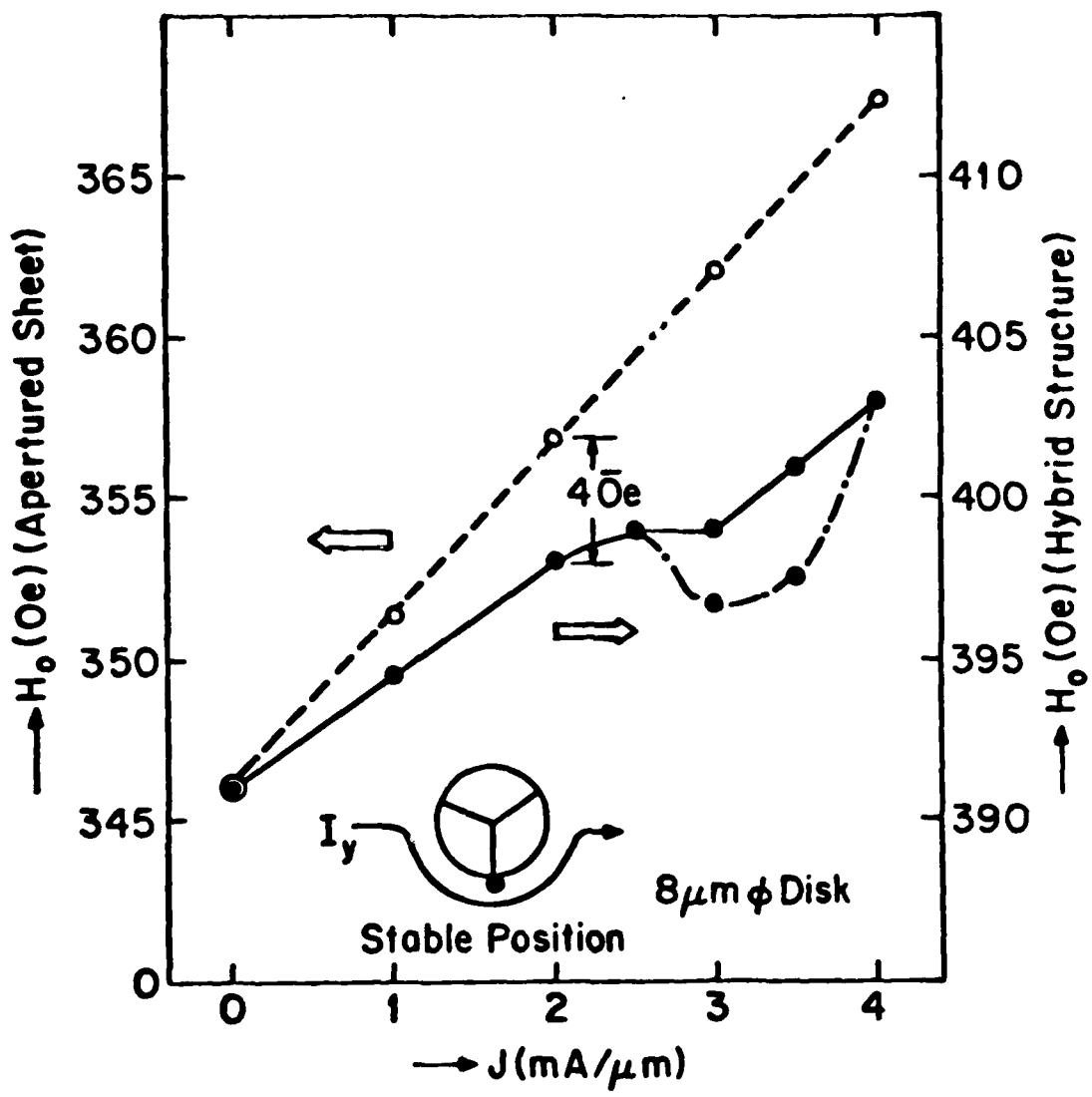
FIGURE 2

FIGURE 3

FIGURE 4
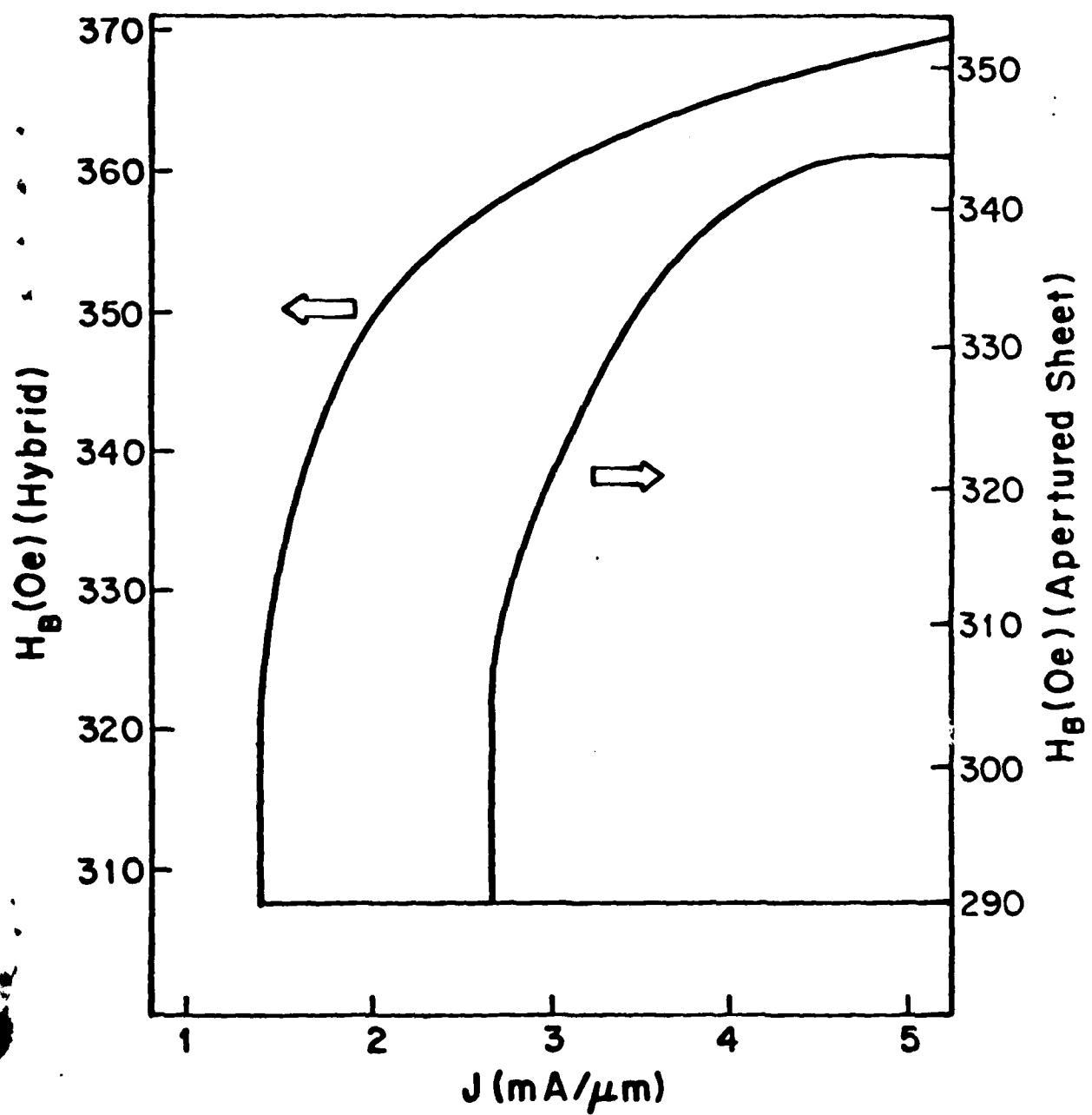
FIGURE 5

END

DATE
FILMED

9 - 82

DTIC